Shear Capacity of Hollow-Core Slabs with Concrete Filled Cores

A THESIS
SUBMITTED TO THE FACULTY OF THE
UNIVERSITY OF MINNESOTA
BY

Matthew R. McDermott

IN PARTIAL FULFILLMENT OF THE REQUIREMENTS
FOR THE DEGREE OF MASTER OF SCIENCE

DR. BENJAMIN Z. DYMOND

August 2018

Acknowledgements

I would like to begin by thanking Molin Concrete Products of Lino Lakes, MN for their generous support in providing specimens and accommodating the unique fabrication needs of this project. Further, my partnership with Paul Kourajian of Molin provided an essential and valuable industry perspective. His thoughtful advice and genuine commitment to the project are much appreciated.

I am thankful for the Precast/Prestressed Concrete Institute which provided financial support through the PCI Daniel P. Jenny Research Fellowship Program. Beyond the monetary commitment, I am grateful for the PCI advisory committee appointed to my project who shared their decades of cumulative precast experience and helped shape the nature of my project to be effective and meaningful for the precast industry.

At the core of my project, I am extremely grateful for the persistent guidance and support from my advisor, Dr. Ben Dymond. He consistently motivated me to be my best, offered genuine encouragement throughout, and served as a role model in the professional world and beyond. His technical expertise and attention to detail were essential to the success and quality of this project.

I also had an exceptional committee of whom I would like to thank. Dr. Brian Hinderliter dedicated much time and sincere effort in reviewing my work. Additionally, Dr. Andrea Schokker was an irreplaceable mentor throughout my time in college. She introduced me to the world of prestressed concrete design, connected me with invaluable professional opportunities, and dedicated much of her time towards reviewing this project.

I am tremendously thankful for my fellow structural graduate students who made my time in graduate school one of the best years yet. They selflessly volunteered their time to help in the lab throughout the project and daily supported me. I will always cherish the relationships we made and the time we spent together, both in school and beyond.

Finally, I would like to sincerely thank my parents for their unwavering encouragement and excitement for my work. Their enthusiasm and committed support were an immense blessing throughout college and this project. I am very thankful for them and proud of the way they raised me.

Abstract

Precast, prestressed, extruded hollow-core slabs are commonly used as floor and roof systems in concrete structures. This member is an economical and efficient cross section because it is fabricated with continuous voids along the length that reduce weight while maintaining strength. The extrusion manufacturing method is not conducive to using transverse shear reinforcement, so concrete failure generally governs the shear capacity. Adding slab cross-sectional area is the intuitive way to increase the available shear capacity, but this increases the unit weight, may require a deeper section, and can raise material costs. This project investigated an alternative method to add shear capacity by filling the cores with concrete where the expected shear demand was greater than the capacity. By targeting the local regions requiring increased shear capacity, this method was a practical means to economically add shear capacity. While this practice is already used in the industry, the core fill performance has not been studied thoroughly.

Core fill concrete was added to cured slabs and added immediately following extrusion of new slabs to characterize how the core fill timing affected the shear strength. One slab that was immediately core-filled was aged for 209 days to study the long-term shear strength of core-filled slabs. Additionally, several novel core fill modifications, such as including welded wire reinforcement in the core fill, roughening the slab walls prior to core filling, using steel fiber-reinforced core fill concrete, and placing longitudinal rebar in the core fill concrete, were tested to evaluate their potential for improving the hollow-core slab shear capacity.

Where core fill concrete was added to cured slabs, the core fill concrete behaved as unreinforced concrete, and slabs with core fill added immediately following extrusion behaved as if the core fill concrete was fully prestressed. The 209-day test of an immediately core-filled slab had a shear strength lower than that of the identically fabricated slab tested about a month after fabrication. Additionally, the core fill concrete of the 209-day specimen behaved as unreinforced concrete. Of the core fill modifications, only the slab wall roughening provided slightly improved shear performance compared to the typical immediate filled specimen. Specimens where the core fill concrete remained

composite with the slab concrete following web-shear failure had the highest web-shear strengths, which indicated that bond between the core fill concrete and slab concrete is a critical factor in the shear strength of hollow-core slabs with filled cores. All test results were compared to an assortment of Code and Specification predictions for web-shear capacity. Using the ACI 318 (2018) web-shear strength equation for the slab with the core fill treated as unreinforced concrete provided consistently conservative estimates of capacity for all of the specimens.

Table of Contents

List of Tables

List of Figures

Notation

A_c = Concrete area, in.^{2}

A_{cf} = Core fill concrete area, in.^{2}

A_{cfp} = Core fill area above the critical point, in.^{2}

A_{cp} = Slab area above the critical point, in.^{2}

A_g = Gross cross-sectional area, in.^{2}

A_{ps} = Area of prestressing steel, in.^{2}

A_s = Area of nonprestressed tension reinforcement, in.^{2}

A_v = Area of shear reinforcement within spacing s, in.^{2}

a = Shear span, in.

a_g = Maximum aggregate size, in.

a/d_p = Shear span-to-depth ratio with reference to the prestressing strand depth, d_p

a/h = Shear span-to-depth ratio with reference to the section depth, h

b_{cf} = Core fill width, in.

b_v = Width of web, in.

b_w = Width of web, in.

d = Distance from extreme compression fiber to centroid of longitudinal tension reinforcement, in.

d_b = Nominal diameter of prestressing strand, in.

d_p = Distance from extreme compression fiber to centroid of prestressing reinforcement, in.

d_v = Effective shear depth taken as the distance, measured perpendicular to the neutral axis, between the resultants of the tensile and compressive forces due to flexure; it need not be taken to be less than the greater of $0.9d_p$ or $0.72h$, in.

E_p = Modulus of elasticity of prestressing steel, ksi

E_s = Modulus of elasticity of transverse steel reinforcement, ksi

f'_c = Nominal compressive strength of slab concrete, psi

f'_{cf} = Nominal compressive strength of core fill concrete, psi

f_{ct} = Splitting tensile strength of slab concrete, psi

f_{cft} = Splitting tensile strength of core fill concrete, psi

f_{pc} = Compressive stress in concrete, after allowance for all prestress losses, at centroid of cross section resisting externally applied loads, psi

f_{pi} = Prestressing steel stress immediately prior to transfer, ksi

f_{po} = Parameter taken as the modulus of elasticity of prestressing tendons multiplied by the locked-in difference in strain between the prestressing and the surrounding concrete, ksi

f_{ps} = Stress in prestressing reinforcement at nominal flexural strength, psi

f_{pu} = Specified tensile strength of prestressing steel, ksi

f_{se} = Effective stress in prestressing reinforcement, after allowance for all prestress losses, psi

f_{yt} = Specified yield strength of transverse reinforcement, psi

h = Section depth, in.

I = Moment of inertia, in.^{4}

I_{cf} = Moment of inertial of core fill about the slab neutral axis, in.^{4}

L = Test span length, in.

L_t = Transfer length, in.

l = Span length of hollow-core slab, ft

M_{cre} = Moment causing flexural cracking at section due to externally applied loads, in.-lbf

M_{max} = Maximum factored moment at section due to externally applied loads, in.-lbf

M_u = Factored moment at critical section, kip-in.

N_u = Factored axial force, taken as positive if tensile and negative if compressive, kips

P = Total prestressing force, kips

Q = First moment of area about the slab neutral axis, in.^{3}

Q_{cf} = First moment of area of the core fill concrete about the slab neutral axis, in.^{3}

s = Center-to-center spacing of transverse reinforcement, in.

s_x = The lesser of the effective shear depth, d_v, or the distance between longitudinal crack control reinforcement, in.

s_{xe} = Crack spacing parameter as influenced by aggregate size, in.

V = Shear force, lbf

V_c = Nominal shear capacity provided by concrete, lbf

V_{cw} = Nominal shear capacity provided by concrete where diagonal cracking results from high principal tensile stress in web, lbf

V_d = Shear force at section due to unfactored dead load, lbf

V_i = Factored shear force at section due to externally applied loads occurring simultaneously with M_{max}, lbf

V_n = Nominal shear resistance of the section considered, lbf

V_p = Vertical component of effective prestress force at section, lbf

V_s = Nominal shear capacity provided by shear reinforcement, lbf

β = Factor relating effect of longitudinal strain on the shear capacity of concrete, as indicated by the ability of diagonally cracked concrete to transmit tension

δ = Measured deflection at load point adjusted for support deformations, in.

δ_{es} = Measured end slip of strand, in.

δ_{LP} = Average of LVDT pair measurements at load point, in.

δ_{S1} = Average of LVDT pair measurements at support nearest applied load, in.

δ_{S2} = Average of LVDT pair measurements at support furthest from applied load, in.

ε_s = Net longitudinal tensile strain at the centroid of prestressing

ϕ = Strength reduction factor

τ = Shear stress, psi

Chapter 1: Introduction

1.1 Background of Hollow-Core Slabs

Precast, prestressed, hollow-core slabs are commonly used as floor and roof systems in concrete buildings, parking garages, and other building structures. This type of member is an economical and efficient cross section because it is fabricated with continuous voids along the length. With the reduced cross-sectional area at mid-depth, the member selfweight is significantly decreased while only slightly affecting flexural capacity because cross-sectional area at the extreme fibers and member depth is maintained thus preserving the internal moment arm. Beyond structural benefits, the voids in hollow-core slabs allow for concealed routing of electrical and ventilation systems. As a floor or roof system, hollow-core slabs behave as a dependable diaphragm for resolution of lateral forces in buildings. Additionally, hollow-core slabs inherently provide significant fire resistance, thermal insulation, and reduction of sound transmission. Finally, since hollow-core slabs are a part of a precast building system, they can be quickly erected and may be constructed in cold climates (Buettner and Becker, 2015).

Hollow-core slabs are most commonly fabricated by either the extrusion or slip-form methods. In both methods, the desired strand configuration is placed on a long (200-800 ft) prestressing bed and tensioned. In the extrusion method, an extruder forcefully drives no-slump concrete through the machine using augers to create the voids. In the slip-form method, low slump concrete is fed into a casting machine with traveling formwork, and fixed pneumatic tubes are used to create the voids. In both methods, a continuous prismatic slab is produced along the entire length of the bed, as shown in Figure 1.1. The continuous slab is cured rapidly by using a steam curing method, and the strand stress is transferred to the concrete member the following day. Commonly, just before production begins again the next day, the large continuous slab is cut (transferring the strand stress) to the project-specific lengths and removed from the fabrication line. With little required manual labor, large production volumes, and quick turnover, these methods allow for extremely efficient and repetitive fabrication of slabs.

The fixed-form method of hollow-core slab production is a different, more conventional method still used in production of shallow or narrow slabs. Reusable steel formwork is used with rubber tubes, which are placed at the desired void locations. The tubes are pneumatically controlled to provide a rigid surface during casting and curing. After the formwork is prepared, the desired prestressing strand configuration is placed and tensioned. With the fixed-form process, the steel form resists the prestress force, which requires substantial formwork rigidity. Following concrete placement, the members are cured in large ovens overnight. After adequate curing, the prestress stress is transferred to the member and the formwork is removed. The rubber tubes also have the ability to collapse during formwork stripping for removal. For simplicity, circular voids are most commonly employed in this fabrication method.

With the manufacturing tools used in production (e.g., standard extruder configuration and steel slip forms), hollow-core cross sections are relatively consistent across the precast industry. Most slabs are produced in 8, 10, 12, or 16 in. deep sections and in 2 or 4 ft widths, with a handful of void geometries. This standardization allows for very efficient production and design, which is the main benefit of precast concrete. Manufacturers offer a variety straight of strand configurations to produce several levels of prestress force that can be tailored to individual project requirements.

Overall, hollow-core slabs are a very efficient and viable solution for floor and roof systems in buildings. Their fabrication is relatively standard across the industry, which allows for simplicity in design and field erection.

1.2 Hollow-Core Filling

1.2.1 Core Filling Methods

The core filling process is relatively simple and easily implemented whether the fill material is added directly after extrusion or months after fabrication. Regardless of the timing, any number of cores can be filled, and the length of the core fill is unrestricted. Since adding core fill increases the rigidity of the filled region relative to the rest of the slab, manufacturers seek to fill cores in a symmetric fashion. For example, if one core is

filled in a hollow-core section with five voids, then the center core will be filled, as shown in Figure 1.2(a). Similarly, if two cores are filled, then the second and fourth core will likely be filled, as shown in Figure 1.2(b). Cores are commonly only filled within the length of the slab where web-shear failure may be an issue. This generally equates to the transfer length of the strands or, where the specific loading location is known, the length between the slab end and the point where shear enhancement becomes required.

When core fill is added during the extrusion process, the top flange above the core to be filled is broken, often with the heel of a worker's boot. The broken flange material is moved by hand to the end of the core fill length away from the slab end and packed into a plug to seal the rest of the unaltered core. This prevents the core fill concrete from moving into the rest of the slab and ensures a full-depth core fill. To fill the core, a portion of the concrete used for the slab material is placed in a small mixer and admixtures and water are added to improve the workability, shown in Figure 1.3. This concrete batch is used to fill the empty core and missing flange material. Finally, the top surface of the slab over the filled core is finished by hand, resulting in a smooth final surface. The entire process is generally completed within an hour after extrusion.

In situations where the loading is not known until after fabrication or where the loading requirements change after a slab is manufactured, the core fill shear enhancement strategy can still be implemented. In this scenario, a concrete saw is used to remove the top flange concrete above the desired core fill region. If the cured slab is still at the fabrication facility, the same concrete used for slab extrusion is often used with admixtures and added water for the core fill material (identical to the method described for immediate core filling). If the slab concrete mix is not available (e.g., if the slab is already on site) a comparable mix is employed. When the core fill concrete is added to the empty core, cardboard cutouts are often used to contain the concrete within the desired core fill length and prevent material from moving further into the slab. This containment step is important because the full-depth of the core fill is anticipated during shear enhancement design. If core fill concrete continues to move down the length of the core, it is difficult to ensure

that the core fill material is full-depth over its intended length. Finally, the surface of the core fill material is finished, and the specimen is allowed to cure.

These two methods of immediate core filling and core filling a cured slab represent the most common scenarios in which cores are filled (Buettner and Becker, 2015). As it relates to design, these scenarios also illustrate the unreinforced concrete and prestressed concrete bounding conditions of predicted core fill behavior. Namely, the core filling a cured slab scenario represents the case where the core fill may behave as unreinforced concrete and the immediate fill scenario represents the case where the core fill may behave as prestressed concrete.

1.2.2 Core Filling Benefits

Regardless of the scenario in which additional shear capacity is required for a hollow-core slab, there are generally several available options to enhance hollow-core shear performance. Some options include modifying the concrete mix of the slab by including fibers, adjusting the slab depth while introducing a concrete topping, and filling one or more cores with additional concrete. Each of these solutions have their own merits and drawbacks, making the most advantageous alternative application-specific.

Filling the cores of a section with additional concrete offers an efficient and flexible method to improve shear capacity of hollow-core sections. Perhaps the most distinguishable benefit is the ability to selectively implement core filling to specific slabs and locations within a slab. Often, shear capacity is only an issue where large bearing walls or columns transfer load to an individual slab. Across a floor system, these cases are generally isolated and unique. Unlike other methods, only the regions in a job-specific floor system that need additional shear capacity are modified with core filling. This decreases the overall required labor and increases the efficiency of this shear enhancement technique.

Additionally, cores can be filled at any stage of the manufacturing or installation process, which offers further implementation flexibility. Other solutions, such as steel fiber-reinforced concrete slabs, can only be implemented at a specific point in the lifespan of a slab (e.g., at fabrication in the plant), whereas additional core fill concrete can be added to freshly extruded slabs as well as cured slabs. Changes in applied load requirements late

in the design stage of a project is one of the reasons designers are faced with shear issues. In some cases, the additional shear demand is not realized until weeks after a slab is extruded. Flexibility in core fill timing can make this solution advantageous.

1.2.3 Core Filling Drawbacks

There are a few disadvantages associated with core filling that do not necessarily discredit the viability of this solution, rather they simply must be considered during design. First, filling cores with additional concrete requires labor. If cores are filled directly after extrusion, workers must factor the core filling delay into their production schedule. While the process only takes minutes, core filling many slabs in a production line can lead to a reasonable delay. Since precast facilities focus on efficient production of members, this additional labor time may be undesirable. Second, the extra core fill material adds to the selfweight of hollow-core slabs, which slightly decreases the overall structural efficiency of the cross section. Considering an entire slab, the added weight of core fill concrete is a small percentage of the selfweight. Finally, hollow-core slabs with core fill on both ends of the slab may experience issues with water drainage in conditions where the slab is exposed to moisture. If the structure is in a cold climate, trapped water may deteriorate the slab after many freeze-thaw cycles. Since the damage would be on the inside of a slab, deficiencies in structural integrity could go unnoticed. While these drawbacks must be considered, they do not generally negate core filling as a viable shear enhancement solution.

1.3 Impetus for Research

Hollow-core slabs are commonly employed in mid-sized commercial and residential construction. In these applications, a few lower levels of precast construction are frequently topped with several floors of wood construction, as shown in Figure 1.4. In these situations, wood bearing walls bear on hollow-core sections, as shown in Figure 1.5. Due to architectural floor layouts, sometimes the bearing walls fall in parallel with the length of a hollow-core section, as shown in Figure 1.6, and in other cases the bearing walls

fall transversely with the slab, as shown in Figure 1.7. Both scenarios may generate a significant line load that must be supported by a hollow-core section.

Per the Precast/Prestressed Concrete Institute (PCI) Manual for the Design of Hollow-core Slabs (2015), flexural demand is permitted to be resisted by a width larger than the section width in the middle region of the member span, as shown in Figure 1.8. Since load is distributed between slabs in the middle, the flexural demand for an individual section is alleviated. Unlike flexure, the distribution of shear at the ends of slabs in a hollow-core floor system is more convoluted. Slab loading is often eccentric, which results in torsional stresses across the section. Additionally, the shear keys between slabs enforce equal edge displacements among adjacent slabs and consequently cause some shear and torsion forces to transfer between the slabs. Due to the complexity of shear transfer in a hollow-core floor system, the current PCI design procedure does not allow for shear distribution at the ends of adjacent slabs to account for a worst-case shear loading. Therefore, a single hollow-core slab must carry the entire shear loading itself.

In a precast building with upper levels constructed with wood, the precast floor system generally has a well distributed design load over most of the floor, with the exception of large bearing or point loads at isolated locations. As a result, the depth of a hollow-core floor system is frequently designed to be sufficient for the general occupancy loading. Columns and bearing walls that are aligned longitudinally or transversely with a hollow-core slab may require additional web-shear capacity and possibly flexure-shear capacity at specific bearing wall or column locations. For each of these instances, additional shear capacity may need to be added since no shear load redistribution is permitted at the slab ends. To avoid deeper hollow-core sections where extra capacity is needed and maintain a consistent floor depth, internal hollow-core modification may be desired.

Web-shear capacity is influenced by several properties, including concrete tensile strength, axial prestress, cross-sectional area, and the vertical component of prestress. Web-shear behavior occurs at the ends of simply supported members and generally exists within the transfer length of prestressing strands. Hollow-core slabs are produced with straight

prestressing strand profiles placed low in the section to provide a greater prestressing strand moment arm from the slab neutral axis for slab flexural capacity. Due to common hollow-core slab manufacturing methods, it is not practical to include transverse shear reinforcement or employ hold-downs to generate draped strand profiles. Therefore, no vertical component of prestressing can contribute to web-shear capacity in hollow-core slabs. One common method of enhancing web-shear capacity in hollow-core slabs is to fill one or more of the cores with concrete, thus increasing the concrete cross-sectional area without affecting mix design or standard prestressing profiles. This method offers a direct solution to selectively increase the web-shear capacity of regions in slabs requiring shear enhancement. Additionally, the depth of the hollow-core slab remains the same, allowing for a consistent floor system depth.

While increasing cross-sectional area through core filling may improve web-shear capacity, it is difficult for designers to reliably quantify the increase in capacity. The American Concrete Institute (ACI) 318 Building Code Requirements for Structural Concrete (2014) offers an equation to calculate unreinforced concrete shear capacity as well as an equation to calculate prestressed concrete web-shear capacity. It is reasonable to expect the added core fill concrete to provide, at a minimum, the shear capacity calculated as if the core fill was an independent, unreinforced piece of concrete. In some scenarios, a hollow-core slab is fabricated months before the specific loading for a project is defined. In this case, if additional web-shear capacity is required, the fully cured section is cut open and fresh concrete will be added to the core. Because this new fill concrete is simply placed within a cured specimen, the core fill may act independently and have the shear capacity of unreinforced concrete. In a more common scenario, cores are filled at the time of fabrication. In this case, hollow-core slabs are extruded on a prestressing bed and specific cores are filled inside the still fresh slab concrete prior to transferring the strand stress. Because the extruded hollow-core concrete is in contact with the core fill concrete and allowed to cure before the strands are released, the core fill concrete could have the calculated shear capacity of prestressed concrete as a maximum.

Due to the differences in these two scenarios and variability in producer-specific manufacturing processes, designers have little certainty regarding the additional shear capacity provided by filled cores. As a result, designers can conservatively treat all core fill concrete as unreinforced concrete for shear design. Beyond demonstrating the fact that adding core fill concrete to a section will increase the overall shear capacity (Palmer and Schultz, 2009), little research has been conducted to investigate and quantify the additional shear capacity provided by the core fill concrete. Furthermore, there is a knowledge gap related to the potential for the core fill concrete to behave has fully or partially prestressed concrete.

While core filling is a common practice to improve shear capacity (Buettner and Becker, 2015), little research has been conducted to explore innovative ways to further enhance the shear capacity of concrete filled cores. This project included several tests of specimens with exploratory alterations to potentially improve the shear capacity of concrete filled cores with practical modifications to the core fill or core-filling method.

1.4 Research Objectives

This research program experimentally investigated the added web-shear capacity of hollow-core sections with concrete filled cores and quantified the core fill shear strength contribution. The program explored the effects of core fill timing relative to slab age and compared the results to various prediction methods from Codes and the literature. Additionally, several core fill strength enhancement strategies were explored, including: steel fiber-reinforced concrete core fill, roughening the slab core wall prior to core fill placement, introducing a longitudinal headed steel bar into the core fill material, and placing vertically-oriented welded wire steel mesh in the core fill. Ultimately, the project objective was to provide design recommendations to be used for reliably predicting the additional shear capacity of core fill concrete and experimentally identify potentially promising core fill improvement strategies.

1.5 Thesis Organization

Chapter 2 discusses the web-shear failure mode and presents an assortment of web-shear prediction methods currently used by designers. Additionally, a summary of relevant hollow-core research is presented. Portions of the previous research were used as a basis to generate the test matrix and experimental setup for this project.

Chapter 3 steps through the section selection, laboratory arrangement process and reasoning for the tests included in the testing matrix in this project. Furthermore, the specimen fabrication and laboratory procedures are discussed.

Chapter 4 describes slab behavior during testing and presents the shear test results of each specimen. Additionally, several shear strength prediction methods are evaluated, and the web-shear crack angles are discussed with regard to the shear test results.

Chapter 5 summarizes the testing program, provides conclusions based on this research program, and discusses recommendations for future research.

Figure 1.1. Extruding machine producing a long prismatic slab on a casting bed

Figure 1.2. (a) Hollow-core slab with one core filled in the center of the cross section and (b) hollow-core slab with two cores filled symmetrically

Figure 1.3. Small batch concrete mixer used to add admixtures and water to the slab concrete for production of the core fill concrete

Figure 1.4. Several floors of timber construction built on top of a precast hollow-core substructure

Figure 1.5. Wood bearing wall on a hollow-core floor system.

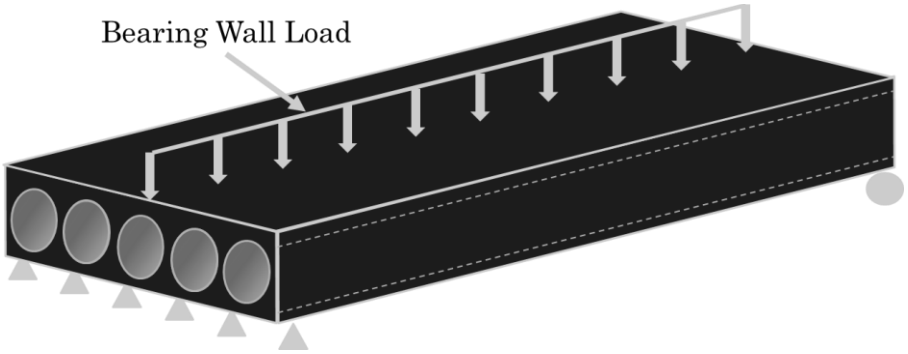

Figure 1.6. Bearing wall distributed load in-line with the longitudinal axis of a hollow-core slab

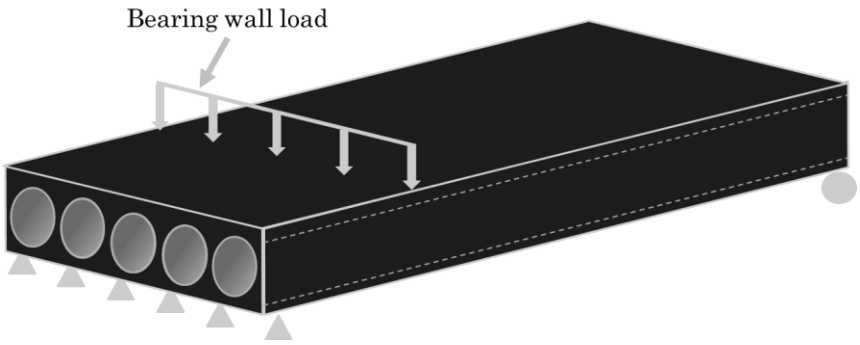

Figure 1.7. Bearing wall distributed line load transverse to the longitudinal axis of a hollow-core slab

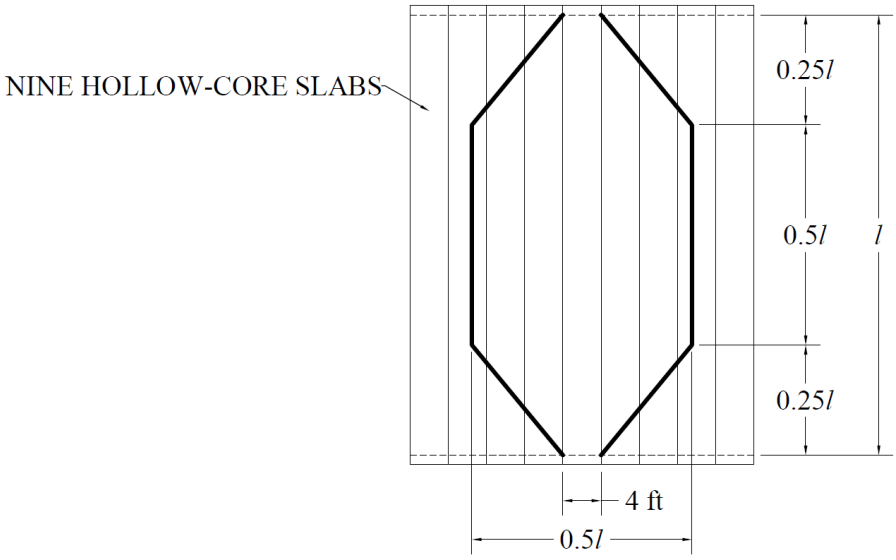

Figure 1.8. Plan view of a floor composed of nine hollow-core slabs showing the effective flexural resisting width

Chapter 2: Literature Review

2.1 Web-Shear Failure

The governing shear failure mode varies along the length of a prismatic, homogeneous, simply supported member. There are two different shear failure modes in prestressed concrete members. Typically, the flexure-shear failure mode controls closer to midspan. Flexure-shear cracks begin as vertical flexural cracks at the extreme fiber of a section. As they propagate, the combined effects of bending and shear cause the orientation of the cracks to shift more diagonally. Near the end regions of a span, where strands may not be fully developed, web-shear failure typically controls. This failure mechanism begins with cracking near the mid-depth of a given section and quickly propagates in a diagonal direction towards the extreme fibers of the section. The flexure-shear and web-shear failure modes and locations apply to most loading scenarios, but the specific bounds of each region along the beam length may vary. Figure 2.1 shows the typical shear failure mode regions and their respective crack profiles for a simply supported hollow-core slab.

Web-shear failure is fundamentally related to the principal tensile stress of the concrete. In hollow-core sections, the initial crack originates in one of the several webs where the vertical normal force from the support diminishes and the axial prestress force is not fully developed. This point is typically located near mid-depth of the section at about *h/2* from the support and is called the critical point. Web-shear failure occurs at the limiting web-shear capacity and the slab has very little residual strength following initial cracking, resulting in a brittle failure.

An understanding of the fundamental mechanics of web-shear failure is necessary to understand the basis on which design Codes are formulated. Several basic assumptions are typically adopted for idealization of concrete mechanics. These include assuming plane sections remain plane and the section behaves as a linear elastic, isotropic, and homogeneous material. While these assumptions may not perfectly characterize concrete due to its inherent variability, design provisions generally treat concrete as an idealized material and adopt the assumptions for the basis of their predictions.

2.2 Parameters Affecting Web-Shear Capacity of Prestressed Members

2.2.1 Cross-Sectional Geometry

Yang (1994) pioneered research regarding the influence of cross-sectional hollow-core geometry on web-shear capacity. Yang conducted a research program that included numerous finite element analyses and experimental tests, which were used to formulate a detailed design procedure for hollow-core slab web-shear capacity. Yang's Method attempted to incorporate additional parameters, such as the moment of inertia and first moment of area, which are not considered in ACI 318 (2014) shear predictions. Furthermore, the location of initial cracking, called the critical point, varies depending on cross section geometry in Yang's Method.

The critical point is the initial geometric location of cracking at the onset of web-shear failure. Yang found that the location of this point differed greatly depending on the hollow-core cross-sectional geometry. The shape of hollow-core voids and relative width of each web were found to be the most influential geometric features. The ACI 318 (2014) web-shear equation is based on the assumption that the critical point is located at *h/2* from the support face and at mid-depth of the section. Non-circular voids, as well as non-uniform web widths, affect the depth and location along the slab of the critical point. Due to the unique geometry of hollow-core slabs, Yang's Method often does not coincide with the ACI 318 (2014) predictions. Through development of this design procedure, shown in Equation 2.1, Yang showed that cross-sectional geometry influenced the critical point.

$$V_c = \frac{b_w I}{Q}\left\{\begin{array}{c} \frac{b_w}{2Q} f_{ct} x_{cp} z_{cp} + \frac{Q}{b_w}\left(\frac{e}{I} - \frac{A_{cp}}{A_c Q}\right)\frac{dN_p}{dx} + \\ \left[\left(\frac{b_w}{2Q} f_{ct} x_{cp} z_{cp}\right)^2 + \left(\frac{e}{I} - \frac{A_{cp}}{A_c Q}\right) f_{ct} x_{cp} z_{cp} \frac{dN_p}{dx} + \right. \\ \left. \left(\frac{1}{A_c} - \frac{z_{cp} e}{I}\right) N_p f_{ct} + {f_{ct}}^2 \right]^{1/2} \end{array}\right\} \qquad 2.1$$

For hollow-core slabs with non-circular voids, Yang stated that the critical point depth is located at the intersection of the narrowest web width and the bottom flange of the

slab. For voids that are perfectly circular and vertically centered in the section depth, this means the critical point will be located at mid-depth of the section. However, for voids that are non-circular, the critical point will be lower in the cross section profile. The intersection of a line extending from the support at an angle of 35° and a horizontal line denoting the critical point depth locates the critical point along the length of a section, as shown in Figure 2.2 (Yang, 1994). Consequently, the critical point will be located closer to the end of a hollow-core slab with non-circular voids because the critical point is lower in the cross section. Since web-shear failures generally occur within the prestressing transfer length, the axial prestress may be lower at the critical point of hollow-core slabs with non-circular voids than predicted by ACI 318 (2014) provisions, which assume the critical point is at mid-depth. Since the web-shear capacity is directly related to axial prestress, a lower prestress force will also reduce the web-shear capacity of a slab. From a design perspective, it is important to reassess the validity of shear design assumptions when hollow-core slabs with non-circular voids are used. While the ACI 318 (2014) prestressed concrete shear capacity equations may be the design Code specified on a project, structural engineers must evaluate whether the ACI 318 (2014) assumption of the critical point being at mid-depth applies to non-traditional hollow-core slab geometries during design.

2.2.2 Shear Lag of Prestressing

The straight prestressing strand pattern used in hollow-core slabs creates a horizontal axial precompression stress. In combination with the shear stress, the axial precompression causes the center of Mohr's circle to shift along the *x*-axis resulting in a decreased principal stress. Web-shear failure occurs on a diagonal plane perpendicular to the principal stress direction, so a decreased principal stress results in less demand at a given point in the section. The principal stress direction relative to a web-shear crack and the axial precompression force is shown in Figure 2.3. Since web-shear capacity generally controls within the transfer length where the prestress force is not fully developed and the transfer length can only be estimated, the exact precompression force is difficult to predict at a given section, which makes the web-shear capacity more difficult to predict.

In addition to uncertainty in the prestressing magnitude at a given section, shear lag influences the actual precompression stress at the critical depth for web-shear cracking. Shear lag is defined as a variation in the prestress force at a point in a cross section as a function of the distance between the given point and the prestressing strand. This "lag" can be assumed to radiate outward from the strand at an angle of 45° since concrete is not a perfectly rigid material. Within the transfer length of a hollow-core slab with straight prestressing strands, the axial concrete stress due to prestressing in the concrete immediately adjacent to a given strand will be greater than the axial concrete stress due to prestressing at a point radially further from the strand within the same plane along the longitudinal axis. With regards to web-shear capacity, this variation in axial prestress due to shear lag makes the magnitude of the axial prestressing component influencing the concrete tensile stress at the critical point difficult to precisely determine.

Several experimental programs have noted the influence of section depth on web-shear capacity, stating that unreinforced sections deeper than 12.5 in., as defined by ACI 318 (2014), without transverse shear reinforcement fail at stresses lower than predicted by ACI 318 (2014) previsions (Hawkins and Ghosh, 2006; Palmer and Schultz, 2009). While these findings are related to section depth, shear lag may be the direct reason for the phenomenon (Palmer and Schultz, 2009). Prestressing strand is commonly placed near the bottom extreme fiber of a section, while web-shear failure generally originates near mid-depth of a section. Thus, when the section depth increases, the eccentricity between the prestressing force and the web-shear critical point will increase. Since prestressing shear lag is a function of distance from the strand, the greater the strand eccentricity, the lower the prestress force will be at mid-depth of a given section along the transfer length. As a result, the shear stress at failure of hollow-core sections deeper than 12.5 in. may be lower than the shear stress at failure of shallower analogous sections because less axial prestress force is available at the critical point.

Since shear lag radiates in all directions from a given strand, the locations of strands and potential variations in precompression stress between strands (due to differences in strand sizes and their corresponding areas) may lead to differences in web-shear capacity

among specific webs of a hollow-core section. While an equally distributed axial prestress force is assumed in design, the slight variations in axial prestress realized in each web in a hollow-core section may affect their individual web-shear capacity.

2.2.3 Concrete Tensile Strength

The concrete contribution to web-shear capacity is also characterized by the concrete tensile strength. Unfortunately, tests to determine concrete tensile strength, such as the split cylinder test, are less commonly performed and often generate more widely scattered results compared to compressive tests (Hawkins et al., 2005). As a result, the compressive strength is often converted to a tensile strength by means of a power function. For example, the commentary for ACI 318 (2014) Section 19.2.4 relates concrete tensile strength to compressive strength as shown in Equation 2.2.

$$f_{ct} = 6.7\sqrt{f'_c} \tag{2.2}$$

It would be reasonable to expect web-shear strength to increase linearly with concrete tensile strength, but web-shear strength has been observed to increase with slightly diminishing returns when compared to increasing compressive strength. Some researchers believe this is because the diagonal shear crack surfaces are smoother in higher strength concrete, which may reduce the crack interface capacity (Hawkins et al., 2005).

2.2.4 Shear Span-to-Depth Ratio

Conventional Bernoulli beam behavior is more complex in the region near the supports of a member due to the influence of the supports. As a result, additional considerations such as arching action and bearing stresses must be examined when predicting the shear capacity near a member end. Specifically, arching action provides an inclined compression strut stemming from a support to the load and can significantly increase the shear capacity in regions near the support (Hawkins et al., 2005). Figure 2.4 shows a depiction of the inclined strut. Arching action was reduced by selecting an appropriate shear span span-to-depth ratio, a/d_p, as shown in Figure 2.5. This ratio can be used to characterize how the support location influences beam behavior. In the region with

an a/d_p ratio less than 2.5, arching action significantly impacts web-shear capacity (Hawkins et al., 2005). Through arching action, an inclined strut from the support to the load point is likely to form, which can significantly add to the shear capacity. This addition in strength is not considered in predictions based solely on the member cross section (Hawkins et al., 2005). As a result, it is important for experimental shear testing to mitigate arching action in the test arrangement to guarantee only shear behavior is exhibited for consideration by selecting a proper shear span.

2.3 Methods to Predict Shear Capacity

2.3.1 ACI 318 Building Code Requirements for Structural Concrete

The ACI 318 Building Code Requirements for Structural Concrete defines the nominal shear capacity of a section as the sum of the concrete shear capacity and transverse shear reinforcement capacity in ACI 318 (2014) Equation 22.5.1.1, as presented in Equation 2.3. The capacity of transverse steel based on ACI (2014) Equation 22.5.10.5.3 is presented in Equation 2.4.

$$V_n = V_c + V_s \tag{2.3}$$

$$V_s = \frac{A_v f_{yt} d}{s} \tag{2.4}$$

The transverse steel contribution to shear strength in Equation 2.3 is taken as zero for extruded hollow-core slabs because the extrusion manufacturing method is not conducive for the placement of traditional transverse shear reinforcement. In design, a strength reduction factor, ϕ, is applied to the nominal shear strength, V_n, to ensure a conservative design is achieved. To accurately compare shear capacity predictions with laboratory research, measured shear values needed to be compared to the nominal predicted shear strength. Therefore, the shear strength reduction factor was taken as 1.0.

ACI 318 (2014) provides several concrete shear capacity prediction methods for different member types and levels of detail. These equations are permitted irrespective of

cross-sectional geometry. For the shear design of prestressed hollow-core members, the explicit calculations of web-shear and flexure-shear capacity are most applicable. The ACI 318 (2014) ACI 318 (2014) Equation 22.5.8.3.1 for flexure-shear capacity and Equation 22.5.8.3.2 for web-shear are shown in Equations 2.5 and 2.6, respectively.

$$V_{ci} = 0.6\sqrt{f'_c}b_w d_p + V_d + \frac{V_i M_{cre}}{M_{max}} \geq 1.7\sqrt{f'_c}b_w d \tag{2.5}$$

$$V_{cw} = \left(3.5\sqrt{f'_c} + 0.3f_{pc}\right) b_w d_p + V_p \tag{2.6}$$

Only straight prestressing profiles are employed in extruded hollow-core sections because hold-downs to construct draped patterns are nearly impossible to incorporate in the common manufacturing processes. Therefore, the vertical component of prestressing force, V_p, is taken as zero in Equation 2.6. The web-shear equation in ACI 318 (2014), Equation 2.6, considers the nominal shear stress in a section, not the maximum shear stress. While this makes Equation 2.6 inherently conservative, it may better characterize a wider variety of prestressed concrete members.

ACI 318 (2014) Equation 25.4.8.1 specifies transfer length as shown in Equation 2.7. This equates to about $50d_b$ for prestressing with an ultimate tensile strength, f_{pu}, of 270 ksi stressed to $0.7f_{pu}$ with 20% total losses. While this simplified equation is widely used in normal concrete design, it may not capture the true bond behavior of the strands as only the strand diameter and stress are considered. For the calculation of shear in prestressed concrete members, ACI 318 (2014) Section 22.5.9.1 specifies that $50d_b$ be used as the transfer length of prestressing reinforcement.

$$L_t = \frac{f_{se}}{3000} d_b \tag{2.7}$$

The ACI transfer and development length equations were developed and validated through experimental analysis. According to the commentary in ACI 318 (2014) Section

R25.4.8, the experimental programs referenced to establish current transfer and development equations were based on results from testing sections fabricated with wet cast concrete and may not provide accurate results if extrapolated to no-slump concrete.

In this study, core fill shear strength was estimated to perform as an individual unreinforced piece of concrete at a minimum. Unreinforced concrete shear strength is predicted using ACI Equation 22.5.5.1, as shown in Equation 2.8.

$$V_c = 2\sqrt{f'_c}b_w d \tag{2.8}$$

ACI 318 (2014) shear capacity predictions consider the average shear stress across the entire cross-sectional area of a given member. Based on mechanics, the shear stress is parabolically distributed through the depth of a section with the maximum occurring at mid-depth (Boresi and Schmidt, 2003). This distribution is especially important for hollow-core sections because the narrow web widths generally occur at or near the mid-depth of a section.

2.3.2 PCI Design Handbook, 8th Edition

The PCI Design Handbook, 8th Edition (2017) provides the same detailed shear equations as in ACI 318 (2014) for prestressed concrete and unreinforced concrete. Specifically, the web-shear capacity presented in PCI Equation 5-28 matches Equation 2.5 in this thesis.

2.3.3 AASHTO LRFD Bridge Design Specifications, 8th Edition

The American Association of State Highway and Transportation Officials (AASHTO) Load and Resistance Factored Design (LRFD) Bridge Design Specification 8th Edition (2018) employs a simplified version of the modified compression field theory (MCFT) for predicting shear capacity of prestressed members. This method accounts for the combined effects of axial load, flexure, and prestressing (Hawkins et al., 2005). By individually evaluating the strain due to several parameters and summing their effects, this AASHTO shear design method provides a comprehensive prediction.

The nominal shear capacity of a section defined by AASHTO Equation 5.7.3.3-1 is presented in Equation 2.9.

$$V_n = V_c + V_s + V_p \leq 0.25f'_c b_w d_v + V_p \quad 2.9$$

Transverse shear reinforcement is not generally used in hollow-core slabs due to the extrusion manufacturing process, thus eliminating the V_s term. Similarly, draped strand profiles are impractical for implementation with the extrusion manufacturing process. With only straight prestressing profiles available in extruded hollow-core slabs, no vertical component of prestressing, V_p, is present, and the nominal shear capacity reduces to only the concrete contribution as presented in Equation 2.10.

$$V_n = V_c = 0.0316\beta\sqrt{f'_c} b_w d_v \leq 0.25f'_c b_w d_v \quad 2.10$$

The concrete compressive strength, f'_c, is in units of ksi for all AASHTO equations. The 0.0316 coefficient in Equation 2.10 represents the conversion factor for the concrete compressive strength from ksi to psi ($0.0316 * \sqrt{1000} = 1.0$). This AASHTO concrete shear strength equation has a similar form to the ACI unreinforced concrete shear equation, shown in Equation 2.8, but an additional modification factor, β, is included in place of the ACI 318 (2014) 2.0 coefficient. This β term captures the degree to which stress can be carried across cracked concrete. The β modification factor used in Equation 2.10 is permitted to be determined using an equations from ASSHTO Chapter 5 (2018) or tables from the AASHTO Appendix B5 (2018). AASHTO provides an equation for sections that meet minimum transverse reinforcement requirements and for those that do not. Per AASHTO Equation 5.7.2.3-1, transverse shear reinforcement is required where the design shear demand is greater than half of the factored concrete shear capacity plus the vertical component of prestressing. Because the shear demand of hollow-core slabs needing extra shear capacity (i.e., from filled cores) exceeds half of the factored shear capacity and transverse reinforcement is not present, predictions made in this report will assume the

minimum transverse shear requirement is not met. AASHTO Equation 5.7.3.4.2-2 presents the applicable equation for β, which can be found in Equation 2.11.

$$\beta = \frac{4.8}{(1 + 750 * \varepsilon_s)} + \frac{51}{(39 + s_{xe})} \quad 2.11$$

Equation 2.11 employs the net longitudinal tensile strain at the centroid of prestressing, $\mathcal{E}_s$, which is determined using AASHTO Equation 5.7.3.4.2-4 and presented in Equation 2.12. Furthermore, Equation 2.11 requires the crack spacing parameter as influenced by aggregate size, s_{xe}, which is evaluated using AASHTO Equation 5.7.3.4.2-7 and presented in Equation 2.13.

$$\varepsilon_s = \frac{\frac{|M_u|}{d_v} + 0.5N_u + |V_u - V_p| - A_{ps}f_{po}}{E_sA_s + E_pA_{ps}} \quad 2.12$$

$$s_{xe} = 12\ in. \leq s_x \frac{1.38}{a_g + 0.63} \leq 80\ in. \quad 2.13$$

The f_{po} term in Equation 2.12 is generally taken as $0.7f_{pu}$ for prestressed concrete applications. In the transfer length region, the f_{po} term varies linearly from zero to $0.7f_{pu}$. The crack spacing parameter, s_x, is equal to the effective shear depth, d_v in extruded hollow-core sections. AASHTO specifies the maximum aggregate size, a_g, to be taken as 0 in. for sections with concrete compressive strength greater than 10,000 psi (Hawkins et al., 2005). The specified transfer length used to determine the axial precompression, N_u, in Equation 2.12 is presented in Equation 2.14.

$$L_t = 60d_b \quad 2.14$$

Alternatively, the AASHTO LRFD Bridge Design Specification 7th Edition (2014) provided a simplified procedure for prestressed sections that is of similar form to the ACI 318 (2014) web-shear and flexure-shear equations, shown in Equations 2.6 and 2.5. This

procedure was not included in the AASHTO LRFD Bridge Design Specification 8th Edition (2018). The AASHTO flexure-shear Equation 5.8.3.4.3-1 is shown in Equation 2.15 and the web-shear AASHTO Equation 5.8.3.4.3-3 is shown in Equation 2.16.

$$V_{ci} = 0.02\sqrt{f'_c}b_v d_v + V_d + \frac{V_i M_{cre}}{M_{max}} \geq 0.06\sqrt{f'_c}b_v d_v \quad 2.15$$

$$V_{cw} = \left(0.06\sqrt{f'_c} + 0.30f_{pc}\right) b_v d_v + V_p \quad 2.16$$

In these AASHTO equations, f'_c and f_{pc} are in units of ksi, V_d, V_i, and V_p are in units of kips, and M_{cre} and M_{max} are in units of kip-in. Due to the extrusion manufacturing process, the vertical component of prestressing in Equation 2.16 is taken as zero. After converting the concrete compressive strength to psi in Equation 2.16, the coefficient preceding the square root of the concrete compressive strength is 1.9, which does not match that of Equation 2.6. Although the AASHTO (2014) simplified web-shear equation is not identical to the ACI 318 (2014) web-shear equation, it was not calculated in this study because it is no longer included in the current AASHTO LRFD Bridge Design Specification 8th Edition (2018).

2.3.4 Application of Shear Prediction Methods to Core-Filled Hollow-Core Slabs

This project calculated the core fill concrete contribution to shear separately from the main slab concrete contribution to shear and summed each for the total shear capacity. Core fill shear strength may be bounded by unreinforced concrete behavior or fully prestressed concrete behavior depending on fill timing. For example, Equation 2.17 and Equation 2.18 represented the added shear strength predictions for unreinforced and prestressed core fill concrete behavior, respectively, based on ACI (2014) provisions.

$$V_c = \left(3.5\lambda\sqrt{f'_c} + 0.3f_{pc}\right) b_w d_{ps} + 2\lambda\sqrt{f'_{cf}}A_{cf} \quad 2.17$$

$$V_c = \left(3.5\lambda\sqrt{f'_c} + 0.3f_{pc}\right) b_w d_{ps} + \left(3.5\lambda\sqrt{f'_{cf}} + 0.3f_{pc}\right) A_{cf} \quad 2.18$$

The AASHTO shear prediction method for prestressed concrete, Equation 2.10, relies upon the strain of longitudinal reinforcement in the concrete. This method is not applicable to core fill concrete because no longitudinal reinforcement is present in the core fill concrete. As a result, the unreinforced concrete shear strength simplification in AASHTO Section 5.7.3.4.1 was used for the core fill concrete. This section specifies that the β term in Equation 2.10 be set equal to 2.0. For AASHTO shear strength predictions in this project, Equation 2.19 was used, which sums the prestressed shear prediction of the slab concrete with the unreinforced shear prediction of the core fill.

$$V_c = 0.0316\beta\sqrt{f'_c} b_w d_v + 0.0316(2)\sqrt{f'_{cf}} A_{cf} \quad 2.19$$

When Yang's Method was applied to hollow-core slabs with filled cores in this project, the core fill concrete was treated as either unreinforced concrete using Equation 2.8 or prestressed concrete using Equation 2.1. In the prestressed core fill concrete behavior case, several variables in Equation 2.1 were calculated for the added core fill concrete including: concrete area, A_{cf}, web width, b_{cf}, moment of inertia, I_{cf}, first moment of area, Q_{cf}, concrete tensile strength, f_{cft}, and the area above the critical point, A_{cfp}. Equations 2.20 and 2.21 were used to predict the web-shear capacity of the entire slab with the core fill concrete treated as unreinforced and prestressed, respectively.

$$V_c = \frac{b_w I}{Q}\left\{\begin{array}{c} \frac{b_w}{2Q} f_{ct} x_{cp} z_{cp} + \frac{Q}{b_w}\left(\frac{e}{I} - \frac{A_{cp}}{A_c Q}\right)\frac{dN_p}{dx} + \\ \left[\left(\frac{b_w}{2Q} f_{ct} x_{cp} z_{cp}\right)^2 + \left(\frac{e}{I} - \frac{A_{cp}}{A_c Q}\right) f_{ct} x_{cp} z_{cp} \frac{dN_p}{dx} + \right]^{1/2} \\ \left(\frac{1}{A_c} - \frac{z_{cp} e}{I}\right) N_p f_{ct} + {f_{ct}}^2 \end{array}\right\} + 2\sqrt{f'_{cf}} A_{cf} \quad 2.20$$

$$V_c = \frac{b_w I}{Q}\left\{\begin{array}{c}\frac{b_w}{2Q}f_{ct}x_{cp}z_{cp} + \frac{Q}{b_w}\left(\frac{e}{I} - \frac{A_{cp}}{A_c Q}\right)\frac{dN_p}{dx} + \\ \left[\left(\frac{b_w}{2Q}f_{ct}x_{cp}z_{cp}\right)^2 + \left(\frac{e}{I} - \frac{A_{cp}}{A_c Q}\right)f_{ct}x_{cp}z_{cp}\frac{dN_p}{dx} + \right.^{1/2} \\ \left.\left(\frac{1}{A_c} - \frac{z_{cp}e}{I}\right)N_p f_{ct} + {f_{ct}}^2\right]\end{array}\right\} +$$

$$\frac{b_{cf}I_{cf}}{Q_{cf}}\left\{\begin{array}{c}\frac{b_{cf}}{2Q_{cf}}f_{cft}x_{cp}z_{cp} + \frac{Q_{cf}}{b_{cf}}\left(\frac{e}{I_{cf}} - \frac{A_{cfp}}{A_{cf}Q}\right)\frac{dN_p}{dx} + \\ \left[\left(\frac{b_{cf}}{2Q_{cf}}f_{cft}x_{cp}z_{cp}\right)^2 + \left(\frac{e}{I_{cf}} - \frac{A_{cfp}}{A_{cf}Q_{cf}}\right)f_{cft}x_{cp}z_{cp}\frac{dN_p}{dx} + \right.^{1/2} \\ \left.\left(\frac{1}{A_{cf}} - \frac{z_{cp}e}{I_{cf}}\right)N_p f_{cft} + {f_{cft}}^2\right]\end{array}\right\} \quad 2.21$$

2.4 Previous Shear Research on Hollow-Core Slabs

2.4.1 Transverse Shear Reinforcement

ACI 318 (2014) requires transverse shear reinforcement for members deeper than 12.5 in. with shear demand greater than half of the factored capacity. Hollow-core slabs were exempt from this requirement in the 1971 to 2008 ACI 318 Codes. At the beginning of the exemption, Becker and Buettner (1985) launched an experimental program that tested 33 hollow-core slabs in web-shear and flexure-shear failure. The program was intended to evaluate the appropriateness of the transverse shear reinforcement exemption and provide shear data specific to hollow-core slabs. Additionally, the Becker and Buettner research program validated the application of Code provisions for the lower slump and more dense concrete commonly used in hollow-core slab fabrication.

Becker and Buettner (1985) tested 31 hollow-core slabs at 8 and 10 in. deep with varying levels of prestress and shear span-to-depth ratios ranging from approximately 3.0 to 5.6. Beyond flexural failures, 14 flexure-shear failures and 8 web-shear failures were observed. While only one test performed below the unfactored ACI 318 (1983) shear prediction, no tests performed below the factored predictions (i.e., one test was below V_n and none were below ϕV_n). Consequently, Becker and Buettner concluded that the

transverse shear reinforcement exemption was suitable for 8 and 10 in. hollow-core slabs. No conclusions were made about 12 in. deep hollow-core slabs because the research scope only considered 8 and 10 in. deep sections.

Several decades later, Hawkins and Ghosh (2006) observed the shear strength of deep (16 in.) hollow-core slabs to be much lower than ACI 318 (2005) predictions. Consequently, ACI 318 (2008) re-introduced the language requiring stirrups for hollow-core slabs deeper than 12.5 in. when the shear demand is greater than half of the factored shear capacity.

Palmer and Schultz (2009) investigated the effect of section depth on web-shear capacity of hollow-core sections to address ACI 318 (2008) predictions for deep hollow-core slabs (i.e., deeper than 12.5 in.). As a result, they proposed a web-shear capacity equation based on experimental and analytical work, as presented in Equation 2.22. Due to the manufacturing process, only straight prestressing profiles are available in extruded hollow-core slabs, so the vertical component of prestressing, V_p, in Equation 2.22 is zero.

$$V_{cw} = \left(0.5f_{ct} + 0.3f_{pc}\right)b_w \frac{I}{Q} + V_p \qquad 2.22$$

Palmer and Schultz assumed a linear gradient of prestress strand development within the transfer length to determine f_{pc} for use in Equation 2.22. While ACI 318 (2005) suggested $50d_b$ as the prestressing transfer length, Palmer and Schultz found that this suggestion did not prove to correctly characterize the transfer length in hollow-core slabs. Rather, they found the transfer length could be more accurately determined using strand slip, δ_{es}, measurements, as shown in Equation 2.23. Unfortunately, stand slip can only be measured once a slab is manufactured, which means the strand slip information is not available during design. Therefore, strand slip measurements can be used to indicate how accurate the design assumptions for transfer length are relative to the actual manufactured slab.

$$L_t = 5\delta_{es}\frac{E_p}{f_{pi}} \qquad 2.23$$

Palmer and Schultz provided Equations 2.24 and 2.25 to simplify Equation 2.22, which can be rewritten as Equation 2.26.

$$f_{ct} = 5\sqrt{f'_c} \tag{2.24}$$

$$\frac{I}{Q} = 0.85 * d_p \tag{2.25}$$

$$V_n = V_c = V_{cw} = \left(2.125\sqrt{f_c} + 0.255 f_{pc}\right) b_w d_p + V_p \tag{2.26}$$

Two distinctive alterations were suggested in Equation 2.26 compared to the ACI 318 (2008) web-shear Code provision. The first was to consider the limiting biaxial tensile strength of concrete more accurately than the original ACI 318 (2008) web-shear equation. Palmer and Schultz suggested using the splitting tensile strength of concrete instead of the compressive strength to be more accurate when predicting the limiting shear strength. Therefore, the $3.5\sqrt{f'_c}$ term in Equation 2.5 was replaced with $5\sqrt{f'_c}$ by substituting Equation 2.24 into Equation 2.5.

The second modification in their suggested web-shear prediction addresses the nonuniform shear stress distribution through the depth of a section. Consequently, the *I/Q* ratio was suggested instead of the ACI d_p term. By substituting Equation 2.25 into Equation 2.5, the coefficients in Equation 2.5 were again modified resulting in the final simplified form shown in Equation 2.26.Equation 2.25 was specifically determined for the 16 in. deep hollow-core sections used in the Palmer and Schultz research program and was substituted into Equation 2.22 as shown in Equation 2.26.

The development of Equation 2.26 was intended to better characterize the web-shear capacity of unaltered hollow-core sections. When applied to core-filled hollow-core slabs, the core fill may be predicted to behave as unreinforced concrete or prestressed concrete, just as with the ACI predictions of Equations 2.17 and 2.18. For the Palmer and

Shultz shear capacity predictions, Equations 2.27 and 2.28 were used to predict unreinforced and prestressed core fill concrete behavior, respectively.

$$V_c = \left(2.125\sqrt{f_c} + 0.255f_{pc}\right)b_w d_{ps} + 2\lambda\sqrt{f'_{cf}}A_{cf} \quad 2.27$$

$$V_c = \left(2.125\sqrt{f_c} + 0.255f_{pc}\right)b_w d_{ps} + \left(2.125\sqrt{f'_{cf}} + 0.255f_{pc}\right)A_{cf} \quad 2.28$$

2.4.2 Steel Fiber-Reinforced Concrete

Steel fiber-reinforced concrete (SFRC) can be used as an alternative to traditional bar reinforcement in many different structural concrete members for a variety of reasons, including enhanced structural performance. Additionally, SFRC helps to control cracking due to the release of strands, camber, and thermal effects (Simasathien and Chao, 2015). The behavior of SFRC is difficult to extrapolate from regular, nonprestressed concrete members to hollow-core slabs. This is due to the complex geometry and unique manufacturing process of hollow-core slabs. Since the common hollow-core manufacturing processes does not allow for the use of traditional transverse reinforcement, using SFRC for the entire slab material offers an appealing alternative for shear strength improvement. Additionally, use of SFRC can avoid or mitigate some of the disadvantages of core filling, such as the addition of manual labor, increase in member selfweight, and drainage issues.

In an early feasibility study, Peaston et al. (1999) conducted experimental research on small SFRC hollow-core slabs in web-shear. The testing matrix consisted of six SFRC slabs and two non-SFRC control slabs, all of which were 7.87 in. deep and 78.75 in. long. Using shear span-to-depth ratios of 2.0 and 2.8, and steel fiber volume fractions of 0.5% and 1.0%, their experimental results validated the improvement in shear capacity for SFRC slabs compared to non-SFRC slabs (of about 25%). The volume fraction indicates the ratio of steel fiber volume to concrete volume. Since steel fibers do not engage until after

cracking, little improvement was observed for the cracking strength of the SFRC specimens compared to the control specimens.

During mixing, some challenges were experienced with proper consolidation and placement of the SFRC, so the water-to-cement ratio was slightly increased. Following curing, Peaston et al. inspected the sawcut face and observed a relatively random distribution of steel fibers across the cross section. Within the hollow-core webs, the orientation of the fibers was not random and appeared to favor the vertical direction. This anomaly was attributed to the extrusion manufacturing process, which led to a vertical alignment of the fibers within the narrow webs.

More recently, Dudnik and Milliman (2015) as well as Simasathien and Chao (2015) evaluated the shear strength of SFRC hollow-core slabs. The re-introduction of minimum transverse shear reinforcement requirements in ACI 318 (2008) prompted these investigations related to using SFRC in hollow-core slabs. Due to the inability to provide transverse reinforcement in hollow-core slabs, the Code change effectively cut the design strength of slabs deeper than 12.5 in. in half. Therefore, an investigation of using steel fibers as a type of shear reinforcement in hollow-core slabs was the primary incentive of these research programs.

Dudnik and Milliman studied various steel fiber volume fractions including 0.00%, 0.375%, 0.50%, and 0.75%. Tests were conducted on 14 total slabs of 12 and 16 in. depths. Additionally, shear span-to-depth ratios of 3.0 and 3.5 were investigated to identify and mitigate the influence of arching action. Throughout the testing, the SFRC hollow-core slabs outperformed similar non-SFRC slabs for all specimens with proper consolidation of the SFRC. The 16 in. test specimens had a greater increase in shear capacity (by up to 88%) than the 12 in. test specimens (by up to 27%) when compared to results from the respective non-SFRC test specimens. Little difference in the amount of capacity increase was observed between the 0.50% and 0.75% fiber volume fraction specimens. Rather, workability was hindered by a larger steel fiber volume fraction (0.75%), resulting in difficult and unreliable concrete consolidation. Since all slabs were fabricated using the extrusion method with no-slump concrete, Dudnik and Milliman suggested an optimal steel

fiber volume fraction of 0.50% to ensure proper fiber distribution and concrete consolidation, while still providing notable shear enhancement.

Simasathien and Chao (2015) tested eight 18 in. deep wet-cast slabs with a 0.75% steel fiber volume fraction and shear span-to-depth ratios ranging from 2.73 to 5.09. Excluding the two control specimens which had no steel fibers, three slabs failed in web-shear and three failed in flexure-shear. Compared to ACI 318 (2014) predictions, the web-shear strengths were underestimated by as much as 45% and the flexure-shear strengths were underestimated by up to 100% of the observed capacity. As a result, Simasathien and Chao concluded that steel fiber reinforcement could serve as a suitable minimum shear reinforcement alternative in hollow-core slabs. Furthermore, they proposed replacing the constant value of 3.5 in Equation 2.5 with a constant value of 5.5 for prestressed concrete hollow-core members. Because this was a proof of concept study, the investigators noted further consideration should be given to using this proposed equation modification for dry-cast hollow-core members.

Simasathien and Chao (2015) suggested two explanations as to why the SFRC specimens outperformed the ACI 318 (2014) predictions for non-SFRC prestressed hollow-core members. First, the steel fibers likely improved prestress bond, thus providing increased axial prestress at the critical point (Chao et al., 2006). Second, the observed preferential vertical orientation of the steel fibers near the critical point in the hollow-core slab webs likely provided higher shear resistance than randomly arranged fibers.

Overall, SFRC in hollow-core slabs has been shown to increase the web-shear capacity. Since the research on SFRC hollow-core slabs has only been performed on a few types of hollow-core slabs, further research is necessary to provide a representative shear prediction for the variety hollow-core sections available in the industry.

2.4.3 Core Fill

As a part of a larger research program investigating the shear behavior of deep hollow-core slabs, Palmer and Shultz (2011) conducted four exploratory tests on two ends of two slabs with one filled core each. The specimens were 16 in. deep, 28 or 32 ft long, and contained 4 ft of core fill at the ends. All of the core fill investigation tests used the

same core fill concrete mixture, but two tests also included synthetic fibers at 0.67% and 1.0% volume fractions in the core fill concrete mixture.

Data from all four tests exhibited increases in hollow-core slab shear strength compared to similar unfilled specimens tested in the primary matrix of the research program. For the two tests with no synthetic fibers in the core fill concrete, the increase in web-shear strength due to the core fill was only about half of that predicted by the ACI 318 (2008) formula for web-shear capacity in prestressed members (0.5*Equation 2.6). In these tests, the diagonal shear crack angle of the core fill concrete was about 10° steeper from the horizontal plane compared to the adjacent webs of the slab concrete. Palmer and Schultz concluded that this crack angle difference was due to cracking of the slab material followed by cracking of the core fill. A steeper crack angle indicated less axial stress. If the webs of the hollow-core slab crack first, causing the strands to slip, significantly less axial prestress will be available in the core material at the initiation of core fill cracking. Slip between the core fill and slab concrete could also explain this difference in crack angle, but observations following testing indicated that the core fill slipped from the adjacent slab webs.

The two core fill tests with synthetic fibers in the core fill concrete outperformed shear capacity of the specimens no synthetic fibers in the core fill concrete. Fiber-reinforced concrete is not considered in ACI 318 (2008) shear provisions, so Palmer and Schultz suggested that web-shear capacity be predicted using the tensile strength of concrete for fiber-reinforced concrete. Upon examining the cracked specimens, the location and angle of cracking in the fiber-reinforced core fill tests were nearly identical to the respective unfilled specimens. The fibers were still engaged at wide crack widths, which suggested that they likely provided a notable amount of additional shear capacity.

Core filling is a common practice in the hollow-core precast industry, but little research has been conducted to quantify the shear enhancement afforded by core fill concrete. With the widespread application of this shear improvement strategy, better characterization of core fill performance would be useful to the industry.

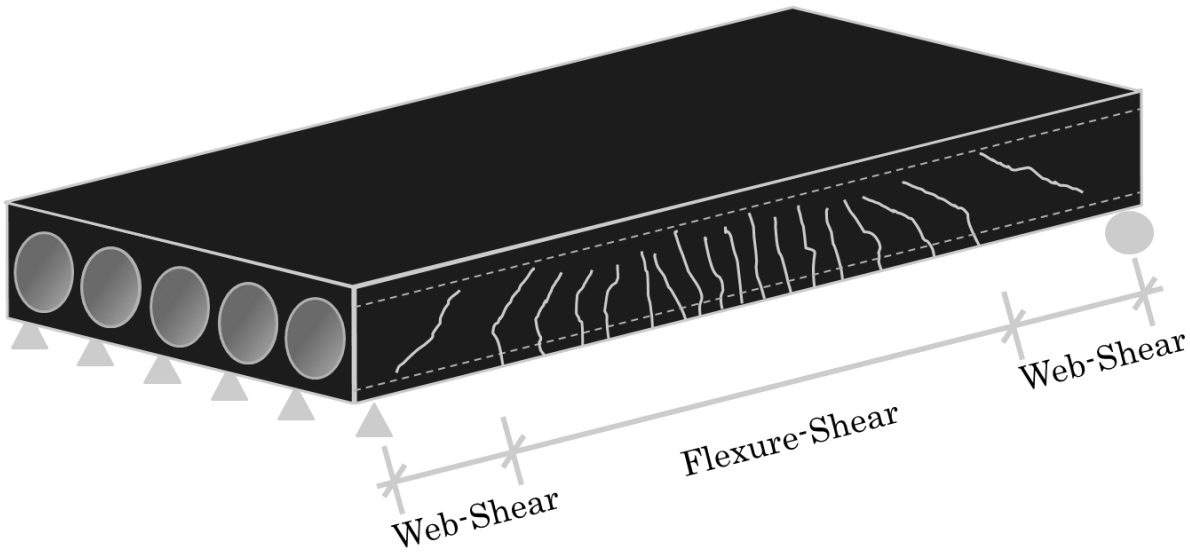

Figure 2.1. Governing shear failure modes along the length of a simply supported hollow-core slab

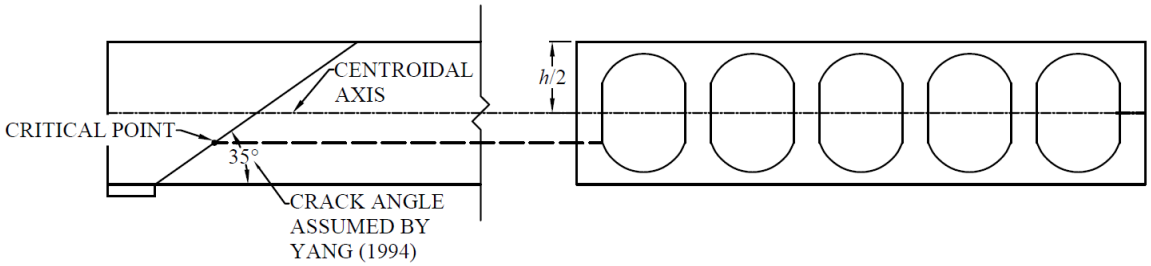

Figure 2.2. Location of the critical point along the length of a hollow-core slab with non-circular void geometries

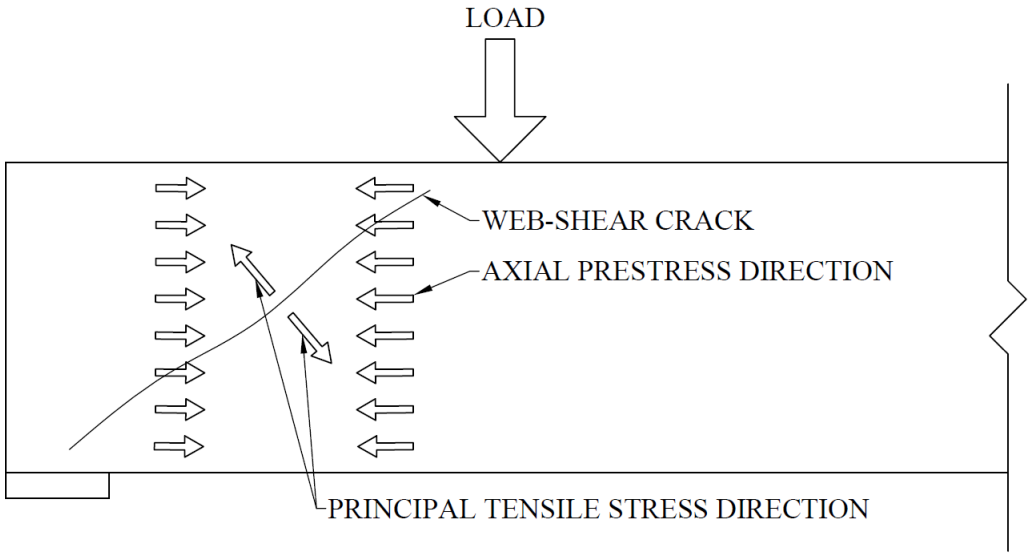

Figure 2.3. Orientation of the axial prestress direction and the resulting principal tensile stress direction relative to a web-shear crack

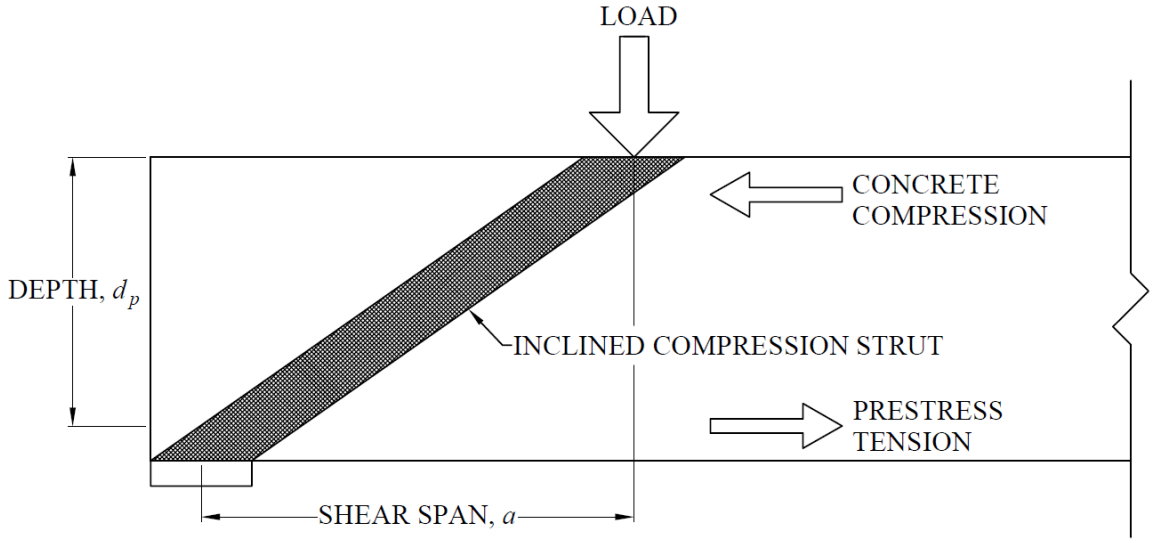

Figure 2.4. Depiction of an inclined compression strut acting within the shear span region to provide arching action

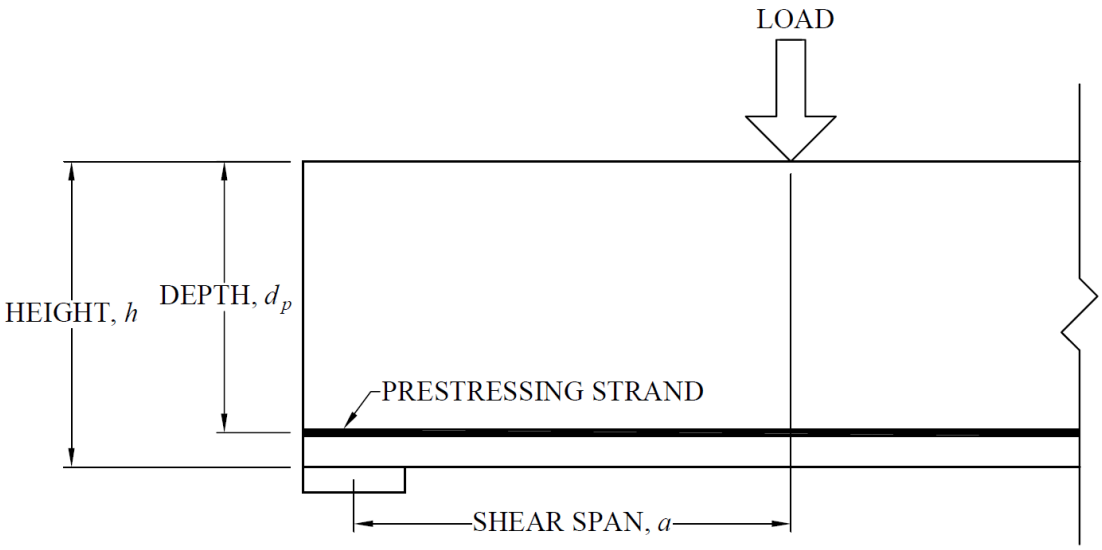

Figure 2.5. Shear span, *a*, depth, d_p, and height, *h*, of a hollow-core slab

Chapter 3: Hollow-Core Slab Design, Testing Matrix, Fabrication, and Testing

3.1 Slab Design and Test Setup Geometry

3.1.1 Introduction

This section summarizes the slab design and test setup geometry considerations that dictated the final testing arrangement. The available space and testing equipment within the University of Minnesota Duluth (UMD) Structural Engineering Laboratory limited the slab size feasible for testing. Only one actuator with the capacity to apply 110 kips of force was available, so it was critical that the applied load required to generate a shear failure be less than 110 kips. Beyond laboratory-specific considerations, several slab-specific constraints also affected the final slab design. The slab design and test setup configuration were selected to investigate the web-shear capacity of hollow-core slabs with filled cores. Thus, sufficient moment capacity was necessary to prevent premature flexural failure. Furthermore, the transfer and development length were considered in the flexure and shear designs. Arching action at the supports was mitigated by selecting a proper shear span-to-depth ratio.

3.1.2 Laboratory Constraints

3.1.2.1 Actuator Capacity

The maximum available actuator capacity of 110 kips constrained several design decisions including section depth, web width, and number of cores filled. Testing of a 16 in. deep section was preferable because the manufacturer most commonly core-fills 16 in. deep sections. Unfortunately, the load required to fail a 16 in. deep section in web-shear assuming a fully prestressed section exceeded the actuator capacity, so a 12 in. deep section was selected. At a 12 in. depth, the industry supplier could fabricate both a light and a heavy hollow-core section, which allows for demand-specific section selection and, consequently, better material efficiency. The heavy section has wider webs, which provide greater shear resistance. In a given scenario where additional shear capacity is required, the

heavy section would typically be used in place of the light section. In the same scenario, a 16 in. deep section could suffice to increase shear capacity, but sometimes floor depth limits the space available for hollow-core slabs. If the 12 in. deep heavy section still could not supply the required shear capacity, cores of the heavy section would be filled appropriately. Filling cores in a heavy 12 in. section was desired to replicate real-world practice. Unfortunately, the predicted shear capacity of a heavy section with one filled core treated as fully prestressed concrete increased the slab capacity by about 25%, which required the applied load to be near the available actuator capacity. To allow for reserve actuator capacity and ensure a complete failure was achieved, the light 12 in. section was used for all testing.

3.1.2.2 Number of Cores Filled

Shear capacity contributions from the core fill material are more distinguishable when they are significant compared to the slab shear capacity with no filled cores. In all concrete testing, there is bound to be some variability between repeated tests due to nonhomogeneous and anisotropic concrete behavior. Since this testing program sought to characterize the direct increase in shear capacity due to core filling, a greater difference between increased shear capacity and original shear capacity was desired for a better distinction of core fill performance. Practically, this meant filling at least two cores was desired. Depending on the timing and method of core filling, the solid fill material could potentially behave as fully prestressed concrete in shear at a maximum. This upper bound provided a maximum applied load likely needed to generate a web-shear failure. While desirable, the higher required loading to account for the added shear capacity of two cores treated as prestressed concrete exceeded the maximum actuator capacity of 110 kips. Consequently, only one filled core was used for all testing.

3.1.2.3 Specimen and Span Length

Each slab was tested twice to gather the most data from the finite number of slabs included in this program. Rather than performing one test per specimen in a simply supported arrangement, both ends (Side A and Side B) of each specimen were tested. To

do so, the end opposite from initial testing, Side B, was overhung beyond its support for protection. This ensured virgin material was being tested when the slab was spun and tested a second time. Specifically, the distance from the support to the end of the section on the overhung end (45.5 in.) exceeded the distance between the actuator and the testing end support (30 in.). Furthermore, the length of the core fill (48 in.) extended beyond the point of loading to ensure its full shear contribution was realized. An overall slab length of 20 ft was selected due to laboratory space constraints. A longer slab was not needed for shear testing. Consequently, a test span length of 16 ft was employed. A simplified summary of the supports, loading, and overhang is shown in Figure 3.1. For each of the individual slabs, the same core fill modification was fabricated on both ends, which provided a redundant test and the ability to average the experimental shear capacity.

3.1.3 Shear Capacity

Shear capacity was predicted using the ACI 318 (2014) web-shear and flexure-shear equations. The shear demand on the hollow-core slab at *h/2* (6 in.) from the centerline of the support nearest the applied load was compared with the predicted web-shear capacity to determine the shear force required for web-shear failure. With this required shear demand, the applied load for testing was determined. The strength reduction factor, ϕ, was taken as 1.0 to accurately compare shear capacity predictions with laboratory research. During slab design for testing, an over-strength factor of 1.2 was applied to the hollow-core slab web-shear capacity to ensure a complete web-shear failure could be achieved in the laboratory. This factor accounted for any incidental variability in the hollow-core concrete performance. Consequently, the applied load required for web-shear was increased due to the slab over-strength factor. An example hollow-core slab design for web-shear failure can be found in Appendix A.

Transfer length directly affects the prestress gradient within the end region of a member. Web-shear strength was evaluated at *h*/2 (6 in.) from the testing support, which was within the transfer length. Since the extruded hollow-core slabs used in this research employed no-slump concrete, the accuracy of ACI transfer length equation, Equation 2.7, was questionable. Since axial precompression influences the web-shear capacity at a given

section, uncertainty in the transfer length may have led to a less certain prediction of web-shear resistance.

Preliminary calculations for determining the testing setup geometry modeled the transfer length behavior as a function of the strand area in contact with the slab concrete along the length of the strand. A bond stress of 400 psi between the strand and concrete was assumed (Buckner, 1995). Beginning with no prestress force at the end of the hollow-core slab, the prestress force was assumed to linearly increase along the length of the strand as the amount of strand area in contact with the concrete increased. This linear gradient was assumed until the effective prestress, f_{se}, was achieved. The equation used to determine the transfer length is shown in Equation 3.1.

$$L_t = \frac{A_{ps}}{\frac{4}{3}\pi d_b}\frac{f_{se}}{400\ psi} \tag{3.1}$$

3.1.4 Shear Span-to-Depth Ratio

The shear span-to-depth ratio, a/d_p, was considered during both the preliminary shear and flexural design. Based on previous hollow-core shear research, a minimum shear span-to-depth ratio of 2.5 was selected to null the effects of arching action (Hawkins et al., 2005). Due to the alignment of the testing supports with floor anchors in the structural engineering laboratory, a shear span-to-depth ratio, a/d_p, of 3.0 was selected.

The depth in the shear span-to-depth ratio is commonly the depth from the top of a section to the center of longitudinal reinforcement, d_p, not the entire section depth, h. This is because many concrete members endure some flexural cracking at the extreme tension fiber prior to failure, thus reducing the effective depth of the section to the depth of the longitudinal reinforcement. Given the testing geometry in this research, the cracking moment capacity would be very near the flexural demand at the loading point at the load necessary for web-shear failure. If the section experienced no flexural cracking during testing, the entire section depth, h, would more realistically characterize the shear span-to-depth ratio of the section. Therefore, a shear span-to-depth ratio, a/d_p, of 3.0 was selected,

which created an *a/h* ratio of 2.5, which was comparable to the suggested minimum ratio from the literature of 2.5.

3.1.5 Flexural Capacity

The design process began with a 16 ft long simply supported 12 in. deep hollow-core section with a transversely distributed point load near one of the supports to generate web-shear failure. The adequate flexural capacity required to allow for complete web-shear failure was considered. Hollow-core slabs are commonly fabricated with various combinations of strand size, configuration, and number. Since the applied load required for web-shear failure was within the transfer length, the full flexural capacity would not be available at the point of maximum moment. Ideally, many small diameter strands would have been employed as their transfer length would be reduced and flexural capacity could be increased near the end of the member at the point of maximum moment. Due to fabrication scheduling at the manufacturer, 0.6 in. diameter strands needed to be used as opposed to the preferred 0.5 in. diameter strands. Therefore, the maximum of six 0.6 in. diameter strands stressed to $0.7f_{pu}$ were selected to achieve the most flexural capacity. This was the maximum number of 0.6 in. diameter strands allowed by the manufacturer.

Beyond transfer length considerations, initial and long-term prestress losses were considered in the flexural design. All prestress loss calculations were calculated using ACI 423.10R Guide to Estimating Prestress Loss (2016). Specifically, elastic shortening, creep, shrinkage, and relaxation were calculated and deducted from the initial jacking prestress. The ambient relative humidity was assumed to be 70% throughout the slab life. A complete example calculation of the flexural capacity incorporating prestress losses can be found in Appendix A.

With a shear span-to-depth ratio of 3.0 and the selected strand configuration of six 0.6 in. diameter strands, the flexural demand at the point of applied load slightly exceeded the flexural capacity. The marginal lack of flexural capacity did not cause alarm since flexural predictions are based on transfer length approximations and other estimated values such as prestressing losses and concrete strength, which generally are generally conservative. For the purposes of this project, the stress in the strands was considered to

increase linearly from zero at the member end to the effective prestress stress, f_{se}, at the transfer length. Between the transfer length and development length, the prestress stress was considered to increase linearly form the effective prestress stress, f_{se}, to the maximum prestressing stress, f_{ps}. This relationship between the prestressing strand stress and the distance from the member end was presented in the ACI 318 (2014) commentary Section R25.4.8.3.

3.1.6 Summary

Several design iterations that considered the many laboratory constraints, shear capacity, and flexural capacity were considered. A light 12 in. deep, 48 in. wide, and 20 ft long hollow-core section with six 0.6 in. diameter strands stressed to $0.7f_{pu}$ at a depth, d_p, of 9.875 in. was selected for fabrication and tested at a span length of 16 ft. The transversely distributed point load was placed 30 in. from the support centerline, providing a shear span-to-depth ration, a/d_p, of 3.0 and a a/h ratio of 2.5. All slabs had the center core filled for a length of 4 ft on each end with identical core fill modifications at each end of each slab. A detailed cross section geometry for all the slabs is presented in Figure 3.3 and a complete elevation of the testing setup is presented in Figure 3.4.

3.2 Testing Matrix

The fundamental research goals of this program were to study how core fill timing and innovative core filling affected shear capacity. Consequently, the testing matrix was divided into two phases to address each of these objectives. To provide dependable recommendations for inclusion in Code provisions, many replicate tests would be required. However, the nature of this research program did not lend itself to gathering a wealth of repeated test data for refining Code provisions. Rather, this project sought to quantitatively understand shear capacity related to the current core filling practice and was also used as an opportunity to explore innovative core fill techniques. As a result, the testing matrix was primarily designed to provide conclusions concerning the actual behavior of core filling as it is currently applied in practice. The second half of the testing matrix was used to identify potentially promising avenues for enhancing the performance of filled cores. A typical,

unfilled slab was tested to provide control data for comparison. For each slab, two duplicate tests were performed, one on each end of a slab.

3.2.1 Core Fill Timing Specimens

Four slabs were used to study the effects of core fill timing on performance. Within the core fill timing portion of the matrix, both the slab age at the time of core fill and the age of the core-filled slab were studied. The manufacturer's standard core fill practice was used to the represent real-world fabrication of slabs filled during fabrication. Two identical slabs were fabricated this way. One was tested soon after fabrication and the other was tested 209 days following fabrication. The slab tested at 209 days after fabrication was used to consider long-term slab and core fill concrete shrinkage because the remaining specimens would be tested within a few months of fabrication. Shrinkage would cause the core fill material to move inward and the slab material to move outward from a void, which means that the interlock between core fill and slab material could become compromised over time. Therefore, the aged slab helped to understand the long-term performance of core-filled slabs. Additionally, the slab with cores filled at fabrication, tested shortly after fabrication, also served as a baseline for all of the novel core fill enhancement strategies examined in the second phase of testing. Each of these novel modifications altered the fill of a typically filled core, so comparisons between each enhancement and the unaltered typical fill provided an indication of the improvement due to the novel technique.

Core filling may or may not be performed at the time of the slab fabrication. The case where the slab is core-filled after curing and strand release (less common) is very different from the immediate fill case because a definite cold joint between the core fill and slab material exists. Furthermore, there is often concrete dust left in the cores from saw cutting each slab to length. This residual dust is powdery when dry and coats the entire interior core surface for several feet in each direction from the cut, as shown in Figure 3.5(a). Consequently, there is very little likelihood of composite action between the core fill and slab concrete. To compare the difference of slab age at the time of core filling, a slab was cast in-line with the first set of slabs and allowed to cure approximately 3 weeks before core filling. Unfortunately, there was some miscommunication with the fabricators

and the first cold joint core fill slab was only core filled 2 ft from the ends of the slab. Since loading would be applied greater than 2 ft from the support, the core fill was not completely effective over the entire length of applied shear. While this slab was still tested, its results were not useful for comparison with the other core-filled specimens and the results were not reported. Consequently, a second cold joint core fill slab was extruded with the second phase of slabs and filled to the proper 4 ft length after approximately 3 weeks of curing. This cold joint core fill slab captured the other most common core filling practice. A summary of the core fill timing specimens can be found in Phase 1 of Table 3.1.

3.2.2 Core Fill Enhancement Specimens

3.2.2.1 Steel Fiber-Reinforced Concrete Core Fill

Peaston et al. (1999), Dudnik and Milliman (2015), and Simasathien and Chao (2015) all tested hollow-core slabs with SFRC slab material. Each research program showed improved shear capacity in SFRC specimens. Furthermore, SFRC has been used in a variety of concrete applications exhibiting promising structural and serviceability benefits. To improve the shear strength of the core fill, one slab in the testing matrix, shown in Table 3.1, employed SFRC for the core fill material. Based on the literature, a 0.5% volume fraction of steel fibers was used in the core fill concrete. The volume fraction indicates the ratio of steel fiber volume to concrete volume. This fraction was chosen to maximize steel fiber contribution to strength while maintaining workability. Figure 3.6 shows fresh SFRC placed in the core.

3.2.2.2 Roughened Core Wall

A truly monolithic section with core fill would ideally behave as a fully prestressed section. For this to be achieved in a core-filled specimen, the core fill would need to act compositely with the slab material. In a specimen where the core is filled immediately after extrusion, the core fill concrete is in contact with the slab material before either is set, which may result in some bonding. Unfortunately, the surface of extruded no-slump concrete is smooth due to vibration of the extruder for compaction. This means the likelihood of core fill material completely bonding with no-slump slab material is unlikely.

Furthermore, no mixing occurs by simply placing core fill material adjacent to slab material, which likely results in no aggregate interaction across the boundary of the materials. There was potential for enhancement since this situation lends itself to a less than composite scenario.

Roughening the slab core wall surface prior to core fill placement may provide a mechanism for composite interaction. For this enhancement, both transverse and longitudinal grooves were initially considered. A horizontal (longitudinal) groove may facilitate shear transfer between the slab and core fill like a shear key, while a vertical (transverse) groove may provide a path for axial prestress to transfer to the core fill. Overall, a truly monolithic section was sought, so the vertical orientation of grooves was selected as it would lend itself to prestress transfer to the core fill, rather than the core fill individually resisting additional shear force. Vertical grooves were made using a small handheld garden rake, which provided a 0.25 in. deep indentation spaced at about 1 in. on center in the slab web walls, as shown in Figure 3.7.

3.2.2.3 Headed Steel Bar in Core Fill

Additional longitudinal reinforcement was added to the core fill to potentially maintain the axial prestress in both the core fill and slab during web-shear failure, which is often associated with prestressing strand slip. Specifically, a 4 ft long #6 bar with 0.25 by 2 by 2 in. steel plates welded to each end was placed at the bottom of the void prior to core filling, as shown in

Figure 3.8 and listed in Table 3.1. The end plates provided anchorage to account for development length issues related to the relatively short bar length. The goal of the end plates was to potentially increase the effectiveness of the bar and maximize its load-carrying capacity.

As it relates to web-shear capacity, this core fill modification had two specific potential benefits. First, strand slip under applied load may have been reduced because some of the longitudinal force could be carried by the bar. During loading, prestressing strands slip causing the overall prestress force to decrease. With the addition of a bar in the core fill, some of the load carried by the strands may be transferred to the rebar, thus

reducing the slip and maintaining more axial precompression. Second, the headed bar was intended to maintain any axial precompression of the core fill. Since the slab and core fill web-shear capacity were additive because the cores were filled before slab curing and transfer of prestress force, an increase in axial precompression of the core fill may have improved its web-shear capacity. This would also increase the overall specimen web-shear strength.

While both mechanisms have merit, it was impractical to quantitatively predict the exact contribution of the headed bar to the web-shear strength. Both the uncertainty in bond between the core fill and slab and the actual axial prestress initially present in the core fill were unknown, which made an accurate prediction infeasible. Rather, the results of this core fill enhancement were intended to be compared to the typical immediate fill specimen to identify whether a headed bar could provide any notable improvement worthy of further investigation.

3.2.2.4 Welded Wire Reinforcement in Core Fill

In typical reinforced concrete design, transverse shear reinforcement is used as the default way to provide additional shear capacity where necessary. Unfortunately, the common hollow-core fabrication methods do not lend themselves to transverse shear reinforcement placement, which makes it difficult to easily increase shear capacity. Furthermore, the lack of transverse reinforcement can lead to implementation of additional Code requirements in design due to not satisfying minimum transverse reinforcement requirements. To add transverse reinforcement, one slab in the testing matrix incorporated welded wire reinforcement (WWR) in the core fill, as shown in Table 3.1. Each filled core had two 4 ft long by 8 in. tall pieces of 4-gauge welded wire reinforcement with a 4 by 4 in. grid placed vertically in the core, as shown in Figure 3.9. The WWR may have provided improved web-shear capacity in two ways. First, the vertical bars in the mesh provided regularly spaced transverse reinforcement. Traditional stirrups often have hooks at the ends to provide anchorage, but only straight, smooth bars are used in WWR. Fortunately, the perpendicular longitudinal bars welded to the vertical bars in the WWR provided a means of anchorage. Second, the longitudinal bars in the WWR served as a way to potentially

maintain any axial prestress in the core fill and possibly alleviate slip in the prestressing strands, similar to the potential behavior of the headed steel bar specimen.

3.3 Specimen Fabrication

All of the hollow-core slabs were constructed at Molin Concrete Products in Lino Lakes, MN. The testing matrix, Table 3.1, was divided into two separate fabrications to incorporate results from the first phase of testing into the development of the second phase of testing and alleviate space limitations in the UMD structures laboratory. Each of the sets of slabs were extruded in-line with the manufacturer's ongoing project schedule.

There were two main methods of core filling used by the manufacturer depending on the age of the slab. For slabs with cores filled immediately after extrusion, the entire fabrication and core filling process was completed within an hour of extrusion. In this case, the top flange of the middle core to be filled was first collapsed by the heel of a worker's boot, as shown in Figure 3.10. This broken flange concrete was collected by hand and gathered at the end of the intended core fill length to create a plug of concrete. Since the core fill concrete could move down the core, this plug of concrete prevented excess fill material from traveling down the length of the entire core and maintained the depth of the core fill over its intended length. With the empty core ready, a portion of no-slump concrete mix used for slab extrusion was placed in a small mixer to prepare the core fill material. After the addition of superplasticizers and water, the core fill material was placed in the desired core and the top was finished, as shown in Figure 3.11 and Figure 3.12. After filling the core, the slab was covered with burlap and allowed to steam cure overnight. The next morning, the prestressing strands were released and individual slabs were cut to length.

In the case where cured slabs were core-filled, an unaltered hollow-core section was fabricated and allowed to cure for a few weeks before core filling. For the 2 ft cold joint core fill specimen, 20 days passed between extrusion and core filling. For the 4 ft cold joint core fill specimen, 24 days passed between extrusion and core filling. To access the cured slab core, the top flange of the desired middle core was removed using a concrete saw. Figure 3.13 shows a cured slab following removal of the top flange. Cardboard cut-outs were placed at each end of the core fill length to contain the core fill material. For both

cold joint core fill specimens, the same no-slump concrete mix used for slab extrusion, with the addition of superplasticizers and water, was used for the core fill material. Following core filling, the top surface was finished, and the slab was left to cure.

3.4 Materials

3.4.1 Concrete

For all specimens, the typical concrete mix design used by the manufacturer in hollow-core production was also employed. This concrete mix was designed with a water-to-cement ratio of 0.35 and developed to have no slump for use in an extruding machine. Specific mix design ingredients and parameters for the slab material are listed in Table 3.2. In all of the core fill mixtures, the same slab concrete mix was used with the addition of superplasticizers and water.

Slabs fabricated in-line with one another incorporated multiple concrete batches concrete over the length of the slabs. At 20 ft in length, each slab required approximately 1.47 yd^3 of concrete, but 2 yd^3 of concrete were mixed per batch. Since the same mix design was used in each batch, the concrete was assumed to be consistent across all slabs. Numerous cylinders were prepared for hardened concrete property tests on each test day for each of the slabs. These cylinders were taken from multiple batches during the fabrication of a line of slabs. Since each individual slab was likely made from multiple batches of concrete, the test cylinders were not associated with any specific slab.

An assortment of 4 by 8 in. concrete cylinders was made to test the hardened properties. To ensure proper characterization of slab performance on each test day, three concrete compressive tests were performed on the respective slab material cylinders and core fill material cylinders following ASTM C39 (2017). A summary of test day compressive strengths can be found in Table 3.3. Six additional slab concrete cylinders and six additional core fill concrete cylinders were also produced in the first phase of testing. After curing for 28 days, three slab concrete cylinders and three core fill concrete cylinders were tested in compression following ASTM C39 (2017). Similarly, a split cylinder test was conducted according to ASTM C496 (2017) on the remaining three slab concrete

cylinders and three core fill concrete cylinders at 28 days. With the compressive and tensile strengths of both the slab and core fill concrete on the same day, a relationship between compressive and tensile strength was determined. Table 3.4 shows a summary of these 28 day tests.

The tensile strength of SFRC can be much different than unreinforced concrete, so additional hardened property tests were performed on the SFRC core fill. Three additional SFRC core fill cylinders and three additional slab cylinders were made for split cylinder tensile tests. These tensile tests were performed on the same day as testing the SFRC core fill specimen (48 days), so the compressive tests of the SFRC core fill and slab concrete were also available. A summary of the compressive and tensile strengths for the SFRC core fill and slab concrete is presented in Table 3.5.

3.4.2 Prestressing Strands

All of the slabs were constructed with 0.6 in. diameter 7-wire strands. These strands had a nominal ultimate tensile strength of 270 ksi. Furthermore, the steel was treated to have low-relaxation over time. The nominal strand properties from Nilson (1987) and the manufacturer provided strand properties are shown in Table 3.6. The manufacturer provided strand properties were used throughout analysis calculations in this project.

3.4.3 Steel Fibers

For the SFRC core fill specimens, Dramix 3D 55/30BG fibers manufactured by the Bekaert Corporation were used at a volume fraction of 0.5% in the core fill material. The fibers were 1.18 in. long with a diameter of 0.022 in., resulting in an aspect ratio (length/diameter) of 55, as shown in Figure 3.14. The manufacturer provided fiber tensile strength was 160 ksi. For ease of mixing, the steel fibers were glued together with water-soluble glue during manufacturing, which would allow the fibers to disperse when added to a concrete batch.

3.5 Laboratory Setup

3.5.1 Boundary Conditions

Equal transmission of load across the section at the applied load and supports was essential to ensure proper shear failure in multiple webs. Without adequate load distribution, the applied load or support reactions could become eccentric and induce unwanted torsional stresses. Furthermore, insufficient bearing could lead to an unequal division of load between the six webs. Should this be the case, the slab may fail at an unrealistically low load due to some webs not resisting shear. Therefore, several additional features were included in the testing arrangement to address load distribution concerns.

A spreader beam and several neoprene pads were used to properly load and support each slab. Specifically, a 4 ft long W8x31 stiffened steel spreader beam was attached to the actuator crosshead to transversely distribute the applied point load over the 4 ft specimen width. To mitigate minor top surface imperfections of the slab, a 1 in. thick by 12 in. wide neoprene pad (manufactured to the ASTM D2000 standard) was placed between the slab and actuator. Upon inspecting the hollow-core finished top surface, there was notable sag in the top flange over each of the voids of up to 0.375 in. The relatively stiff neoprene pad was insufficient to account for this imperfection, so a 1 in. thick by 6 in. wide mortar pad was cast atop each hollow-core slab and transversely centered under the loading point, as shown in Figure 3.15. For the final arrangement, the neoprene pad was placed between the mortar pad and spreader beam as shown in Figure 3.16.

At the supports, 0.5 in. thick by 5 in. wide neoprene bearing pads were placed between the slab and steel support. These pads were provided by the hollow-core slab manufacturer and are used in practice to provide bearing between precast members. To match the real-world arrangement, the bearing pad edge was aligned with the sawcut edge of the slab. Consequently, the centerline of the support nearest the applied load was 2.5 in. from the end of each slab. In some situations, the bottom surface of the slab and top steel plate of the support were not perfectly parallel. In these cases, very thin shims were wedged to fill the small gap and ensure full contact between the slab and support prior to applying load.

A pin and roller were designed, fabricated, and used in conjunction to allow for free longitudinal movement of the slabs during testing. The pin supported the end not being tested so that the larger portion of the slab would not roll uncontrollably following a web-shear failure. Should the slab completely break into two pieces at failure, a secondary support made of stacked concrete masonry units was provided near the loading point to prevent the free portion of the slab from falling to the ground and becoming damaged. Figure 3.17 shows the pin, roller, and neoprene pads at the support boundary conditions.

3.5.2 Mortar

Mortar pads were cast at the loading point on each specimen to ensure an even distribution of load across the 4 ft slab width. Dayton Superior Recrete 20-minute repair mortar was mixed and placed within small formwork attached to each slab. The mortar was mixed with a water-to-solids ratio of 0.37 to provide a flowable mix that self-leveled within the mortar pad formwork to ensure consistent bearing from the spreader beam attached to the actuator. The mortar had a specified 1-day strength of 3000 psi. With the mortar pad bearing area of 288 $in.^2$ and a maximum actuator capacity of 110 kips, the maximum possible bearing stress that could be expected to be applied to the pad was 382 psi. Therefore, the pad had sufficient strength for the purposes of this research.

3.5.3 Instrumentation

Linear variable differential transformers (LVDTs) and a load cell were used to collect data during testing. Additionally, an assortment of video cameras was used to document loading and crack formation. This collection of data was used to both quantitatively and qualitatively compare shear capacity and failure characteristics among specimens in the testing matrix.

To measure load, the actuator was equipped with an Interface Model 1000 fatigue rated high capacity load cell with a capacity of +/- 100 kips. The applied load was proportioned using statics based on the distance between the load point and each support (2.5 ft to the nearest support and 13.5 ft to the support furthest from the load) to determine the applied shear force at the critical point ($h/2$ = 0.5 ft from the support centerline).

Additionally, member selfweight was factored into the peak shear force. An example calculation of member loading can be found in Appendix A.

While efforts were made to ensure equal distribution of load across the section and flush bearing surfaces, several LVDTs were placed around the test setup to identify unexpected slab motion during testing. The LVDTs were manufactured by Trans-Tek and had a working range of +/- 0.5 in. The deflections expected and measured at web-shear failure were on the order of tenths of an inch, making it very difficult to visually identify changes in slab position. While deflection was not of critical importance for shear capacity, the relative difference in deflections across the width or along the length of the slab could identify any undesirable twisting motion of the specimen. Since the slab had a symmetric cross section, slab twisting was indicative of improper load distribution or bearing contact. Should this be the case, additional torsional stresses could be induced on the section, thus reducing the capacity of the slab to resist vertical shear. If these torsional stresses were notable, the results of a test would not be suitable for comparison with other properly loaded tests that were not influenced by extraneous torsional stresses. Consequently, two LVDTs were directly attached to the slab on either side at the load point and each support for a total of six external LVDTs.

Figure 3.18 shows the arrangement of LVDTs in the laboratory. Prior to testing, all six external LVDTs were calibrated with a linear relationship between measured voltage and reported displacement.

Following testing, the actual deflection at the load point was calculated by subtracting the averaged deflections at the supports from the averaged deflection at the load. By excluding the deformations of the bearing pads and support structures, the true slab deflection at the load point could be determined. Since the load point was not midway between supports, a geometric correction for the offset was performed following Equation 3.2. Figure 3.19 provides a visual depiction of this correction.

$$\delta = \delta_{LP} - \left(\delta_{S1} - \left(\frac{a}{L} * \delta_{S2}\right)\right) \quad 3.2$$

To visually compare crack propagation and failure characteristics between each test, four video cameras were arranged around the testing end of each slab. Two cameras provided an elevation view of each side of the slab across the shear span. One camera captured the interior of the cores via an end view. Finally, a fourth camera was placed above and away from the slab to monitor the overall behavior of the slab from a bird's eye view. The placement and view of the video cameras can be seen in Figure 3.20. Beyond using the footage as a comparison between tests, the video cameras were also intended to record any mishaps during testing, should they occur. While only a precaution, the footage could be very useful to explain unreasonable data during the data analysis stage.

3.5.4 Data Acquisition

A Shore Western controller with a National Instruments data acquisition system was used to control the hydraulic system for loading and collect data from external LVDTs and a load cell. All seven channels were recorded at 10 Hz and the data were saved as text files. Following each test, the data were imported into Microsoft Excel for further processing and analysis.

3.6 Test Procedure

Prior to each test, a series of slab preparation tasks were completed. First, a 1 in. thick by 6 in. wide by 48 in. long mortar pad was cast at least 24 hours prior to loading. The mortar pad center line was placed at the centerline of the applied load and was intended to improve the load distribution across the width of the slab. Second, the ends of each prestressing strand were painted with spray paint to allow for visual identification of strand slip during testing, as seen in Figure 3.18. Upon saw cutting each slab to length at the manufacturing facility, the strands initially slipped inward. By painting the strand ends and surrounding concrete prior to testing, the additional strand slip due to testing could easily be differentiated from the initial strand slip, as shown in Figure 3.21. Beyond visual inspection, the initial strand slips and strand slips after web-shear failure were also measured to the nearest 0.01 in. using a tire tread measuring tool. Third, the outer surfaces of the slab and inside faces of the cores were thoroughly cleaned to reduce saw cut residual

dust by lightly grinding with a stiff wire brush attachment. Since a large wet saw is used to cut each individual slab, a significant amount of concrete dust accumulation is left on the slab and within the cores. Consequently, a clean concrete surface was necessary to clearly identify and document crack location following failure. A comparison of the interior of a core before and after cleaning is shown in Figure 3.5(a) and (b).

After slab preparation, the specimen was moved in place under the load frame and instrumented with the external LVDTs. Before loading, each specimen was thoroughly photographed to document the shear span, bearing conditions, and instrumentation. While each test arrangement was nearly identical, the pre-test photographs were also used to document slab defects from handling and transportation. Next, the LVDTs and load cell were zeroed and checked for proper connections prior to loading.

Loading of the slab was intended to last 30 minutes before web-shear failure to thoroughly capture slab performance. To pace the loading in a controlled manner, the actuator was advanced in a displacement-controlled mode at a specified rate. In general, the actuator was advanced at 0.008 in./sec for the first 10 kips and at 0.004 in./sec after reaching an applied load of 10 kips until web-shear failure. The increased initial displacement rate reduced the time required for settlement of the neoprene pad, mortar pad, and bearing pads. Immediately following each web-shear failure, crosshead advancement was paused, and strand slip measurements were recorded. For the first test on each slab, this signified the end of the test. For the second test on the second end of each slab, loading was resumed after web-shear failure to widen the cracks. This allowed for easier dismantling of the broken concrete for documentation of the crack face. Following all tests, all web cracking and the overall failed slab were photographed.

3.7 Crack Face Documentation

The crack angle at the critical depth of a section indicates the orientation of the principal stresses upon web-shear failure. This angle is useful for determining the amount of axial prestress and overall characterization of stresses at a given point. The angle of the core fill crack face compared to the adjacent hollow-core webs likely indicates a difference

in axial prestress. This measure could also suggest the level of prestress transmitted between the core fill and slab and effectiveness of the core fill enhancement.

An Artec3D Eva scanner and the accompanying Artec Studio 12 Professional data collection and post-processing software were used to capture a three-dimensional (3D) scan of one side of each core-filled specimen failure plane. A high-resolution 3D point cloud was captured and processed to generate a realistic surface model within the software. Figure 3.22(a) and (b) show a photograph of a crack face and the corresponding 3D scan, respectively. Within the model, the axis system was oriented with the *xy*-plane flush to the side of the slab. Next, two points were selected along the shear key notch to establish the longitudinal direction of the slab, which was denoted by the *x*-axis. Another two points were selected on each of the web concrete faces and the core fill concrete face. One of these points was slightly above mid-depth and the other point was slightly below mid-depth. The slope of the line connecting the crack face points was calculated relative to the longitudinal *x*-axis to determine each web or core fill concrete crack angle. Initially, crack angles were manually measured using a protractor. Unfortunately, this method was cumbersome and only accurate within 5°. Fortunately, crack angles determined through 3D scanning were in strong agreement with manual measurements, so scanned crack angles were ultimately used for crack face documentation.

Beyond measuring crack angles, the 3D scans were used for visual comparison between slabs throughout the testing matrix. Due to laboratory space limitations, a maximum of four broken slabs were housed at one time (others were taken for disposal by the manufacturer), so slabs could not be physically compared side-by-side to all of the other slabs in the matrix. While photographs of each crack face were useful, the 3D models provided the ability to compare crack face angles between multiple slabs. Furthermore, these scans could be used for comparison with future research after disposal of the slabs.

Table 3.1. Variables investigated in experimental program

Core Modification	No. of Slabs	No. of Tests	Core Fill Concrete Type	Core-Filled Slab Age	Phase
1) Empty cores	1	2	----	----	1
2) Cold joint core fill, 2 ft fill	1	2	Typical mix	Mature[1]	1
3) Cold joint core fill, 4 ft fill	1	2	Typical mix	Mature[1]	2
4) Typical immediate fill	1	2	Typical mix	Early[2]	1
5) 209-day typical fill[3]	1	2	Typical mix	Early	1
6) Fiber-reinforced fill – 0.5% volume fraction	1	2	Steel fiber-reinforced concrete	Early	2
7) Core wall surface enhancement	1	2	Typical mix	Early	2
8) Steel bar placed in core fill	1	2	Typical mix	Early	2
9) Welded wire reinforcement in core fill	1	2	Typical mix	Early	2

[1] Approximately 3 weeks after extruding slabs
[2] Approximately 1 hour after extruding slabs, typical at all early core fills
[3] Immediately core-filled slab allowed to cure for 209 days prior to testing

Table 3.2. Mix design ingredients and parameters for the hollow-core slab material

Ingredient	Quantity per cubic yard
Type III Cement (lb)	448
Fly Ash (lb)	192
9/16 in. Rock (lb)	1,686
Sand (lb)	1,665
MasterMatrix 33 (oz.)	26
MB AE 90 (oz.)	5
Water-to-cement ratio	0.35

Table 3.3. Measured concrete compressive strength on the day of testing

Core Modification	Slab Side	Slab Concrete Compressive Strength (psi), f'_c	Core Fill Concrete Compressive Strength (psi), f'_{cf}
1) Empty cores	A	12,960	N/A
	B	12,880	N/A
	Average	12,920	N/A
2) Cold joint core fill, 2 ft fill	A	12,340	7,720
	B	12,530	8,100
	Average	12,440	7,910
3) Cold joint core fill, 4 ft fill	A	12,940	7,290
	B		
	Average	12,940	7,290
4) Typical immediate fill	A	13,300	8,130
	B	13130	8,000
	Average	13,210	8,070
5) 209-day typical fill	A	13640	9040
	B		
	Average	13640	9040
6) Fiber-reinforced fill – 0.5% volume fraction	A	11,940	7,300
	B		
	Average	11,940	7,300
7) Core wall surface enhancement	A	10,640	6,100
	B	10,520	6,000
	Average	10,580	6,050
8) Steel bar placed in core fill	A	11,350	7,100
	B		
	Average	11,350	7,100
9) Welded wire reinforcement in core fill	A	11,430	7,290
	B		
	Average	11,430	7,290

Table 3.4. Measured compressive and tensile strengths of the slab and core fill concrete at 28 days

Material	Compressive Strength (psi), f'_c	Tensile Strength (psi), f_{ct}	$\frac{f_{ct}}{\sqrt{f'_c}}$
Slab	12,340	999	9.0
Core Fill	6,901	484	5.8

Table 3.5. Measured compressive and tensile strengths of the slab and SFRC core fill concrete at 42 days

Material	Compressive Strength (psi), f'_c	Tensile Strength (psi), f_{ct}	$\frac{f_{ct}}{\sqrt{f'_c}}$
Slab	11,935	895	8.2
Core Fill	7,298	780	9.2

Table 3.6. Prestressing strand material properties

Material Property	Manufacturer Provided
Diameter (in.)	0.6
Area ($in.^2$)	0.217
Modulus of Elasticity (ksi)	28,500
Ultimate Stress (ksi)	270

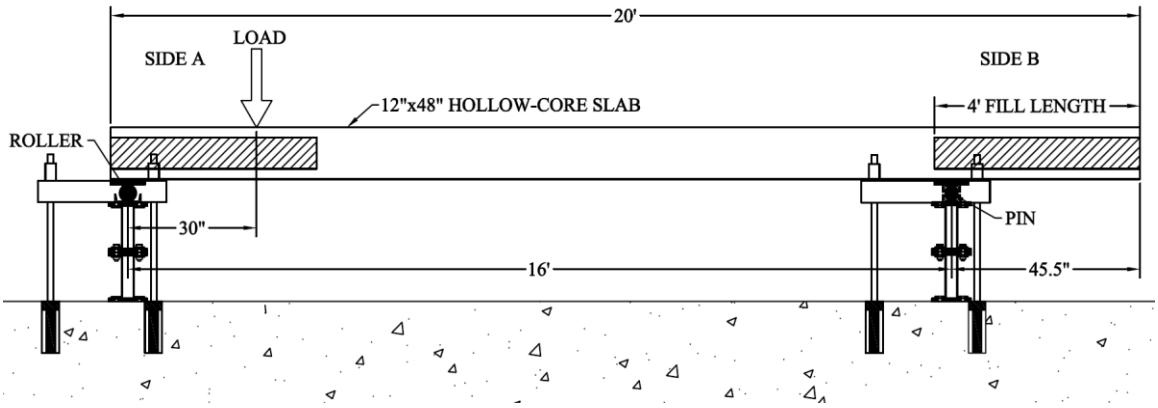

Figure 3.1. Simplified layout of supports, loading, core fill, and overhang

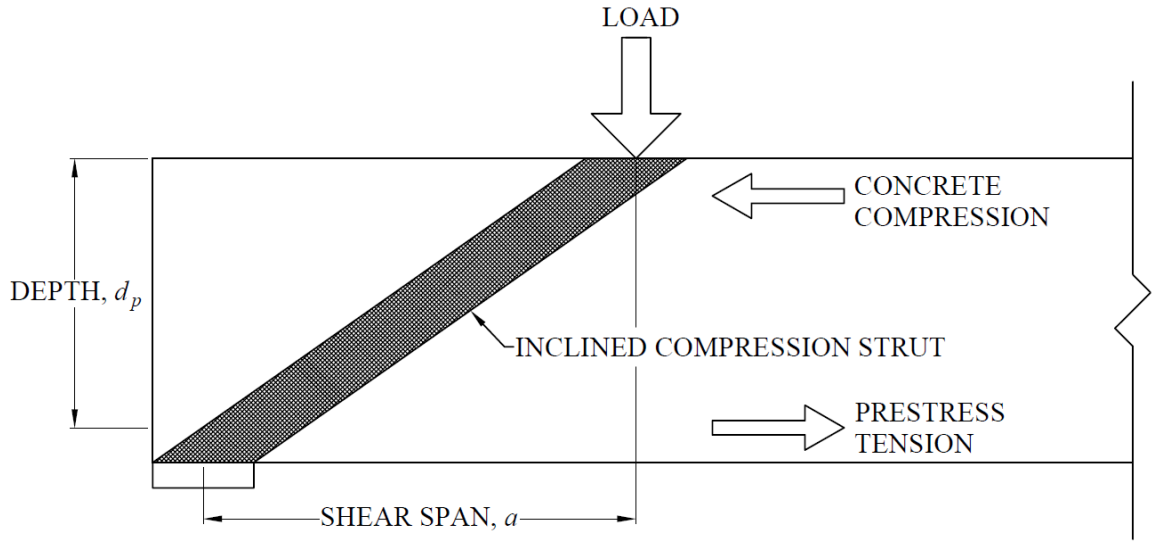

Figure 3.2. Depiction of an inclined compression strut acting within the shear span region to provide arching action

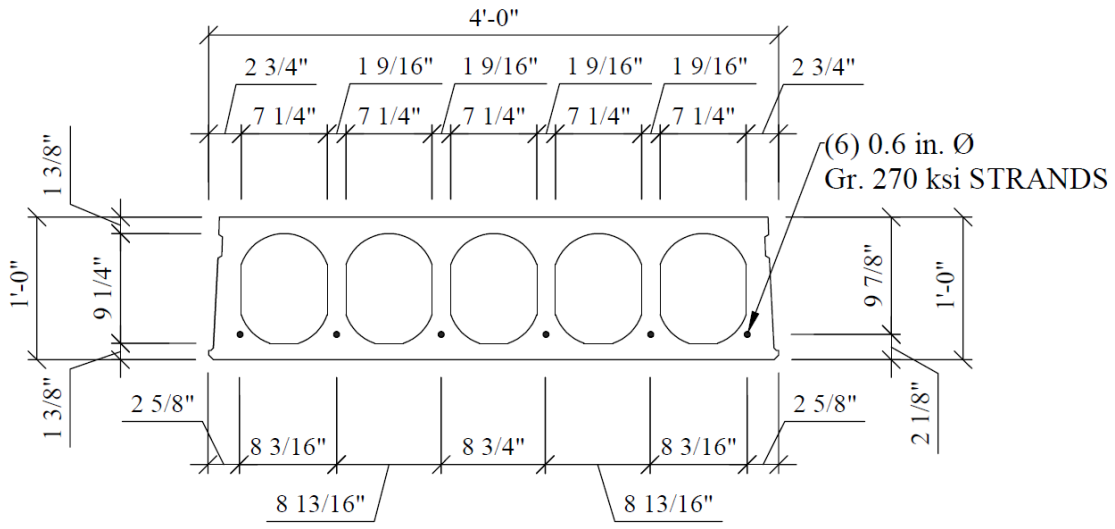

Figure 3.3. Cross section geometry of the 12 in. light hollow-core slab design

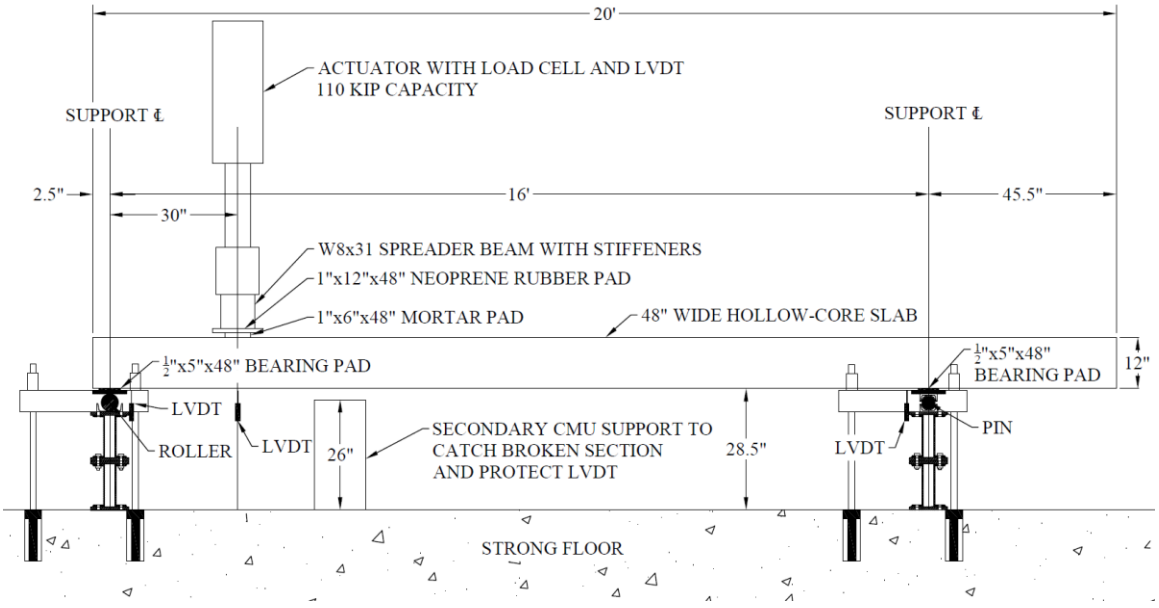

Figure 3.4. Test setup elevation

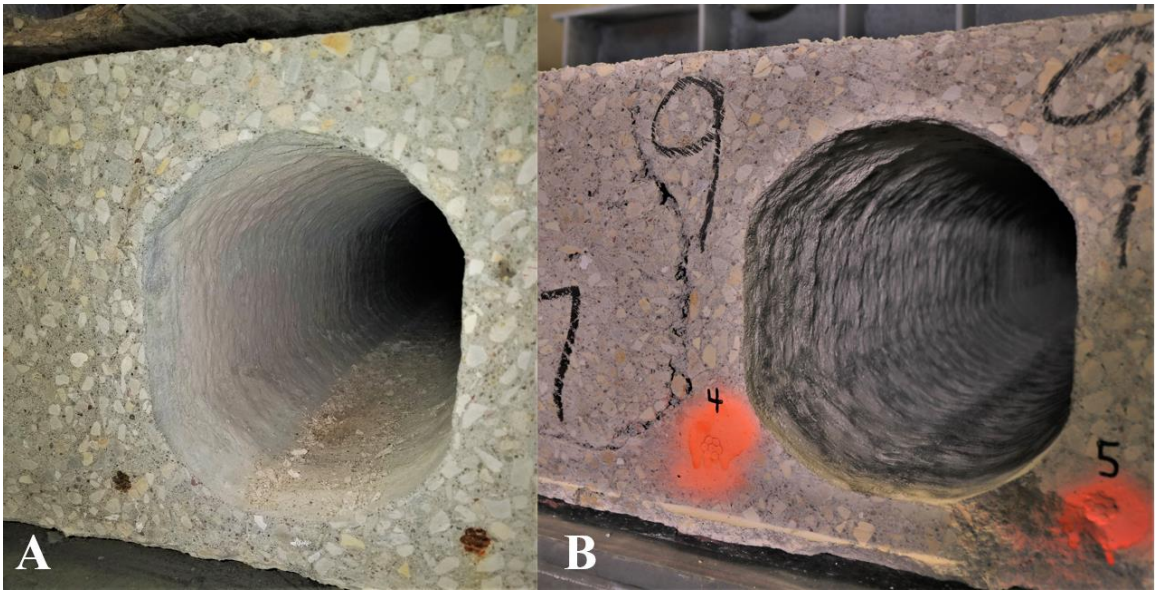

Figure 3.5. (a) Saw cut residual dust coating the interior of the core prior to cleaning; (b) cleaned interior of the core following grinding with a wire brush

Figure 3.6. Fresh steel fiber-reinforced concrete placed in a hollow-core

Figure 3.7. Roughening a core wall with 0.25 in. deep vertical indentations 1 in. on center with a garden rake

Figure 3.8. Headed #6 bar 4 ft long with 0.25 by 2 by 2 in. plate welded to each end and placed at the bottom of the core

Figure 3.9. Two 4 ft long by 8 in. tall pieces of 4-gauge welded wire reinforcement with a 4 by 4 in. grid placed vertically in the core

Figure 3.10. Top flange removal in the middle core using the heel of a worker's boot

Figure 3.11. Core fill concrete placed in the opened middle core

Figure 3.12. Finishing of the top surface following core filling

Figure 3.13. Empty middle core of a cured slab exposed following saw cutting

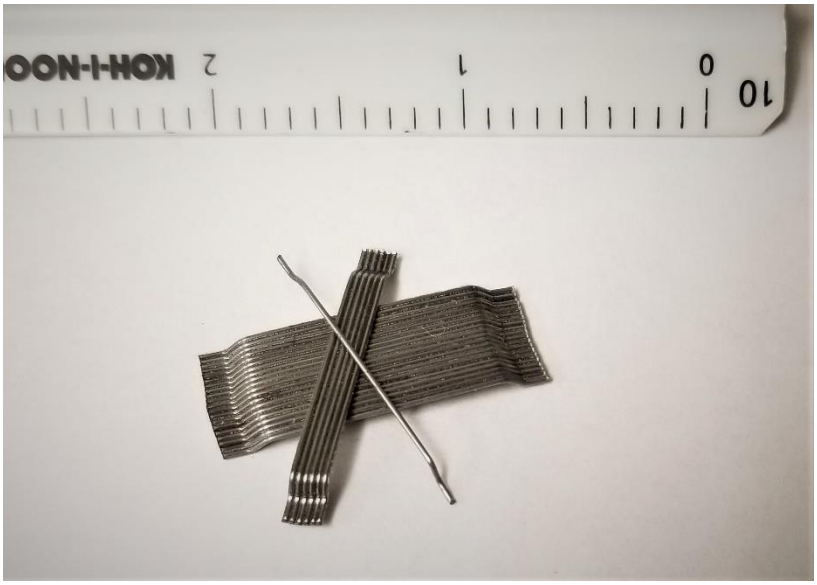

Figure 3.14. Dramix 3D 55/30BG steel fibers

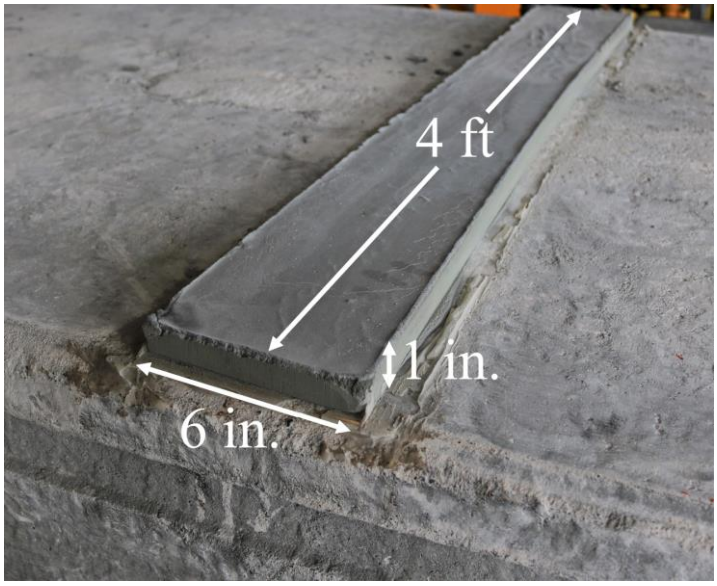

Figure 3.15. Transverse mortar pad cast on top flange to provide a level bearing surface for the applied load

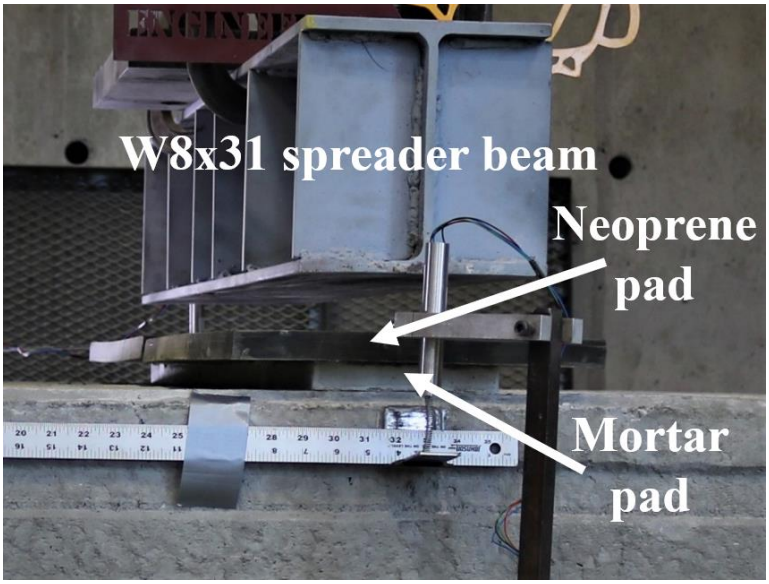

Figure 3.16. Transverse spreader beam, neoprene pad, and mortar pad at actuator

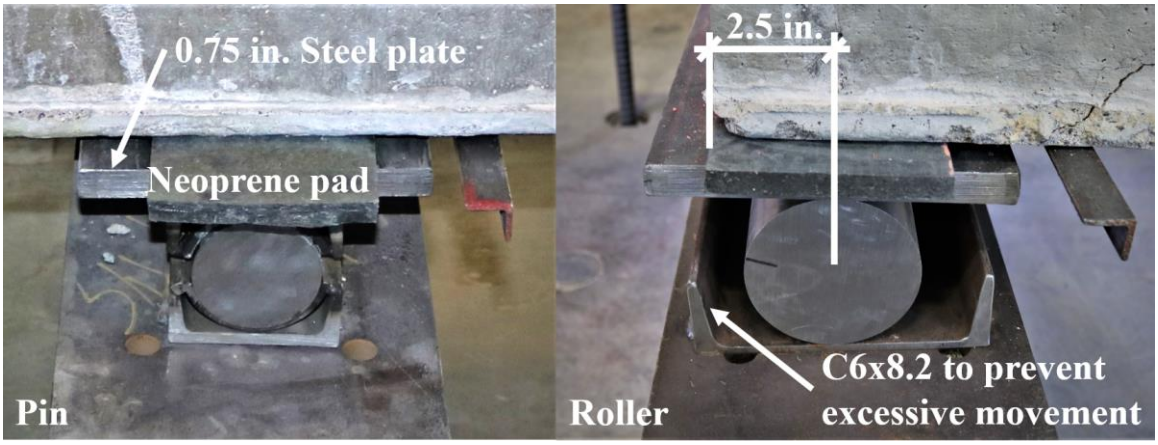

Figure 3.17. (a) Pin and (b) roller boundary conditions used to support the slabs

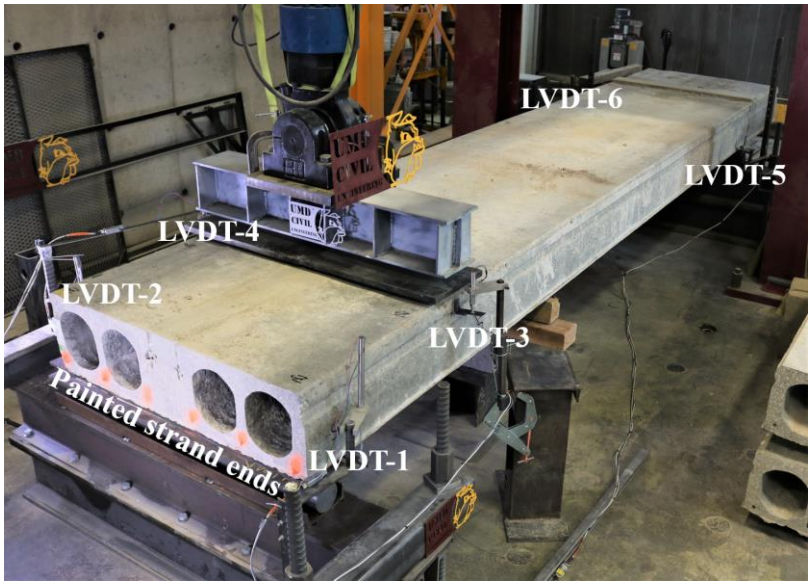

Figure 3.18. Arrangement of the external LVDTs for testing and the painted strand ends

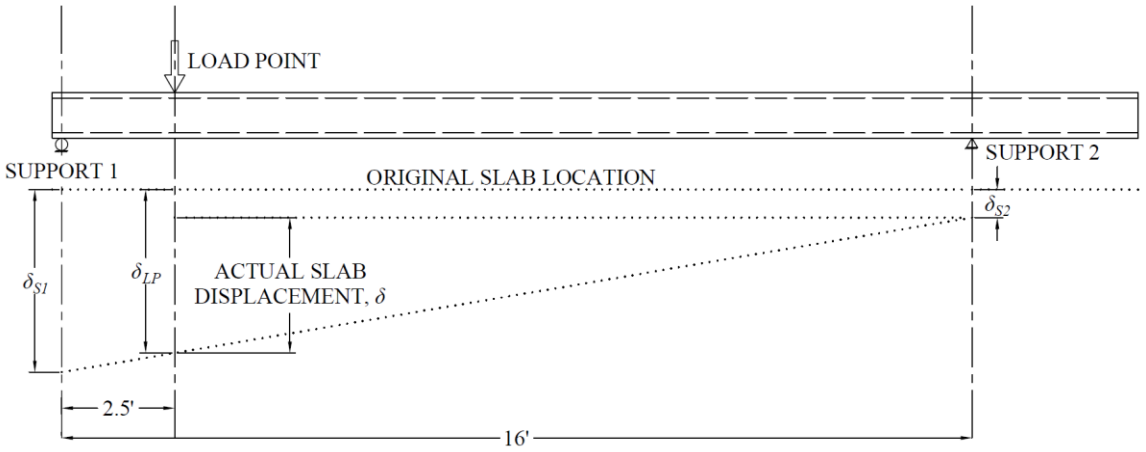

Figure 3.19. Geometric correction of the external LVDT measurements to calculate the actual slab deflection

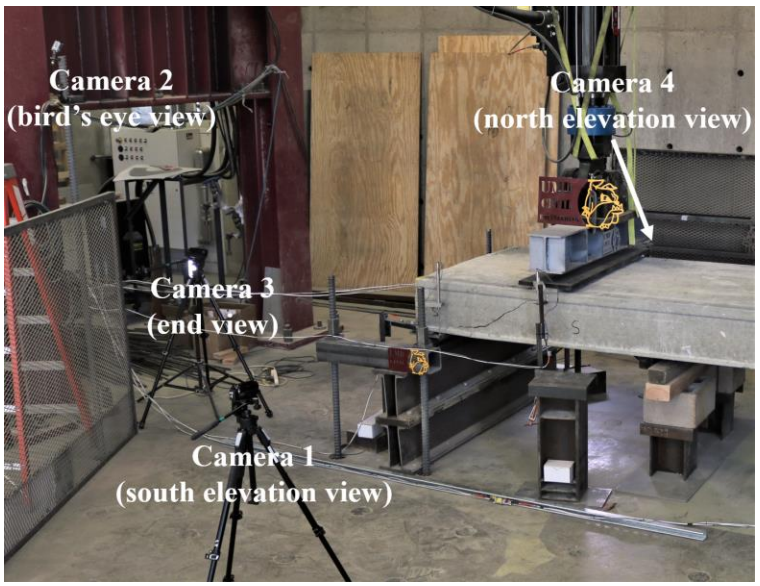

Figure 3.20. Arrangement of the video cameras during testing

Figure 3.21. Strand slip due to testing evident from exposed unpainted concrete surrounding the strand

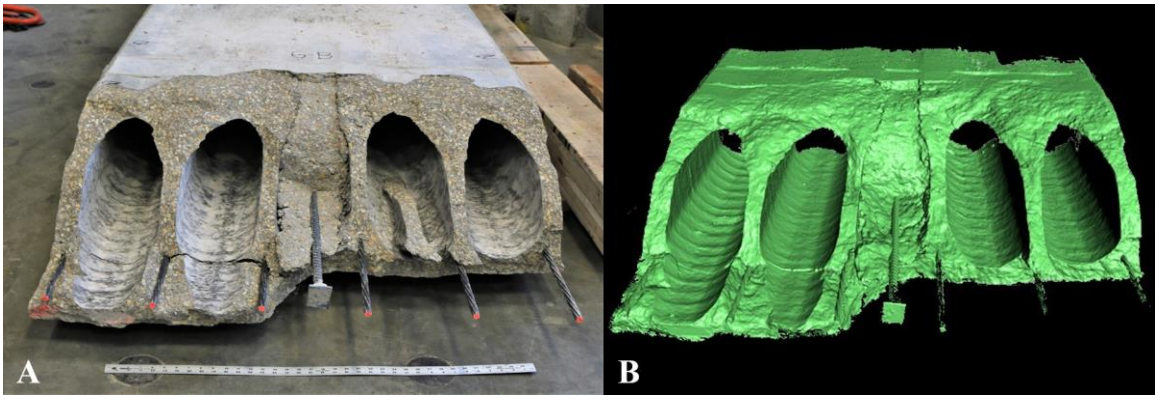

Figure 3.22. Example (a) photograph of the crack faces and (b) scanned 3D surface model of the crack face

Chapter 4: Results

4.1 Behavior at Failure

4.1.1 Load and Displacement

Load was applied at a displacement-controlled rate throughout each test to gradually approach the limiting web-shear capacity and precisely capture the peak applied load. Failure was defined as the maximum load applied to a slab prior to the sudden drop of applied load and abrupt deflection due to web-shear cracking. Advancement of the actuator was able to be paused directly following web-shear cracking and further deterioration of the slab was prevented. During this pause, cracking, strand slip, and overall slab behavior were inspected and documented for each test specimen.

While most of the shear capacity was lost following web-shear cracking, all slabs had some residual capacity due to the remaining engagement of the prestressing strands. At approximately the same time as web-shear cracking, the prestressing strands slipped 0.1 in. on average for each slab. After failure, the prestressing strands were generally still engaged with the concrete near the end of the slab and could carry some load. Additionally, the top flange of the slab remained in contact with the rest of the slab following cracking. As a result, a moment couple between the prestressing strands and remaining concrete compression block in the flange offered some residual moment capacity, as shown in Figure 4.1. Potential aggregate interlock across the web-shear crack and dowel action of the prestressing strands may have provided a load path for supplemental shear resistance as well.

After post-failure inspections were completed on each side of the slab, load was re-applied to the second side of each specimen. This second phase of loading was performed to widen the web-shear cracks and allow for ease of dismantling the broken slab end for further inspection. During the continued actuator advancement, the applied load gradually decreased until the prestressing strands completely disengaged. If load was applied past this point, the applied load sharply dropped to less than a few kips. In one case, the slab completely broke apart and fell onto the secondary support. The additional actuator

displacement during this second phase of loading was about 1 in. The applied load versus slab deflection plots for each test are shown in Appendix B.

4.1.2 Crack Propagation

No shear or flexure cracking was observed in any of the test specimens prior to web-shear cracking. Rather, a web-shear crack appeared across each of the webs at nearly the same time upon failure. These brittle web-shear cracks appeared abruptly, resulting in a sudden drop of web-shear capacity. While it was visually indistinguishable to determine the critical point at which web-shear cracking began, the resulting crack propagated from the load point to the prestressing strand diagonally. At the strand depth, the crack shifted direction and traveled longitudinally along the prestressing strand to the support, as shown in Figure 4.2.

Prior to testing, some of the specimens had a crack on the top flange between the core fill and slab material, likely due to shrinkage between the core fill concrete and slab concrete, as shown in Figure 4.3. This pre-existing crack along the joint widened during testing. Additionally, transverse cracking of the bottom flange near the support and top flange near the load occurred during testing on some of the test specimens, as shown in Figure 4.4(a) and (b).

4.1.3 Core Fill Behavior

In each test specimen, the core fill concrete exhibited a web-shear crack near the adjacent web-shear cracks in the slab. This indicated that the core fill concrete was engaged and carried some of the shear force, as intended. Following testing, it was apparent that the core fill concrete slipped and was not composite with both adjacent webs of the slab concrete in the cold joint core fill, SFRC core fill, and steel bar in core fill specimens. Upon dismantling the broken end of these slabs, the core fill concrete was observed to be completely non-composite with the slab concrete as shown in Figure 4.5. In the cold joint core fill slab, a powdery dust was found on the outer surface of the core fill, as shown in Figure 4.6. This material was likely residual concrete dust from slab saw cutting that was

not removed prior to core filling. In the four other core-filled test specimens, the core fill concrete remained composite with one or both of the adjacent slab webs.

4.2 Experimental Shear Test Results

All of the specimens exhibited a sudden brittle web-shear failure (except side A of the SFRC specimen which showed minor ductility). The peak shear force ranged from 53.3 to 72.9 kips and the slab displacements at failure ranged from 0.16 to 0.20 in. throughout the tests. A summary of the peak shear force and the accompanying slab displacement for each test is shown in Table 4.1.

Since the specimens were tested on different days and some of the duplicate tests were performed at different times, the concrete strength of both the slab and core fill varied. As a result, the peak shear force presented in Table 4.1 cannot be directly compared. Consequently, it is useful to compare the experimentally measured shear capacity with the respective predicted capacity to assess the performance of each test. This comparison normalizes the differences in concrete strength between each of the individual tests and allows for a realistic comparison between specimens. To specifically investigate the differences in core fill between specimens, several variables were held constant throughout the testing matrix, including: slab depth, void shape, slab concrete mix design, prestressing level, loading rate, and shear span. Aside from the cold joint core fill specimen, all cores were filled immediately following extrusion.

There were several approaches used in this report to present the test data for comparison between specimens in the testing matrix. The most comprehensive plot compared the peak shear force of each test with the web-shear capacity predicted using ACI 318 (2014), as shown in Figure 4.7. The *x*-axis presents each of the core fill modifications with two bars, which represent both of the tests performed on each slab. The *y*-axis quantifies the shear force at *h*/2 (6 in.) from the support. Three predicted web-shear capacities were calculated for each of the tests as shown by the horizontal solid lines. The "No Core Fill" line represented the web-shear capacity calculated using Equation 2.6, which only determined the web-shear contribution of the slab concrete. The "Unreinforced Fill Behavior" line and "Prestressed Fill Behavior" lines included the core fill contribution

to web-shear capacity as calculated by Equations 2.8 and 2.6, respectively. For all predicted web-shear capacities, the test-day concrete strength of the slab and core fill concrete were used. As a result, the predicted web-shear capacities varied. Figure 4.7 is not intended to be used for directly comparing the magnitude of the vertical bars between each slab and core fill modification. Rather, the relative difference in magnitude of the bars with their respective predicted web-shear capacities may be compared separately for each slab and core fill modification.

Figure 4.7 summarizes all of the testing and allowed for a comparison between tests after accounting for differences in concrete strength, but it can be difficult to interpret. Consequently, simplifications were incorporated in the development of Figure 4.8. First, the peak shear force of the two duplicate tests for each core fill modification was averaged. The *y*-axis of Figure 4.8 shows the ratio of the peak shear force to the predicted web-shear capacity of a slab with no core fill (Equation 2.6). In this simplified view, the performance of each of the core fill modifications can be more easily compared, but the core fill concrete strength is not normalized.

The web-shear strength of the empty core fill specimen was expected to most closely match the predicted web-shear capacity of Equation 2.6. For several possible reasons, the average experimentally measured shear capacity of the empty cores specimen was 23% greater than the predicted web-shear capacity (likely due to the built-in conservatism of Equation 2.6). Comparison of the specimen shear capacities to the shear capacity of the empty cores slab baseline was more useful because the inaccuracies from the prediction equations were excluded. The baseline web-shear capacity of the hollow-core section used in this testing matrix was determined by two tests of a slab with no core fill. In Figure 4.9, the *y*-axis shows the ratio between the peak shear force applied to each specimen and the peak shear force applied to the empty cores specimen (i.e., the column for the empty cores specimens does not show the conservatism of 23% between the measured shear capacity and predicted shear capacity to make Figure 4.9 easier to read, even though this conservatism is still inherently present in all of the specimens).

While Figure 4.7 through Figure 4.9 allowed for comparison among the core fill modifications in the testing matrix, they are not particularly useful for design. One of the main objectives of this project was to determine whether the core fill concrete behaved as unreinforced concrete or as fully prestressed concrete. Oftentimes, shear strength is quantified by a multiple of the square root of the concrete strength multiplied by its respective area. For example, unreinforced concrete shear strength uses a coefficient of 2, as shown in Equation 2.8. The shear strength of the core fill in each specimen is presented in Figure 4.10 by deducting the predicted slab web-shear strength from the peak shear force and expressing the remaining shear capacity in terms of a multiple of the square root of the core fill concrete compressive strength. Because all of the slabs were of identical cross section and prestressing, the slabs should have had no difference in web-shear capacity between tests when normalized for slab concrete strength. By deducting the shear contribution of the slab concrete, the shear strength of the core fill concrete was quantified in Figure 4.10. In Figure 4.10, horizontal reference lines for unreinforced and prestressed core fill concrete behaviors are shown. Per Equation 2.8, the unreinforced concrete behavior reference line is shown at 2. Since the prediction for prestressed web-shear capacity shown in Equation 2.6 includes a term for the axial precompression of the member, the axial precompression term was divided by the square root of the core fill concrete strength as shown in Equation 4.1 to present an equivalent multiple of the square root of the core fill concrete strength.

$$3.5 + \frac{0.3f_{pc}}{\sqrt{f'_{cf}}} \qquad 4.1$$

The axial precompression at the time of testing each side of the specimen was nearly identical and the core fill concrete strength was somewhat consistent between tests. By using the average axial precompression and core fill concrete strength of each test in Equation 4.1, the average adjusted coefficient multiplied by the square root of the core fill

concrete strength was 4.2. This coefficient is shown in Figure 4.10 to reference the fully prestressed behavior of the core fill concrete.

4.2.1 Core Fill Timing Specimens

4.2.1.1 Core Fill Fabrication Timing

The first objective of the project sought to understand how core fill timing affected its contribution to web-shear capacity. In practice, slabs are core filled either after the slab has been cured and the prestressing strands have been released or immediately following extrusion prior to strand release. When a cured slab has core fill concrete added to it, there is a cold joint between the core fill concrete and the slab concrete. As a result, the core fill concrete likely behaves as unreinforced concrete. In the latter case, where slabs are core-filled immediately following extrusion, the slab and core fill concrete cure together prior to prestressing strand release. In this case, the core fill concrete potentially holds some axial compression and could exhibit prestressed concrete shear behavior.

The first three specimens in the testing matrix served to investigate the difference in core fill timing. As shown in Figure 4.10, the typical immediate fill specimen exceeded the web-shear capacity of the cold joint core fill specimen, both of which exceeded the web-shear capacity of the baseline empty core specimen. This trend indicated that the three specimens behaved as expected. Specifically, the cold joint core fill tests exceeded the predicted capacity of unreinforced core fill concrete, indicating that the cold joint core fill concrete exceeded its expected shear capacity. Furthermore, the typical immediate fill specimen slightly exceeded the predicted fully prestressed core fill concrete behavior. As expected, this indicated that the core fill concrete acted as prestressed concrete.

The baseline empty core specimen tests exceeded the predicted slab web-shear capacity by 23%, which was likely due to the built-in conservatism of Equation 2.6. It is difficult to explicitly measure the slab web-shear contribution in core-filled specimens because the contribution of the slab concrete and core fill concrete to the overall slab shear capacity cannot be differentiated. Since the over-conservatism in the estimated slab web-shear contribution was likely included in all of the core-filled tests, the web-shear contribution of the core fill concrete presented in Figure 4.10 likely attributed more web-

shear capacity to the core fill concrete than was exhibited. As a whole, the cold joint core fill tests exceeded the predicted web-shear capacity of a slab with unreinforced core fill by 10% on average and the typical immediate fill tests exceeded the predicted web-shear capacity of a slab with prestressed core fill concrete by 5% on average. These percentages were determined by dividing the average peak applied shear force from Figure 4.7 by the respective predicted shear capacity and subtracting a value of one to convert to a percentage.

4.2.1.2 Aged Core-Filled Slab

Since precast concrete systems are intended to be resilient, long-lasting structures, the long-term performance of core-filled hollow-core slabs was considered. Other than the cold joint specimen, all specimens were immediately core filled following extrusion and before prestressing strand release. For these specimens to have any axial prestress, the bond between the core fill concrete and slab concrete was essential. Testing in this project was performed within one to three months from fabrication. Over longer periods of time, the bond between the slab and core fill concrete could be compromised due to shrinkage. Should the slab and core fill behave independently, they would shrink away from each other, which could produce a gap around the core fill. To address this concern, a slab identical to the typical immediate fill slab was tested 209 days (approximately 7 months) after fabrication.

The aged core-filled specimen did not perform as well as the typical immediate fill specimen, as shown in Figure 4.10. The aged core-filled specimen should perform similar to the typical immediate fill specimen if no time-dependent detrimental effects were present. Unfortunately, the aged core-filled specimen behaved more as if the core fill concrete was unreinforced concrete, indicating that the bond between the slab and core fill concrete was poor. Upon dismantling the broken slab, the core fill concrete was clearly free from the slab concrete as shown in Figure 4.5, further indicating a poor composite behavior between the slab and core fill concrete.

The decreased web-shear performance of the aged core-filled specimen over time is critical. Precast structures are intended to perform as designed throughout their service

life. Therefore, it would not be appropriate to design core-filled hollow-core slabs as fully prestressed concrete if the filled cores behave more like unreinforced concrete over time. Very little variation existed between the peak shear force recorded in the two 209-day tests (< 2%), suggesting some reliability in the test results, though not based on statistics. As with all of the specimens, only two tests were performed on the aged core-filled specimen.

4.2.2 Core Fill Enhancement Specimens

4.2.2.1 Steel Fiber-Reinforced Concrete Core Fill

Previous testing of SFRC in the slab material showed improvements in shear capacity, but several secondary benefits due to the fibers also contributed to the overall slab strength of these SFRC hollow-core slabs. First, the prestressing bond was shown to be improved by fiber content (Chao et al., 2006). Secondly, the vertical steel fiber orientation in the hollow-core webs due to their manufacturing methods was ideal (Simasathien and Chao, 2015). Both added benefits cannot be realized when only the core fill material is made of SFRC. Therefore, while improvements were shown in slabs made entirely from SFRC material, somewhat smaller improvements were expected in the SFRC core fill tests. The goal of the two SFRC core fill tests was to improve the overall slab shear capacity by improving the shear performance of the core fill concrete.

Unfortunately, the SFRC core fill specimen had the worst web-shear performance of all the specimens in the testing matrix. In fact, the empty core baseline specimen outperformed the SFRC core-filled specimen, as shown in Figure 4.9. These results were unexpected as a core-filled specimen should have outperformed a slab with no core fill. Little explanation is available for why both SFRC core fill tests performed so poorly. The second phase of testing was intended to identify potentially promising core fill enhancement strategies. It was concluded that the SFRC core fill specimen did not show promise for greatly improving performance compared to the typical immediate fill specimen.

4.2.2.2 Headed Steel Bar in Core Fill

The headed steel bar core-filled specimen was expected to at least perform as well as the typical immediate fill specimen because they were fabricated identically. The addition of a headed #6 rebar was intended to maintain axial prestress in the core fill and alleviate the longitudinal demand on the prestressing strands during loading. Unexpectedly, the headed steel bar core-filled specimen performed lower than the typical immediate fill specimen as shown in Figure 4.10. Since the only intentional difference between the two specimens was the headed steel bar, the bar was suspected to have had an undesirable effect.

The cracking of the core fill concrete in the headed steel bar specimen was unlike all of the other core-filled specimens, which exhibited a consistent diagonal crack through the entire core fill concrete depth. Instead, the core fill concrete of the headed bar specimen cracked more steeply from the top flange to the steel bar depth. At the bar level, the core fill concrete cracking traveled longitudinally following the steel bar to the member end, as shown in Figure 4.11. This suggested that that steel bar promoted a failure plane along itself that was uncharacteristic of the shear cracking observed in the other specimens. As a result, the core fill concrete area beneath the steel bar likely did not contribute to the core fill shear strength. Since the predicted web-shear capacity of the specimen with the core fill concrete considered the entire core fill area, this reduced core fill area (approximately 15% less area) for shear could explain why the specimen appeared to underperform.

4.2.2.3 Vertical Welded Wire Reinforcement in Core Fill

The addition of WWR in the core fill provided vertical steel reinforcement, which was intended to provide transverse shear reinforcement, similar to traditional stirrups. This modification sought to improve the core fill web-shear strength. The WWR specimen performed slightly worse than the typical immediate fill specimen as shown in Figure 4.10. These results could be interpreted two ways. First, the core fill concrete may have underperformed and the WWR provided additional web-shear capacity so that the specimen performed similar to the typical immediate fill specimen. Second, the test results

could indicate that the WWR did not add additional web-shear capacity and the core fill concrete performed as prestressed.

Upon dismantling the broken end of the WWR specimen, the WWR bars were found to not be completely ruptured. This may mean that the WWR did not provide much web-shear capacity. Since dismantling required further damage of the specimen, it was difficult to determine if the WWR had yielded during testing. If the steel contribution to shear of 4.8 kips, calculated with Equation 2.4, was subtracted from the peak shear force in Figure 4.10 of 66.8 kips, the coefficient multiplied by the square root of the core fill concrete strength would have been 3.3. Aside from the addition of the WWR, the WWR specimen and typical immediate fill specimen were constructed identically. Since they performed nearly identical, the WWR did not seem to have any notable effect. It was also observed that the core fill concrete of the WWR specimen remained connected to the adjacent slab webs, which indicated a good bond between the slab and core fill concrete (this also occurred with the typical immediate fill and core wall surface enhancement specimens). Since the core fill was well bonded, more axial prestress was likely present in the core fill concrete, which consequently would result in more web-shear strength. This axial prestress could have been maintained by the longitudinal bars of the WWR.

4.2.2.4 Core Wall Surface Enhancement

Rather than improving the core fill concrete shear strength, roughening of the core wall prior to core filling was intended to improve the bond between the core fill concrete and slab concrete to promote the transfer of axial prestress to the core fill concrete. The core wall surface enhancement specimen slightly outperformed the typical immediate fill specimen and exceeded the prediction calculated as if the core fill concrete was prestressed, as shown in Figure 4.10. The core wall surface enhancement specimen slightly outperformed the typical immediate fill specimen and exceeded the prediction calculated as if the core fill concrete was prestressed. At a minimum, the enhancement did not have any detrimental effects.

4.2.3 Core Fill Fabrication Timing and Enhancement Discussion

Of the four core fill enhancement specimens, only the core wall surface enhancement and WWR specimens performed similar to the typical immediate fill specimen and exceeded the prediction calculated as if the core fill concrete behaved as prestressed. The core wall surface enhancement sought to improve the bond between the slab and core fill concrete. The WWR core fill modification was intended to improve the web-shear strength of the core fill. However, the web-shear capacity was slightly less than the typical immediate fill specimen, as shown in Figure 4.10, indicating that the WWR did not have a significant effect. It was observed that enhancing the core fill concrete for greater web-shear capacity was not particularly useful because the two other core fill enhancement strategies intended to improve the core fill underperformed (steel fiber-reinforced and steel bar placed in core fill).

After investigating the broken, deconstructed specimens, it was likely not a coincidence that the core fill concrete remained composite with the adjacent slab webs for the three specimens that performed the best (typical immediate fill, core wall surface enhancement, and WWR in the core fill). The crack faces on these three specimens, shown in Figure 4.12, indicated that the core fill concrete acted monolithically with the slab concrete because the crack face across the slab webs and core fill concrete was somewhat similar and uniform. This general observation suggests that the bond between the slab and core fill concrete is a critical factor in the web-shear strength of core-filled hollow-core slabs.

4.2.4 Slab Displacements and Rotations

LVDT pair differential displacements between each side of the slab at both supports and the load point were determined to identify if torsional stresses were introduced on the slab due to improper load distribution and potentially non-uniform bearing. Specifically, the difference in the measured displacement of each LVDT pair at the peak shear load of each test were calculated and summarized in Table 4.2. LVDT pair differential displacements are okay provided the differential is about the same at each LVDT pair along the length of the slab because no torsional stress would be induced (this would mean the

slab slightly rotated uniformly). Torsional stresses would be induced when the LVDT pair differential displacements were different along the span length. For example, if the LVDT pair differential displacement at the support nearest the load was 0.02 in. and the LVDT pair differential displacement at the load point was 0.10 in., then the slab was likely "twisted" across the shear span and additional torsional stresses may have been present. Should inadvertent torsional stresses be present, the measured shear capacity could be lower than the predicted capacities that assumed no torsional stresses were present. This is because the shear flow due to torsional stresses would add to the intended shear stress creating a magnified stress and promote shear cracking at a load less than would be realized under pure vertical shear loading. A summary of the LVDT pair differential displacements between the testing end support and load point and between the overhang support and load point are presented in Table 4.3.

To consider whether the magnitudes of slab twist experienced in this testing matrix disrupted the measured shear capacities, Table 4.3 was compared with the peak shear force from Table 4.1 and Figure 4.7. Two identical tests were performed for each core fill modification on each end of a slab and the slab side with more twist was identified in Table 4.3. Comparing the two identical tests for each slab, the test of the slab end with more twist also had the lower peak shear force from Table 4.1 and Figure 4.7 for all specimens except for the steel bar placed in core fill and WWR placed in core fill modifications. However, the steel bar placed in core fill specimen had very little slab twist and the two peak shear forces varied by about 1 kip. This correlation suggested that the observed slab twisting did influence the measured slab shear capacity. Since slab twist was present in all of the tests it is likely that some unwanted torsional stresses were induced during all of the tests.

The slab twist observations suggested torsional stresses may have been present in addition to the intended shear stress induced by vertical shear forces. While this may have slightly disrupted the comparisons between predicted and measured shear strengths, real-world erection of hollow-core slabs likely lends itself to less than ideal bearing surfaces and potentially eccentric loading. Consequently, testing that induced minimal slab twist was considered to encapsulate the realities of real-world conditions.

4.3 Theoretical Shear Strength Predictions

4.3.1 Shear Strength Prediction Methodology

ACI 318 (2014) shear equations were used to predict the slab behavior for the development of the test setup and slab geometry. While ACI 318 (2014) is commonly used and specified for building design, several other prediction methods were considered for analysis of results, including the Palmer and Shultz (2009) web-shear equation, the AASHTO LRFD Bridge Design Specification (2018) equation for shear, and Yang's Method (1994). The ACI 318 and Palmer and Shultz predictions were calculated for both unreinforced and prestressed core fill concrete behavior, as shown in Equations 2.17, 2.18, 2.27, and 2.28, respectively. The AASHTO prediction was calculated using Equation 2.19 and Yang's Method of shear capacity prediction was calculated using Equation 2.1.

Several similar assumptions and practices were used across all of the prediction methods. First, prestress losses were estimated and incorporated to provide an accurate prediction of the prestress force at testing. Second, concrete strengths were all based on the average of three compressive tests of 4 by 8 in. concrete cylinders broken on the same day as testing for both the slab concrete and core fill concrete. For the Palmer and Schultz (2009) web-shear equation, test day concrete compressive strengths of the slab concrete and core fill concrete were used to calculate the respective concrete tensile strengths based on Equation 2.2. Third, all load and resistance factors were set to unity, which allowed the shear capacity predictions to be directly compared with test results. Finally, the peak shear force was determined using the applied load and included member selfweight demand at the critical section.

4.3.1.1 Transfer Length

The predicted web-shear capacity is directly influenced by the method used to determine the prestressing strand transfer length. Since the critical point for web-shear capacity prediction generally occurs within the transfer length of the prestressing strands, an accurate estimation of the axial precompression along the length of a member is necessary. There are a variety of methods available to estimate the transfer length of

prestressing strands. ACI 318 (2014) recommends that the transfer length be calculated using Equation 2.7. This equation may not be appropriate in this project because the research used to develop the transfer length equation was based on normal weight concrete (ACI 318-14 R25.4.8), whereas the hollow-core slabs tested in this research were extruded with no-slump concrete (i.e., the concrete used in hollow-core slabs is usually more dense, with a unit weight of 154 pcf, than normal weight concrete, with a unit weight of 145 pcf, due to the no-slump application). Palmer and Schultz (2009) found that the transfer length calculated with Equation 2.7 using prestressing strands with an ultimate tensile strength, f_{pu}, of 270 ksi stressed to $0.7f_{pu}$ and 20% total losses (equivalent to $50d_b$) did not correctly characterize the transfer length in hollow-core slabs. As a result, they developed a transfer length equation based on initial strand slip measurements. When hollow-core slabs are cut to length, the prestressing strands slip inward, as shown in Figure 4.13. By correlating this contraction with the modulus of elasticity of the strands and the prestress after initial losses, the transfer length was estimated by Palmer and Schultz with Equation 2.23. A summary of the initial strand slips and strand slip immediately following web-shear failure is shown in Table 4.4.

Prior to each test, the initial strand slip of the prestressing strands was measured using a tire tread depth gauge with an accuracy of 0.01 in. These measurements were averaged for the six strands in the slab and used in Equation 2.23 to calculate the slab-specific transfer lengths. This transfer length was used for all web-shear predictions in Figure 4.7 through Figure 4.10. A comparison of the transfer lengths using Buckner (1995), AASHTO (2018), ACI 318 (2014), and the Palmer and Schultz (2009) equation are presented in Table 4.5.

4.3.1.2 Prestress Losses

The ACI 423.10R Guide to Estimating Prestress Loss (2016) was used for the ACI, Palmer and Schultz, and Yang's Method web-shear capacity prediction and the AASHTO (2018) approximate prestress loss method was used in the AASHTO web-shear capacity prediction. Each method evaluated initial and long-term losses. To account for the concrete and prestressing strand material properties, several material coefficients in each method

were incorporated. Among a variety of differences, the ACI method did not incorporate concrete age whereas the AASHTO method did. Despite differences in each prestress loss calculation method, the magnitudes of total prestress loss were very close. The ACI and AASHTO methods predicted a 15% and 14% loss of prestress following jacking to service, respectively.

4.3.2 Comparison of Results from Prediction Methods and Experimental Shear Testing

There were several differences between each shear prediction methodology. Some of the most notable differences included the determination of transfer length, cross section geometry parameters, and limiting concrete stress (i.e., compressive concrete strength or tensile concrete strength). For example, Yang's Method (1994) employed variables such as the first moment of area, moment of inertia, and gradient of prestressing, all of which were not considered in the other three prediction methods. Detailed sample calculations of each web-shear prediction method are shown in Appendix C.

For the ACI 318 (2014), Palmer and Schultz (2009), and AASHTO (2018) methods, the slabs were evaluated at $h/2$ (6 in.) from the support centerline. For Yang's Method (1994), the slabs were specifically evaluated at the critical point of 5.4 in. from the support centerline. To compare each prediction method with the test results, the measured peak shear force was divided by the predicted web-shear capacity. This means that values greater than 1.0 indicated the prediction method was conservative in estimating the web-shear capacity of a slab. Similarly, values less than 1.0 indicated that a given prediction method overestimated the slab web-shear capacity. The ratios of peak shear load to predicted values were averaged for the two tests conducted on each slab and are presented in Figure 4.14. The average ratio between peak shear force and predicted web-shear capacity across all of the tests in this project for each prediction method are shown in Table 4.6.

The ACI 318 (2014) web-shear predictions with the core fill treated as unreinforced concrete consistently provided conservative predictions across all of the specimens. The ratios shown in Figure 4.14 ranged from 1.01 to 1.22 for the core-filled specimens, with an average conservatism of 13% for the core-filled specimens. The ACI 318 (2014) web-shear

predictions with the core fill treated as prestressed concrete provided both conservative and unconservative predictions with the ratios in Figure 4.14 for core-filled specimens ranging from 0.87 to 1.06 with an average ratio of 0.97 for core-filled specimens. The web-shear predictions treating the core fill concrete as prestressed overestimated the capacity of the 209-day typical fill, SFRC core fill, and steel bar placed in core fill specimens (ratios ranging from 0.87 to 0.95), which all had cores immediately filled during fabrication and had the potential to behave as prestressed concrete. Since these three specimens did not demonstrate fully prestressed concrete behavior, it may not be appropriate to treat the core fill concrete as prestressed in the ACI 318 (2014) web-shear predictions.

The Palmer and Shultz (2009) web-shear equation with the core fill concrete evaluated as unreinforced and prestressed were both unconservative for the core-filled specimens. On average, the ratios between peak shear force and predicted capacity for the unreinforced and prestressed core fill concrete behavior of the core-filled specimens were 0.98 and 0.89, respectively. Since the Palmer and Schultz web-shear equation was developed to better model the behavior of deep hollow-core slabs with no core fill, an imperfect prediction of web-shear capacity was possible for the core-filled hollow-core slabs in this research. The Palmer and Schulz prediction for the empty core tests was very accurate, with an average ratio of 1.03 as shown in Figure 4.14. While adding core fill likely led to error in the Palmer and Shultz web-shear equation, the empty cores 12 in. deep section was expected to be predicted accurately.

Since the AASHTO (2018) method of predicting web-shear capacity relied upon the strain of the longitudinal reinforcement and no longitudinal reinforcement was present in the core fill concrete, it was not appropriate to include the core fill as monolithic with the slab concrete. Rather, the core fill was calculated separately as unreinforced concrete as shown in Equation 2.19. The AASHTO predictions consistently overestimated the shear capacity of the slabs in this testing program, with the ratios of peak shear force to predicted capacity of the core-filled specimens in Figure 4.14 ranging from 0.79 to 0.97 (average of 0.88).

Yang's Method used Equation 2.20 to calculate the web-shear capacity of the slab and the core fill concrete contribution when it was treated as unreinforced concrete. This prediction method was consistently unconservative with ratios of peak shear force to predicted capacity for the core-filled specimens in Figure 4.14 ranging from 0.79 to 0.90 (average of 0.84). When the core fill was treated as prestressed concrete in Equation 2.21, the Yang's Method predictions for core-filled specimens consistently overestimated the slab capacity with ratios in Figure 4.14 ranging from 0.66 to 0.79 (average 0.72). When Yang's Method was used to predict the empty cores specimen, the ratio of peak shear force to predicted capacity was 0.86. This suggests that Yang's Method was unconservative for the hollow-core slabs tested in this project even before core fill concrete was introduced.

Only the ACI 318 (2014) prediction with the core fill treated as unreinforced concrete consistently generated an average peak shear force to predicted capacity ratio greater than 1.00 for both the empty cores specimen and core-filled specimens, as shown in Table 4.6. It is desirable for the nominal predicted shear capacity to be consistently conservative for application in Code equations. Therefore, the ACI 318 (2014) prediction with the core fill treated as unreinforced concrete was the most appropriate prediction method.

4.4 Web-Shear Crack Angles

4.4.1 Crack Angle Predictions

Web-shear cracking propagates perpendicular to the principal tensile stresses in a diagonal direction between the member top flange and prestressing strand depth. The predicted crack angles as measured from the horizontal plane were calculated for each specimen using Mohr's circle with an average angle of 42°. In this method, the axial stress was calculated by dividing the effective prestress force by the cross-sectional area the shear stress was calculated using Equation 4.2, considering the shear force at $h/2$ (6 in.) from the support. Axial prestress was determined using the transfer length calculated with Equation 2.23 for each test. A summary of the predicted crack angles is shown in Table 4.7 and a

detailed sample calculation of a crack angle calculation based on Mohr's circle is shown in Appendix D.

$$\tau = \frac{VQ}{Ib_w} \tag{4.2}$$

4.4.2 Observed Crack Angles

All of the diagonal web-shear crack angles observed during testing were measured using a 3D scanner as discussed in Section 3.7, except for the empty core specimen, which was measured by hand with a protractor. Specifically, the web-shear crack angle of the six webs and the filled core was measured at approximately mid-depth of the section for each specimen. The webs were numbered 1 through 6 from left to right with the slab viewed from the end. Because only one end of each specimen was deconstructed, all of the web-shear crack angle measurements were performed on side B of each specimen. The crack angles of the slab webs in all of the specimens were fairly consistent and averaged 33°. This average was about 9° shallower than the average predicted web-shear crack angles shown in Table 4.7. The core fill crack angles varied between specimens and ranged from 32 to 69°. A summary of the measured web-shear crack angles is shown in Table 4.8.

4.4.3 Crack Angle Discussion

Since the core fill concrete was expected to have shear behavior that ranged between unreinforced and prestressed concrete, the crack angle of the core fill relative to the slab webs could serve as an indication of the amount of prestress present in the core fill concrete. Based on Mohr's circle, concrete with no precompression will crack at 45° under an applied shear force. As more axial precompression is added to a member that is also carrying an applied shear force, the angle of cracking will become shallower relative to the horizontal plane.

The specimens where the core fill concrete behaved the most like prestressed concrete (i.e., where the measured capacity of the core fill exceeded that of the predicted prestressed core fill concrete behavior) were the typical fill, core wall surface enhancement,

and WWR in core fill specimens, as shown in Figure 4.10. Not coincidentally, the core fill crack angles of these three specimens were shallow (34°, 41°, and 32°) and near the average web crack angle of 33°. This suggested that the core fill concrete had substantial axial prestress, which contributed to additional web-shear capacity. Similarly, the cold joint core fill, SFRC core fill, and steel bar in core fill specimens, which had the steepest crack angles (60°, 69°, and 60°), were the weakest of the slabs, further supporting this correlation. For the 209-day typical fill specimen, the core fill crack angle of 40° was near the average crack angle of the slab webs (33°), but the shear capacity of the slab was lower than the predicted capacity with the core fill treated as prestressed concrete. This was the only specimen that did not fit the correlation between core fill crack angle and shear performance.

Of the core fill enhancement strategies tested in this program, the SFRC core fill, steel bar in core fill, and WWR in core fill specimens all attempted to improve the shear capacity of the core fill concrete. However, none of these three enhancements demonstrated evidence of significant additional shear capacity compared to the typical immediate fill specimen. Rather, the bond between the core fill concrete and the slab concrete appeared to be most important regarding the slab performance in shear. For four of the core-filled specimens, the core fill concrete remained connected to at least one slab web after deconstruction. These four specimens were the specimens with the shallowest crack angles shown in Table 4.8 (i.e., indicating the most axial prestress present in the core fill concrete), and three of these specimens had core fill concrete that behaved as fully prestressed concrete based on ACI 318 (2014), as shown in Figure 4.10.

4.5 Discussion of Web-Shear Capacity Prediction Variability and Uncertainty

4.5.1 Web-Shear Capacity Prediction Methods

In LRFD design, load and resistance factors are used to provide conservative and safe structural designs. These factors were taken as unity in the prediction methods used in this research to consider the actual web-shear predicted capacity. Ideally, the predicted and

experimentally measured web-shear capacities should align. The web-shear prediction equations of ACI 318 (2014) and AASHTO LRFD (2018) incorporate some conservatism. Concrete shear behavior often exhibits notable variability. In the development of these Code and Specification provisions, the web-shear prediction equations were designed to be a lower bound of the available shear test data, which is scatted due to concrete variability, thus providing conservative and reliable estimations. Therefore, the web-shear capacity predicted by the ACI 318 (2014) and AASHTO LRFD (2018) web-shear equations have a strong likelihood of underpredicting the actual web-shear capacity of the tested hollow-core slabs.

4.5.2 Concrete Strength

Concrete exhibits variability in its material properties and structural performance. For the testing of hollow-core slabs in this project, several factors generated and influenced variability in concrete strength. Since all of the web-shear prediction methods used in this research relied on the concrete compressive or tensile strength, the actual concrete strength of the slab and core fill concrete at the time of each test was required for an accurate web-shear capacity prediction.

Concrete strength was determined by performing compressive and split cylinder tensile tests on 4 by 8 in. concrete cylinders. While cylinder strengths are commonly used to characterize member performance, several factors may have led to differences in concrete strength between the cylinder and slab or core fill concrete. First, the concrete cylinders did not experience the exact same curing environment as the hollow-core slabs. The concrete cylinders were left in their molds until they were broken, whereas the hollow-core slabs were left uncovered. Additionally, all of the concrete cylinders were shipped to the UMD structures laboratory with the first shipment of each batch of hollow-core slabs, but multiple shipments of slabs at different times were required to accommodate laboratory space constraints. As a result, some of the hollow-core slabs were housed outdoors at the fabrication facility while their respective concrete cylinders were stored indoors at the UMD Structures laboratory. Second, the concrete cylinder strength tests exhibited some

variability. For each concrete strength determination, three cylinders were tested to generate an averaged value, and variability existed between the cylinder strength results.

4.5.3 Prestressing Transfer Length

All of the web-shear prediction equations used in this research incorporated the axial prestress force in the concrete at the critical point, which was at $h/2$ (6 in.) from the support centerline (5.4 in. from the support centerline for Yang's Method). Since web-shear capacity generally controls within the transfer length of a prestressed member, an accurate prediction of the prestress gradient was necessary for an accurate web-shear capacity prediction. Since the recommended ACI 318 (2014) transfer length (Equation 2.7) was not applicable for the no-slump concrete used to manufacture the hollow-core slabs, the transfer length presented in Equation 2.23 was used in the web-shear calculations for the ACI 318 (2014) method, Palmer and Schultz (2009) method, and Yang's Method (1994). AASHTO (2018) specified a transfer length of $60d_b$, which was incorporated in to the AASHTO web-shear calculations. All of the transfer length functions assumed a linear gradient of prestress force from the member end (zero force) to the end of the transfer length (full prestress force). A summary of the predicted transfer lengths based on these three methods can be found in Table 4.5.

Quantifying the transfer length of these hollow-core slabs was outside the scope of this project. Therefore, the differences in transfer length between the three prediction methods generated some uncertainty in the corresponding axial precompression in each slab. Additionally, the strand force could have been parabolically distributed across the transfer length (Yang, 1994). If a parabolic prestress gradient was assumed, the axial precompression would be greater at a given section in the member than if a linear prestress gradient is employed. As a result, some uncertainty existed related to the distribution of prestress force within the transfer length in addition to the transfer length distance. Both of these factors added to the uncertainty of web-shear capacity predictions.

4.5.4 Prestress Losses

Estimated prestress losses also affected the axial precompression, which affected web-shear capacity predictions. Prestress loss estimations included consideration of environmental conditions and material properties, which can be difficult to accurately define. Relative ambient humidity was the only environmental factor and was recommended to be 70% for both the ACI (2016) and AASHTO (2018) prestress loss estimation methods. This value was assumed to be consistent throughout the life of the hollow-core slabs prior to testing. However, the relative ambient humidity likely varied at different times because the slab was housed indoors at fabrication, outdoors during the winter at the fabrication facility, and indoors again at the UMD structures laboratory.

Table 4.1. Peak shear force and accompanying slab displacements

Core Modification	Slab Side	Peak Shear Force (kips)	Slab Deflection at Failure (in.)
1) Empty cores	A	61.3	0.16
	B	56.2	0.17
2) Cold joint core fill	A	65.5	0.20
	B	62.7	0.17
3) Typical immediate fill	A	72.9	0.20
	B	69.0	0.19
4) 209-day typical fill	A	72.1	0.18
	B	70.7	0.17
5) Fiber-reinforced fill – 0.5% volume fraction	A	53.3	0.19
	B	59.5	0.17
6) Core wall surface enhancement	A	60.6	0.18
	B	68.4	0.18
7) Steel bar placed in core fill	A	60.2	0.18
	B	58.7	0.17
8) Welded wire reinforcement in core fill	A	63.2	0.18
	B	70.3	0.20

Table 4.2. Differential LVDT displacements at each support and the load point

Core Modification	Slab Side	Differential Displacement (in.)		
		At Testing End Support	At Load Point	At Overhang Support
1) Empty cores	A	0.09	0.11	0.06
	B	0.25	0.10	0.05
2) Cold joint core fill	A	0.11	0.13	0.07
	B	0.13	0.07	0.09
3) Typical immediate fill	A	0.02	0.02	0.07
	B	0.08	0.01	0.02
4) 209-day typical fill	A	0.13	0.15	0.09
	B	0.01	0.09	0.04
5) Fiber-reinforced fill – 0.5% volume fraction	A	0.17	0.10	0.02
	B	0.09	0.08	0.04
6) Core wall surface enhancement	A	0.11	0.05	0.01
	B	0.05	0.01	0.00
7) Steel bar placed in core fill	A	0.02	0.03	0.02
	B	0.07	0.04	0.01
8) Welded wire reinforcement in core fill	A	0.06	0.06	0.02
	B	0.05	0.05	0.01

Table 4.3. Variation in differential LVDT displacements between the testing end support and load point and the overhang support and load point

Core Modification	Slab Side	Variation in Differential Displacements (in.)		Slab Side with More Twist
		Between the Testing End Support and Load Point	Between the Overhang Support and Load Point	
1) Empty cores	A	0.02	0.05	B
	B	0.16	0.04	
2) Cold joint core fill	A	0.01	0.06	B
	B	0.05	0.02	
3) Typical immediate fill	A	0.00	0.05	B
	B	0.07	0.01	
4) 209-day typical fill	A	0.01	0.06	B
	B	0.08	0.05	
5) Fiber-reinforced fill – 0.5% volume fraction	A	0.06	0.08	A
	B	0.02	0.03	
6) Core wall surface enhancement	A	0.06	0.04	A
	B	0.03	0.01	
7) Steel bar placed in core fill	A	0.02	0.05	A
	B	0.03	0.03	
8) Welded wire reinforcement in core fill	A	0.00	0.03	B
	B	0.00	0.04	

Table 4.4. Average measured prestressing strand slips before loading and immediately following web-shear failure

Core Modification	Slab Side	Average Prestressing Strand Slip (in.)		
		Before Loading	After Failure	Difference
1) Empty cores	A	0.08	0.15	0.08
	B	0.05	0.20	0.14
2) Cold joint core fill	A	0.05	0.21	0.16
	B	0.05	0.15	0.10
3) Typical immediate fill	A	0.08	0.14	0.06
	B	0.06	0.12	0.07
4) 209-day typical fill	A	0.08	0.14	0.06
	B	0.08	0.19	0.10
5) Fiber-reinforced fill – 0.5% volume fraction	A	0.06	0.19	0.12
	B	0.07	0.17	0.10
6) Core wall surface enhancement	A	0.06	0.19	0.13
	B	0.05	0.20	0.15
7) Steel bar placed in core fill	A	0.07	0.19	0.12
	B	0.07	0.17	0.10
8) Welded wire reinforcement in core fill	A	0.06	0.16	0.10
	B	0.07	0.12	0.05

Table 4.5. Transfer length estimations using Buckner (1995), AASHTO (2018), ACI (2014), and Palmer and Schultz (2009)

Core Modification	Slab Side	Transfer Length (in.)			
		Eq. 3.1 Buckner (1995)	Eq. 2.14 AASHTO (2018)	Eq. 2.7 ACI (2014)	Eq. 2.23 Palmer/Schultz (2009)
1) Empty cores	A	34.7	36	32.5	60
	B	34.7	36	32.5	40
2) Cold joint core fill	A	34.7	36	32.5	42
	B	34.7	36	32.5	41
3) Typical immediate fill	A	34.7	36	32.5	59
	B	34.7	36	32.5	41
4) 209-day typical fill	A	34.7	36	32.5	61
	B	34.7	36	32.5	65
5) Fiber-reinforced fill – 0.5% volume fraction	A	34.7	36	32.5	49
	B	34.7	36	32.5	52
6) Core wall surface enhancement	A	34.7	36	32.5	47
	B	34.7	36	32.5	34
7) Steel bar placed in core fill	A	34.7	36	32.5	56
	B	34.7	36	32.5	55
8) Welded wire reinforcement in core fill	A	34.7	36	32.5	46
	B	34.7	36	32.5	54
Average		34.7	36	32.5	50

Table 4.6. Ratio of average peak shear force to predicted shear capacity for each prediction method

Prediction Method	$\frac{V_{peak}}{V_n}$	
	Empty Cores Specimen	**Core-Filled Specimens**
ACI 318 (2014) Unreinforced Core Fill	1.24	1.13
ACI 318 (2014) Prestressed Core Fill	1.24	0.97
Palmer and Schultz (2009) Unreinforced Core Fill	1.03	0.98
Palmer and Schultz (2009) Prestressed Core Fill	1.03	0.89
AASHTO (2018)	0.92	0.88
Yang (1994) Unreinforced Core Fill	0.86	0.84
Yang (1994) Prestressed Core Fill	0.86	0.72

Table 4.7. Predicted diagonal web-shear crack angles calculated using Mohr's circle

Core Modification	Slab Side	Crack Angle Measured from the Horizontal Plane (degrees)
1) Empty cores	A	43
	B	41
2) Cold joint core fill	A	41
	B	41
3) Typical immediate fill	A	43
	B	42
4) 209-day typical fill	A	43
	B	43
5) Fiber-reinforced fill – 0.5% volume fraction	A	41
	B	42
6) Core wall surface enhancement	A	42
	B	41
7) Steel bar placed in core fill	A	42
	B	42
8) Welded wire reinforcement in core fill	A	42
	B	43
Average		42

Table 4.8. Measured diagonal web-shear crack angles at mid-depth of each web and core fill

Core Modification	Crack Angle Measured from the Horizontal Plane (degrees)							
	Web 1	**Web 2**	**Web 3**	**Core Fill**	**Web 4**	**Web 5**	**Web 6**	**Average of Webs**
1) Empty cores[1]	32.5	40	17.5	N/A	24	30	38.5	30
2) Cold joint core fill	39	40	38	60	19	25	24	31
3) Typical immediate fill	41	44	45	34	48	21	31	38
4) 209-day typical fill	33	31	30	40	43	23	30	32
5) Fiber-reinforced fill – 0.5% volume fraction	39	29	18	69	24	21	28	27
6) Core wall surface enhancement	49	50	28	41	41	32	53	42
7) Steel bar placed in core fill	35	31	23	60	30	25	35	30
8) Welded wire reinforcement in core fill	39	40	34	32	39	37	29	36
							Average	33

[1] Crack angles were measured by hand with a protractor

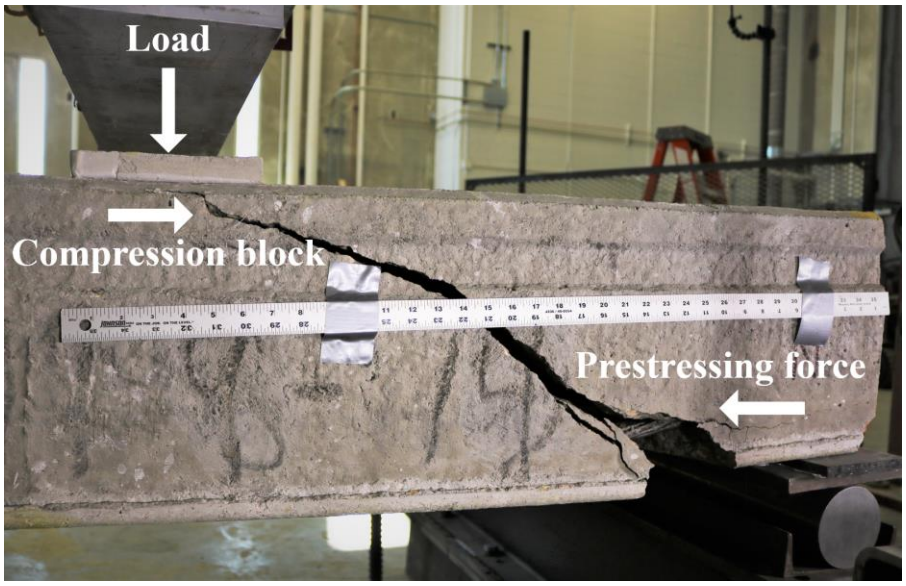

Figure 4.1. Internal moment couple between the concrete compression block and the residual prestressing force after failure

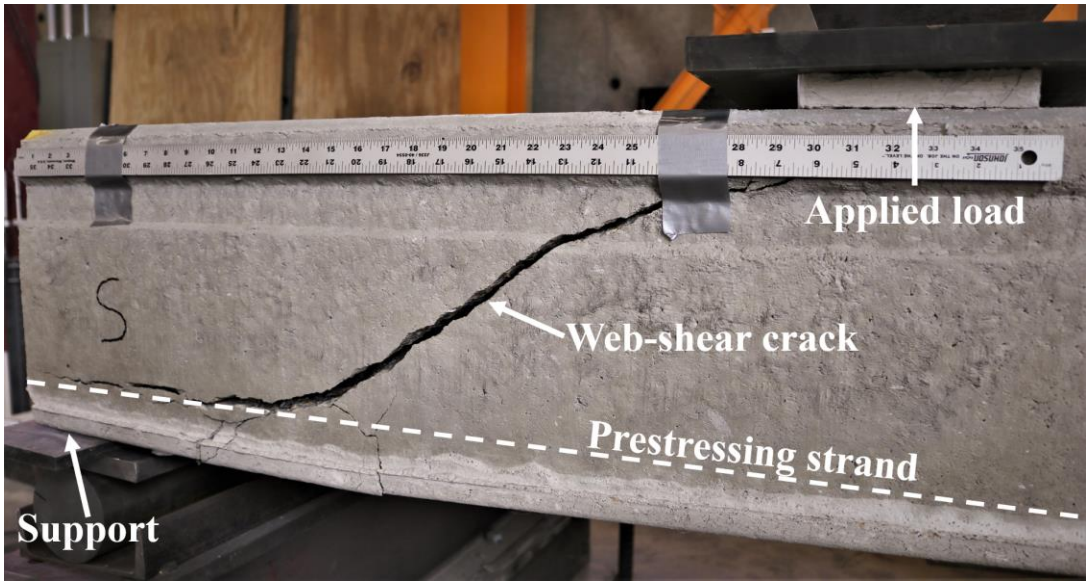

Figure 4.2. Typical web-shear crack extending diagonally from the applied load to the prestressing strand and following the prestressing strand to the support

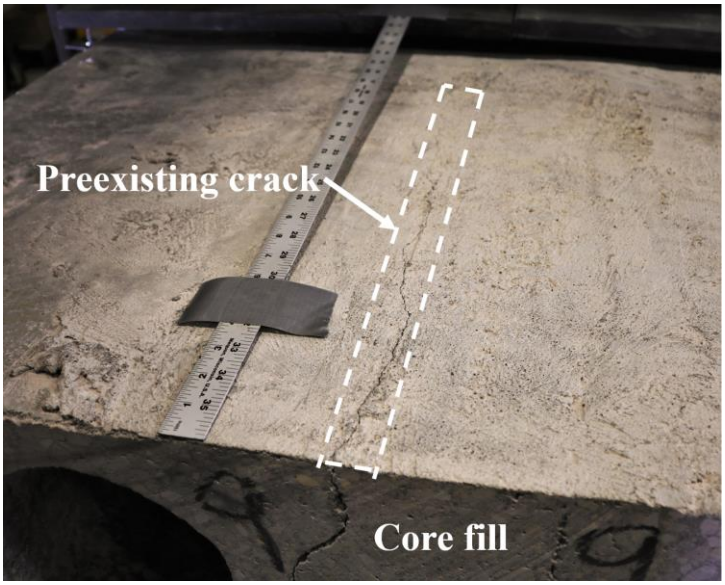

Figure 4.3. Example of preexisting top flange crack between the core fill concrete and the slab concrete as viewed from the end of the member

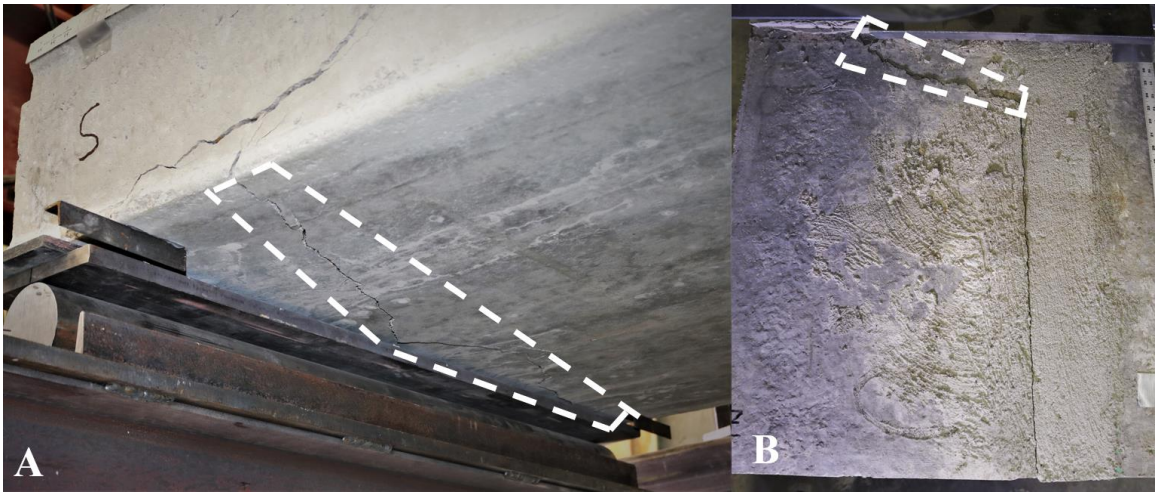

Figure 4.4. (a) Bottom flange cracking near the support; (b) top flange cracking near the load as viewed from the end of the member

Figure 4.5. Example core fill concrete found to be separate from the slab concrete after dismantling of the 209-day typical fill specimen

Figure 4.6. Residual saw cut dust on the bottom of the core fill concrete from the cold joint core fill specimen

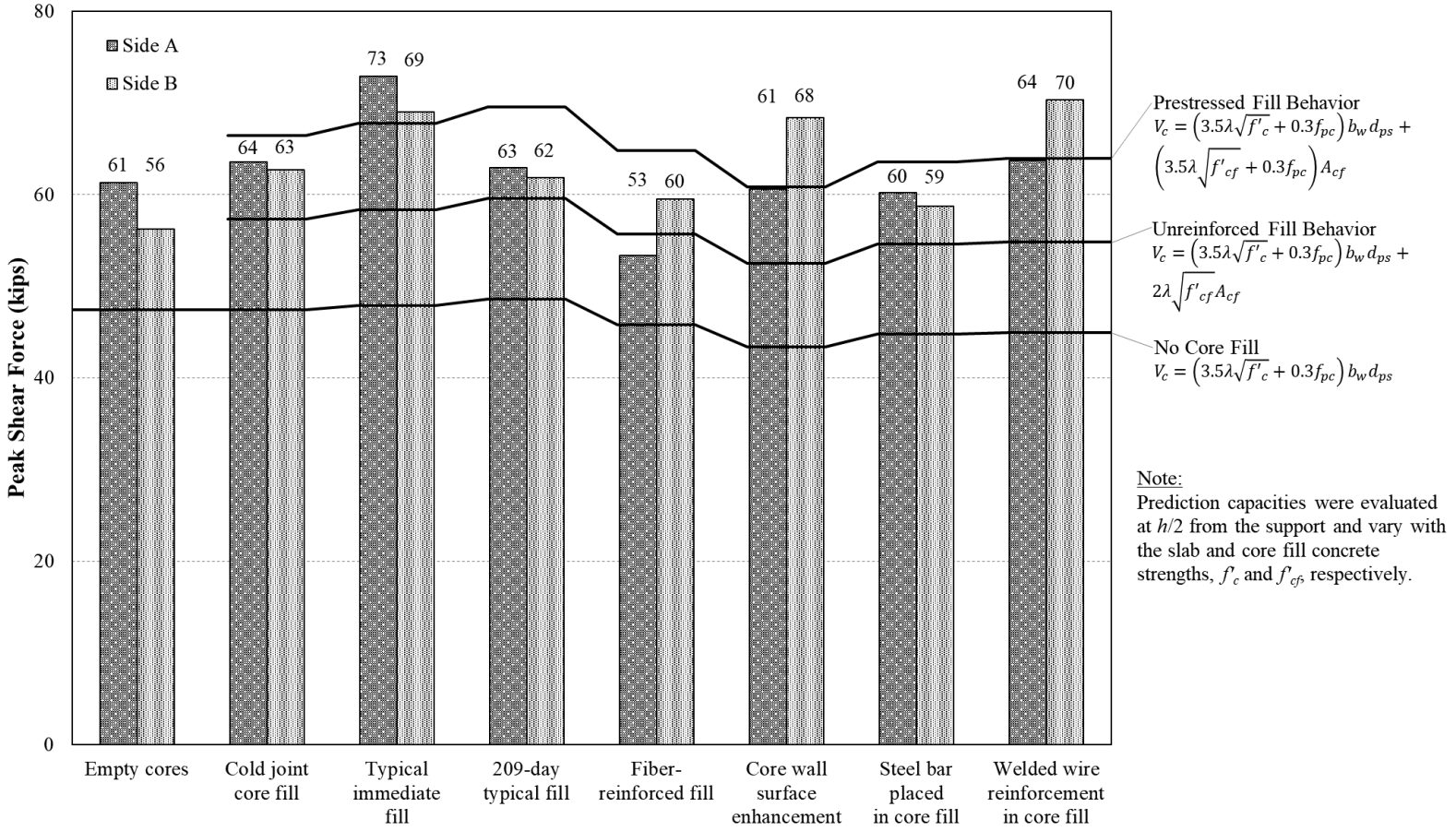

Figure 4.7. Peak shear force for each test relative to the respective predicted web-shear capacities

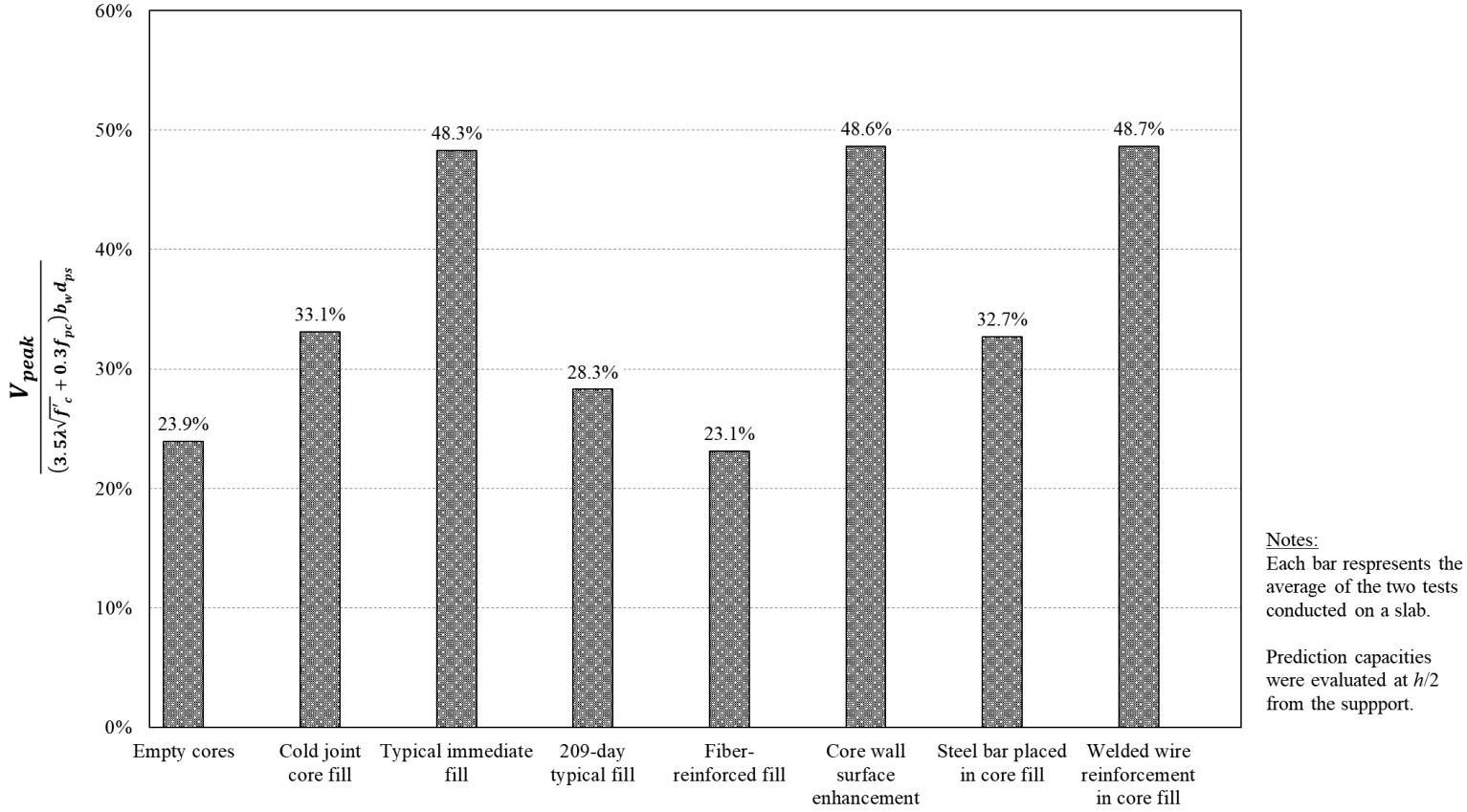

Figure 4.8. Average peak shear force for each core fill modification presented as a ratio to the predicted web-shear capacity of a slab with no core fill

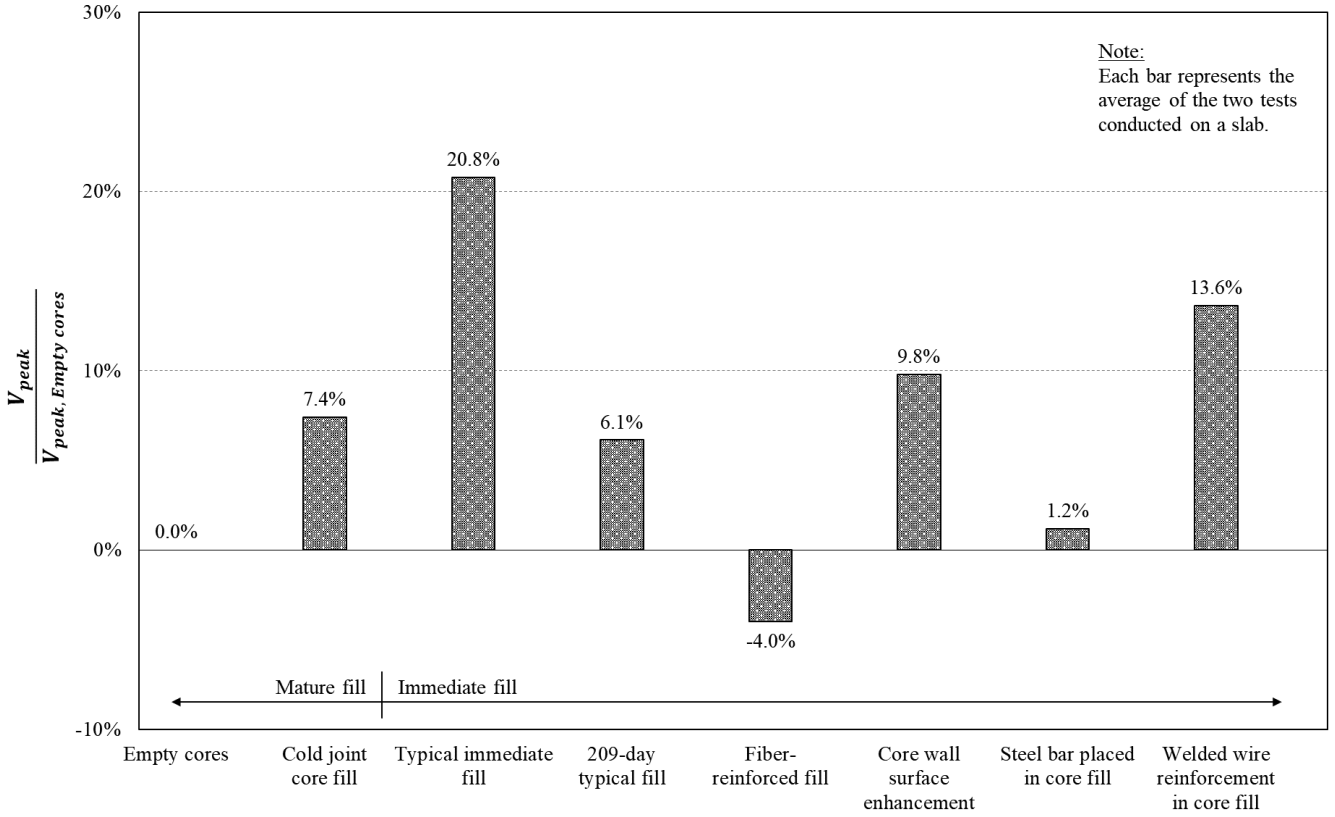

Figure 4.9. Average peak shear force for each core fill modification presented as a ratio to the peak shear force of the baseline tests with no core fill

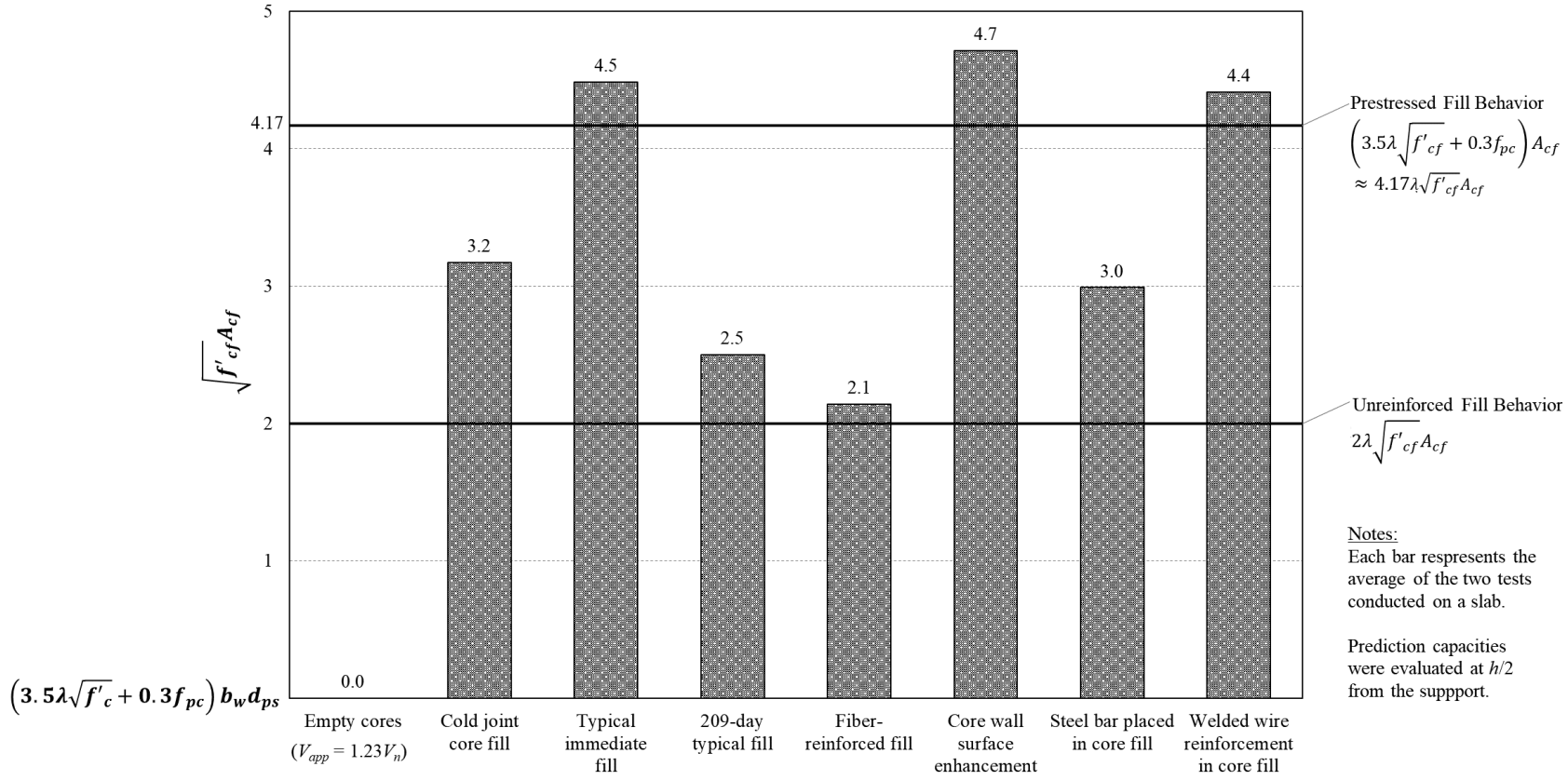

Figure 4.10. Coefficient of the square root of the core fill concrete compressive strength multiplied by the core fill area in excess of the predicted hollow-core slab web-shear strength

Figure 4.11. Steep core fill concrete crack face compared to the adjacent web crack faces in the headed bar in core fill specimen

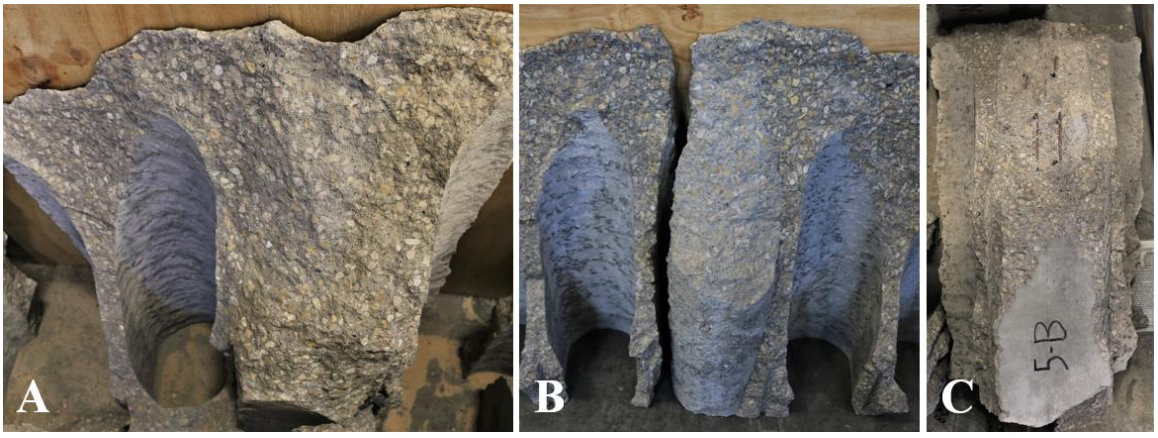

Figure 4.12. Core fill concrete with a crack face angle similar to the adjacent slab webs for (a) typical immediate fill, (b) core wall surface enhancement, and (c) WWR core fill

Figure 4.13. Initial prestressing strand slip observed in a cured hollow-core slab prior to applying load in the laboratory

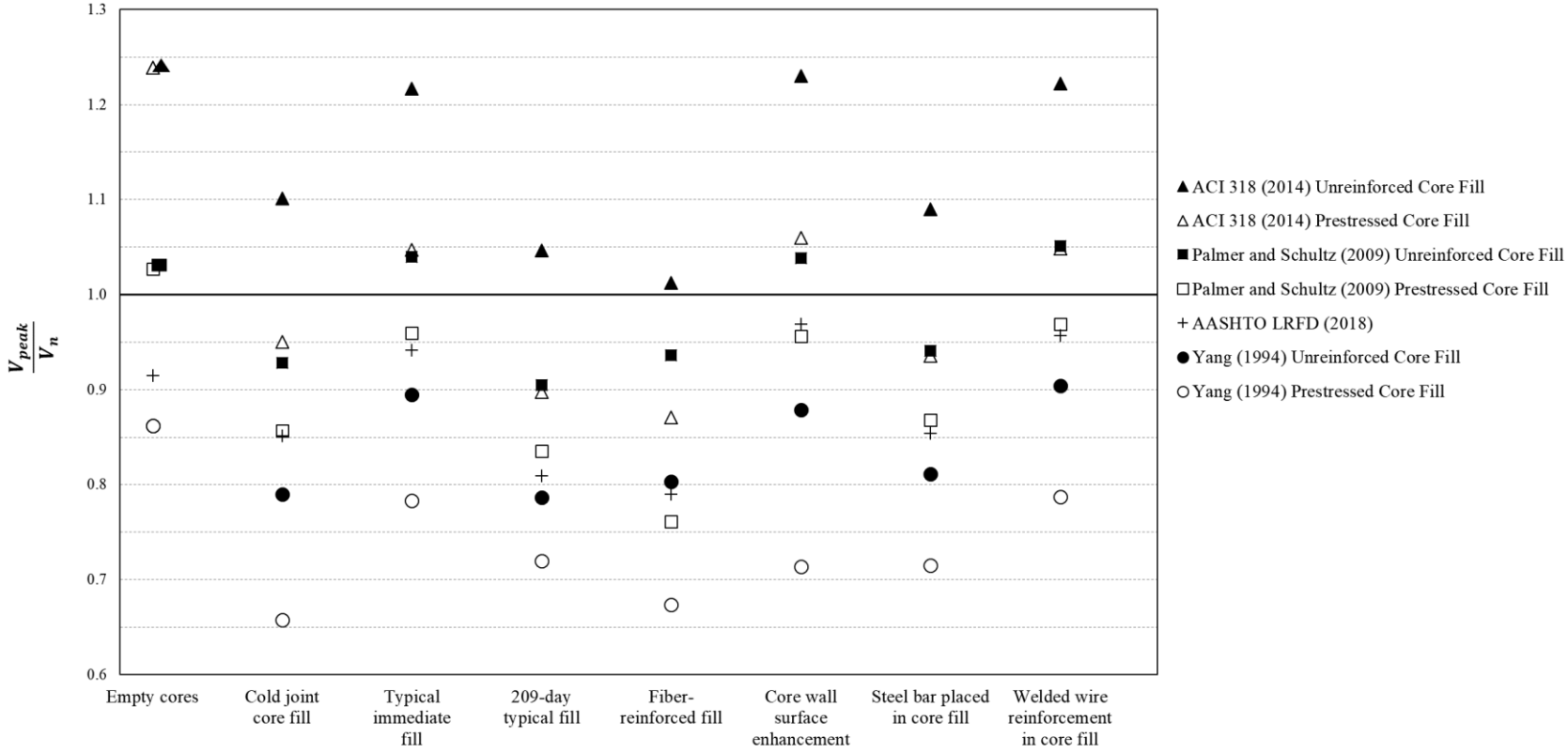

Figure 4.14. Ratio of the average peak shear force to predicted shear capacity for each specimen

Chapter 5: Summary, Conclusions, and Recommendations

5.1 Summary

This project studied the web-shear capacity of hollow-core slabs with a concrete filled core through experimental testing. The primary goals were to characterize the effect of core fill timing on slab shear capacity and explore ways to enhance the core fill concrete shear capacity. Specifically, core fill timing was investigated by testing slabs with core fill added immediately after extrusion and a slab with core fill added weeks after the slab had cured (cold joint core fill specimen). Additionally, a typical immediately filled slab was aged 209 days before testing to investigate the long-term performance of core-filled hollow-core slabs. The second phase of the project tested novel core fill enhancement strategies including: using SFRC core fill concrete, vertically roughening the slab web walls prior to core filling, placing a headed steel bar in the core fill concrete, and placing vertically oriented WWR in the core fill concrete. All of the slabs were 12 in. deep, 48 in. wide, and 20 ft long. Each slab was tested with span length of 16 ft and a shear span-to-depth ratio, a/d_p, of 3.0 (a/h of 2.5) to investigate the web-shear capacity. For each core fill modification, two identical tests were performed, one on each end of a single slab.

Several web-shear prediction methods were calculated including: the ACI 318 (2014) method, Palmer and Schultz (2009) method, AASHTO (2018) method, and Yang's Method (1994). For comparison and evaluation of the test results, the ACI 318 (2014) web-shear capacity prediction method was used as it is the governing Code for most precast concrete design. The cold joint specimen slightly outperformed the predicted performance of a slab with unreinforced core fill concrete and the typical immediate fill specimen slightly outperformed the predicted performance of a slab with prestressed core fill concrete. Both specimens outperformed the baseline specimen with empty cores. Of all the specimens, the typical immediate fill, core wall surface enhancement, and WWR in the core fill specimens performed the best in regards to the Code predictions, and their shear capacities all exceeded the predicted shear capacity of fully prestressed core fill concrete. The web-shear crack angles were measured for one test of each core fill modification and

demonstrated a strong correlation with shear performance of the core fill concrete (i.e., unreinforced or prestressed concrete behavior). Specifically, the core fill concrete crack angles ranged from 32 to 69°, and the three specimens with core fill concrete that behaved like prestressed concrete had a core fill concrete crack angle of 41° or less.

5.2 Conclusions from Testing

The following conclusions were drawn based on the results and observations of the tests performed within this project:

1. When a core was filled with concrete within an hour after hollow-core slab extrusion and allowed to cure with the slab prior to prestressing strand release, the total web-shear capacity of the slab had the potential to perform as if the slab and core fill concrete were both fully prestressed.
2. When the prestressing strands of a slab were released and the slab was cured prior to core filling, a cold joint between the cured slab concrete and core fill concrete existed. Hollow-core slabs with core fill concrete added in this timeline performed as if the core fill was non-prestressed, unreinforced concrete.
3. When hollow-core slabs with core fill added immediately after extrusion were allowed to age approximately seven months, the core fill concrete shear strength decreased from prestressed concrete behavior to unreinforced concrete behavior. This decrease in core fill shear strength was attributed to concrete shrinkage, which compromised the bond between the slab and core fill concrete. As the bond weakened, the axial prestress present in the core fill concrete decreased, resulting in a lower shear capacity of the of the hollow-core specimen.
4. The SFRC core fill, steel bar placed in the core fill, and WWR placed in the core fill enhancements did not show promise for improving the core fill shear capacity. The SFRC core fill and steel bar placed in the core fill specimens underperformed compared to the typical immediately filled specimen and exhibited a capacity less than the prediction that assumed the core fill concrete was prestressed. The WWR specimen was slightly less than the capacity of the typical immediate fill specimen and

outperformed the prediction of prestressed core fill concrete behavior. This was attributed to the core fill concrete capacity and not the WWR because no additional strength was exhibited compared to the typical immediate fill specimen web-shear capacity.

5. Vertically roughening the slab web wall prior to placing core fill concrete improved the shear strength of the hollow-core specimen. This was evident because the core wall surface enhancement specimen outperformed the typical immediately filled specimen. The increase in core fill shear capacity was attributed to a stronger bond and mechanical interlock between the slab concrete and core fill concrete.
6. Bond between the slab concrete and core fill concrete is a critical factor in the shear capacity of core fill concrete. The core fill concrete remained connected to at least one of the adjacent slab webs for the three specimens with the greatest shear capacity of the core-filled specimens. Conversely, the core fill concrete was not composite with the slab webs after testing for the other four core-filled specimens. In particular, the cold joint core fill specimen, which had saw cut dust between the core fill concrete and slab concrete, had one of the lowest shear capacities. Adequate bond between the slab concrete and core fill concrete allows the core fill concrete to have axial precompression, which in turn increases the core fill concrete shear capacity. This conclusion was supported by the observed crack angles of the core fill concrete. Specifically, the three core-filled specimens with the greatest shear capacity had shallow core fill concrete crack angles relative to the horizontal plane, which indicated the presence of axial prestress in the core fill concrete and good bond with the slab concrete. Conversely, the three core-filled specimens with the lowest shear capacity had steep core fill concrete crack angles, which indicated a lack of axial precompression and poor bond with the slab concrete. Because admixtures and water are added to the core fill concrete mix for workability reasons, incompatibility between the stiffness and compressive strength of the core fill concrete and slab concrete should be considered as this could affect the bond.

7. The slab web-shear capacity predicted by ACI 318 (2014) with the core fill treated as unreinforced concrete underpredicted the slab web-shear capacity. This prediction method provided consistently conservative estimates of capacity for all of the specimens tested in this project (including the 209-day typical fill specimen, which had a lower shear capacity than the identically constructed typical immediate fill specimen tested soon after fabrication). The slab web-shear capacity predicted by ACI 318 (2014) with the core fill concrete treated as prestressed concrete both overpredicted and underpredicted the slab web-shear capacities. The average ratio of observed to predicted web-shear capacity was 0.97 for the core-filled specimens in this study. The Palmer and Schultz (2009) web-shear equation with the core fill concrete treated as unreinforced and as prestressed, the AASHTO (2018) predictions, and Yang's Method (1994) with the core fill concrete treated as unreinforced and as prestressed all overestimated the web-shear capacity, providing unconservative predictions.

5.3 Recommendations for Future Research

The intent of this project was to understand the behavior of core-filled hollow-core slabs with various fabrication timing and modifications. Due to the variety of core fill modifications investigated, only two identical tests were performed for each core fill modification. While the results provided an indication of the core fill behavior, more testing is necessary to generate a reliable design procedure for codification to predict the shear behavior of hollow-core slabs with core fill. There was variation in the shear capacity between the two identical tests for each core fill modification in this project. To accurately quantify the web-shear capacity of core-filled hollow-core slabs with experimental testing, at least ten duplicate tests are recommended. The typical immediate fill specimen outperformed the predicted shear capacity treating the core fill concrete as fully prestressed and only the core wall roughening specimen showed minor shear capacity improvements beyond the typical immediate fill specimen shear capacity. As a result, more duplicate tests of the typical immediate fill and empty cores specimens are recommended to more accurately quantify the shear capacity of a typical core-filled hollow-core slab and establish a reliable baseline shear capacity of a hollow-core slab with empty cores.

All of the slabs tested in this project were of identical cross section and fabricated by the same manufacturer. Variations in the void shapes of hollow-core slabs has been shown to affect the web-shear capacity (Yang, 1994) and concrete mixtures can vary significantly between manufacturers. To develop a codifiable design procedure for shear behavior of core-filled hollow-core slabs immediately filled with concrete and without further modifications, a wide assortment of void shapes, slab depths, and slabs from various manufacturers should be tested.

Bibliography

ACI Committee 318. (1971). Building Code Requirement for Structural Concrete (ACI 318-71) and Commentary (ACI 318R-71), Farmington Hills, MI.

ACI Committee 318. (1983). Building Code Requirement for Structural Concrete (ACI 318-83) and Commentary (ACI 318R-83), Farmington Hills, MI.

ACI Committee 318. (2005). Building Code Requirement for Structural Concrete (ACI 318-05) and Commentary (ACI 318R-05), Farmington Hills, MI.

ACI Committee 318. (2008). Building Code Requirement for Structural Concrete (ACI 318-08) and Commentary (ACI 318R-08), Farmington Hills, MI.

ACI Committee 318. (2014). Building Code Requirement for Structural Concrete (ACI 318-14) and Commentary (ACI 318R-14), Farmington Hills, MI.

American Association of State Highway and Transportation Officials (AASHTO) (2014). AASHTO LRFD Bridge Design Specifications (7th Edition). Washington, DC.

American Association of State Highway and Transportation Officials (AASHTO) (2018). AASHTO LRFD Bridge Design Specifications (8th Edition). Washington, DC.

ASTM C39/C39M-17b. (2017). "Standard Test Method for Compressive Strength of Cylindrical Concrete Specimens." ASTM International, West Conshohocken, PA.

ASTM C496/C496M-17. (2017). "Standard Test Method for Splitting Tensile Strength of Cylindrical Concrete Specimens." ASTM International, West Conshohocken, PA.

Becker, R.J. & D. R. Buettner. (1985). "Shear Tests of Extruded Hollow-Core Slabs." *PCI Journal* 30 (2): 40–54.

Boresi, A. P., & Schmidt, R. J. (2003). Advanced Mechanics of Materials (6th Edition).

Buckner, C.D. (1995). "A Review of Strand Development Length for Pretensioned Concrete Members." *PCI Journal* 40 (2): 84–105.

Buettner, D. R., & Becker, R. J. (2015). PCI Manual for the Design of Hollow-core Slabs (3rd Edition).

Chao, S.H., A. E. Naaman, & G. J. Parra-Montesinos. (2006). "Bond Behavior of Strands Embedded in Fiber Reinforced Cementitious Composites." *PCI Journal* 51 (6): 56–71.

Dudnik, V. S., & Milliman, L. R. (2015). Shear Strength of Prestressed Steel Fiber Reinforced Concrete Hollow-Core Slabs (Master's thesis). University of Wisconsin, Madison, WI.

Hawkins, N. M., & Ghosh, S. K. (2006). Shear Strength of Hollow-Core Slabs. *PCI Journal*, 51(1), 110-114.

Hawkins, N. M., Kuchma, D. A., Mast, R. F., Marsh, M. L., & Reineck, K.-E. (2005). Simplified Shear Design of Structural Concrete Members. Washington, DC: Transportation Research Board.

Mathcad (Version 15.0) [Computer software]. (2015). PTC.

Nilson, A. H. (1987). Design of Prestressed Concrete (2nd Edition). John Wiley & Sons, New York.

Palmer, K. D., & Schultz, A. E. (2009). Web Shear Strength of Precast, Prestressed Concrete Hollow Core Slab Units (Master's thesis). University of Minnesota, Minneapolis, MN.

Palmer, K. D., & Schultz, A. E. (2011). Experimental Investigation of the Web-Shear Strength of Deep Hollow-Core Units. *PCI Journal*, 56(4), 83-104.

Peaston, C., Elliott, K., & Paine, K. (1999). "Steel Fiber Reinforcement for Extruded Prestressed Hollow-core Slabs," Structural Applications of Fiber Reinforced Concrete, Special Publication 182-6, pp. 87–108. Farmington Hills, MI.

Precast/Prestressed Concrete Institute. (2017). *PCI Design Handbook*, 8th Ed., Chicago, IL.

Simasathien, S., & Chao, S.-H. (2015). Shear Strength of Steel-Fiber-Reinforced Deep Hollow-Core Slabs. *PCI Journal*, 60(4), 85-101.

Yang, L. (1994). Design of Prestressed Hollow-core Slabs with Reference to Web Shear Failure. *Journal of Structural Engineering*, 120(9), 2675-2696.

Appendices

Appendix A: Slab Design for Laboratory Testing Sample Calculation

All calculations presented in this appendix were generated using Mathcad (2015).

TESTING GEOMETRY BASED ON ACI 318-14

DESIGN PARAMETERS

Lab Arangement

Total Length of Beam	$L_{tot} := 20 \cdot ft$	
CL Support to Beam End - Testing End	$L_1 := 2.5 \cdot in$	
CL Support to Beam End - Overhang	$L_2 := 3 \cdot ft + 9.5 \cdot in$	$L_2 = 3.792\,ft$
Length of Beam Tested	$L := L_{tot} - L_1 - L_2$	$L = 16\,ft$
Actuator to CL Supports	$L_a := 2 \cdot ft + 6 \cdot in$	

Section Properties

Section Depth	$h := 12 \cdot in$	
Section Width	$b := 48 \cdot in$	
Web Width	$b_w := 10.626 \cdot in$	
Cross-Sectional Area	$A_c := 269.76 \cdot in^2$	
Moment of Inertia	$I_x := 5248 \cdot in^4$	
Neutral Axis to Bottom Extreme Fiber	$y_b := 6.095 \cdot in$	
Neutral Axis to Top Extreme Fiber	$y_t := h - y_b$	$y_t = 5.905 \cdot in$
Section Modulus - Top	$S_t := \frac{I_x}{y_t}$	$S_t = 888.7 \cdot in^3$
Section Modulus - Bottom	$S_b := \frac{I_x}{y_b}$	$S_b = 861 \cdot in^3$

Material Properties

Concrete Unit Weight	$\gamma_c := 154 \cdot pcf$	
Concrete Compressive Strength	$f_c = 13643\,psi$	
Young Concrete Compressive Strength	$f_{ci} := 5500 \cdot psi$	
Concrete Compressive Strength at Lab	$f_{ci\_lab} := 7500 \cdot psi$	
Core Fill Compressive Strength	$f_{c\_cf} = 9040\,psi$	
Concrete Modification Factor	$\lambda := 1$	
Modulus of Elasticity - Concrete *(Ref. ACI 318-14 Eq. 19.2.2.1a)*	$E_c := \left(\frac{\gamma_c}{pcf}\right)^{1.5} \cdot 33 \cdot \sqrt{f_c \cdot psi}$	$E_c = 7366 \cdot ksi$
Modulus of Elasticity - Young Concrete *(Ref. ACI 318-14 Eq. 19.2.2.1a)*	$E_{ci} := \left(\frac{\gamma_c}{pcf}\right)^{1.5} \cdot 33 \cdot \sqrt{f_{ci} \cdot psi}$	$E_{ci} = 4677 \cdot ksi$
Modulus of Elasticity - Strand	$E_{ps} := 28500 \cdot ksi$	
Ultimate Strength of Strand	$f_{pu} := 270 \cdot ksi$	
Number of 6/10" Strands	$n_{s0.6} := 6$	
Diameter of 6/10" Strands	$d_{0.6} := 0.6 \cdot in$	
Strand Area - 6/10" Diameter	$A_{ps0.6} := 0.217 \cdot in^2$	
Total Strand Area	$A_{ps} := n_{s0.6} \cdot A_{ps0.6}$	$A_{ps} = 1.302 \cdot in^2$
Strand Eccentricity from Neutral Axis	$e := y_b - 2.125 \cdot in$	$e = 3.97 \cdot in$
Strand Stressing	$ss := 0.70$	
Initial Jacking Force	$F_{pj} := ss \cdot (A_{ps} \cdot f_{pu})$	$F_{pj} = 246.1 \cdot kip$
Depth of Prestressing	$d_p := e + y_t$	$d_p = 9.875 \cdot in$
Shear Span-to-Depth Ratios	$\frac{L_a}{d_p} = 3.04$	$\frac{L_a}{h} = 2.5$

LOADING

Middle of Beam - Testing Span $x_m := L_1 + 0.5 \cdot L$ $x_m = 8.208\ ft$

Applied Point Load $P = 70.703 \cdot kip$

Distributed Self-Weight $w_{sw} := \gamma_c \cdot A_c$ $w_{sw} = 288 \cdot plf$

Shear for Applied Load

$$V_{s\_ap}(x) := \begin{cases} 0 \cdot kip & \text{if } x < L_1 \\ \frac{P \cdot (L - L_a)}{L} & \text{if } L_1 \le x \le L_1 + L_a \\ -\frac{P \cdot L_a}{L} & \text{if } L_1 + L_a < x \le L_1 + L \\ 0 \cdot kip & \text{if } L_1 + L < x \le L_{tot} \end{cases}$$

Shear for Self Weight

$$V_{s\_sw}(x) := \begin{cases} 0 \cdot kip & \text{if } x < L_1 \\ \left[\frac{w_{sw}}{2 \cdot L} \cdot \left(L^2 - L_2^{\,2}\right)\right] - w_{sw} \cdot (x - L_1) & \text{if } L_1 \le x \le L_1 + L \\ w_{sw} \cdot \left[L_2 - (x - L_1 - L)\right] & \text{if } x > L_1 + L \end{cases}$$

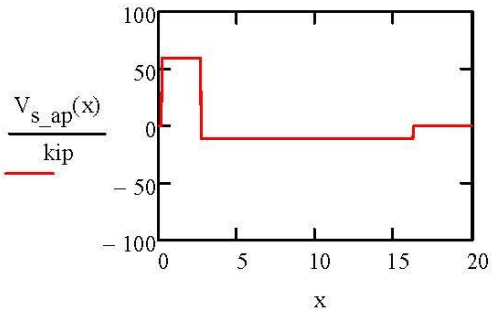

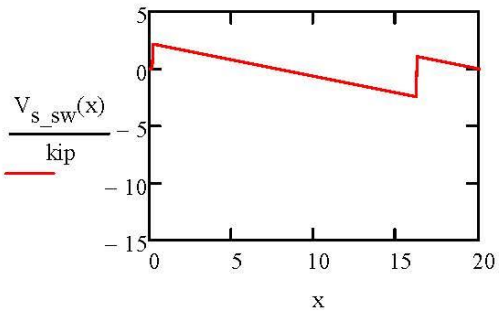

Moment for Self Weight SS Span $M_{ss}(x) := \frac{w_{sw} \cdot x}{2} \cdot (L_{tot} - x)$

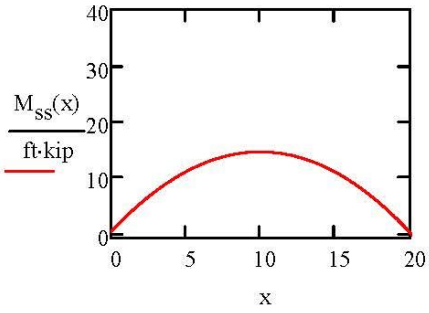

Moment for Appled Load $M_{s\_ap}(x) := \begin{cases} 0 \text{ if } x < L_1 \\ \frac{P\cdot(L - L_a)\cdot(x - L_1)}{L} \text{ if } L_1 \le x \le L_1 + L_a \\ \frac{P\cdot L_a\cdot(L - L_a)}{L}\cdot\left[1 - \frac{x - (L_1 + L_a)}{L - L_a}\right] \text{ if } L_1 + L_a < x \le L_1 + L \\ 0 \text{ if } L_1 + L < x \le L_{tot} \end{cases}$

Moment for Self Weight $M_{s\_sw}(x) := \begin{cases} 0 \text{ if } x < L_1 \\ \frac{w_{sw}\cdot(x - L_1)}{2\cdot L}\cdot\left[L^2 - L_2{}^2 - (x - L_1)\cdot L\right] \text{ if } L_1 \le x \le L_1 + L \\ \frac{-w_{sw}}{2}\cdot\left[L_2 - \left[x - (L_1 + L)\right]\right]^2 \text{ if } x > L_1 + L \end{cases}$

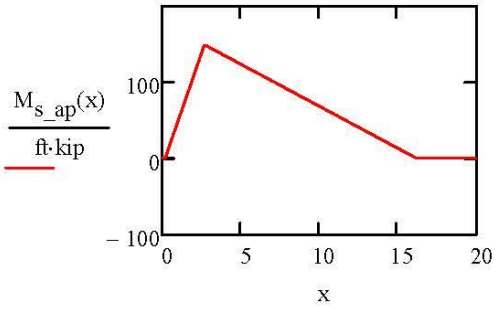

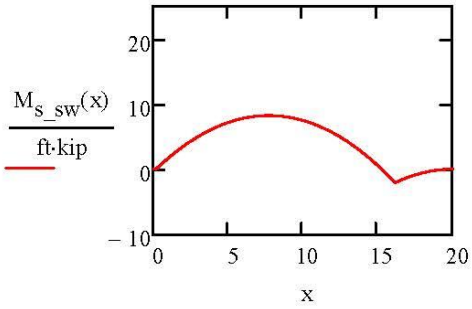

Unfactored Shear Demand $V_u(x) := \left|V_{s\_ap}(x) + V_{s\_sw}(x)\right|$

Unfactored Moment Demand $M_u(x) := \left|M_{s\_ap}(x) + M_{s\_sw}(x)\right|$

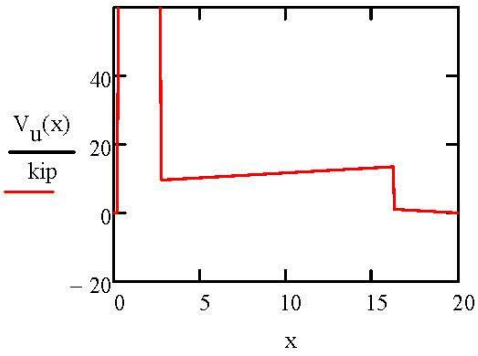

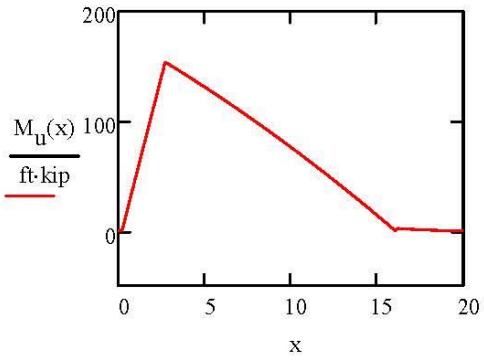

LOSSES

Elastic Shortening - ACI 423.10R-16 4.3

Moment Due to Self-Weight $M_g := \frac{w_{sw}}{8 \cdot L^2} \cdot (L + L_2)^2 \cdot (L - L_2)^2$ $M_g = 8 \cdot ft \cdot kip$

Eccentricity of Strand $e_p := e$ $e_p = 4 \cdot in$

Force in Strands Immediately Before Release $P_j := F_{pj}$ $P_j = 246 \cdot kip$

Initial Assumption for Approximation $K_{cir} := 0.9$ *(pretensioned member)*

Concrete Stress at Tendon Level *(Ref ACI 423.10R-16 Eq. 4.3.2b)* $f_{cir} := K_{cir} \cdot \left(\frac{P_j}{A_c} + \frac{P_j \cdot e_p^2}{I_x} \right) - \frac{M_g \cdot e_p}{I_x}$ $f_{cir} = 1411 \cdot psi$

Initial Elastic Shortening Loss Stress $\Delta f_{pES} := f_{cir} \cdot \frac{E_{ps}}{E_c}$ $\Delta f_{pES} = 5.5 \cdot ksi$

Creep - ACI 423.10R-16 5.2

Moment Due to Permanent Superimposed Load $M_{sd} := 0 \cdot ft \cdot kip$ $M_{sd} = 0 \cdot ft \cdot kip$

Concrete Stress due to Superimposed Loads $f_{cds} := \frac{M_{sd} \cdot e_p}{I_x}$ $f_{cds} = 0$

Concrete Weight Factor $K_{cr} := 2.0$

Long-Term Loss - Creep *(Ref ACI 423.10R-16 Eq. 5.2.1a)* $\Delta f_{pCR} := K_{cr} \cdot (f_{cir} - f_{cds}) \cdot \frac{E_{ps}}{E_c}$ $\Delta f_{pCR} = 10.9 \cdot ksi$

Shrinkage - ACI 423.10R-16 5.3

Relative Humidity $RH := 70$

Slab Outer Perimeter $P_o := 9 \cdot ft + 11.125 \cdot in$ $P_o = 119.125 \cdot in$

Core Perimeter $P_c := 2 \cdot ft + 3.5 \cdot in$ $P_c = 27.5 \cdot in$

Volume to Surface Area Ratio $VS := \frac{A_c}{P_o + 5 \cdot P_c}$ $VS = 1.051 \cdot in$

Coefficient for Prestressing $K_{sh} := 1.0$

Long-Term Loss - Shrinkage *(Ref ACI 423.10R-16 Eq. 5.3)*

$$\Delta f_{pSH} := \left(8.2 \cdot 10^{-6}\right) \cdot K_{sh} \cdot E_{ps} \cdot \left(1 - \frac{0.06 \cdot VS}{in}\right) \cdot (100 - RH) \qquad \Delta f_{pSH} = 6.6 \cdot ksi$$

Relaxation - ACI 423.10R-16 5.4

Coefficient for Relaxation, K.re
(Ref ACI 423.10R-16 Tbl. 5.4)

$K_{re} := 5000 \cdot psi$

Coefficient for Relaxation, J
(Ref ACI 423.10R-16 Tbl. 5.4)

$J := 0.040$

Ratio of Jacking to Ultimate Stress

$$ju := \frac{\left(\frac{F_{pj}}{A_{ps}}\right)}{f_{pu}} \qquad ju = 0.7$$

Coefficient for Relaxation, C
(Ref ACI 423.10R-16 Eq. 5.4.2a & 5.4.2b)

$$C := \text{if}\left[ju \geq 0.54, \left(\frac{ju}{0.21}\right) \cdot \left(\frac{ju}{0.9} - 0.55\right), \frac{ju}{4.24}\right] \qquad C = 0.759$$

Long-Term Loss - Relaxation
(Ref ACI 423.10R-16 Eq. 5.4)

$$\Delta f_{pRE} := \left[K_{re} - J \cdot \left(\Delta f_{pSH} + \Delta f_{pCR} + \Delta f_{pES}\right)\right] \cdot C \qquad \Delta f_{pRE} = 3.1 \cdot ksi$$

Totals

Total Initial Losses

$\Delta f_{pI} := \Delta f_{pES}$ $\Delta f_{pI} = 5.5 \cdot ksi$

Total Long-Term Losses

$\Delta f_{pLT} := \Delta f_{pCR} + \Delta f_{pSH} + \Delta f_{pRE}$ $\Delta f_{pLT} = 20.6 \cdot ksi$

Initial Stress After Losses

$$f_{pi} := \frac{F_{pj}}{A_{ps}} - \Delta f_{pI} \qquad f_{pi} = 183.5 \cdot ksi$$

Initial Force After Losses

$p_i := A_{ps} \cdot f_{pi}$ $p_i = 239 \cdot kip$

Effective Stress After Losses

$$f_{se} := \frac{F_{pj}}{A_{ps}} - \Delta f_{pI} - \Delta f_{pLT} \qquad f_{se} = 162.9 \cdot ksi$$

Effective Force After Losses

$p_{eff} := A_{ps} \cdot f_{se}$ $p_{eff} = 212.2 \cdot kip$

Total Loss Percentage

$$TL := 1 - \frac{p_{eff}}{P_j} \qquad TL = 13.8 \cdot \%$$

CONCRETE ALLOWABLES - TRANSFER FROM PLANT

Length Along Beam at End

$$x_e := 0 \cdot ft$$

Length Along Beam at Middle

$$x_m := 0.5 \cdot L_{tot} \qquad x_m = 10\,ft$$

Allowable Compressive Stress Function
(ACI 318-14 Tbl. 24.5.3.1)

$$C_{tall\_ss}(x) := \begin{cases} 0.7 \cdot f_{ci} & \text{if } x \le 0.25 \cdot L_{tot} \\ 0.6 \cdot f_{ci} & \text{if } 0.25 \cdot L_{tot} < x < 0.75 \cdot L_{tot} \\ 0.7 f_{ci} & \text{if } x \ge 0.75 \cdot L_{tot} \end{cases}$$

Allowable Tensile Stress Function
(ACI 318-14 Tbl. 24.5.3.2)

$$T_{tall\_ss}(x) := \begin{cases} -6 \cdot \sqrt{\frac{f_{ci}}{psi}} \cdot psi & \text{if } x \le 0.25 \cdot L_{tot} \\ -3 \cdot \sqrt{\frac{f_{ci}}{psi}} \cdot psi & \text{if } 0.25 \cdot L_{tot} < x < 0.75 \cdot L_{tot} \\ -6 \cdot \sqrt{\frac{f_{ci}}{psi}} \cdot psi & \text{if } x \ge 0.75 \cdot L_{tot} \end{cases}$$

Allowable Compressive Stress at End

$$C_{tall\_e} := C_{tall\_ss}(x_e) \qquad C_{tall\_e} = 3850\,psi$$

Allowable Compressive Stress at Middle

$$C_{tall\_m} := C_{tall\_ss}(x_m) \qquad C_{tall\_m} = 3300\,psi$$

Allowable Tensile Stress at End

$$T_{tall\_e} := T_{tall\_ss}(x_e) \qquad T_{tall\_e} = -445\,psi$$

Allowable Tensile Stress at Middle

$$T_{tall\_m} := T_{tall\_ss}(x_m) \qquad T_{tall\_m} = -222\,psi$$

CONCRETE ALLOWABLES - TRANSFER AT LAB

Length Along Beam at End

$$x_e := 0 \cdot ft$$

Length Along Beam at Middle

$$x_{m\_lab} := 0.5 \cdot L \qquad x_{m\_lab} = 8\ ft$$

Allowable Compressive Stress Function
(ACI 318-14 Tbl. 24.5.3.1)

$$C_{tall\_lab}(x) := \begin{cases} 0.7 \cdot f_{ci\_lab} & \text{if } x \le 0.25 \cdot L_{tot} \\ 0.6 \cdot f_{ci\_lab} & \text{if } 0.25 \cdot L_{tot} < x < 0.75 \cdot L_{tot} \\ 0.7 \cdot f_{ci\_lab} & \text{if } x \ge 0.75 \cdot L_{tot} \end{cases}$$

Allowable Tensile Stress Function
(ACI 318-14 Tbl. 24.5.3.2)

$$T_{tall\_lab}(x) := \begin{cases} -6 \cdot \sqrt{\frac{f_{ci\_lab}}{psi}} \cdot psi & \text{if } x \le 0.25 \cdot L_{tot} \\ -3 \cdot \sqrt{\frac{f_{ci\_lab}}{psi}} \cdot psi & \text{if } 0.25 \cdot L_{tot} < x < 0.75 \cdot L_{tot} \\ -6 \cdot \sqrt{\frac{f_{ci\_lab}}{psi}} \cdot psi & \text{if } x \ge 0.75 \cdot L_{tot} \end{cases}$$

Allowable Compressive Stress at End

$$C_{tall\_e\_lab} := C_{tall\_lab}(x_e) \qquad C_{tall\_e\_lab} = 5250\ psi$$

Allowable Compressive Stress at Middle

$$C_{tall\_m\_lab} := C_{tall\_lab}(x_m) \qquad C_{tall\_m\_lab} = 4500\ psi$$

Allowable Tensile Stress at End

$$T_{tall\_e\_lab} := T_{tall\_lab}(x_e) \qquad T_{tall\_e\_lab} = -520\ psi$$

Allowable Tensile Stress at Middle

$$T_{tall\_m\_lab} := T_{tall\_lab}(x_m) \qquad T_{tall\_m\_lab} = -260\ psi$$

TRANSFER/DEVELOPMENT LENGTHS

Factor of PS Type
(ACI Tbl. 20.3.2.3.1)

$\gamma_p := 0.28$ *(low-lax PS)*

Equivalent Rectangular Stress Distribution
(ACI Tbl. 22.2.2.4.3)

$$\beta_1 := \begin{cases} 0.85 & \text{if } 2500\cdot psi \le f_c \le 4000\cdot psi \\ 0.85 - \dfrac{0.05\cdot\left(f_c - 4000psi\right)}{1000psi} & \text{if } 4000\cdot psi < f_c < 8000\cdot psi \\ 0.65 & \text{if } f_c \ge 8000\cdot psi \end{cases} \qquad \beta_1 = 0.65$$

Ratio of A.ps to bd.p - Prestressed Steel

$$\rho_p := \frac{A_{ps}}{b\cdot d_p} \qquad \rho_p = 0.003$$

Stress in Prestressing
(Ref. ACI Eq. 20.3.2.3.1)

$$f_{ps} := f_{pu}\cdot\left[1 - \frac{\gamma_p}{\beta_1}\cdot\left(\rho_p\cdot\frac{f_{pu}}{f_c}\right)\right] \qquad f_{ps} = 264\cdot ksi$$

Diameter of 0.6" Strand

$d_b := 0.6\cdot in$

Transfer Length
(ACI 318-14 Eq. 25.4.8.1)

$$l_{t\_ACI} := \frac{f_{se}}{3000\cdot psi}\cdot d_b \qquad l_{t\_ACI} = 32.6\cdot in \qquad \frac{l_{t\_ACI}}{d_b} = 54$$

Transfer Length
(Buckner, 1995)

$$l_t := \frac{A_{ps0.6}}{\frac{4}{3}\cdot\pi\cdot d_b}\cdot\frac{f_{se}}{400\cdot psi} \qquad l_t = 35.2\cdot in \qquad \frac{l_t}{d_b} = 59$$

Inital Strand Slip

$\delta_{es} = 0.04\cdot in$

Transfer Length
(Palmer and Schultz, 2009)

$$l_{t\_PS} := 5\cdot\delta_{es}\cdot\frac{E_{ps}}{f_{pi}} \qquad l_t = 35.2\cdot in \qquad \frac{l_t}{d_b} = 59$$

Development Length
(Ref. ACI 318-14 Eq. 25.4.8.1)

$$l_d := l_t + \frac{f_{ps} - f_{se}}{1000\cdot psi}\cdot d_b \qquad l_d = 95.6\cdot in \qquad \frac{l_d}{d_b} = 159$$

Transfer and Development Length Function

$$TD(x) := \begin{cases} \frac{x}{l_t}\cdot\frac{f_{se}}{f_{ps}} & \text{if } x \le l_t \\ \frac{x - l_t}{l_d - l_t}\cdot\left(1 - \frac{f_{se}}{f_{ps}}\right) + \frac{f_{se}}{f_{ps}} & \text{if } l_t < x \le l_d \\ 1 & \text{if } l_d < x \le L_{tot} - l_d \\ 1 - \frac{x - (L_{tot} - l_d)}{l_d - l_t}\cdot\left(1 - \frac{f_{se}}{f_{ps}}\right) & \text{if } L_{tot} - l_d < x \le L_{tot} - l_t \\ \left(\frac{f_{se}}{f_{ps}}\right) - \frac{x - (L_{tot} - l_t)}{l_t}\cdot\left(\frac{f_{se}}{f_{ps}}\right) & \text{if } L_{tot} - l_t < x \le L_{tot} \end{cases}$$

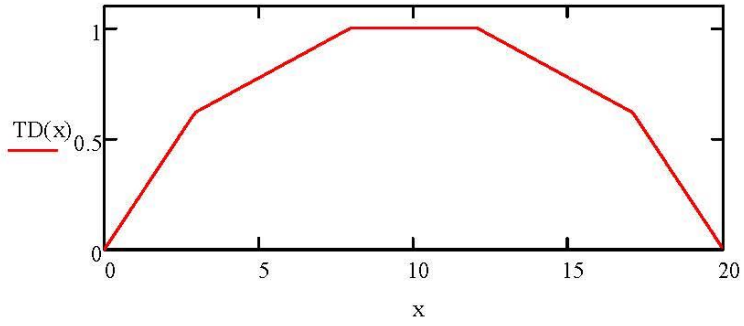

Initial Prestressing Force - Transfer

$$P_i(x) := \begin{cases} x\cdot\frac{p_i}{l_t} & \text{if } x \le l_t \\ p_i & \text{if } l_t < x < L_{tot} - l_t \\ p_i - \frac{p_i}{l_t}\left[x - (L_{tot} - l_t)\right] & \text{if } L_{tot} - l_t \le x \end{cases}$$

INITIAL PRESTRESSING - TRANSFER LENGTH

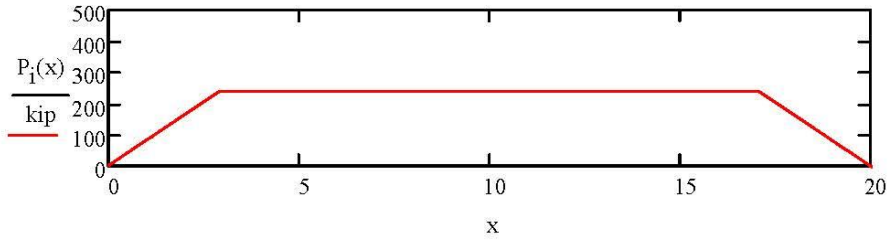

Effective Prestressing Force - Transfer

$$P_{eff}(x) := \begin{cases} x \cdot \frac{p_{eff}}{l_t} & \text{if } x \le l_t \\ p_{eff} & \text{if } l_t < x < L_{tot} - l_t \\ p_{eff} - \frac{p_{eff}}{l_t}\left[x - \left(L_{tot} - l_t\right)\right] & \text{if } L_{tot} - l_t \le x \end{cases}$$

Effective Prestressing Force - Ultimate

$$P_{effu}(x) := \left(f_{ps} \cdot A_{ps}\right) \cdot TD(x)$$

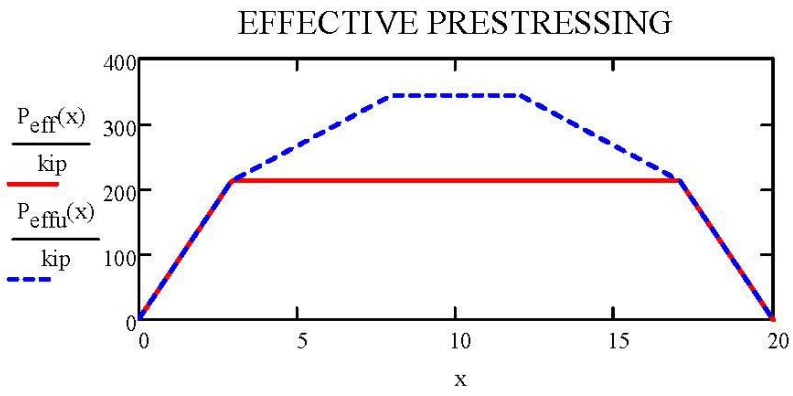

STRESSES AT TRANSFER FROM PLANT

Moment Along Beam

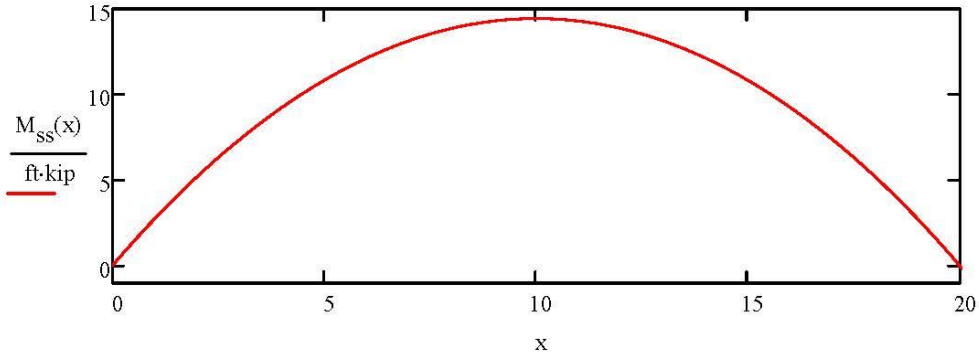

Moment at Ends $M_{te} := M_{ss}(x_e)$ $M_{te} = 0 \cdot kip \cdot ft$

Moment at Middle of Testing Span $M_{tm} := M_{ss}(x_m)$ $M_{tm} = 14.4 \cdot kip \cdot ft$

Stress Function at Top $f_{tt}(x) := \frac{P_i(x)}{A_c} - \frac{P_i(x) \cdot e}{S_t} + \frac{M_{ss}(x)}{S_t}$

Stress Function at Bottom $f_{tb}(x) := \frac{P_i(x)}{A_c} + \frac{P_i(x) \cdot e}{S_b} - \frac{M_{ss}(x)}{S_b}$

(Note: Subscript nomenclature is "transfer/service - top/bottom - end/middle" ~ "t/s - t/b - e/m")

Stress at Top - Ends $f_{tte} := f_{tt}(x_e)$

$f_{tte} = 0\,psi$ < $T_{tall\_e} = -445\,psi$ OK

Stress at Top - Middle $f_{ttm} := f_{tt}(x_m)$

$f_{ttm} = 13\,psi$ < $T_{tall\_m} = -222\,psi$ OK

Stress at Bottom - Ends $f_{tbe} := f_{tb}(x_e)$

$f_{tbe} = 0\,psi$ < $C_{tall\_e} = 3850\,psi$ OK

Stress at Bottom - Middle $f_{tbm} := f_{tb}(x_m)$

$f_{tbm} = 1787\,psi$ < $C_{tall\_m} = 3300\,psi$ OK

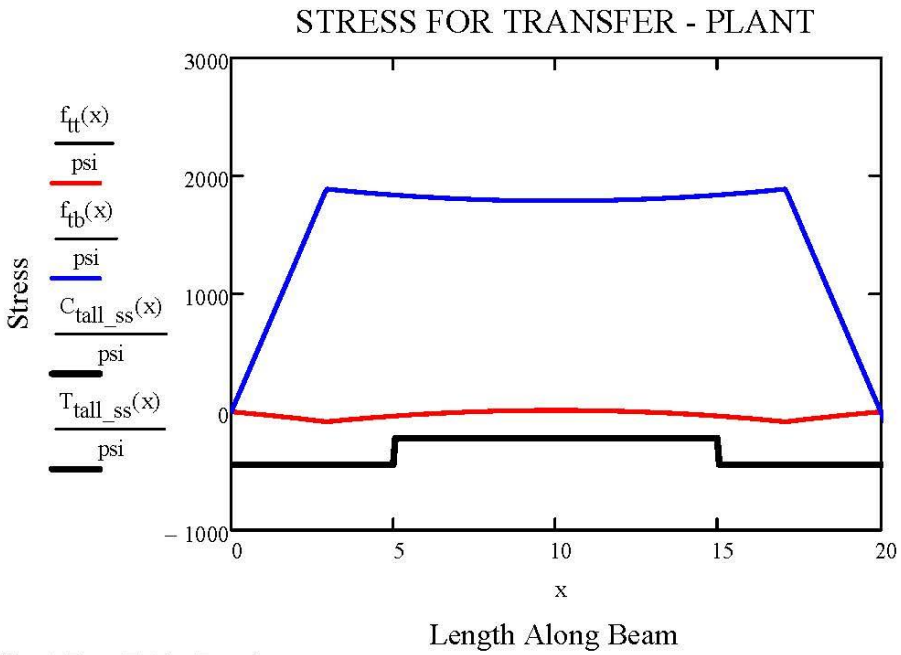

Check Pass/Fail for Transfer

$t := 0$

$$T\_ss := \left| \begin{array}{l} \text{for } i \in 0 .. \frac{L}{in} \\ \quad \left| \begin{array}{l} r \leftarrow i \cdot in \\ t \leftarrow t + 1 \quad \text{if } f_{tt}(r) > C_{tall\_ss}(r) \\ t \leftarrow t + 1 \quad \text{if } f_{tb}(r) > C_{tall\_ss}(r) \\ t \leftarrow t + 1 \quad \text{if } f_{tt}(r) < T_{tall\_ss}(r) \\ t \leftarrow t + 1 \quad \text{if } f_{tb}(r) < T_{tall\_ss}(r) \end{array} \right. \\ p \leftarrow \text{"FAIL"} \quad \text{if } t > 0 \\ p \leftarrow \text{"PASS"} \quad \text{if } t < 1 \\ p \end{array} \right.$$

$T\_ss = \text{"PASS"}$

STRESSES AT TRANSFER IN LAB

Factored Moment Along Beam

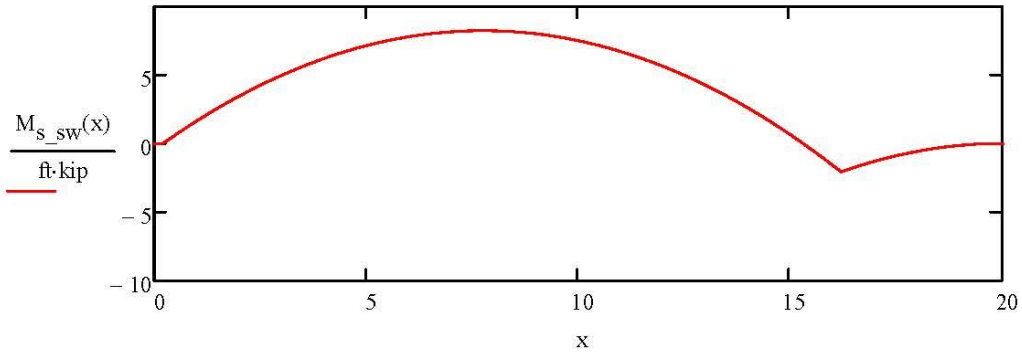

Moment at Middle Support $M_{te} := M_{s\_sw}(L_1 + L)$ $M_{te} = -2.1 \cdot kip \cdot ft$

Moment at Middle of Testing Span $M_{tm} := M_{s\_sw}(x_m)$ $M_{tm} = 7.5 \cdot kip \cdot ft$

Stress Function at Top $f_{tt\_lab}(x) := \frac{P_i(x)}{A_c} - \frac{P_i(x) \cdot e}{S_t} + \frac{M_{s\_sw}(x)}{S_t}$

Stress Function at Bottom $f_{tb\_lab}(x) := \frac{P_i(x)}{A_c} + \frac{P_i(x) \cdot e}{S_b} - \frac{M_{s\_sw}(x)}{S_b}$

(Note: Subscript nomenclature is "transfer/service - top/bottom - end/middle" ~ "t/s - t/b - e/m")

Stress at Top - Middle Support $f_{tte\_lab} := f_{tt\_lab}(L_1 + L)$

$f_{tte\_lab} = -210\,psi$ < $T_{tall\_m\_lab} = -260\,psi$ OK

Stress at Top - Middle or Testing $f_{ttm\_lab} := f_{tt\_lab}(L_1 + 0.5 \cdot L)$

$f_{ttm\_lab} = -71\,psi$ < $T_{tall\_m\_lab} = -260\,psi$ OK

Stress at Bottom - Middle Support $f_{tbe\_lab} := f_{tb\_lab}(L_1 + L)$

$f_{tbe\_lab} = 2017\,psi$ < $C_{tall\_m\_lab} = 4500\,psi$ OK

Stress at Bottom - Middle of Testing $f_{tbm\_lab} := f_{tb\_lab}(L_1 + 0.5 \cdot L)$

$f_{tbm\_lab} = 1873\,psi$ < $C_{tall\_m\_lab} = 4500\,psi$ OK

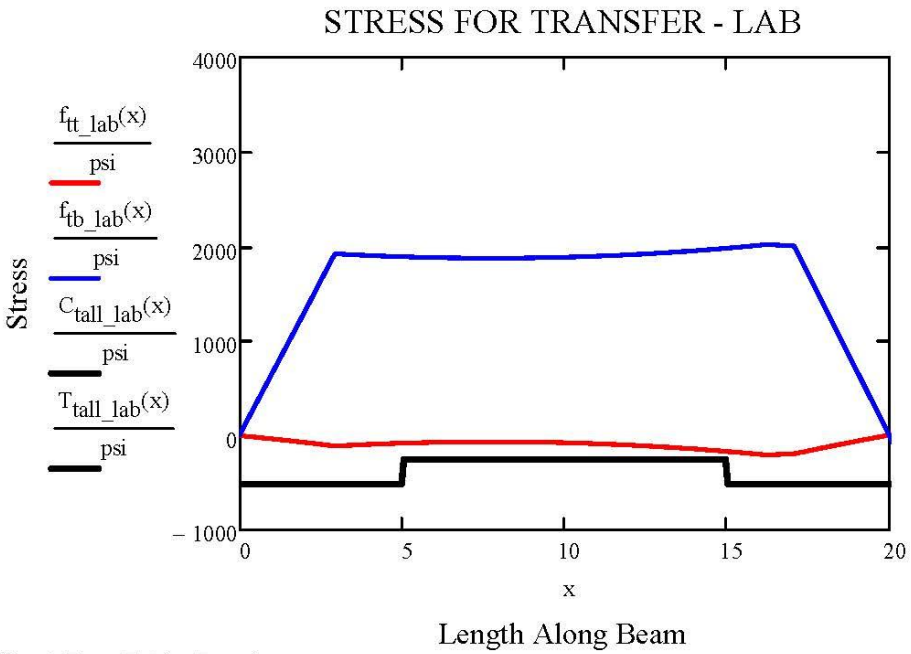

Check Pass/Fail for Transfer

$u := 0$

$T_{lab} :=$ for $i \in 0..\frac{L}{in}$

  $r \leftarrow i \cdot in$

  $u \leftarrow u + 1$ if $f_{tt\_lab}(r) > C_{tall\_lab}(r)$

  $u \leftarrow u + 1$ if $f_{tb\_lab}(r) > C_{tall\_lab}(r)$

  $u \leftarrow u + 1$ if $f_{tt\_lab}(r) < T_{tall\_lab}(r)$

  $u \leftarrow u + 1$ if $f_{tb\_lab}(r) < T_{tall\_lab}(r)$

  $p \leftarrow$ "FAIL" if $u > 0$

  $p \leftarrow$ "PASS" if $u < 1$

  p

$T_{lab} =$ "PASS"

CONCRETE ALLOWABLES - SERVICE

Allowable Compressive Stress
(Ref. ACI Tbl. 24.5.4.1)

$C_{sall} := 0.60 \cdot f_c$ $\quad C_{sall} = 8185.8\,psi$

Allowable Tensile Stress Function
(Ref. ACI Tbl. 24.5.2.1)

$T_{sall} := -12 \cdot \sqrt{\frac{f_c}{psi}} \cdot psi$ $\quad T_{sall} = -1402\,psi$

STRESSES AT SERVICE

Unfactored Moment Along Beam

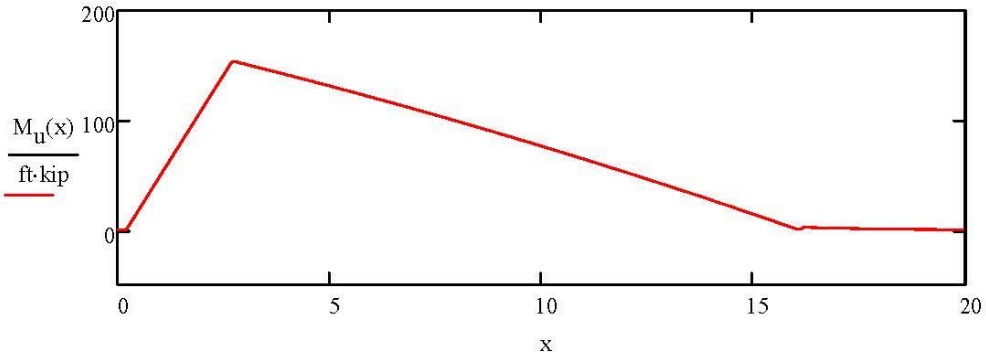

Moment at Middle Support $M_{se} := M_u(L_1 + L)$ $M_{se} = 2.074 \cdot kip \cdot ft$

Moment at Appled Load $M_{sm} := M_u(L_1 + L_a)$ $M_{sm} = 154 \cdot kip \cdot ft$

Stress Function at Top $f_{st}(x) := \frac{P_{eff}(x)}{A_c} - \frac{P_{eff}(x) \cdot e}{S_t} + \frac{M_u(x)}{S_t}$

Stress Function at Bottom $f_{sb}(x) := \frac{P_{eff}(x)}{A_c} + \frac{P_{eff}(x) \cdot e}{S_b} - \frac{M_u(x)}{S_b}$

Stress at Top - Middle Support $f_{ste} := f_{st}(L_1 + L)$

$f_{ste} = -133\,psi$ < $C_{sall} = 8186\,psi$ OK

Stress at Top - Applied Load $f_{stm} := f_{st}(L_1 + L_a)$

$f_{stm} = 1926\,psi$ < $C_{sall} = 8186\,psi$ OK

Stress at Bottom - Middle Support $f_{sbe} := f_{sb}(L_1 + L)$

$f_{sbe} = 1736\,psi$ < $C_{sall} = 8186\,psi$ OK

Stress at Bottom - Applied Load $f_{sbm} := f_{sb}(L_1 + L_a)$

$f_{sbm} = -511\,psi$ < $T_{sall} = -1402\,psi$ OK

STRESS FOR SERVICE

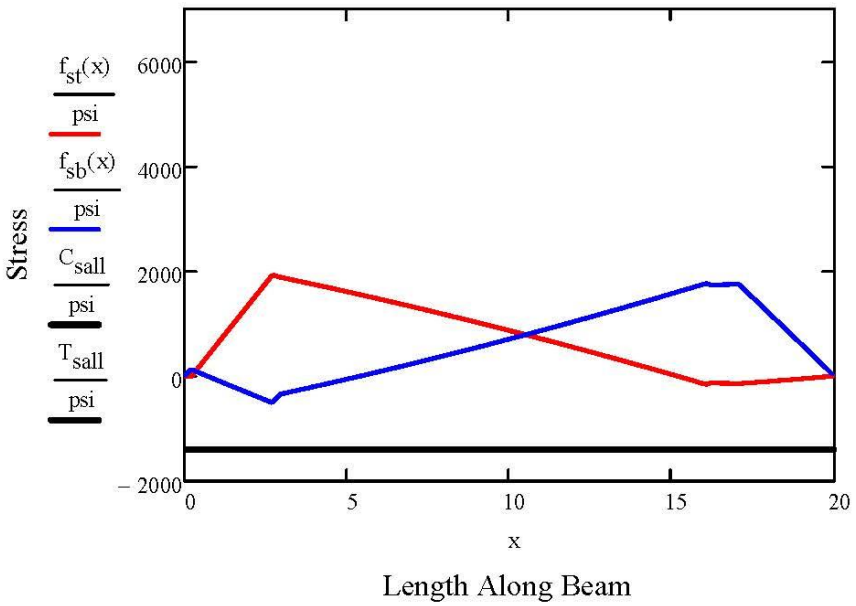

Length Along Beam

Check Pass/Fail for Service

$t := 0$

$S :=$ for $i \in 0 .. \frac{L}{in}$

$r \leftarrow i \cdot in$

$t \leftarrow t + 1$ if $f_{st}(r) > C_{sall}$

$t \leftarrow t + 1$ if $f_{sb}(r) > C_{sall}$

$t \leftarrow t + 1$ if $f_{st}(r) < T_{sall}$

$t \leftarrow t + 1$ if $f_{sb}(r) < T_{sall}$

$p \leftarrow$ "FAIL" if $t > 0$

$p \leftarrow$ "PASS" if $t < 1$

p

$S =$ "PASS"

ULTIMATE STRENGTH CALCULATIONS

Factor of PS Type
(Ref. ACI Tbl. 20.3.2.3.1)

$\gamma_p := 0.28$ *(low-lax PS)*

Equivalent Rectangular Stress Distribution
(Ref. ACI Tbl. 22.2.2.4.3)

$$\beta_1 := \begin{cases} 0.85 \text{ if } 2500\cdot psi \le f_c \le 4000\cdot psi \\ 0.85 - \dfrac{0.05\cdot\left(f_c - 4000psi\right)}{1000psi} \text{ if } 4000\cdot psi < f_c < 8000\cdot psi \\ 0.65 \text{ if } f_c \ge 8000\cdot psi \end{cases} \qquad \beta_1 = 0.65$$

Effective Tensile Stress in PS

$f_{se} = 163\cdot ksi$

Check for eq. 20.3.2.3.1 Applicability

$ck := \text{if}\left(f_{se} \ge 0.5\cdot f_{pu}, \text{"OK"}, \text{"NG"}\right) = \text{"OK"}$

All prestressing in tension zone. OK

Stress in Prestressing
(Ref. ACI Eq. 20.3.2.3.1)

$f_{ps} = 264\cdot ksi$ *(Defined earlier)*

Depth of Whitney Stress Block

$a := \dfrac{A_{ps}\cdot f_{pu}}{0.85\cdot f_c\cdot b}$ $\quad a = 0.632\cdot in$

Nominal Capacity

$M_n := A_{ps}\cdot f_{pu}\cdot\left(d_p - \dfrac{a}{2}\right)$ $\quad M_n = 280\cdot ft\cdot kip$

Extreme Compression Fiber to Neutral Axis
(Ref. ACI Eq. 22.2.2.4.1)

$c := \dfrac{a}{\beta_1}$ $\quad c = 0.972\cdot in$

Allowable Strain in Concrete

$\varepsilon_c := 0.003$

Strain in Prestressing

$\varepsilon_{ps} := \left(d_p - c\right)\cdot\dfrac{\varepsilon_c}{c}$ $\quad \varepsilon_{ps} = 0.027$

Strength Reduction Factor
(Ref. ACI Tbl. 21.2.2)

$\phi := 1.0$

Allowable Flexural Capacity

$M_{nall}(x) := \phi\cdot TD(x)\cdot M_n$ $\quad M_{nall}\left(L_1 + 0.5\cdot L\right) = 280\cdot ft\cdot kip$

Maximum Factored Moment - Midspan $M_u(x_m) = 76.1 \cdot ft \cdot kip < M_{nall}(L_1 + 0.5 \cdot L) = 280 \cdot ft \cdot kip$ OK

Modulus of Rupture
(Ref. ACI 318-14 Eq. 19.2.3.1)

$$f_r := 7.5 \cdot \lambda \cdot \sqrt{\frac{f_c}{psi}} \cdot psi \qquad f_r = 876 \cdot psi$$

Cracking Moment

$$M_{cr}(x) := S_b \cdot P_{effu}(x) \cdot \left(\frac{1}{A_c} + \frac{e}{S_b} \right) + f_r \cdot S_b$$

Check Cracking $M_{nall}(L_1 + 0.5 \cdot L) = 280 \cdot ft \cdot kip > 1.2 \cdot M_{cr}(x_m) = 321.3 \cdot ft \cdot kip$ OK

ULTIMATE FLEXURE

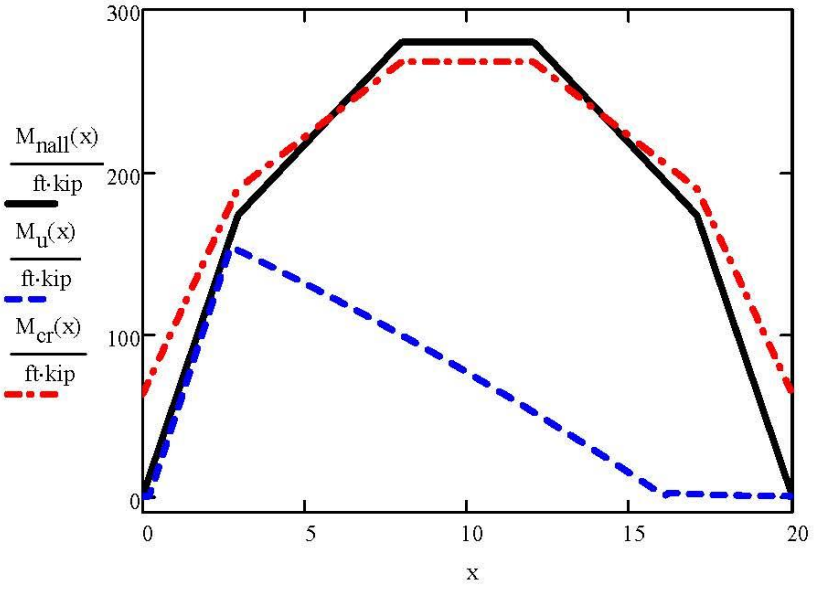

Length Along Beam

Check Pass/Fail for Ultimate Flexure, Under Reinforcement, and Minimum Reinforcement

$t := 0$

$F :=$ for $i \in 0 .. \frac{L}{in}$

$r \leftarrow i \cdot in$

$t \leftarrow t + 1$ if $M_u(r) > M_{nall}(r)$

$t \leftarrow t + 1$ if $\varepsilon_{ps} < 0.005$

$t \leftarrow t + 1$ if $M_{nall}(r) \le M_{cr}(r)$

$p \leftarrow$ "FAIL" if $t > 0$

$p \leftarrow$ "PASS" if $t < 1$

p

$F =$ "FAIL"

SHEAR

Strength Reduction Factor Shear

$$\phi_v := 1$$

Depth of Prestress
(Ref. ACI 318-14 22.5.8.3.1)

$$d_{ps} := \max\left(0.8 \cdot h, d_p\right) \qquad d_{ps} = 9.875 \cdot in$$

Neutral Axis to Tension Face

$$y_{tension} := y_b \qquad y_{tension} = 6.095 \cdot in$$

Core Width

$$b_c := 7.25 \cdot in$$

Number of Cores Filled - Prestressed

$$n_{fc\_ps} = 0$$

Width of Section for Shear - Prestressed

$$b_{wv} := b_w \qquad b_{wv} = 10.6 \cdot in$$

Minimum Concrete Shear Contribution
(Ref. ACI 318-14 Eq. 22.5.5.1)

$$V_{cmin} := 2 \cdot \lambda \cdot \sqrt{\frac{f_c}{psi}} \cdot psi \cdot b_{wv} \cdot d_{ps} \qquad V_{cmin} = 24.5 \cdot kip$$

Flexure-Shear Strength

Compressive Stress in Concrete due to Effective Prestressing at the Extreme Fiber where Tensile Stress is Caused by External Loads

$$f_{pe}(x) := \frac{P_{eff}(x)}{A_c} + \frac{P_{eff}(x) \cdot e}{S_b}$$

Concrete Stress due to Unfactored DL at the Extreme Fiber where Tensile Stress is Caused by External Loads

$$f_d(x) := \frac{M_{s\_sw}(x)}{S_b}$$

Moment Causing Flexural Cracking Due to Externally Applied Loads
(Ref. ACI 318-14 Eq. 22.5.8.3.1c)

$$M_{CRE}(x) := \frac{I_x}{y_{tension}} \cdot \left(6 \cdot \sqrt{\frac{f_c}{psi}} \cdot psi + f_{pe}(x) - f_d(x)\right)$$

Shear Force Due to Unfactored DL

$$V_d(x) := V_{s\_sw}(x)$$

Factored Shear Force Due to External Loads

$$V_i(x) := \left|1.0 \cdot V_u(x)\right|$$

Maximum Factored Moment Due to External Loads

$$M_{max}(x) := 1.0 \cdot M_{s\_ap}(x)$$

Nominal Shear Strength Provided by Concrete Where Diagonal Cracking Results from Combined Shear and Moment
(Ref. ACI 318-14 Eq. 22.5.8.3.1a & b)

$$V_{ci}(x) := \max\left(1.7 \cdot \lambda \cdot \sqrt{\frac{f_c}{psi}} \cdot psi \cdot b_{wv} \cdot d_{ps}, \text{if}\left(M_{max}(x) < 1 \cdot ft \cdot kip, 1000000 \cdot kip, 0.6 \cdot \lambda \cdot \sqrt{\frac{f_c}{psi}} \cdot psi \cdot b_{wv} \cdot d_{ps} \ldots + V_d(x) + \frac{V_i(x) \cdot M_{CRE}(x)}{M_{max}(x)}\right)\right)$$

Web-Shear Strength

Area of Single Core Fill

$A_{cf} := 58 \cdot in^2$ $A_{cf} = 58 \cdot in^2$

Concrete Compressive Stress at Center due to Prestressing Only

$$f_{pc}(x) := \frac{P_{eff}(x)}{A_c + n_{fc\_ps} \cdot A_{cf}}$$

Vertical Component of Prestressing

$V_p := 0 \cdot kip$

Nominal Shear Strength Provided by Concrete Where Diagonal Cracking Results from High Principal Tensile Stress in Web
(Ref. ACI 318-14 Eq. 22.5.8.3.2)

$$V_{cw}(x) := \left(3.5 \cdot \sqrt{\frac{f_c}{psi}} \cdot psi + 0.3 \cdot f_{pc}(x)\right) \cdot b_w \cdot d_{ps} + \left(3.5 \cdot \sqrt{\frac{f_{c\_cf}}{psi}} \cdot psi + 0.3 \cdot f_{pc}(x)\right) \cdot \left(n_{fc\_ps} \cdot A_{cf}\right) + V_p$$

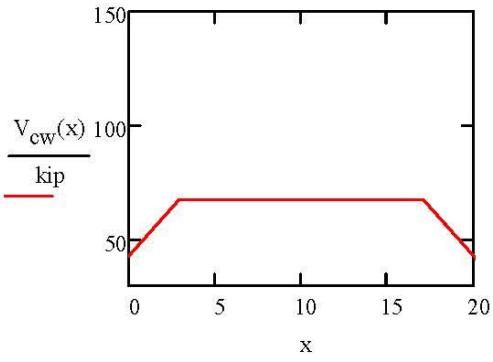

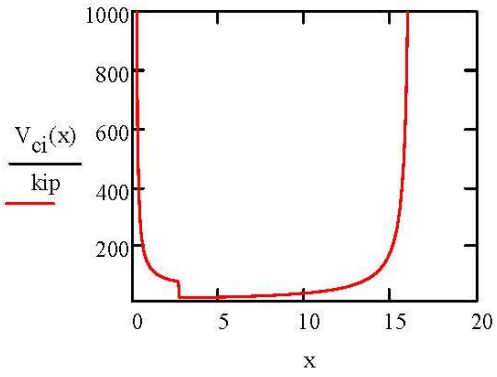

Number of Cores Filled - Plain

$n_{fc\_plain} = 1$

Additional Shear Capacity due to Core-Fill Treated as Plain Concrete

$$V_{core} := 2 \cdot \lambda \cdot \sqrt{\frac{f_{c\_cf}}{psi}} \cdot psi \cdot n_{fc\_plain} \cdot A_{cf}$$ $V_{core} = 11 \cdot kip$

Nominal Shear Strength of Concrete

$$V_c(x) := \phi_v \cdot \max\left(\min\left(V_{ci}(x), V_{cw}(x)\right), V_{cmin}\right) + V_{core}$$

$P \equiv 70.703 \cdot kip$ $f_c \equiv 13643 \cdot psi$ $n_{fc\_plain} \equiv 1$ $n_{fc\_ps} \equiv 0$

$1.2 \cdot P = 84.8 \cdot kip$ $f_{c\ cf} \equiv 9040 \cdot psi$

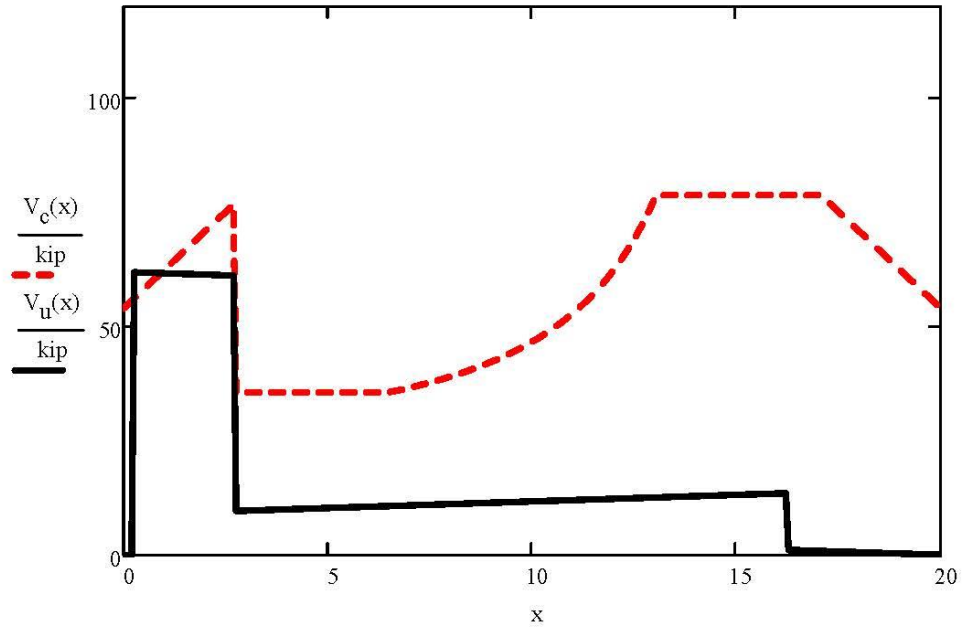

$V_u\left(L_1 + 0.5 \cdot h\right) = 61.7 \cdot kip$ $V_c\left(L_1 + 0.5 \cdot h\right) = 59.9 \cdot kip$

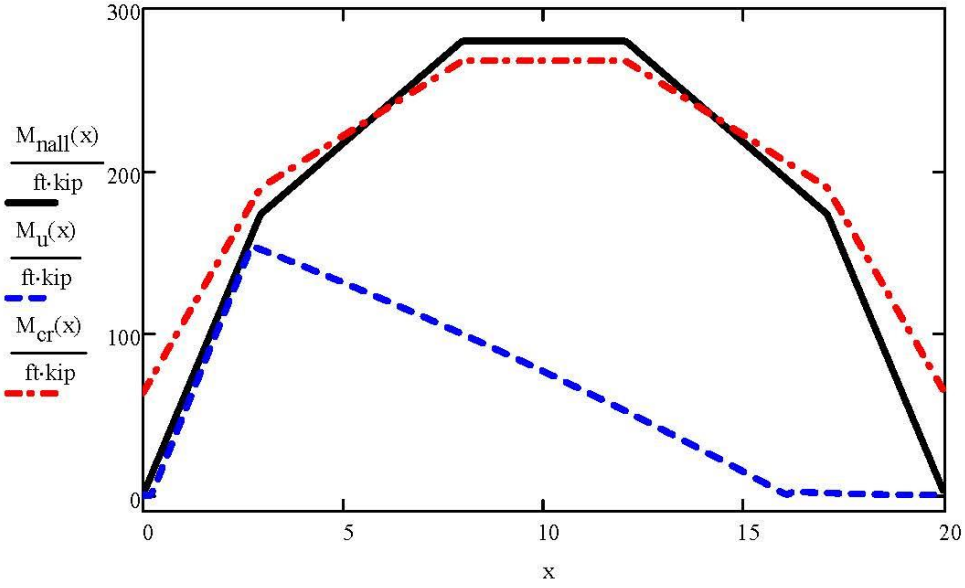

Appendix B: Data from Laboratory Testing

Six external LVDTs were used to measure the slab movement during loading. Additionally, a load cell attached to the actuator was used to capture the applied load. A pair of external LVDTs were attached to each side of the slab at each of the supports and the load point and numbered as depicted in

Figure 3.18. Load versus displacement plots for each LVDT were generated for each test. Additionally, the actual slab displacement was calculated as discussed in Section 3.5.3 and a load versus slab displacement plot was made for each test. All seven load versus displacement plots for each test are presented in this appendix.

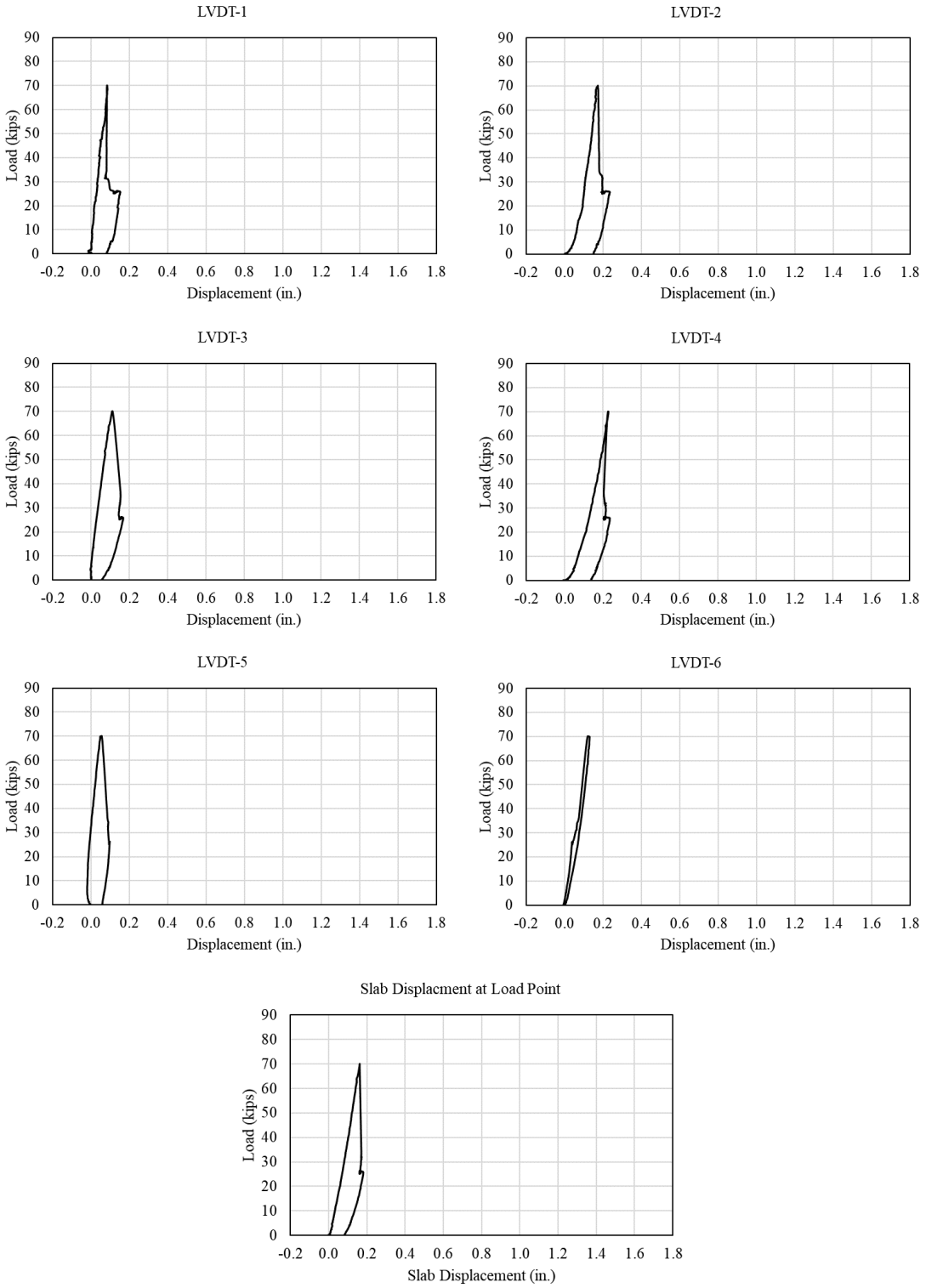

Figure B.1. Empty cores side A instrumentation data

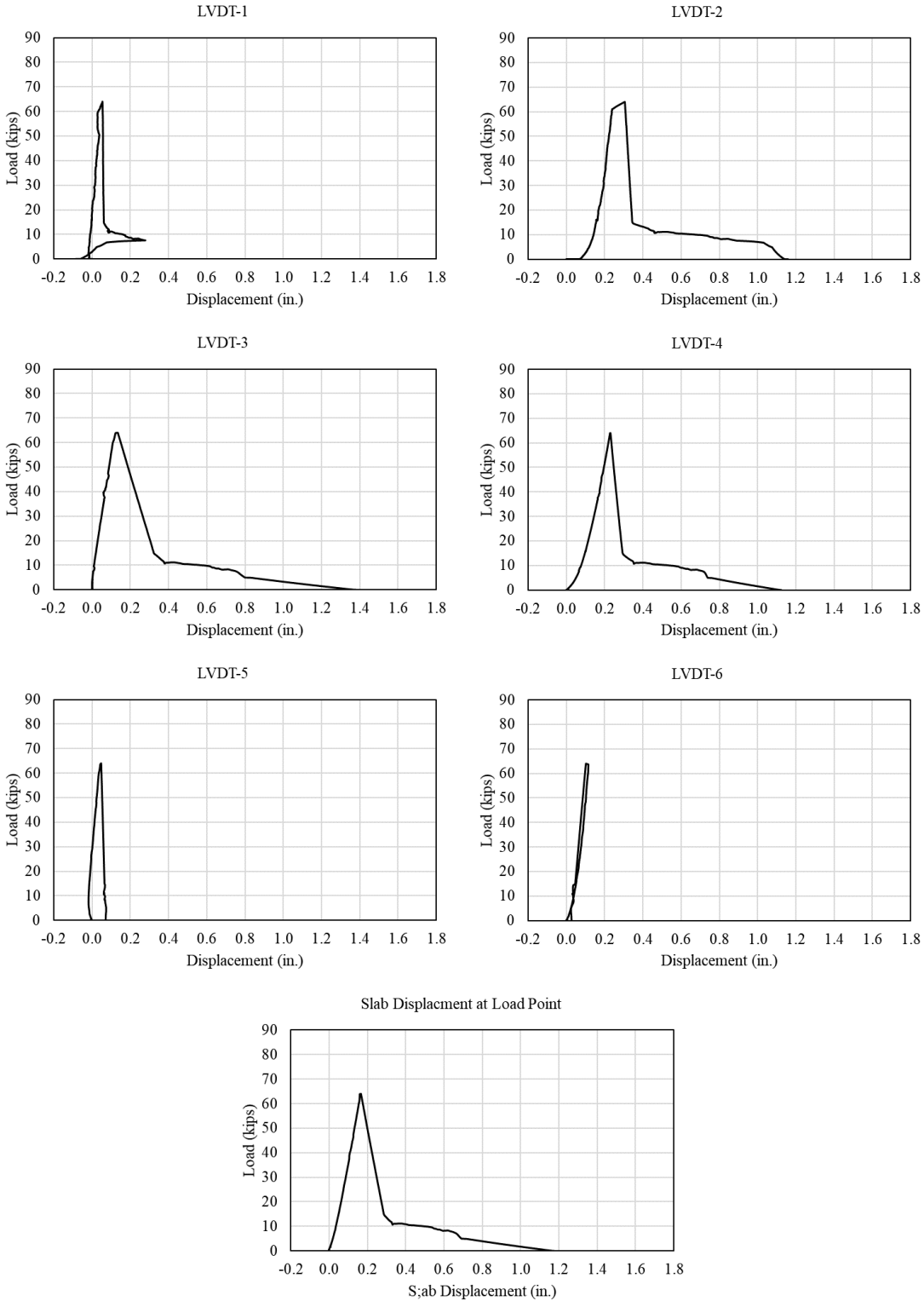

Figure B.2. Empty cores side B instrumentation data

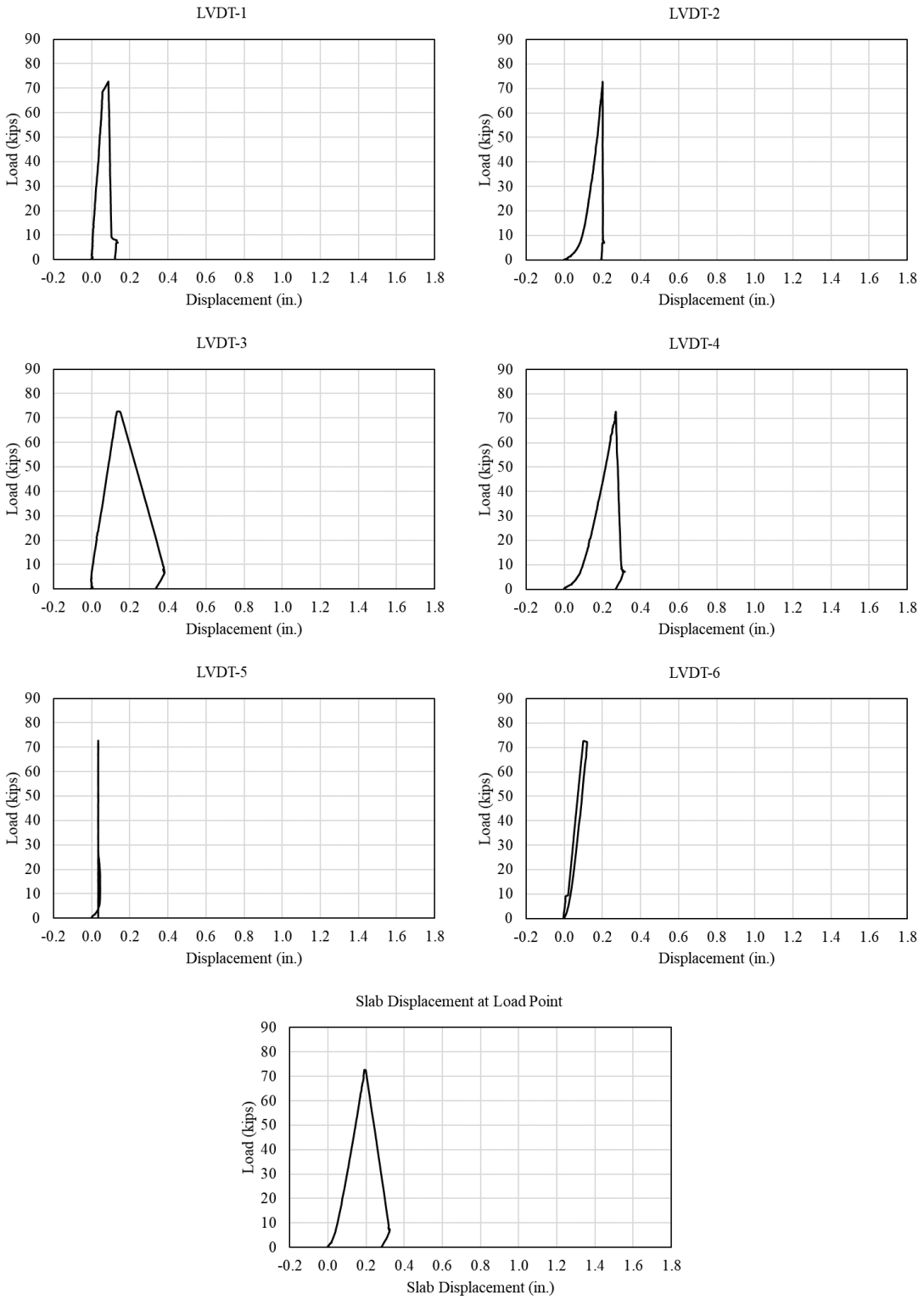

Figure B.3. Cold joint core fill side A instrumentation data

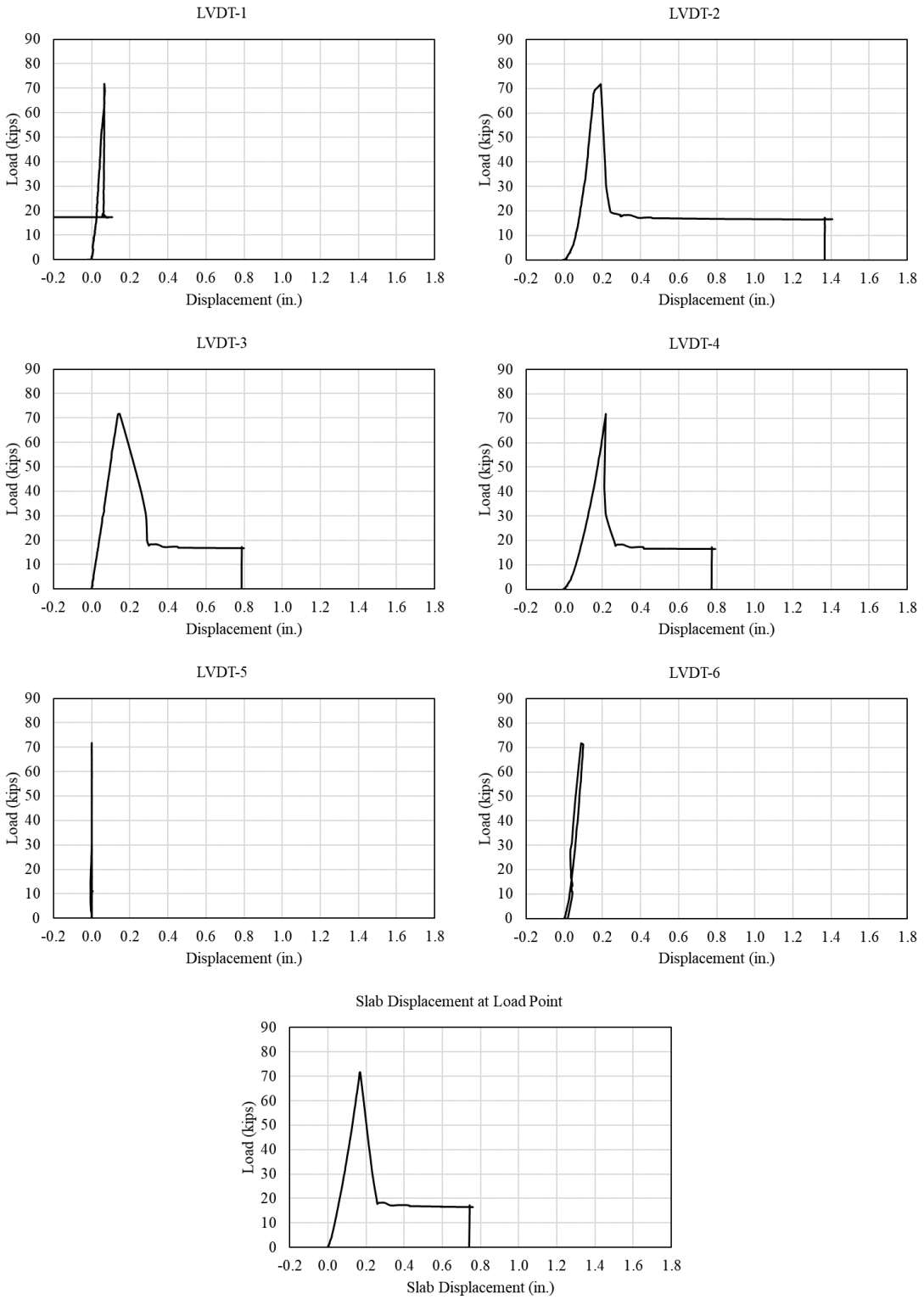

Figure B.4. Cold joint core fill side B instrumentation data

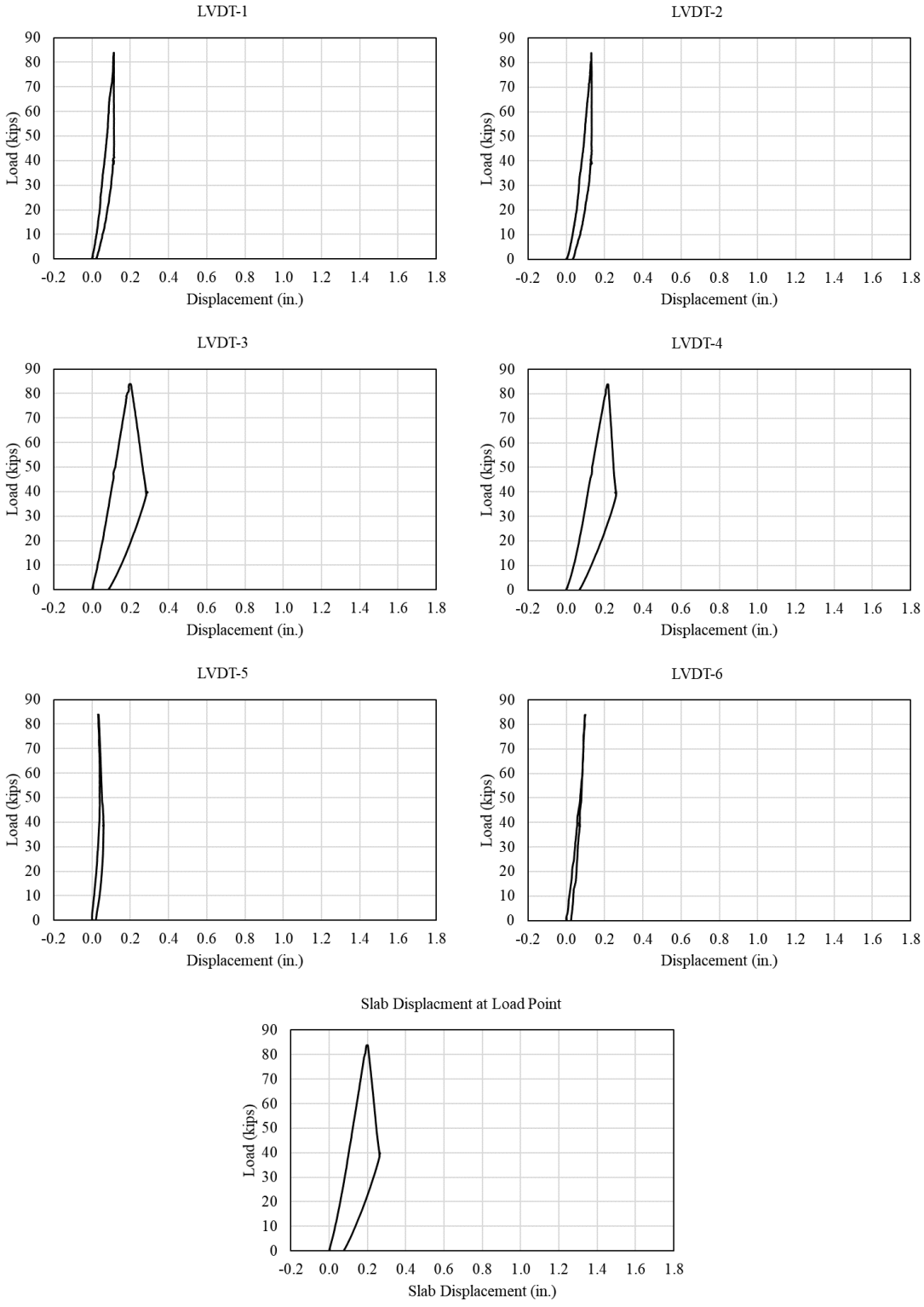

Figure B.5. Typical immediate fill side A instrumentation data

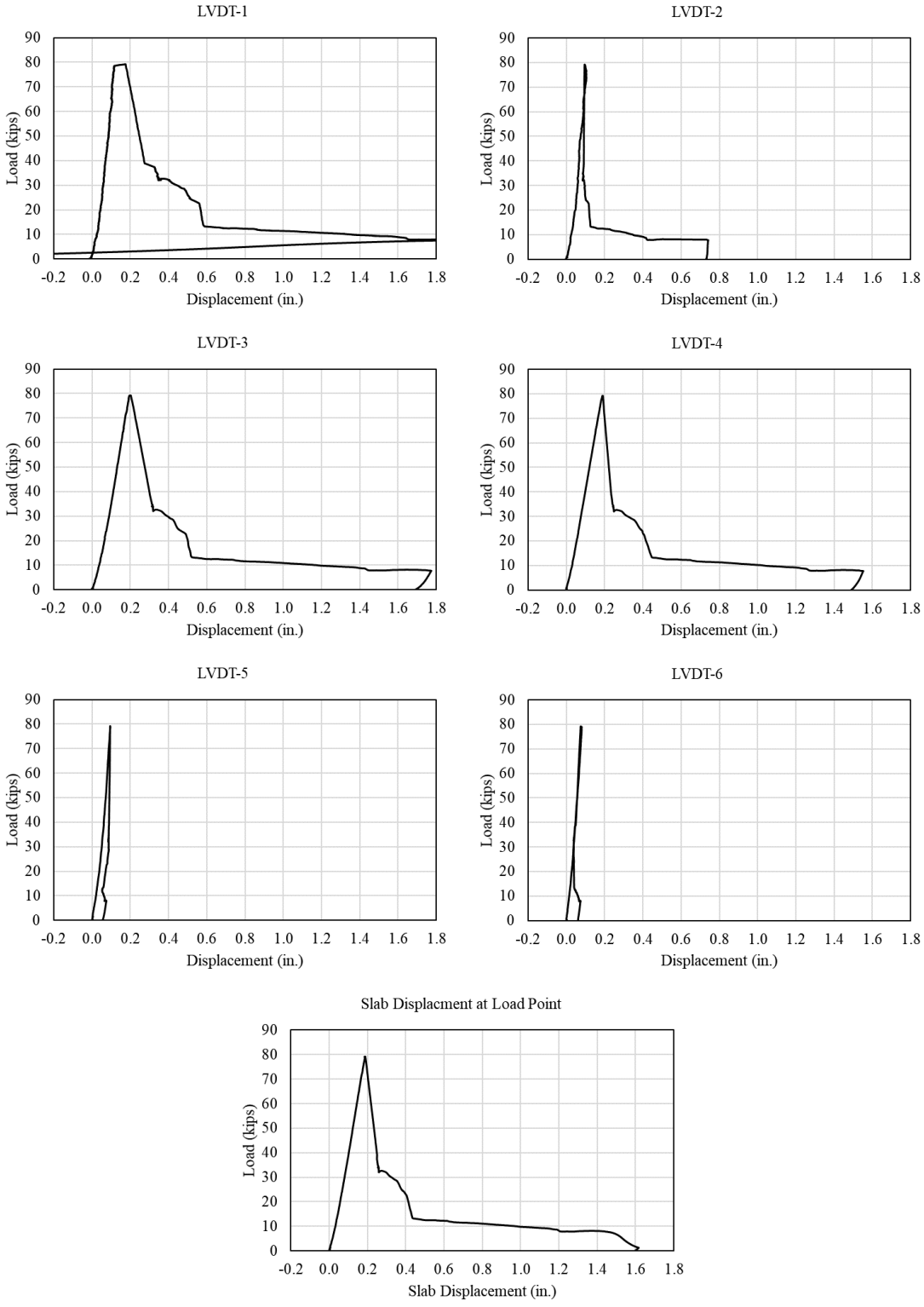

Figure B.6. Typical immediate fill side B instrumentation data

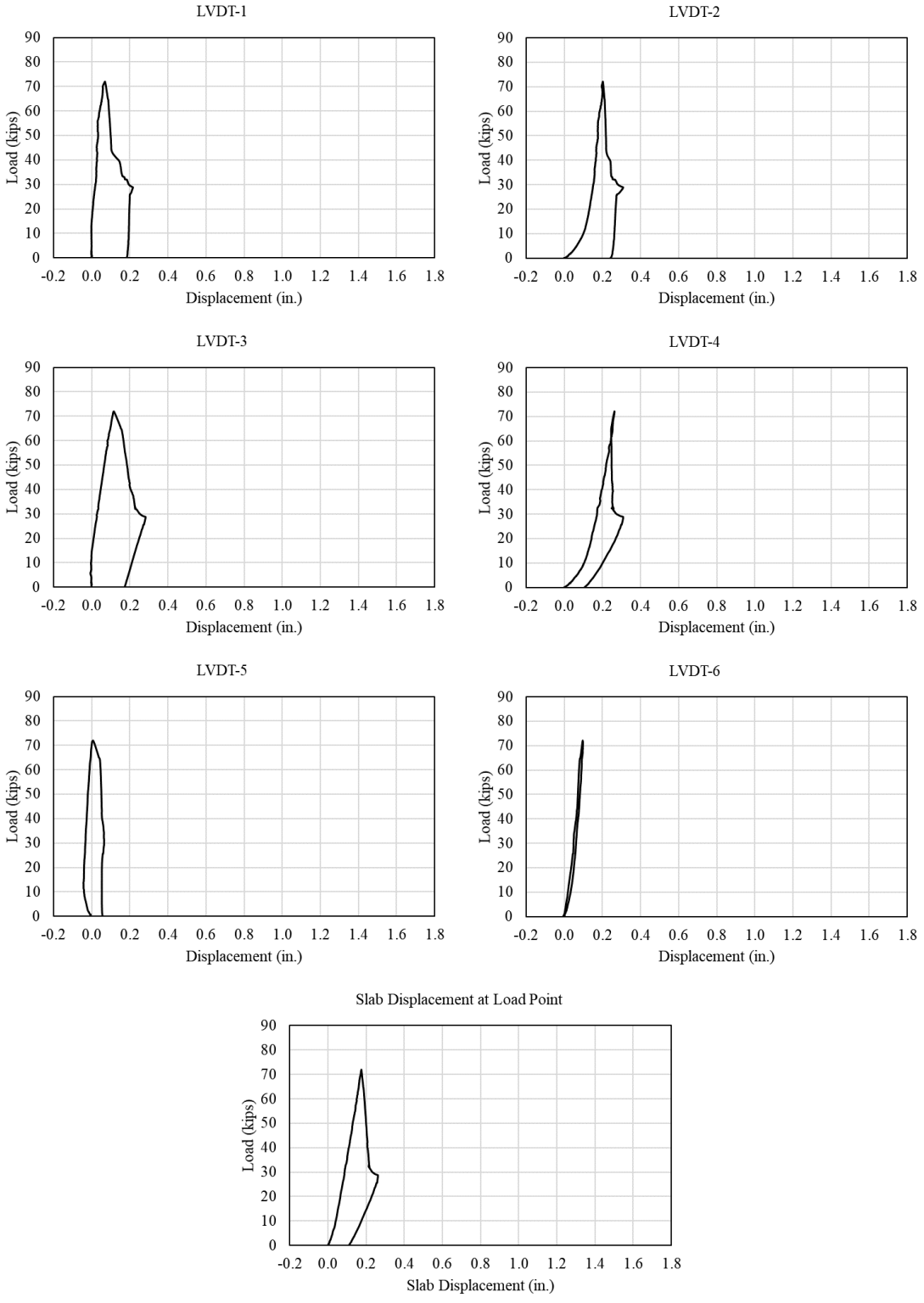

Figure B.7. 209-Day typical fill side A instrumentation data

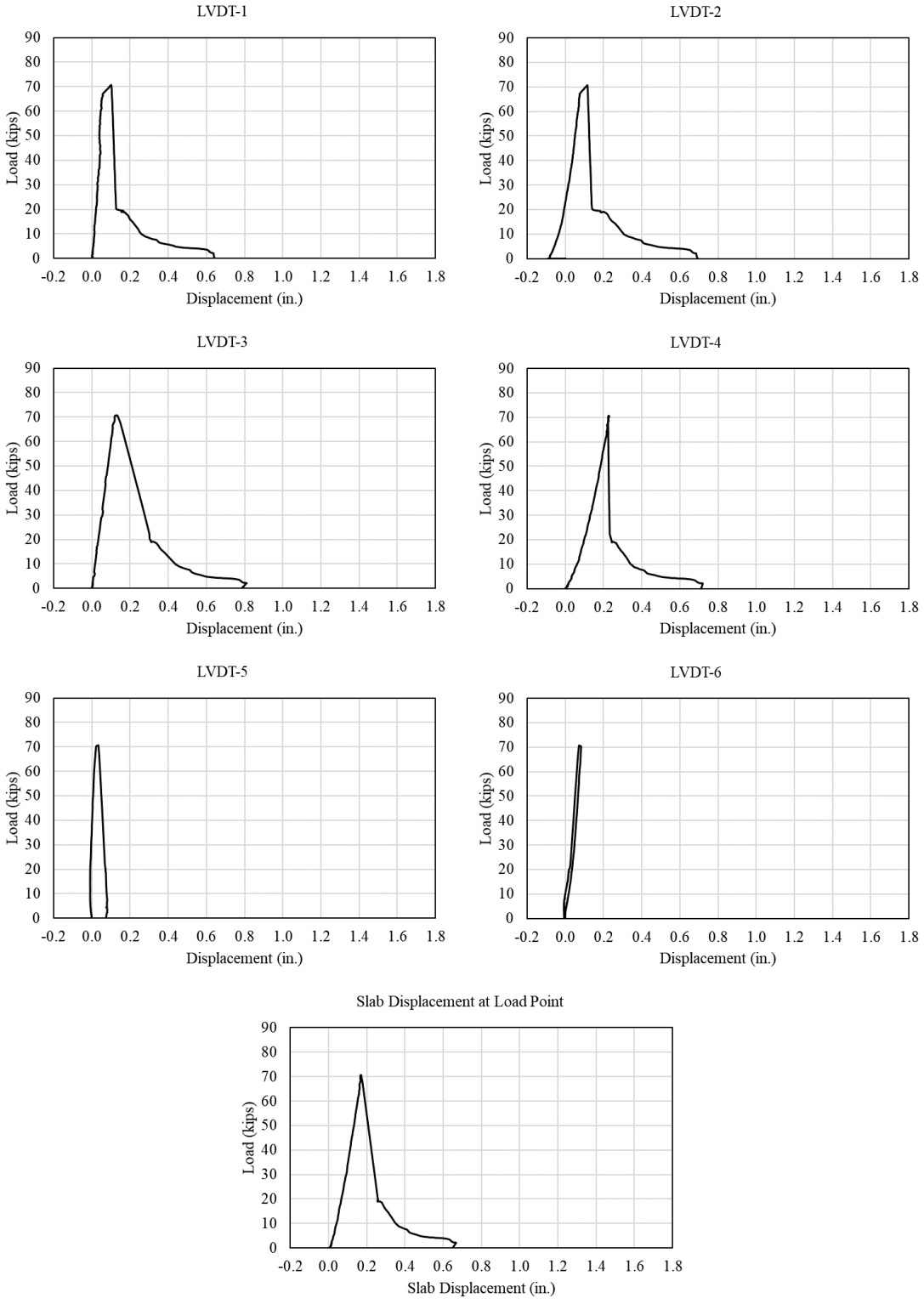

Figure B.8. 209-Day typical fill side B instrumentation data

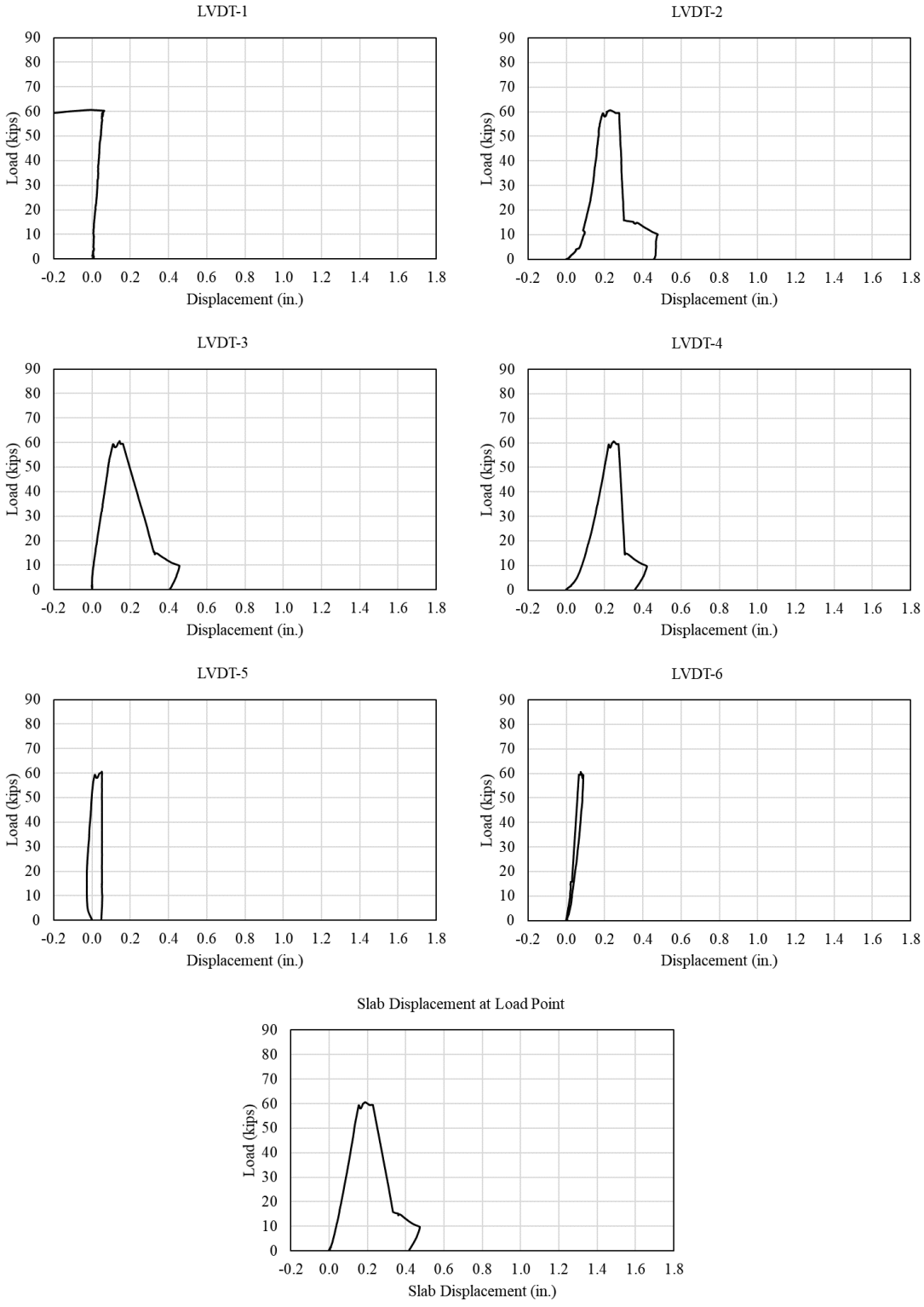

Figure B.9. SFRC fill side A instrumentation data

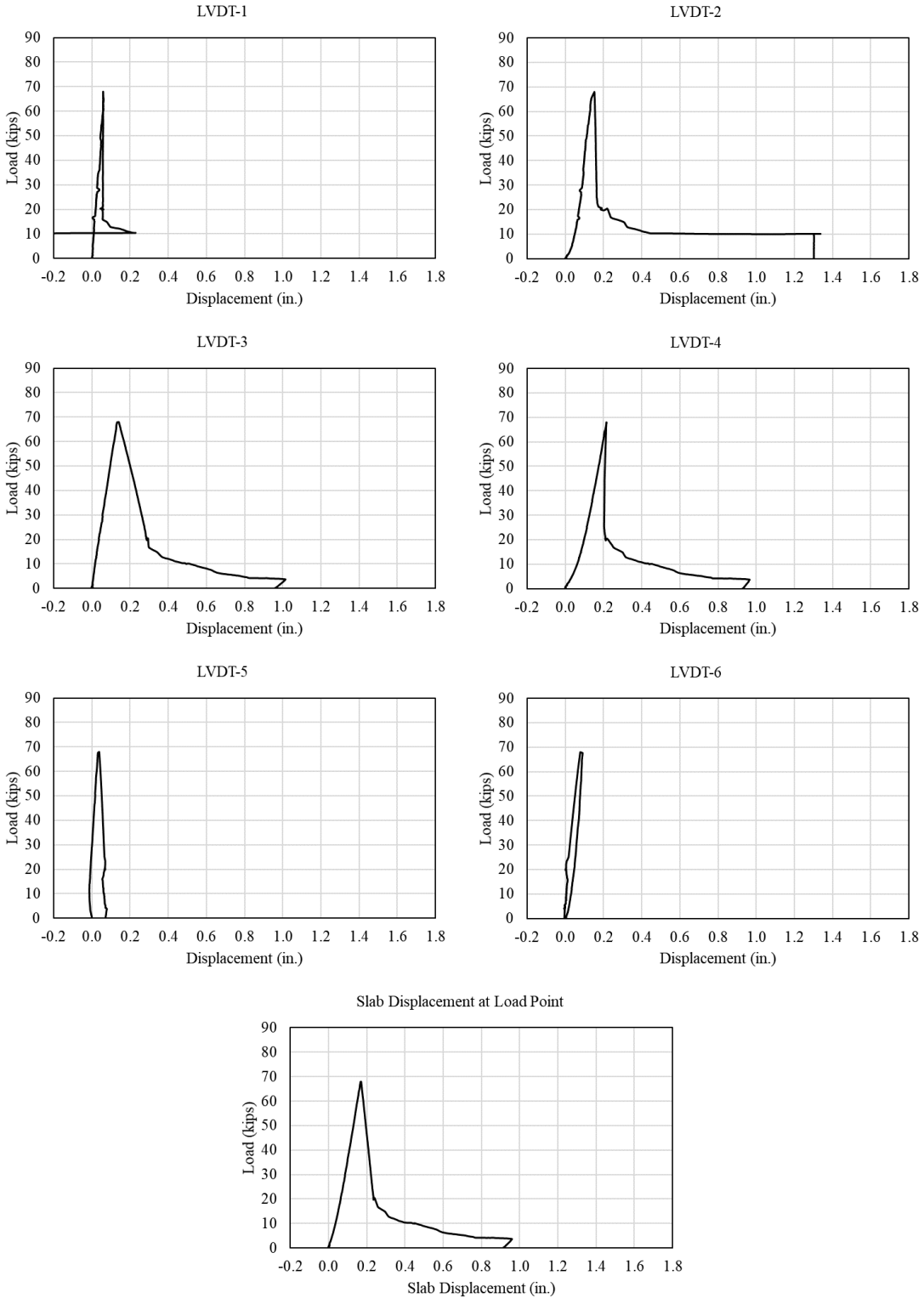

Figure B.10. SFRC fill side B instrumentation data

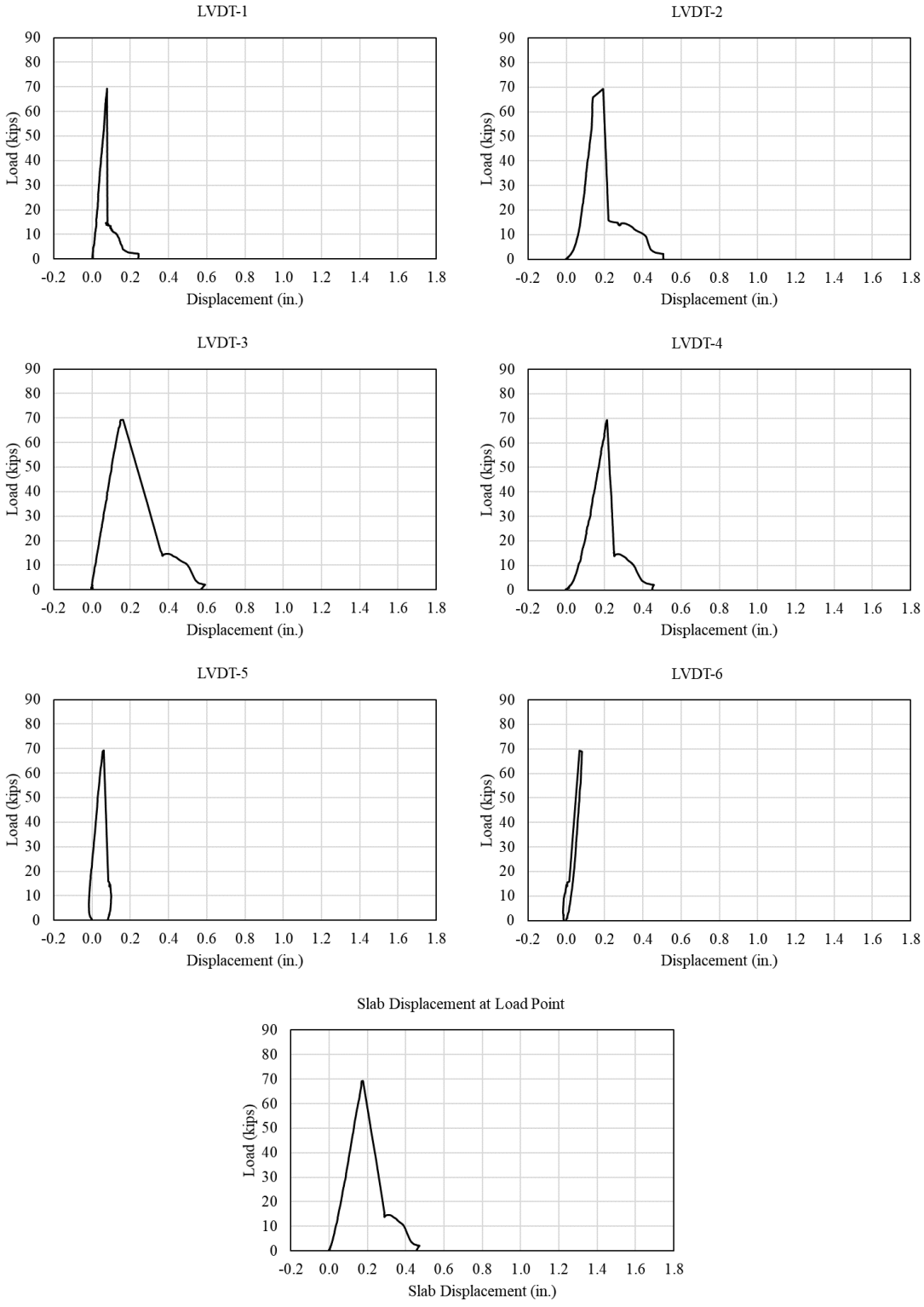

Figure B.11. Core wall surface enhancement side A instrumentation data

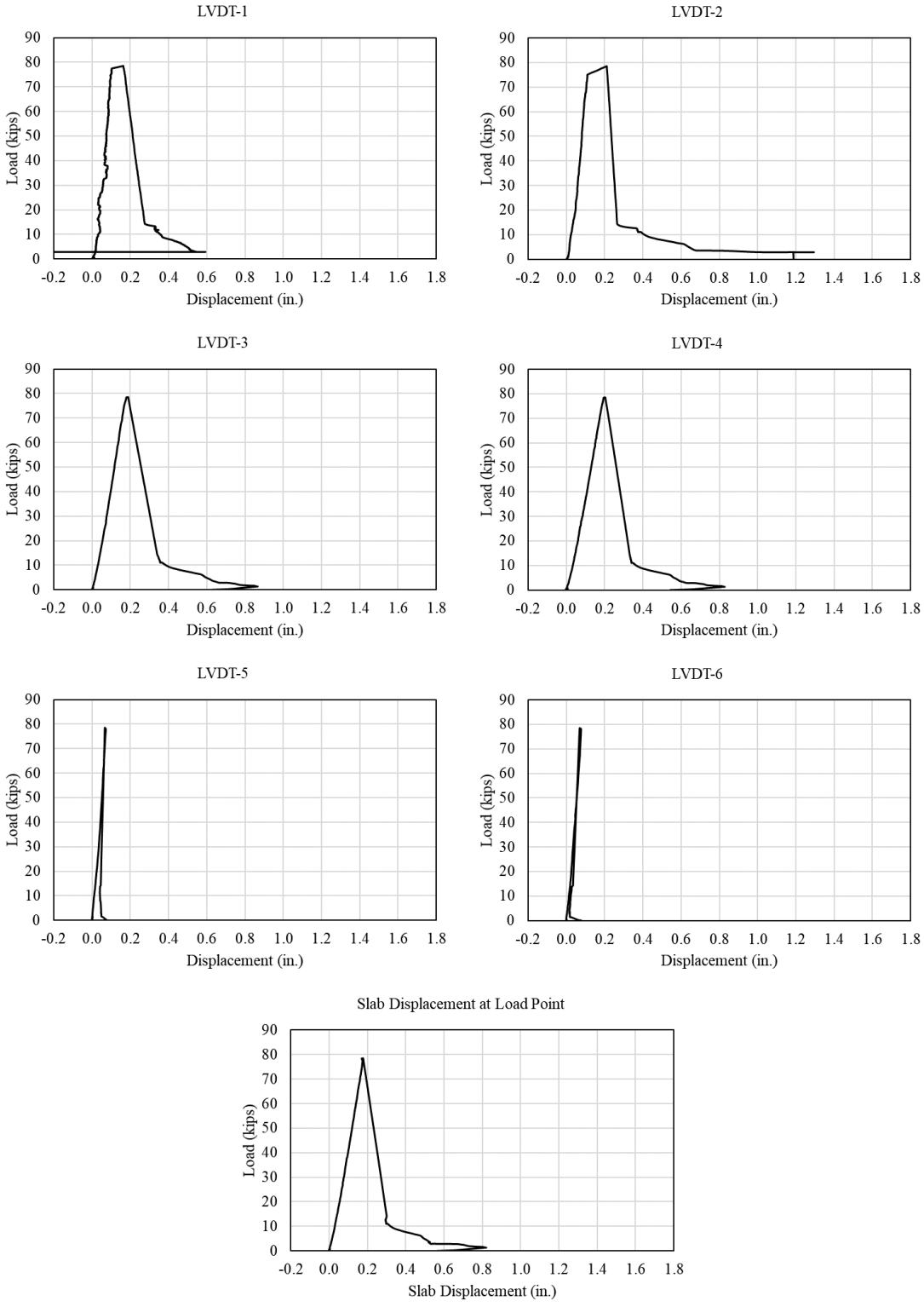

Figure B.12. Core wall surface enhancement side B instrumentation data

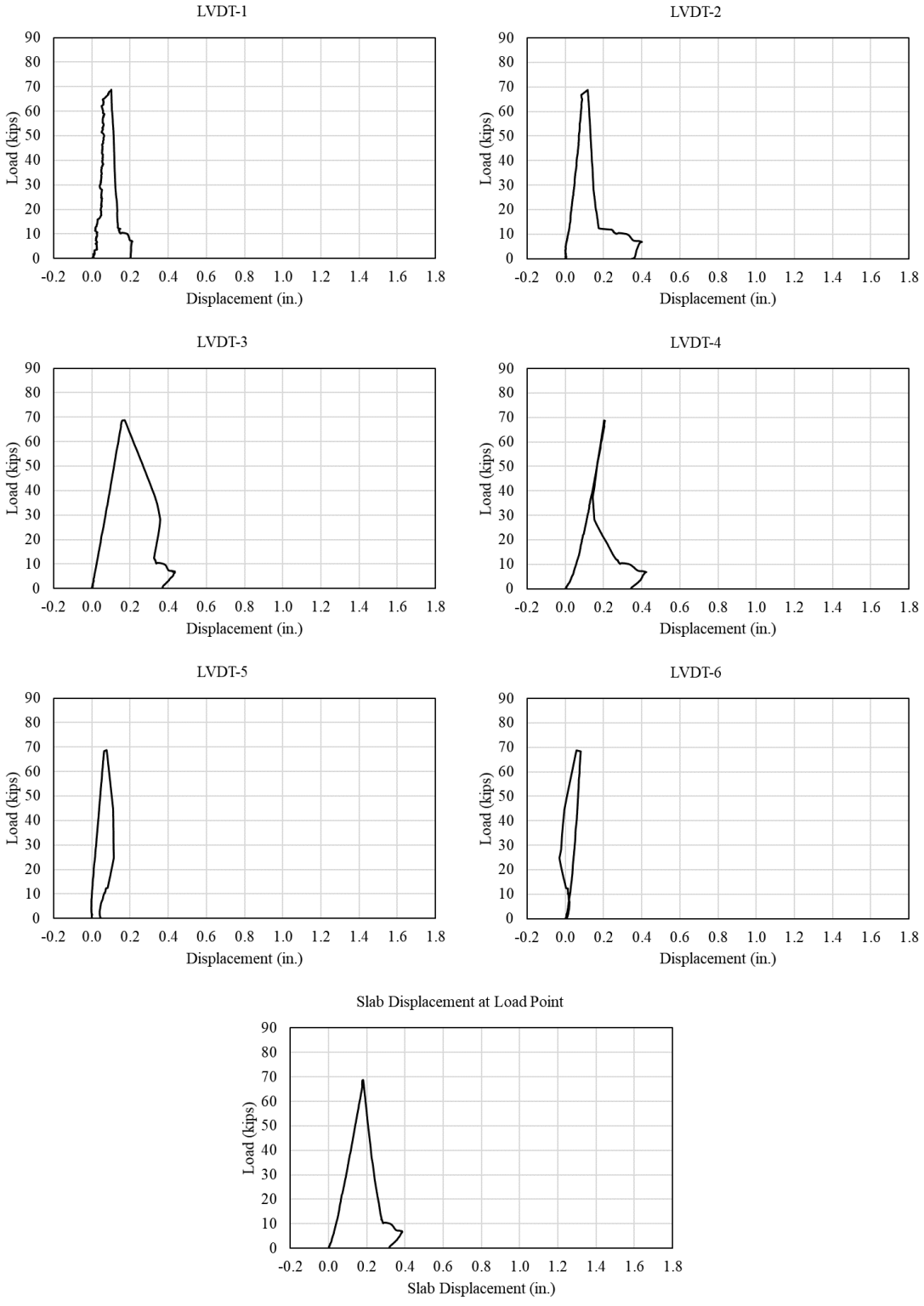

Figure B.13. Steel bar placed in core fill side A instrumentation data

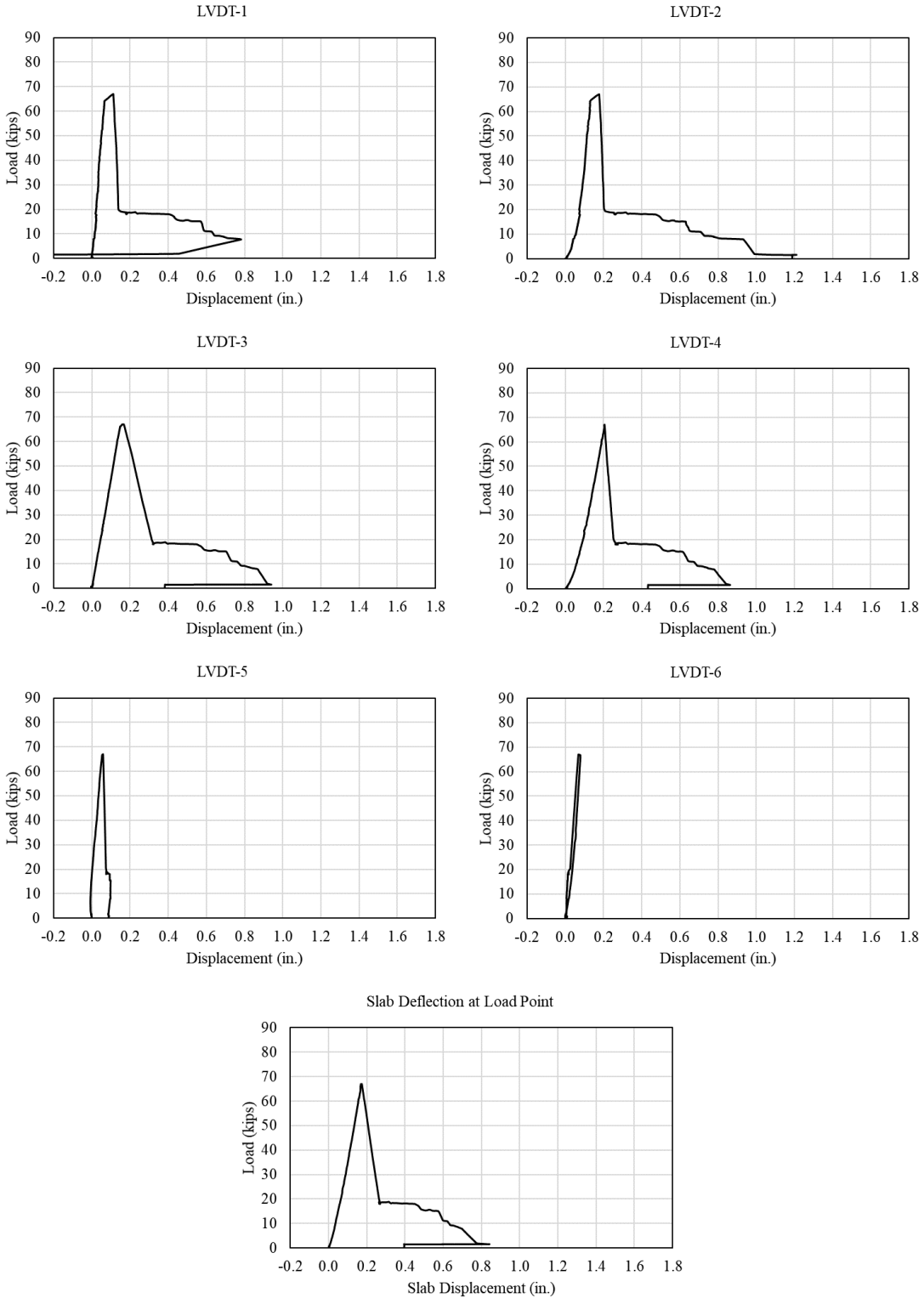

Figure B.14. Steel bar placed in core fill side B instrumentation data

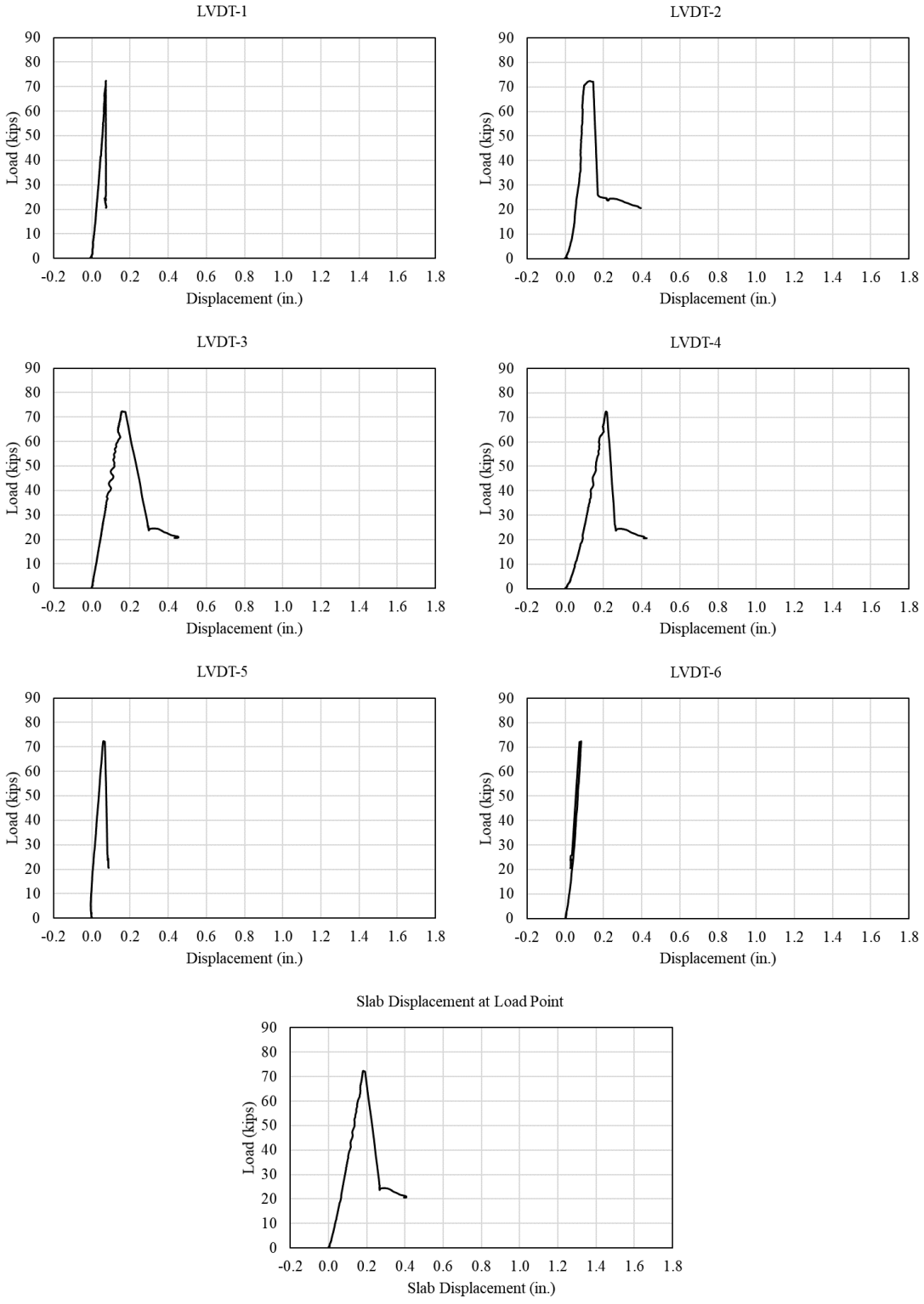

Figure B.15. WWR in core fill side A instrumentation data

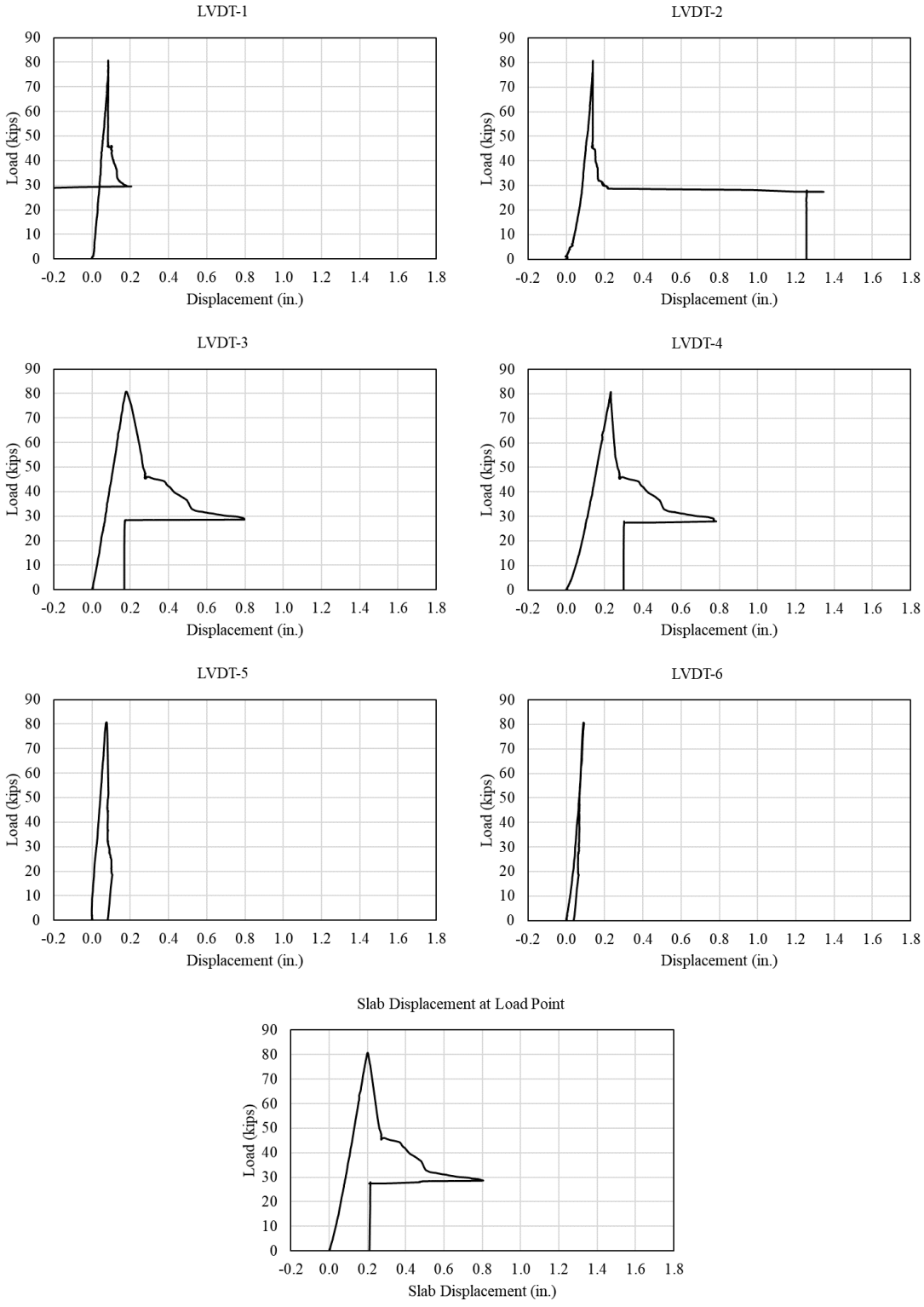

Figure B.16. WWR in core fill side B instrumentation data

Appendix C: Web-Shear Capacity Sample Calculations

All calculations presented in this appendix were generated using Mathcad (2015).

AASHTO LRFD 8TH EDITION SHEAR PREDICTION

DESIGN PARAMETERS

Lab Arangement

Total Length of Beam	$L_{tot} := 20 \cdot ft$	
CL Support to Beam End - Testing End	$L_1 := 2.5 \cdot in$	
CL Support to Beam End - Overhang	$L_2 := 3 \cdot ft + 9.5 \cdot in$	$L_2 = 3.792\,ft$
Length of Beam Tested	$L := L_{tot} - L_1 - L_2$	$L = 16\,ft$
Actuator to CL Supports	$L_a := 2 \cdot ft + 6 \cdot in$	

Section Properties

Section Depth	$h := 12 \cdot in$	
Section Width	$b := 48 \cdot in$	
Web Width	$b_w := 10.626 \cdot in$	
Cross-Sectional Area	$A_c := 269.76 \cdot in^2$	
Moment of Inertia	$I_g := 5248 \cdot in^4$	
Neutral Axis to Bottom Extreme Fiber	$y_b := 6.095 \cdot in$	
Neutral Axis to Top Extreme Fiber	$y_t := h - y_b$	$y_t = 5.905 \cdot in$
Section Modulus - Top	$S_t := \frac{I_g}{y_t}$	$S_t = 888.7 \cdot in^3$
Section Modulus - Bottom	$S_b := \frac{I_g}{y_b}$	$S_b = 861 \cdot in^3$
Strand Eccentricity	$e := y_b - 2.125 \cdot in$	$e = 3.97 \cdot in$

Material Properties

Concrete Unit Weight $\gamma_c := 154 \cdot pcf$

Concrete Compressive Strength $f_c = 13.643 \cdot ksi$

Concrete Strength at Detensionoing $f_{ci} := 5.5 \cdot ksi$

Core Fill Compressive Strength $f_{cf} = 9.04 \cdot ksi$

Modulus of Elasticity of Strand $E_p := 28500 \cdot ksi$

Aggregate Source Factor $k_1 := 1$

Modulus of Elasticity - Transfer
(Ref. AASHTO Eq. 5.4.2.4-1)

$$E_c := 120000 \cdot k_1 \cdot \left(\frac{\gamma_c}{\frac{kip}{ft^3}} \right)^2 \cdot \left(\frac{f_c}{ksi} \right)^{0.33} \cdot ksi \qquad E_c = 6741 \cdot ksi$$

Modulus of Elasticity - Transfer
(Ref. AASHTO Eq. 5.4.2.4-1)

$$E_{ci} := 120000 \cdot k_1 \cdot \left(\frac{\gamma_c}{\frac{kip}{ft^3}} \right)^2 \cdot \left(\frac{f_{ci}}{ksi} \right)^{0.33} \cdot ksi \qquad E_{ci} = 4995 \cdot ksi$$

Ultimate Strength of Strand $f_{pu} := 270 \cdot ksi$

Number of 6/10" Strands $n_{s0.6} := 6$

Diameter of 6/10" Strands $d_{0.6} := 0.6 \cdot in$

Strand Area - 6/10" Diameter $A_{ps0.6} := 0.217 \cdot in^2$

Total Strand Area $A_{ps} := n_{s0.6} \cdot A_{ps0.6}$ $A_{ps} = 1.302 \cdot in^2$

Strand Stressing $ss := 0.70$

Initial Jacking Stress $f_{pj} := ss \cdot f_{pu}$ $f_{pj} = 189 \cdot ksi$

Initial Jacking Force $F_{pj} := f_{pj} \cdot A_{ps}$ $F_{pj} = 246.1 \cdot kip$

Depth of Prestressing $d_p := e + y_t$ $d_p = 9.875 \cdot in$

LOADING

Middle of Beam - Testing Span $x_m := L_1 + 0.5 \cdot L$ $x_m = 8.208\ ft$

Applied Point Load $P = 70.703 \cdot kip$

Distributed Self-Weight $w_{sw} := \gamma_c \cdot A_c$ $w_{sw} = 288 \cdot plf$

Shear for Applied Load

$$V_{s\_ap}(x) := \begin{cases} 0 \cdot kip & \text{if } x < L_1 \\ \frac{P \cdot (L - L_a)}{L} & \text{if } L_1 \le x \le L_1 + L_a \\ -\frac{P \cdot L_a}{L} & \text{if } L_1 + L_a < x \le L_1 + L \\ 0 \cdot kip & \text{if } L_1 + L < x \le L_{tot} \end{cases}$$

Shear for Self Weight

$$V_{s\_sw}(x) := \begin{cases} 0 \cdot kip & \text{if } x < L_1 \\ \left[\frac{w_{sw}}{2 \cdot L} \cdot \left(L^2 - L_2^{\,2}\right)\right] - w_{sw} \cdot (x - L_1) & \text{if } L_1 \le x \le L_1 + L \\ w_{sw} \cdot \left[L_2 - (x - L_1 - L)\right] & \text{if } x > L_1 + L \end{cases}$$

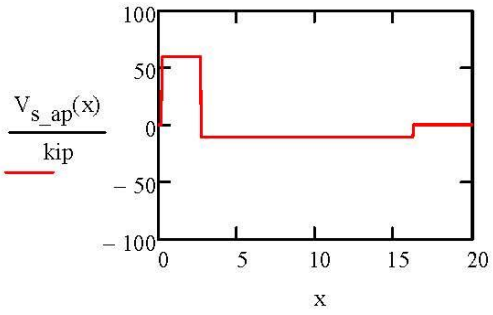

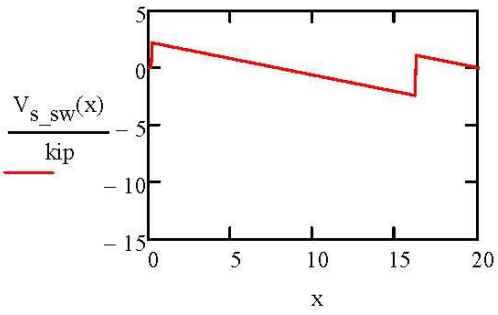

Moment for Self Weight SS Span

$$M_{ss}(x) := \frac{w_{sw} \cdot x}{2} \cdot (L_{tot} - x)$$

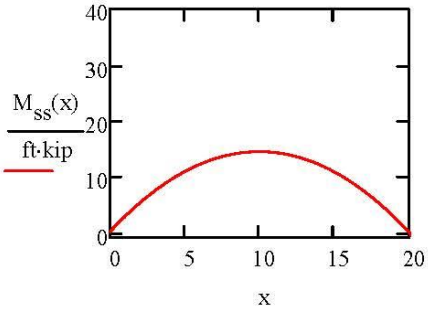

Moment for Appled Load $M_{s\_ap}(x) := \begin{cases} 0 \text{ if } x < L_1 \\ \frac{P \cdot (L - L_a) \cdot (x - L_1)}{L} \text{ if } L_1 \le x \le L_1 + L_a \\ \frac{P \cdot L_a \cdot (L - L_a)}{L} \cdot \left[1 - \frac{x - (L_1 + L_a)}{L - L_a}\right] \text{ if } L_1 + L_a < x \le L_1 + L \\ 0 \text{ if } L_1 + L < x \le L_{tot} \end{cases}$

Moment for Self Weight $M_{s\_sw}(x) := \begin{cases} 0 \text{ if } x < L_1 \\ \frac{w_{sw} \cdot (x - L_1)}{2 \cdot L} \cdot \left[L^2 - {L_2}^2 - (x - L_1) \cdot L\right] \text{ if } L_1 \le x \le L_1 + L \\ \frac{-w_{sw}}{2} \cdot \left[L_2 - \left[x - (L_1 + L)\right]\right]^2 \text{ if } x > L_1 + L \end{cases}$

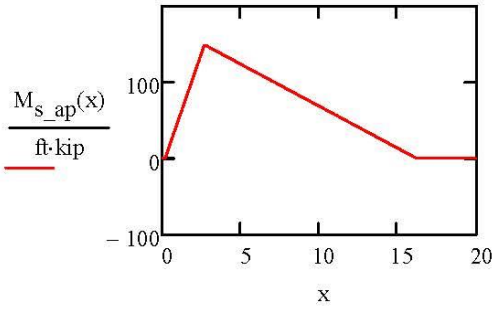

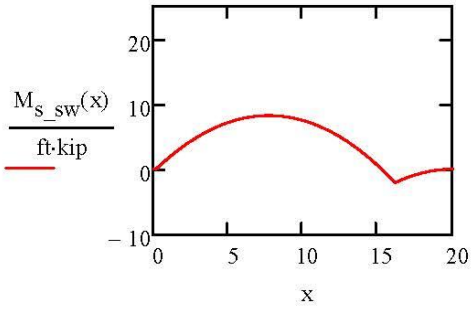

Unfactored Shear Demand $V_u(x) := \left|V_{s\_ap}(x) + V_{s\_sw}(x)\right|$

Unfactored Moment Demand $M_u(x) := \left|M_{s\_ap}(x) + M_{s\_sw}(x)\right|$

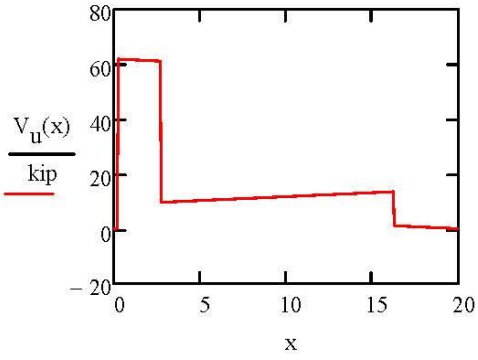

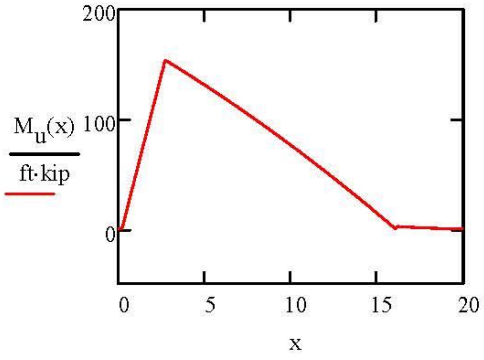

LOSSES

Elastic Shortening - AASHTO 8th Edition 5.9.3.2.3a

Stress in PS Prior to Transfer $f_{pbt} := f_{pj}$

Moment Due to Self-Weight $M_g := \frac{w_{sw}}{8 \cdot L^2} \cdot \left(L + L_2\right)^2 \cdot \left(L - L_2\right)^2$ $M_g = 8 \cdot ft \cdot kip$

Elastic Shortening Loss
(Ref. AASHTO Eq. C5.9.3.2.3a-1)

$$\Delta f_{pES} := \frac{A_{ps} \cdot f_{pbt} \cdot \left(I_g + e^2 \cdot A_c\right) - e \cdot M_g \cdot A_c}{A_{ps} \cdot \left(I_g + e^2 \cdot A_c\right) + \frac{A_c \cdot I_g \cdot E_{ci}}{E_p}} \qquad \Delta f_{pES} = 8.6 \cdot ksi$$

Long-Term Losses (Creep, Shrinkage, and Relaxation) - AASHTO 8th Edition 5.4.2.3.3

Average Anual Ambient Relative Humidity $H := 70$
(Ref. AASHTO Fig. 5.4.2.3.3-1)

Ambient Realitive Humidity Factor $\gamma_h := 1.7 - 0.01 \cdot H$ $\gamma_h = 1$
(Ref. AASHTO Eq. 5.9.3.3-2)

Concrete Strength Factor $\gamma_{st} := \frac{5}{1 + \frac{f_{ci}}{ksi}}$ $\gamma_{st} = 0.769$
(Ref. AASHTO Eq. 5.9.3.3-3)

Estimated Relaxation $\Delta f_{pR} := 2.4 \cdot ksi$

Long-Term Losses
(Ref. AASHTO Eq. 5.9.3.3-1)

$$\Delta f_{pLT} := 10 \cdot \frac{f_{pj} \cdot A_{ps}}{A_c} \cdot \gamma_h \cdot \gamma_{st} + 12 \cdot \gamma_h \cdot \gamma_{st} \cdot ksi + \Delta f_{pR} \qquad \Delta f_{pLT} = 18.6 \cdot ksi$$

Totals

Total Initial Losses $\Delta f_{pI} := \Delta f_{pES}$ $\Delta f_{pI} = 8.6 \cdot ksi$

Initial Stress After Losses $f_{pi} := f_{pj} - \Delta f_{pI}$ $f_{pi} = 180.4 \cdot ksi$

Initial Force After Losses $F_{pi} := A_{ps} \cdot f_{pi}$ $F_{pi} = 234.9 \cdot kip$

Effective Stress After Losses $f_{se} := f_{pj} - \Delta f_{pI} - \Delta f_{pLT}$ $f_{se} = 161.8 \cdot ksi$

Effective Force After Losses $F_{se} := A_{ps} \cdot f_{se}$ $F_{se} = 210.6 \cdot kip$

Total Loss Percentage $TL := 1 - \frac{f_{se}}{f_{pj}}$ $TL = 14.4 \cdot \%$

TRANSFER/DEVELOPMENT LENGTHS

Transfer Length
(Ref. AASHTO 5.9.4.3.1)

$$l_t := 60 \cdot d_{0.6} \qquad l_t = 36 \cdot in$$

Compression Stress Block Factor
(Ref. AASHTO 5.6.2.2)

$$\alpha_1 := \max\left[0.85 - \left[0.02 \cdot \left(\frac{f_c}{ksi} - 10\right)\right], 0.75\right]$$

$$\alpha_1 = 0.777$$

Compression Stress Block Factor
(Ref. AASHTO 5.6.2.2)

$$\beta_1 := \max\left[0.85 - \left[0.05 \cdot \left(\frac{f_c}{ksi} - 4\right)\right], 0.65\right]$$

$$\beta_1 = 0.65$$

Tendon Type Factor

$$k_{ps} := 0.28 \qquad \textit{(Low relaxation strand)}$$

Distance Between Extreme Comprssion Fiber and Neutral Axis

$$c := \frac{A_{ps} \cdot f_{pu}}{\alpha_1 \cdot f_c \cdot \beta_1 \cdot b + k_{ps} \cdot A_{ps} \cdot \frac{f_{pu}}{d_p}} \qquad c = 1.032 \cdot in$$

Average Stress in Prestressing

$$f_{ps} := f_{pu} \cdot \left(1 - k_{ps} \cdot \frac{c}{d_p}\right) \qquad f_{ps} = 262.1 \cdot ksi$$

Member Depth Factor

$$k_d := 1.0$$

Development Length
(Ref. AASHTO Eq. 5.9.4.3.2-1)

$$l_d := k_d \cdot \left(\frac{f_{ps}}{ksi} - \frac{2}{3} \cdot \frac{f_{se}}{ksi}\right) d_{0.6} \qquad l_d = 92.5 \cdot in$$

Transfer and Development Length Function

$$TD(x) := \begin{cases} \frac{x}{l_t}\cdot\frac{f_{se}}{f_{ps}} & \text{if } x \le l_t \\ \frac{x - l_t}{l_d - l_t}\cdot\left(1 - \frac{f_{se}}{f_{ps}}\right) + \frac{f_{se}}{f_{ps}} & \text{if } l_t < x \le l_d \\ 1 & \text{if } l_d < x \le L_{tot} - l_d \\ 1 - \frac{x - (L_{tot} - l_d)}{l_d - l_t}\cdot\left(1 - \frac{f_{se}}{f_{ps}}\right) & \text{if } L_{tot} - l_d < x \le L_{tot} - l_t \\ \left(\frac{f_{se}}{f_{ps}}\right) - \frac{x - (L_{tot} - l_t)}{l_t}\cdot\left(\frac{f_{se}}{f_{ps}}\right) & \text{if } L_{tot} - l_t < x \le L_{tot} \end{cases}$$

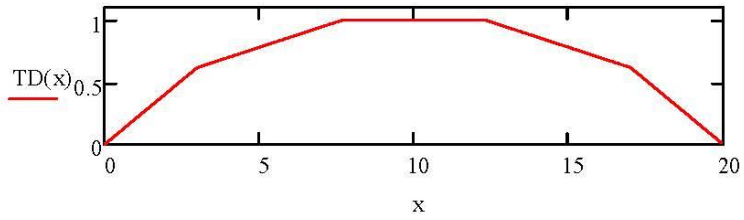

Effective Prestressing Force - Service

$$P_{se}(x) := \begin{cases} x\cdot\frac{F_{se}}{l_t} & \text{if } x \le l_t \\ F_{se} & \text{if } l_t < x < L_{tot} - l_t \\ F_{se} - \frac{F_{se}}{l_t}\left[x - (L_{tot} - l_t)\right] & \text{if } L_{tot} - l_t \le x \end{cases}$$

Effective Prestressing Force - Ultimate

$$P_{ps}(x) := (f_{ps}\cdot A_{ps})\cdot TD(x)$$

EFFECTIVE PRESTRESSING

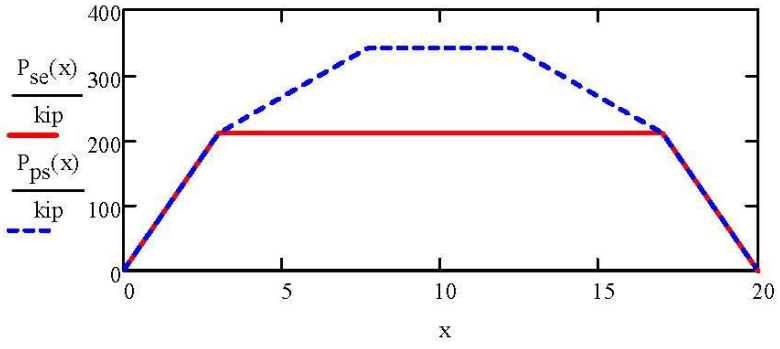

SHEAR STRENGTH PREDICTION

Axial Force Function

$$N_u(x) := P_{se}(x)$$

Vertical Component of Prestressing

$$V_p(x) := 0 \cdot kip$$

Locked-in Difference in Stress Between the Prestressing Steel and Concrete

$$f_{po} := 0.7 \cdot f_{pu} \qquad f_{po} = 189 \cdot ksi$$

Depth of Center of Gravity of Steel
(Ref. AASHTO Eq. 5.7.2.8-2)

$$d_e := \frac{A_{ps} \cdot f_{ps} \cdot d_p}{A_{ps} \cdot f_{ps}} \qquad d_e = 9.875 \cdot in$$

Effective Shear Depth
(Ref. AASHTO 5.7.2.8)

$$d_v := \max\left[h - \left(\frac{c}{2} + 2.125 \cdot in\right), \max\left(0.9 \cdot d_e, 0.72 \cdot h\right)\right] \qquad d_v = 9.359 \cdot in$$

Net Longitudinal Tensile Strain in the Section at the Centriod of the Tesnion Reinforcement
(Ref. AASHTO Eq. 5.7.3.4.2-4)

$$\varepsilon_s(x) := \max\left[\frac{\left(\frac{\max\left(\left|M_u(x)\right|, \left|V_u(x) - V_p(x)\right| \cdot d_v\right)}{d_v} + 0.5 \cdot N_u(x) + \left|V_u(x) - V_p(x)\right| - A_{ps} \cdot f_{po}\right)}{E_p \cdot A_{ps}}, 0\right]$$

Maximum Aggregat Size

$$a_g := \frac{9}{16} \cdot in \qquad a_g = 0.563 \cdot in$$

Crack Spacing Parameter as Influenced by Aggregate Size
(Ref. AASHTO Eq. 5.7.3.4.2-7)

$$s_{xe} := \min\left[\left(\max\left(12, \frac{d_v}{in} \cdot \frac{1.38}{\frac{a_g}{in} + 0.63}\right)\right), 80\right] \qquad s_{xe} = 12$$

Factor Indicating the Ability of Diagonally Cracked Concrete to Transmit Tension and Shear
(Ref. AASHTO Eq. 5.7.3.4.2-2)

$$\beta(x) := \frac{4.8}{\left(1 + 750 \cdot \varepsilon_s(x)\right)} \cdot \frac{51}{\left(31 + s_{xe}\right)}$$

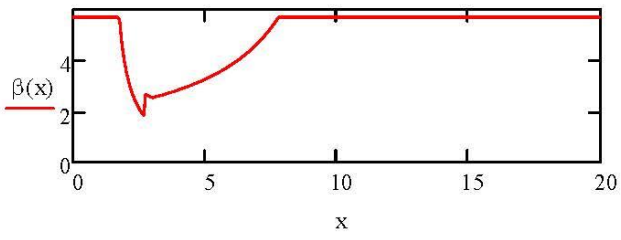

Number of Cores Filled $n_{cf} = 1$

Area of Core Fill $A_{cf} := 58 \cdot in^2$

Factor Indicating the Ability of Diagonally Cracked Concrete to Transmit Tension and Shear
(Ref. AASHTO 5.7.3.4.1) $\beta_{ur} := 2$

Nominal Shear Capacity
(Ref. AASHTO Eq. 5.7.3.3-3)

$$V_n(x) := 0.0316 \cdot \beta(x) \cdot \sqrt{\frac{f_c}{ksi}} \cdot ksi \cdot b_w \cdot d_v + 0.0316 \cdot \beta_{ur} \cdot \sqrt{\frac{f_{cf}}{ksi}} \cdot ksi \cdot \left(n_{cf} \cdot A_{cf}\right)$$

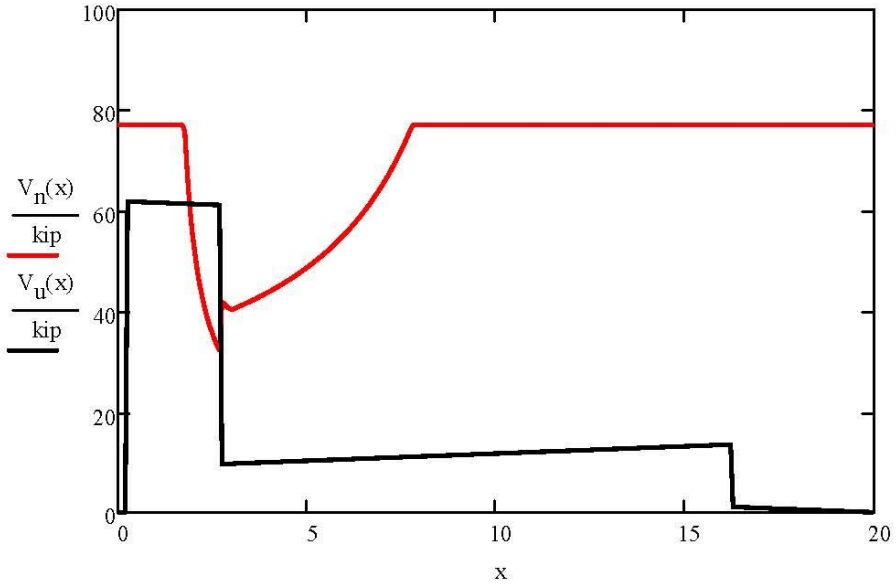

Critical Section for Shear $x_{sh} := L_1 + 0.5 \cdot h$ $x_{sh} = 8.5 \cdot in$

Check Shear at Critical Section $V_u(x_{sh}) = 61.7 \cdot kip$ < $V_n(x_{sh}) = 77.1 \cdot kip$

$$\frac{V_u(x_{sh})}{V_n(x_{sh})} = 0.8$$

$P \equiv 70.703 \cdot kip$ $n_{cf} \equiv 1$

$f_c \equiv 13643 \cdot psi$ $f_{cf} \equiv 9040 \cdot psi$

SHEAR CAPACITY PREDICITON BASED ON PALMER AND SCHULTZ

DESIGN PARAMETERS

Lab Arangement

Total Length of Beam	$L_{tot} := 20 \cdot ft$	
CL Support to Beam End - Testing End	$L_1 := 2.5 \cdot in$	
CL Support to Beam End - Overhang	$L_2 := 3 \cdot ft + 9.5 \cdot in$	$L_2 = 3.792\,ft$
Length of Beam Tested	$L := L_{tot} - L_1 - L_2$	$L = 16\,ft$
Actuator to CL Supports	$L_a := 2 \cdot ft + 6 \cdot in$	

Section Properties

Section Depth	$h := 12 \cdot in$	
Section Width	$b := 48 \cdot in$	
Web Width	$b_w := 10.626 \cdot in$	
Cross-Sectional Area	$A_c := 269.76 \cdot in^2$	
Moment of Inertia	$I_x := 5248 \cdot in^4$	
Neutral Axis to Bottom Extreme Fiber	$y_b := 6.095 \cdot in$	
Neutral Axis to Top Extreme Fiber	$y_t := h - y_b$	$y_t = 5.905 \cdot in$
Section Modulus - Top	$S_t := \frac{I_x}{y_t}$	$S_t = 888.7 \cdot in^3$
Section Modulus - Bottom	$S_b := \frac{I_x}{y_b}$	$S_b = 861 \cdot in^3$

Material Properties

Concrete Unit Weight	$\gamma_c := 154 \cdot pcf$	
Concrete Compressive Strength	$f_c = 13643 \cdot psi$	
Core Fill Compressive Strength	$f_{cf} = 9040\,psi$	
Tensile Strength of Concrete *(Per split cylinder tests)*	$f_{ct} := 9.0 \cdot \sqrt{\frac{f_c}{psi}} \cdot psi$	$f_{ct} = 1051\,psi$
Tensile Strength of Core Fill Concrete *(Per split cylinder tests)*	$f_{cft} := 5.8 \cdot \sqrt{\frac{f_{cf}}{psi}} \cdot psi$	$f_{cft} = 551\,psi$
Concrete Modification Factor	$\lambda := 1$	
Modulus of Elasticity - Concrete *(Ref. ACI 318-14 Eq. 19.2.2.1a)*	$E_c := \left(\frac{\gamma_c}{pcf}\right)^{1.5} \cdot 33 \cdot \sqrt{f_c \cdot psi}$	$E_c = 7366 \cdot ksi$
Modulus of Elasticity - Strand	$E_{ps} := 28500 \cdot ksi$	
Ultimate Strength of Strand	$f_{pu} := 270 \cdot ksi$	
Number of 6/10" Strands	$n_{s0.6} := 6$	
Diameter of 6/10" Strands	$d_{0.6} := 0.6 \cdot in$	
Strand Area - 6/10" Diameter	$A_{ps0.6} := 0.217 \cdot in^2$	
Total Strand Area	$A_{ps} := n_{s0.6} \cdot A_{ps0.6}$	$A_{ps} = 1.302 \cdot in^2$
Strand Eccentricity from Nutral Axis	$e := y_b - 2.125 \cdot in$	$e = 3.97 \cdot in$
Strand Stressing	$ss := 0.70$	
Initial Jacking Stress	$f_{pj} := ss \cdot f_{pu}$	$f_{pj} = 189 \cdot ksi$
Initial Jacking Force	$F_{pj} := f_{pj} \cdot A_{ps}$	$F_{pj} = 246.1 \cdot kip$
Depth of Prestressing	$d_p := e + y_t$	$d_p = 9.875 \cdot in$

LOADING

Middle of Beam - Testing Span $x_m := L_1 + 0.5 \cdot L$ $x_m = 8.208\ ft$

Applied Point Load $P = 70.703 \cdot kip$

Distributed Self-Weight $w_{sw} := \gamma_c \cdot A_c$ $w_{sw} = 288 \cdot plf$

Shear for Applied Load

$$V_{s\_ap}(x) := \begin{cases} 0 \cdot kip & \text{if } x < L_1 \\ \frac{P \cdot (L - L_a)}{L} & \text{if } L_1 \le x \le L_1 + L_a \\ -\frac{P \cdot L_a}{L} & \text{if } L_1 + L_a < x \le L_1 + L \\ 0 \cdot kip & \text{if } L_1 + L < x \le L_{tot} \end{cases}$$

Shear for Self Weight

$$V_{s\_sw}(x) := \begin{cases} 0 \cdot kip & \text{if } x < L_1 \\ \left[\frac{w_{sw}}{2 \cdot L} \cdot \left(L^2 - L_2^{\,2}\right)\right] - w_{sw} \cdot (x - L_1) & \text{if } L_1 \le x \le L_1 + L \\ w_{sw} \cdot \left[L_2 - (x - L_1 - L)\right] & \text{if } x > L_1 + L \end{cases}$$

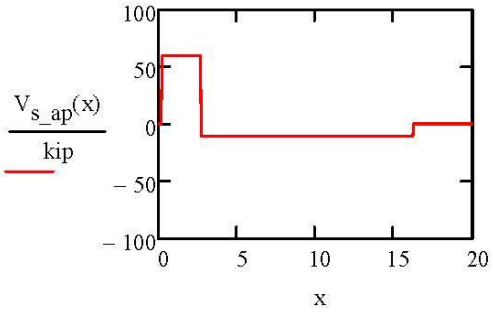

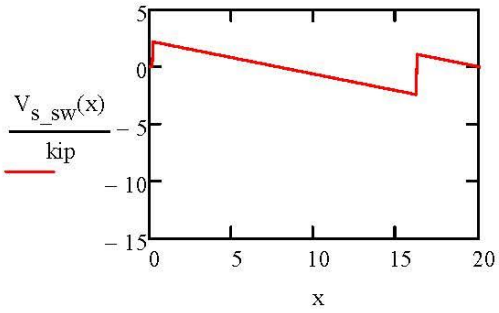

Moment for Self Weight SS Span $M_{ss}(x) := \frac{w_{sw} \cdot x}{2} \cdot (L_{tot} - x)$

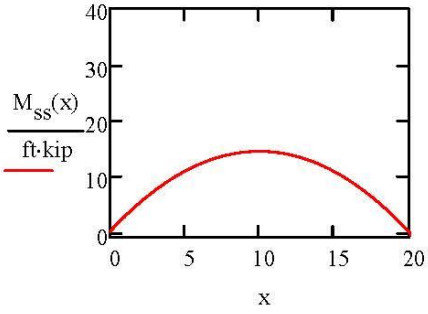

Moment for Appled Load $M_{s\_ap}(x) := \begin{cases} 0 \text{ if } x < L_1 \\ \frac{P\cdot(L - L_a)\cdot(x - L_1)}{L} \text{ if } L_1 \le x \le L_1 + L_a \\ \frac{P\cdot L_a\cdot(L - L_a)}{L}\cdot\left[1 - \frac{x - (L_1 + L_a)}{L - L_a}\right] \text{ if } L_1 + L_a < x \le L_1 + L \\ 0 \text{ if } L_1 + L < x \le L_{tot} \end{cases}$

Moment for Self Weight $M_{s\_sw}(x) := \begin{cases} 0 \text{ if } x < L_1 \\ \frac{w_{sw}\cdot(x - L_1)}{2\cdot L}\cdot\left[L^2 - {L_2}^2 - (x - L_1)\cdot L\right] \text{ if } L_1 \le x \le L_1 + L \\ \frac{-w_{sw}}{2}\cdot\left[L_2 - \left[x - (L_1 + L)\right]\right]^2 \text{ if } x > L_1 + L \end{cases}$

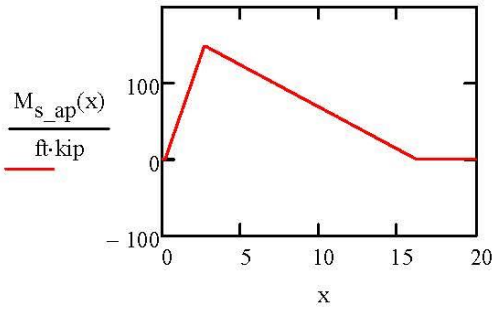

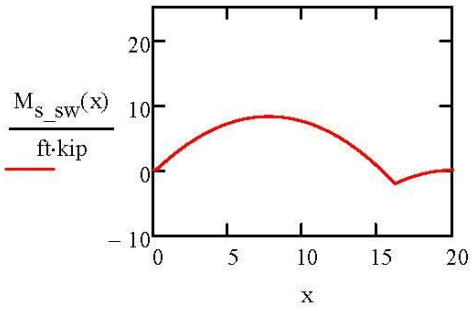

Unfactored Shear Demand $V_u(x) := \left|V_{s\_ap}(x) + V_{s\_sw}(x)\right|$

Unfactored Moment Demand $M_u(x) := \left|M_{s\_ap}(x) + M_{s\_sw}(x)\right|$

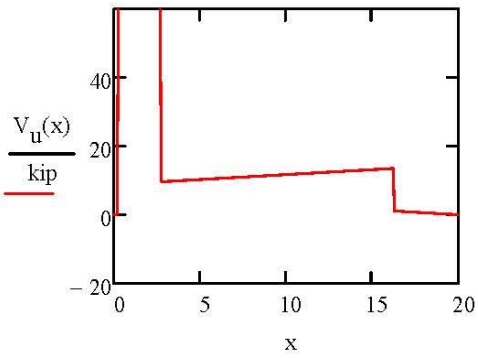

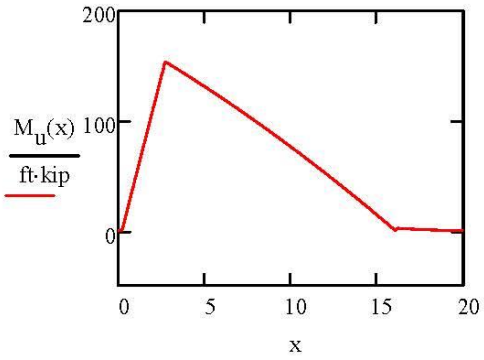

LOSSES

Elastic Shortening - ACI 423.10R-16 4.3

Moment Due to Self-Weight $M_g := \frac{w_{sw}}{8 \cdot L^2} \cdot (L + L_2)^2 \cdot (L - L_2)^2$ $M_g = 8 \cdot ft \cdot kip$

Eccentricity of Strand at 0.4 Point $e_p := e$ $e_p = 4 \cdot in$

Force in Strands Immediately Before Release $P_j := F_{pj}$ $P_j = 246 \cdot kip$

Initial Assumption for Approximation $K_{cir} := 0.9$ *(pretensioned member)*

Concrete Stress at Tendon Level *(Ref ACI 423.10R-16 Eq. 4.3.2b)* $f_{cir} := K_{cir} \cdot \left(\frac{P_j}{A_c} + \frac{P_j \cdot e_p^2}{I_x} \right) - \frac{M_g \cdot e_p}{I_x}$ $f_{cir} = 1411 \cdot psi$

Initial Elastic Shortening Loss Stress $\Delta f_{pES} := f_{cir} \cdot \frac{E_{ps}}{E_c}$ $\Delta f_{pES} = 5.5 \cdot ksi$

Creep - ACI 423.10R-16 5.2

Moment Due to Permanent Superimposed Load $M_{sd} := 0 \cdot ft \cdot kip$ $M_{sd} = 0 \cdot ft \cdot kip$

Concrete Stress due to Superimposed Loads $f_{cds} := \frac{M_{sd} \cdot e_p}{I_x}$ $f_{cds} = 0$

Concrete Weight Factor $K_{cr} := 2.0$

Long-Term Loss - Creep *(Ref ACI 423.10R-16 Eq. 5.2.1a)* $\Delta f_{pCR} := K_{cr} \cdot (f_{cir} - f_{cds}) \cdot \frac{E_{ps}}{E_c}$ $\Delta f_{pCR} = 10.9 \cdot ksi$

Shrinkage - ACI 423.10R-16 5.3

Relative Humidity $RH := 70$

Slab Outer Perimeter $P_o := 9 \cdot ft + 11.125 \cdot in$ $P_o = 119.125 \cdot in$

Core Perimeter $P_c := 2 \cdot ft + 3.5 \cdot in$ $P_c = 27.5 \cdot in$

Volume to Surface Area Ratio $VS := \frac{A_c}{P_o + 5 \cdot P_c}$ $VS = 1.051 \cdot in$

Coefficient for Prestressing $K_{sh} := 1.0$

Long-Term Loss - Shrinkage *(Ref ACI 423.10R-16 Eq. 5.3)*

$$\Delta f_{pSH} := \left(8.2 \cdot 10^{-6}\right) \cdot K_{sh} \cdot E_{ps} \cdot \left(1 - \frac{0.06 \cdot VS}{in}\right) \cdot (100 - RH) \qquad \Delta f_{pSH} = 6.6 \cdot ksi$$

Relaxation - ACI 423.10R-16 5.4

Coefficient for Relaxation, K.re
(Ref ACI 423.10R-16 Tbl. 5.4)

$K_{re} := 5000 \cdot psi$

Coefficient for Relaxation, J
(Ref ACI 423.10R-16 Tbl. 5.4)

$J := 0.040$

Ratio of Jacking to Ultimate Stress

$$ju := \frac{\left(\frac{F_{pj}}{A_{ps}}\right)}{f_{pu}} \qquad ju = 0.7$$

Coefficient for Relaxation, C
(Ref ACI 423.10R-16 Eq. 5.4.2a & 5.4.2b)

$$C := \text{if}\left[ju \geq 0.54, \left(\frac{ju}{0.21}\right) \cdot \left(\frac{ju}{0.9} - 0.55\right), \frac{ju}{4.24}\right] \qquad C = 0.759$$

Long-Term Loss - Relaxation
(Ref ACI 423.10R-16 Eq. 5.4)

$$\Delta f_{pRE} := \left[K_{re} - J \cdot \left(\Delta f_{pSH} + \Delta f_{pCR} + \Delta f_{pES}\right)\right] \cdot C \qquad \Delta f_{pRE} = 3.1 \cdot ksi$$

Totals

Total Initial Losses

$\Delta f_{pI} := \Delta f_{pES}$ $\Delta f_{pI} = 5.5 \cdot ksi$

Initial Stress After Losses

$$f_{pi} := \frac{F_{pj}}{A_{ps}} - \Delta f_{pI} \qquad f_{pi} = 183.5 \cdot ksi$$

Initial Force After Losses

$F_{pi} := A_{ps} \cdot f_{pi}$ $F_{pi} = 239 \cdot kip$

Total Long-Term Losses

$\Delta f_{pLT} := \Delta f_{pCR} + \Delta f_{pSH} + \Delta f_{pRE}$ $\Delta f_{pLT} = 20.6 \cdot ksi$

Effective Stress After Losses

$$f_{se} := \frac{F_{pj}}{A_{ps}} - \Delta f_{pI} - \Delta f_{pLT} \qquad f_{se} = 162.9 \cdot ksi$$

Effective Force After Losses

$F_{se} := A_{ps} \cdot f_{se}$ $F_{se} = 212.2 \cdot kip$

Total Loss Percentage

$$TL := 1 - \frac{F_{se}}{P_j} \qquad TL = 13.8 \cdot \%$$

TRANSFER/DEVELOPMENT LENGTHS

Factor of PS Type
(ACI Tbl. 20.3.2.3.1)

$\gamma_p := 0.28$ *(low-lax PS)*

Equivalent Rectangular Stress Distribution
(ACI Tbl. 22.2.2.4.3)

$$\beta_1 := \begin{cases} 0.85 \text{ if } 2500\cdot psi \le f_c \le 4000\cdot psi \\ 0.85 - \dfrac{0.05\cdot\left(f_c - 4000psi\right)}{1000psi} \text{ if } 4000\cdot psi < f_c < 8000\cdot psi \\ 0.65 \text{ if } f_c \ge 8000\cdot psi \end{cases} \qquad \beta_1 = 0.65$$

Ratio of A.ps to bd.p - Prestressed Steel

$$\rho_p := \frac{A_{ps}}{b\cdot d_p} \qquad \rho_p = 0.003$$

Stress in Prestressing
(Ref. ACI Eq. 20.3.2.3.1)

$$f_{ps} := f_{pu}\cdot\left[1 - \frac{\gamma_p}{\beta_1}\cdot\left(\rho_p\cdot\frac{f_{pu}}{f_c}\right)\right] \qquad f_{ps} = 264\cdot ksi$$

Diameter of 0.6" Strand

$d_b := 0.6\cdot in$

Average Inital Strand Slip

$\delta_{es} = 0.08\cdot in$

Transfer Length
(Palmer and Schultz, 2009)

$$l_t := 5\cdot\delta_{es}\cdot\frac{E_{ps}}{f_{pi}} \qquad l_t = 62.1\cdot in \qquad \frac{l_t}{d_b} = 104$$

Development Length
(Ref. ACI 318-14 Eq. 25.4.8.1)

$$l_d := l_t + \frac{f_{ps} - f_{se}}{1000\cdot psi}\cdot d_b \qquad l_d = 122.5\cdot in \qquad \frac{l_d}{d_b} = 204$$

Transfer and Development Length Function

$$TD(x) := \begin{cases} \frac{x}{l_t}\cdot\frac{f_{se}}{f_{ps}} & \text{if } x \le l_t \\ \frac{x - l_t}{l_d - l_t}\cdot\left(1 - \frac{f_{se}}{f_{ps}}\right) + \frac{f_{se}}{f_{ps}} & \text{if } l_t < x \le l_d \\ 1 & \text{if } l_d < x \le L_{tot} - l_d \\ 1 - \frac{x - (L_{tot} - l_d)}{l_d - l_t}\cdot\left(1 - \frac{f_{se}}{f_{ps}}\right) & \text{if } L_{tot} - l_d < x \le L_{tot} - l_t \\ \left(\frac{f_{se}}{f_{ps}}\right) - \frac{x - (L_{tot} - l_t)}{l_t}\cdot\left(\frac{f_{se}}{f_{ps}}\right) & \text{if } L_{tot} - l_t < x \le L_{tot} \end{cases}$$

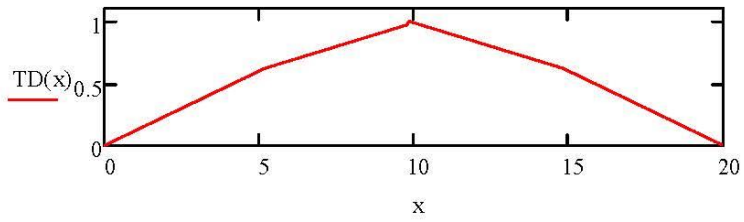

Effective Prestressing Force - Service

$$P_{se}(x) := \begin{cases} x\cdot\frac{F_{se}}{l_t} & \text{if } x \le l_t \\ F_{se} & \text{if } l_t < x < L_{tot} - l_t \\ F_{se} - \frac{F_{se}}{l_t}\left[x - (L_{tot} - l_t)\right] & \text{if } L_{tot} - l_t \le x \end{cases}$$

Effective Prestressing Force - Ultimate

$$P_{ps}(x) := (f_{ps}\cdot A_{ps})\cdot TD(x)$$

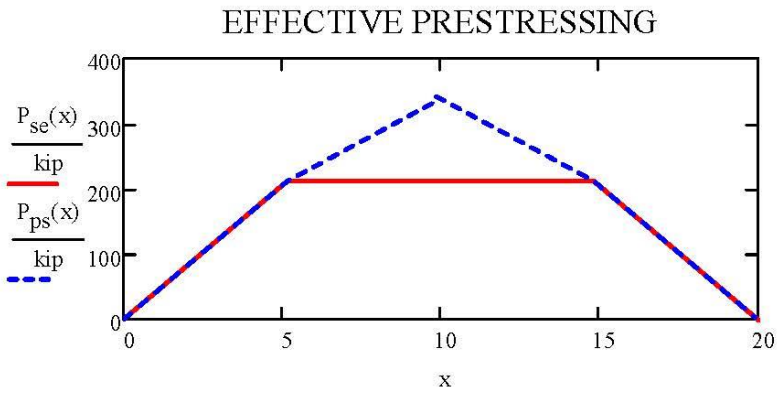

WEB-SHEAR STRENGTH PREDICTION

Strength Reduction Factor Shear $\phi_v := 1$

Depth of Prestress
(Ref. ACI 318-14 22.5.8.3.1) $d_{ps} := \max(0.8 \cdot h, d_p)$ $d_{ps} = 9.875 \cdot in$

Neutral Axis to Tension Face $y_{tension} := y_b$ $y_{tension} = 6.095 \cdot in$

Core Width $b_c := 7.25 \cdot in$

Number of Cores Filled - Prestressed $n_{fc\_ps} = 0$

Number of Cores Filled - Plain $n_{fc\_plain} = 1$

Area of Single Core Fill $A_{cf} := 58 \cdot in^2$ $A_{cf} = 58 \cdot in^2$

Width of Section for Shear - Prestressed $b_{wv} := b_w$ $b_{wv} = 10.6 \cdot in$

Concrete Compressive Stress at Center due to Prestressing Only $f_{pc}(x) := \dfrac{P_{se}(x)}{A_c + n_{fc\_ps} \cdot A_{cf}}$

Vertical Component of Prestressing $V_p := 0 \cdot kip$

Nominal Web-Shear Strength
(Palmer and Schultz, 2009)

$$V_{cw}(x) := \left(0.5 \cdot f_{ct} + 0.255 \cdot f_{pc}(x)\right) \cdot b_w \cdot d_{ps} + \left(0.5 \cdot f_{cft} + 0.255 \cdot f_{pc}(x)\right) \cdot \left(n_{fc\_ps} \cdot A_{cf}\right) + V_p$$

Minimum Concrete Shear Contribution
(Ref. ACI 318-14 Eq. 22.5.5.1) $V_{cmin} := 2 \cdot \lambda \cdot \sqrt{\dfrac{f_c}{psi}} \cdot psi \cdot b_{wv} \cdot d_{ps}$ $V_{cmin} = 24.5 \cdot kip$

Additional Shear Capacity due to Core-Fill Treated as Plain Concrete

$$V_{core} := 2 \cdot \lambda \cdot \sqrt{\frac{f_{cf}}{psi}} \cdot psi \cdot n_{fc\_plain} \cdot A_{cf} \qquad V_{core} = 11 \cdot kip$$

Nominal Shear Strength of Concrete $V_c(x) := \phi_v \cdot \max\left(V_{cw}(x), V_{cmin}\right) + V_{core}$

$P = 70.703 \cdot kip$ $f_c = 13643\,psi$ $\delta_{es} = 0.08 \cdot in$ $n_{fc\_ps} \equiv 0$

$f_{cf} = 9040\,psi$ $n_{fc\_plain} \equiv 1$

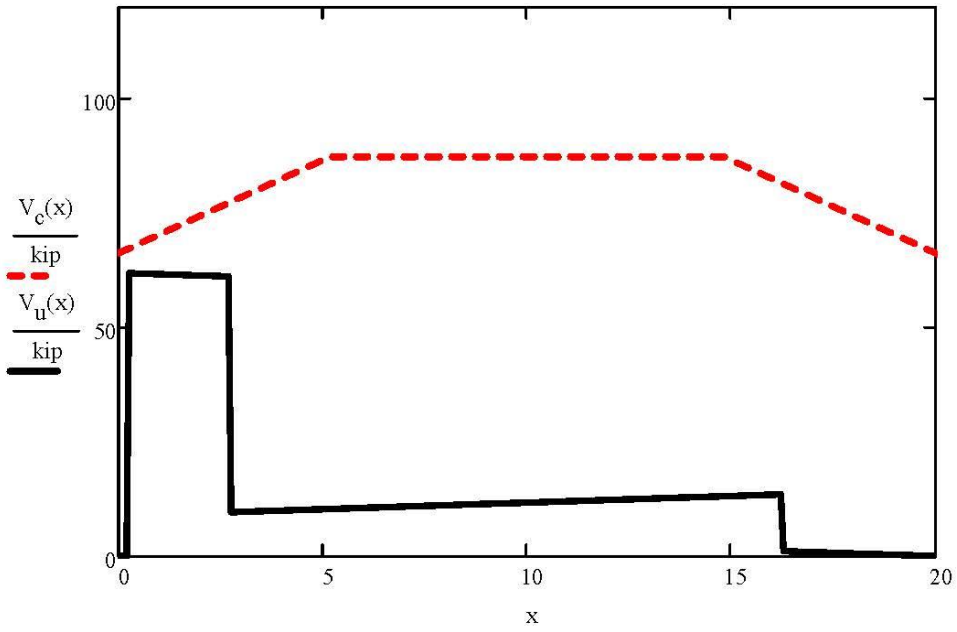

Critical Section for Shear $x_{sh} := L_1 + 0.5 \cdot h$ $x_{sh} = 8.5 \cdot in$

Check Shear at Critical Section $V_u(x_{sh}) = 61.7 \cdot kip$ < $V_c(x_{sh}) = 69.1 \cdot kip$

$$\frac{V_u(x_{sh})}{V_c(x_{sh})} = 0.893$$

YANG'S METHOD

DESIGN PARAMETERS

Lab Arangement

Total Length of Beam	$L_{tot} := 20 \cdot ft$	
CL Support to Beam End - Testing End	$L_1 := 2.5 \cdot in$	
CL Support to Beam End - Overhang	$L_2 := 3 \cdot ft + 9.5 \cdot in$	$L_2 = 3.792\,ft$
Length of Beam Tested	$L := L_{tot} - L_1 - L_2$	$L = 16\,ft$
Actuator to CL Supports	$L_a := 2 \cdot ft + 6 \cdot in$	

Section Properties

Section Depth	$h := 12 \cdot in$	
Section Width at Critical Point	$b := 48 \cdot in$	
Web Width	$b_w := 10.626 \cdot in$	
Core Fill Width	$b_{cf} := 7.25 \cdot in$	
Cross-Sectional Area	$A_c := 269.76 \cdot in^2$	
Area of Core Fill	$A_{cf} := 58 \cdot in^2$	
Area Above Critical Point - Slab	$A_{cp} := 159.29 \cdot in^2$	
Area Above Critical Point - Core Fill	$A_{cfp} := 27.8 \cdot in^2$	
First Area Moment above Critical Point Slab	$Q_{cp} := 872.5 \cdot in^3$	
First Area Moment above Critical Point Core Fill	$Q_{cf} := 275.2 \cdot in^3$	
Moment of Inertia - Slab	$I_y := 5248 \cdot in^4$	
Moment of Inertia - Core Fill	$I_{cf} := 336 \cdot in^4$	
Neutral Axis to Bottom Extreme Fiber	$y_b := 6.095 \cdot in$	
Neutral Axis to Top Extreme Fiber	$y_t := h - y_b$	$y_t = 5.905 \cdot in$
Critical Point to Neutral Axis	$z_{cp} := -1 \cdot (8.2247 \cdot in - y_t)$	$z_{cp} = -2.32 \cdot in$
Critial Point to Bottom	$h_{cp} := y_b + z_{cp}$	$h_{cp} = 3.775 \cdot in$

Angle from Support to Critical Point	$\beta := 35 \cdot deg$	
Horizontal Location of Critical Point *(From CL of Support)*	$x_{cp} := \frac{h_{cp}}{\tan(\beta)}$	$x_{cp} = 5.4 \cdot in$

Material Properties

Concrete Unit Weight	$\gamma_c := 154 \cdot pcf$	
Concrete Compressive Strength	$f_c = 13643\,psi$	
Core Fill Compressive Strength	$f_{cf} = 9040\,psi$	
Tensile Strength of Concrete *(Per split cylinder tests)*	$f_{ct} := 9.0 \cdot \sqrt{\frac{f_c}{psi}} \cdot psi$	$f_{ct} = 1051\,psi$
Tensile Strength of Core Fill Concrete *(Per split cylinder tests)*	$f_{cft} := 5.8 \cdot \sqrt{\frac{f_{cf}}{psi}} \cdot psi$	$f_{cft} = 551\,psi$
Concrete Modification Factor	$\lambda := 1$	
Modulus of Elasticity - Concrete *(Ref. ACI 318-14 Eq. 19.2.2.1a)*	$E_c := \left(\frac{\gamma_c}{pcf}\right)^{1.5} \cdot 33 \cdot \sqrt{f_c \cdot psi}$	$E_c = 7366 \cdot ksi$
Modulus of Elasticity - Strand	$E_{ps} := 28500 \cdot ksi$	
Ultimate Strength of Strand	$f_{pu} := 270 \cdot ksi$	
Number of 6/10" Strands	$n_{s0.6} := 6$	
Diameter of 6/10" Strands	$d_{0.6} := 0.6 \cdot in$	
Strand Area - 6/10" Diameter	$A_{ps0.6} := 0.217 \cdot in^2$	
Total Strand Area	$A_{ps} := n_{s0.6} \cdot A_{ps0.6}$	$A_{ps} = 1.302 \cdot in^2$
Strand Eccentricity from Nutral Axis	$e := y_b - 2.125 \cdot in$	$e = 3.97 \cdot in$
Strand Stressing	$ss := 0.70$	
Initial Jacking Stress	$f_{pj} := ss \cdot f_{pu}$	$f_{pj} = 189 \cdot ksi$
Initial Jacking Force	$F_{pj} := f_{pj} \cdot A_{ps}$	$F_{pj} = 246.1 \cdot kip$
Depth of Prestressing	$d_p := e + y_t$	$d_p = 9.875 \cdot in$

LOADING

Middle of Beam - Testing Span $x_m := L_1 + 0.5 \cdot L$ $x_m = 8.208\ ft$

Applied Point Load $P = 70703\ lbf$

Distributed Self-Weight $w_{sw} := \gamma_c \cdot A_c$ $w_{sw} = 288 \cdot plf$

Shear for Applied Load

$$V_{s\_ap}(x) := \begin{cases} 0 \cdot kip & \text{if } x < L_1 \\ \frac{P \cdot (L - L_a)}{L} & \text{if } L_1 \le x \le L_1 + L_a \\ -\frac{P \cdot L_a}{L} & \text{if } L_1 + L_a < x \le L_1 + L \\ 0 \cdot kip & \text{if } L_1 + L < x \le L_{tot} \end{cases}$$

Shear for Self Weight

$$V_{s\_sw}(x) := \begin{cases} 0 \cdot kip & \text{if } x < L_1 \\ \left[\frac{w_{sw}}{2 \cdot L} \cdot \left(L^2 - L_2^{\,2}\right)\right] - w_{sw} \cdot (x - L_1) & \text{if } L_1 \le x \le L_1 + L \\ w_{sw} \cdot \left[L_2 - (x - L_1 - L)\right] & \text{if } x > L_1 + L \end{cases}$$

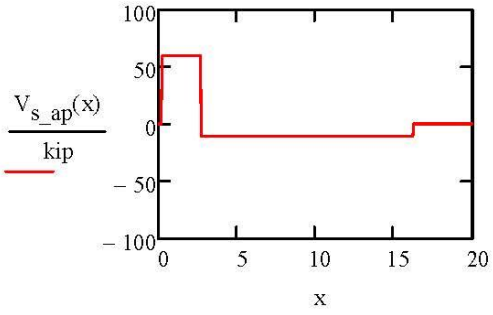

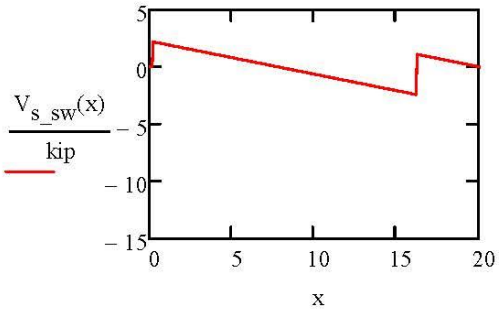

Moment for Self Weight SS Span

$$M_{ss}(x) := \frac{w_{sw} \cdot x}{2} \cdot (L_{tot} - x)$$

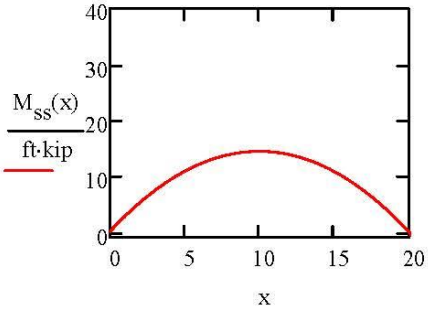

Moment for Appled Load $M_{s\_ap}(x) := \begin{cases} 0 \text{ if } x < L_1 \\ \frac{P\cdot(L - L_a)\cdot(x - L_1)}{L} \text{ if } L_1 \le x \le L_1 + L_a \\ \frac{P\cdot L_a\cdot(L - L_a)}{L}\cdot\left[1 - \frac{x - (L_1 + L_a)}{L - L_a}\right] \text{ if } L_1 + L_a < x \le L_1 + L \\ 0 \text{ if } L_1 + L < x \le L_{tot} \end{cases}$

Moment for Self Weight $M_{s\_sw}(x) := \begin{cases} 0 \text{ if } x < L_1 \\ \frac{w_{sw}\cdot(x - L_1)}{2\cdot L}\cdot\left[L^2 - {L_2}^2 - (x - L_1)\cdot L\right] \text{ if } L_1 \le x \le L_1 + L \\ \frac{-w_{sw}}{2}\cdot\left[L_2 - \left[x - (L_1 + L)\right]\right]^2 \text{ if } x > L_1 + L \end{cases}$

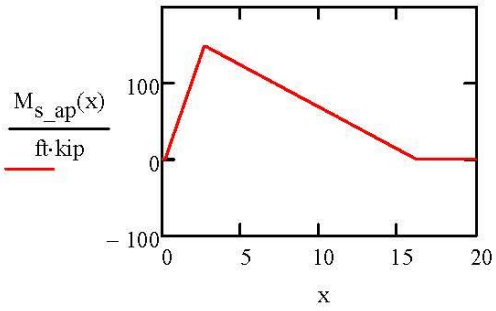

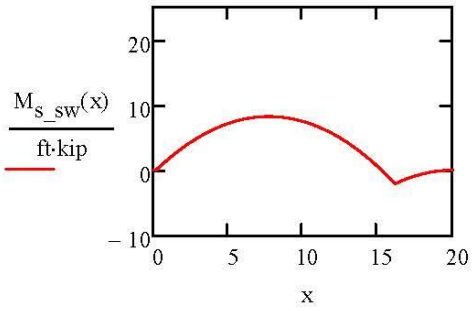

Unfactored Shear Demand $V_u(x) := \left|V_{s\_ap}(x) + V_{s\_sw}(x)\right|$

Unfactored Moment Demand $M_u(x) := \left|M_{s\_ap}(x) + M_{s\_sw}(x)\right|$

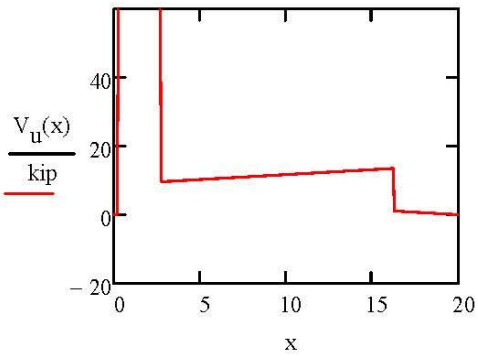

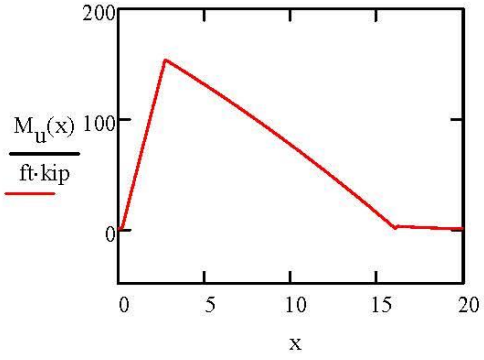

LOSSES

Elastic Shortening - ACI 423.10R-16 4.3

Moment Due to Self-Weight $M_g := \frac{w_{sw}}{8 \cdot L^2} \cdot (L + L_2)^2 \cdot (L - L_2)^2$ $M_g = 8 \cdot ft \cdot kip$

Eccentricity of Strand at 0.4 Point $e_p := e$ $e_p = 4 \cdot in$

Force in Strands Immediately Before Release $P_j := F_{pj}$ $P_j = 246 \cdot kip$

Initial Assumption for Approximation $K_{cir} := 0.9$ *(pretensioned member)*

Concrete Stress at Tendon Level *(Ref ACI 423.10R-16 Eq. 4.3.2b)* $f_{cir} := K_{cir} \cdot \left(\frac{P_j}{A_c} + \frac{P_j \cdot e_p^2}{I_y} \right) - \frac{M_g \cdot e_p}{I_y}$ $f_{cir} = 1411 \cdot psi$

Initial Elastic Shortening Loss Stress $\Delta f_{pES} := f_{cir} \cdot \frac{E_{ps}}{E_c}$ $\Delta f_{pES} = 5.5 \cdot ksi$

Creep - ACI 423.10R-16 5.2

Moment Due to Permanent Superimposed Load $M_{sd} := 0 \cdot ft \cdot kip$ $M_{sd} = 0 \cdot ft \cdot kip$

Concrete Stress due to Superimposed Loads $f_{cds} := \frac{M_{sd} \cdot e_p}{I_y}$ $f_{cds} = 0$

Concrete Weight Factor $K_{cr} := 2.0$

Long-Term Loss - Creep *(Ref ACI 423.10R-16 Eq. 5.2.1a)* $\Delta f_{pCR} := K_{cr} \cdot (f_{cir} - f_{cds}) \cdot \frac{E_{ps}}{E_c}$ $\Delta f_{pCR} = 10.9 \cdot ksi$

Shrinkage - ACI 423.10R-16 5.3

Relative Humidity $RH := 70$

Slab Outer Perimeter $P_o := 9 \cdot ft + 11.125 \cdot in$ $P_o = 119.125 \cdot in$

Core Perimeter $P_c := 2 \cdot ft + 3.5 \cdot in$ $P_c = 27.5 \cdot in$

Volume to Surface Area Ratio $VS := \frac{A_c}{P_o + 5 \cdot P_c}$ $VS = 1.051 \cdot in$

Coefficient for Prestressing $K_{sh} := 1.0$

Long-Term Loss - Shrinkage *(Ref ACI 423.10R-16 Eq. 5.3)*

$$\Delta f_{pSH} := \left(8.2 \cdot 10^{-6}\right) \cdot K_{sh} \cdot E_{ps} \cdot \left(1 - \frac{0.06 \cdot VS}{in}\right) \cdot (100 - RH) \qquad \Delta f_{pSH} = 6.6 \cdot ksi$$

Relaxation - ACI 423.10R-16 5.4

Coefficient for Relaxation, K.re
(Ref ACI 423.10R-16 Tbl. 5.4)

$K_{re} := 5000 \cdot psi$

Coefficient for Relaxation, J
(Ref ACI 423.10R-16 Tbl. 5.4)

$J := 0.040$

Ratio of Jacking to Ultimate Stress

$$ju := \frac{\left(\frac{F_{pj}}{A_{ps}}\right)}{f_{pu}} \qquad ju = 0.7$$

Coefficient for Relaxation, C
(Ref ACI 423.10R-16 Eq. 5.4.2a & 5.4.2b)

$$C := \text{if}\left[ju \geq 0.54, \left(\frac{ju}{0.21}\right) \cdot \left(\frac{ju}{0.9} - 0.55\right), \frac{ju}{4.24}\right] \qquad C = 0.759$$

Long-Term Loss - Relaxation
(Ref ACI 423.10R-16 Eq. 5.4)

$$\Delta f_{pRE} := \left[K_{re} - J \cdot \left(\Delta f_{pSH} + \Delta f_{pCR} + \Delta f_{pES}\right)\right] \cdot C \qquad \Delta f_{pRE} = 3.1 \cdot ksi$$

Totals

Total Initial Losses

$\Delta f_{pI} := \Delta f_{pES}$ $\Delta f_{pI} = 5.5 \cdot ksi$

Initial Stress After Losses

$$f_{pi} := \frac{F_{pj}}{A_{ps}} - \Delta f_{pI} \qquad f_{pi} = 183.5 \cdot ksi$$

Initial Force After Losses

$F_{pi} := A_{ps} \cdot f_{pi}$ $F_{pi} = 239 \cdot kip$

Total Long-Term Losses

$\Delta f_{pLT} := \Delta f_{pCR} + \Delta f_{pSH} + \Delta f_{pRE}$ $\Delta f_{pLT} = 20.6 \cdot ksi$

Effective Stress After Losses

$$f_{se} := \frac{F_{pj}}{A_{ps}} - \Delta f_{pI} - \Delta f_{pLT} \qquad f_{se} = 162.9 \cdot ksi$$

Effective Force After Losses

$F_{se} := A_{ps} \cdot f_{se}$ $F_{se} = 212.2 \cdot kip$

Total Loss Percentage

$$TL := 1 - \frac{F_{se}}{P_j} \qquad TL = 13.8 \cdot \%$$

TRANSFER/DEVELOPMENT LENGTHS

Factor of PS Type
(ACI Tbl. 20.3.2.3.1)

$\gamma_p := 0.28$ *(low-lax PS)*

Equivalent Rectangular Stress Distribution
(ACI Tbl. 22.2.2.4.3)

$$\beta_1 := \begin{cases} 0.85 & \text{if } 2500\cdot psi \le f_c \le 4000\cdot psi \\ 0.85 - \dfrac{0.05\cdot\left(f_c - 4000psi\right)}{1000psi} & \text{if } 4000\cdot psi < f_c < 8000\cdot psi \\ 0.65 & \text{if } f_c \ge 8000\cdot psi \end{cases} \qquad \beta_1 = 0.65$$

Ratio of A.ps to bd.p - Prestressed Steel

$$\rho_p := \frac{A_{ps}}{b\cdot d_p} \qquad \rho_p = 0.003$$

Stress in Prestressing
(Ref. ACI Eq. 20.3.2.3.1)

$$f_{ps} := f_{pu}\cdot\left[1 - \frac{\gamma_p}{\beta_1}\cdot\left(\rho_p\cdot\frac{f_{pu}}{f_c}\right)\right] \qquad f_{ps} = 264\cdot ksi$$

Diameter of 0.6" Strand

$d_b := 0.6\cdot in$

Transfer Length
(Palmer and Schultz, 2009)

$$l_t := \frac{A_{ps0.6}}{\frac{4}{3}\cdot\pi\cdot d_b}\cdot\frac{f_{se}}{400\cdot psi} \qquad l_t = 35.2\cdot in \qquad \frac{l_t}{d_b} = 59$$

Development Length
(Ref. ACI 318-14 Eq. 25.4.8.1)

$$l_d := l_t + \frac{f_{ps} - f_{se}}{1000\cdot psi}\cdot d_b \qquad l_d = 95.6\cdot in \qquad \frac{l_d}{d_b} = 159$$

Transfer and Development Length Function

$$TD(x) := \begin{cases} \frac{x}{l_t}\cdot\frac{f_{se}}{f_{ps}} & \text{if } x \le l_t \\ \frac{x - l_t}{l_d - l_t}\cdot\left(1 - \frac{f_{se}}{f_{ps}}\right) + \frac{f_{se}}{f_{ps}} & \text{if } l_t < x \le l_d \\ 1 & \text{if } l_d < x \le L_{tot} - l_d \\ 1 - \frac{x - (L_{tot} - l_d)}{l_d - l_t}\cdot\left(1 - \frac{f_{se}}{f_{ps}}\right) & \text{if } L_{tot} - l_d < x \le L_{tot} - l_t \\ \left(\frac{f_{se}}{f_{ps}}\right) - \frac{x - (L_{tot} - l_t)}{l_t}\cdot\left(\frac{f_{se}}{f_{ps}}\right) & \text{if } L_{tot} - l_t < x \le L_{tot} \end{cases}$$

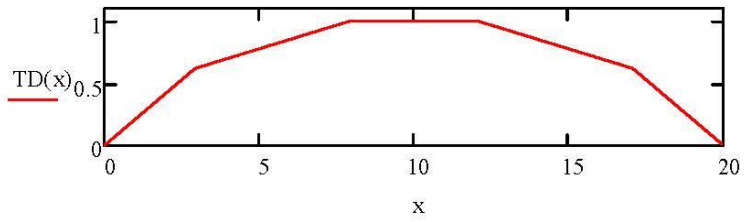

Effective Prestressing Force - Service

$$P_{se}(x) := \begin{cases} x\cdot\frac{F_{se}}{l_t} & \text{if } x \le l_t \\ F_{se} & \text{if } l_t < x < L_{tot} - l_t \\ F_{se} - \frac{F_{se}}{l_t}\left[x - (L_{tot} - l_t)\right] & \text{if } L_{tot} - l_t \le x \end{cases}$$

Effective Prestressing Force - Ultimate

$$P_{ps}(x) := (f_{ps}\cdot A_{ps})\cdot TD(x)$$

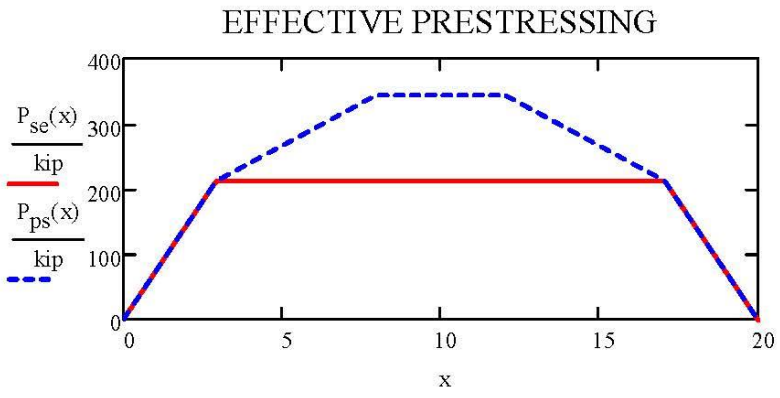

WEB-SHEAR STRENGTH PREDICTION

Minimum Concrete Shear Contribution
(Ref. ACI 318-14 Eq. 22.5.5.1)

$$V_{cf\_ur} := 2\cdot\sqrt{\frac{f_{cf}}{psi}}\cdot psi\cdot A_{cf} \qquad V_{cf\_ur} = 11\cdot kip$$

Effective Prestress Force Function

$$N_p(x) := P_{se}(x)$$

Gradient of Prestressing

$$dN_p := \frac{N_p\left[\left(x_{cp} + L_1\right) + 1\cdot in\right] - N_p\left[\left(x_{cp} + L_1\right) - 1\cdot in\right]}{2\cdot in} \qquad dN_p = 6.03\cdot\frac{kip}{in}$$

Shear Capacity at Critical Point
(Ref. Yang, 1994)

$$V_{max} := \frac{b_w\cdot I_y}{Q_{cp}}\cdot\left[\left[\frac{b_w}{2\cdot Q_{cp}}\cdot f_{ct}\cdot x_{cp}\cdot z_{cp} + \frac{Q_{cp}}{b_w}\cdot\left(\frac{e}{I_y} - \frac{A_{cp}}{A_c\cdot Q_{cp}}\right)\cdot\left(dN_p\right)\right]\ldots + \left[\left(\frac{b_w}{2\cdot Q_{cp}}\cdot f_{ct}\cdot x_{cp}\cdot z_{cp}\right)^2 + \left(\frac{e}{I_y} - \frac{A_{cp}}{A_c\cdot Q_{cp}}\right)\cdot f_{ct}\cdot x_{cp}\cdot z_{cp}\cdot\left(dN_p\right)\ldots + \left(\frac{1}{A_c} - \frac{z_{cp}\cdot e}{I_y}\right)\cdot N_p\left(x_{cp} + L_1\right)\cdot f_{ct} + f_{ct}^{\,2}\right]^{0.5}\right]\ldots + n_{cf\_ps}\cdot\left[\frac{b_{cf}\cdot I_{cf}}{Q_{cf}}\cdot\left[\left[\frac{b_{cf}}{2\cdot Q_{cf}}\cdot f_{cft}\cdot x_{cp}\cdot z_{cp} + \frac{Q_{cf}}{b_{cf}}\cdot\left(\frac{e}{I_{cf}} - \frac{A_{cfp}}{A_{cf}\cdot Q_{cf}}\right)\cdot\left(dN_p\right)\right]\ldots + \left[\left(\frac{b_{cf}}{2\cdot Q_{cf}}\cdot f_{cft}\cdot x_{cp}\cdot z_{cp}\right)^2 + \left(\frac{e}{I_{cf}} - \frac{A_{cfp}}{A_{cf}\cdot Q_{cf}}\right)\cdot f_{cft}\cdot x_{cp}\cdot z_{cp}\cdot\left(dN_p\right)\ldots + \left(\frac{1}{A_{cf}} - \frac{z_{cp}\cdot e}{I_{cf}}\right)\cdot N_p\left(x_{cp} + L_1\right)\cdot f_{cft} + f_{cft}^{\,2}\right]^{0.5}\right]\right] + n_{cf\_ur}\cdot V_{cf\_ur}$$

Shear at Critcal Point

$$V_u\left(x_{cp} + L_1\right) = 61.7\cdot kip \qquad V_{max} = 83.5\cdot kip$$

$$\frac{V_u\left(x_{cp} + L_1\right)}{V_{max}} = 0.739$$

$f_c \equiv 13643\cdot psi$ $f_{cf} \equiv 9040\cdot psi$ $P \equiv 70.703\cdot kip$ $n_{cf\_ur} \equiv 1$ $n_{cf\_ps} \equiv 0$

Appendix D: Mohr's Circle Crack Angle Sample Calculation

All calculations presented in this appendix were generated using Mathcad (2015).

CRACK ANGLE CALCULATION BY MOHR'S CIRCLE

DESIGN PARAMETERS

Lab Arangement		
Total Length of Beam	$L_{tot} := 20 \cdot ft$	
CL Support to Beam End - Testing End	$L_1 := 2.5 \cdot in$	
CL Support to Beam End - Overhang	$L_2 := 3 \cdot ft + 9.5 \cdot in$	$L_2 = 3.792\,ft$
Length of Beam Tested	$L := L_{tot} - L_1 - L_2$	$L = 16\,ft$
Actuator to CL Supports	$L_a := 2 \cdot ft + 6 \cdot in$	
Section Properties		
Section Depth	$h := 12 \cdot in$	
Section Width	$b := 48 \cdot in$	
Web Width	$b_w := 10.626 \cdot in$	
Cross-Sectional Area	$A_c := 269.76 \cdot in^2$	
Neutral Axis to Bottom Extreme Fiber	$y_b := 6.095 \cdot in$	
Neutral Axis to Top Extreme Fiber	$y_t := h - y_b$	$y_t = 5.905 \cdot in$
Material Properties		
Modulus of Elasticity - Strand	$E_{ps} := 28500 \cdot ksi$	
Strand Eccentricity from Neutral Axis	$e := y_b - 2.125 \cdot in$	$e = 3.97 \cdot in$
Depth of Prestressing	$d_p := e + y_t$	$d_p = 9.875 \cdot in$
Diameter of 0.6" Strand	$d_b := 0.6 \cdot in$	

LOADING

Concrete Unit Weight $\gamma_c := 154 \cdot pcf$

Distributed Self-Weight $w_{sw} := \gamma_c \cdot A_c$ $w_{sw} = 288 \cdot plf$

Applied Point Load $P = 71.765 \cdot kip$

Shear for Applied Load

$$V_{s\_ap}(x) := \begin{cases} 0 \cdot kip & \text{if } x < L_1 \\ \dfrac{P \cdot (L - L_a)}{L} & \text{if } L_1 \le x \le L_1 + L_a \\ -\dfrac{P \cdot L_a}{L} & \text{if } L_1 + L_a < x \le L_1 + L \\ 0 \cdot kip & \text{if } L_1 + L < x \le L_{tot} \end{cases}$$

Shear for Self Weight

$$V_{s\_sw}(x) := \begin{cases} 0 \cdot kip & \text{if } x < L_1 \\ \left[\dfrac{w_{sw}}{2 \cdot L} \cdot \left(L^2 - L_2^{\,2}\right)\right] - w_{sw} \cdot (x - L_1) & \text{if } L_1 \le x \le L_1 + L \\ w_{sw} \cdot \left[L_2 - (x - L_1 - L)\right] & \text{if } x > L_1 + L \end{cases}$$

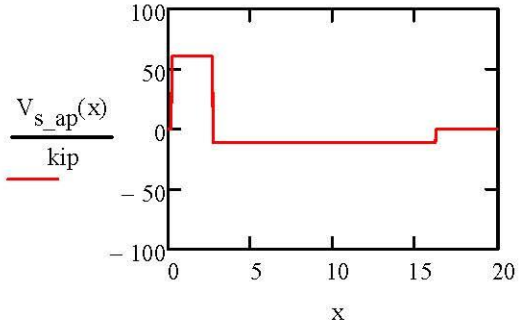

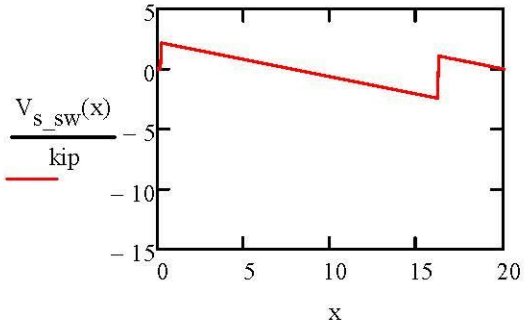

Unfactored Shear Demand $V_u(x) := \left|V_{s\_ap}(x) + V_{s\_sw}(x)\right|$

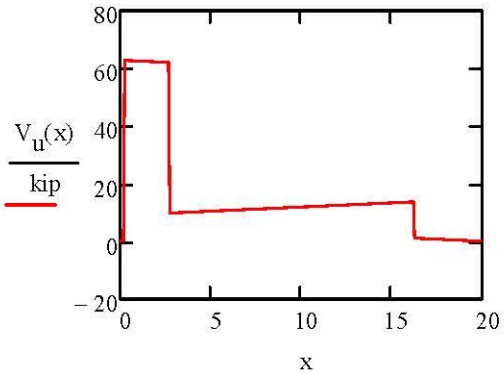

LOSSES AND TRANSFER LENGTH

Initial Stress After Losses
(Per ACI 423.10R-16)

$f_{pi} := 183.5 \cdot ksi$

Effective Stress After Losses

$f_{se} := 162.7 \cdot ksi$

Effective Force After Losses
(Per ACI 423.10R-16)

$p_{se} := 211.9 \cdot kip$

Stress in Prestressing
(Per ACI Eq. 20.3.2.3.1)

$f_{ps} := 264 \cdot ksi$

Inital Strand Slip

$\delta_{es} = 0.08 \cdot in$

Transfer Length
(Palmer and Schultz, 2009)

$l_t := 5 \cdot \delta_{es} \cdot \frac{E_{ps}}{f_{pi}}$ $\quad l_t = 62.1 \cdot in$ $\quad \frac{l_t}{d_b} = 104$

Development Length
(Ref. ACI 318-14 Eq. 25.4.8.1)

$l_d := l_t + \frac{f_{ps} - f_{se}}{1000 \cdot psi} \cdot d_b$ $\quad l_d = 122.9 \cdot in$ $\quad \frac{l_d}{d_b} = 205$

Effective Prestressing Force - Transfer

$$P_{se}(x) := \begin{cases} x \cdot \frac{p_{se}}{l_t} & \text{if } x \le l_t \\ p_{se} & \text{if } l_t < x < L_{tot} - l_t \\ p_{se} - \frac{p_{se}}{l_t}\left[x - \left(L_{tot} - l_t\right)\right] & \text{if } L_{tot} - l_t \le x \end{cases}$$

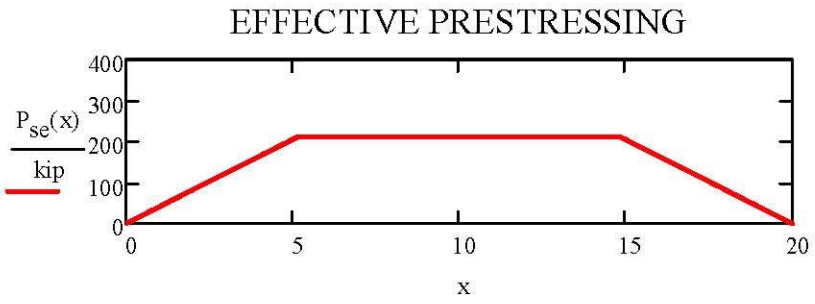

CRACK ANGLE PREDICTION

Evaluation Point $x_{cr} := L_1 + 0.5 \cdot h$ $x_{cr} = 8.5 \cdot in$

Shear Stress $\sigma_{xy}(x) := -\frac{V_u(x) \cdot Q}{I \cdot b_w}$

Axial Stress $\sigma_x(x) := -\frac{P_{se}(x)}{A_c}$

Angle of Rotation $\theta(x) := \frac{1}{2} \cdot \operatorname{atan}\left(\frac{2 \cdot \sigma_{xy}(x)}{\sigma_x(x)}\right)$ $\theta(x_{cr}) = 42.1 \cdot deg$

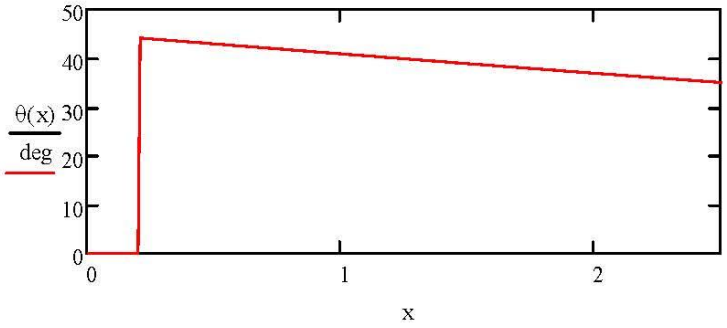

Appendix E: Web-Shear Failure Mechanics

Web-shear failure generally controls near the ends of highly prestressed concrete members. Members with narrow webs are more susceptible to web-shear failure because the applied shear force is distributed over a smaller area. Specifically, the shear stress realized in a section can be defined by Equation E.1.

$$\tau = \frac{VQ}{Ib_w} \tag{E.1}$$

At a differential point located along the centroidal axis of a member, as shown in Figure E.1, both shear, τ, and axial stresses, f_{pc}, are present, as shown in Figure E.2. Using Mohr's circle for this point, as shown in Figure E.3, the original differential point can be rotated by θ and the axial and shear stresses can be transformed into the principal stresses, f_2 and f_t, as shown in Figure E.4. Based on Mohr's circle, the angle of rotation to align the differential element along its principal axis, θ, is defined by Equation E.2. This angle also represents the angle at which initial web-shear cracking will occur. The center and radius of Mohr's circle can be calculated by Equations E.3 and E.4.

$$\theta = \frac{1}{2} tan^{-1}\left(\frac{2\tau}{f_{pc}}\right) \tag{E.2}$$

$$C = \frac{f_{pc} + 0}{2} \tag{E.3}$$

$$R = \sqrt{\frac{1}{4} {f_{pc}}^2 + \tau^2} \tag{E.4}$$

Additionally, the maximum tensile stress can be determined by subtracting E.3 from E.4 as shown in Equation E.5.

$$f_t = \sqrt{\frac{1}{4}{f_{pc}}^2 + \tau^2} - \frac{f_{pc}}{2} \quad \text{E.5}$$

Solving Equation E.5 for τ is shown in Equation E.6. By multiplying the predicted maximum shear stress capacity from Equation E.6 by the appropriate area for shear, the shear capacity of a member based on Mohr's circle can be determined, as shown in Equation E.7.

$$\tau = f_t \sqrt{1 + \frac{f_{pc}}{f_t}} \quad \text{E.6}$$

$$V = \left(f_t \sqrt{1 + \frac{f_{pc}}{f_t}} \right) b d_v \quad \text{E.7}$$

Oftentimes, the concrete tensile strength is not available, so Equation 2.2 is recommended in the commentary for ACI 318 (2014) Section 19.2.4 to relate the concrete tensile strength to the compressive strength. With this simplification, Equation E.6 reduces to Equation E.8.

$$\tau = 6.7\sqrt{f_c} \sqrt{1 + \frac{f_{pc}}{6.7\sqrt{f_c}}} \quad \text{E.8}$$

Since the ACI 318 (2014) equation for web-shear, Equation 2.6, assumes the shear stress, τ, as the nominal shear stress, not the maximum shear stress, a coefficient of 3.5 is used instead of 6.7, as shown in Equation E.9.

$$\tau = 3.5\sqrt{f_c} \sqrt{1 + \frac{f_{pc}}{3.5\sqrt{f_c}}} \quad \text{E.9}$$

Equation E.9 is well approximated by Equation E.10, which coincides with the stress in the ACI 318 (2014) web-shear equation, shown in Equation 2.2.

$$\tau = 3.5\sqrt{f_c} + 0.3 f_{pc} \qquad \text{E.10}$$

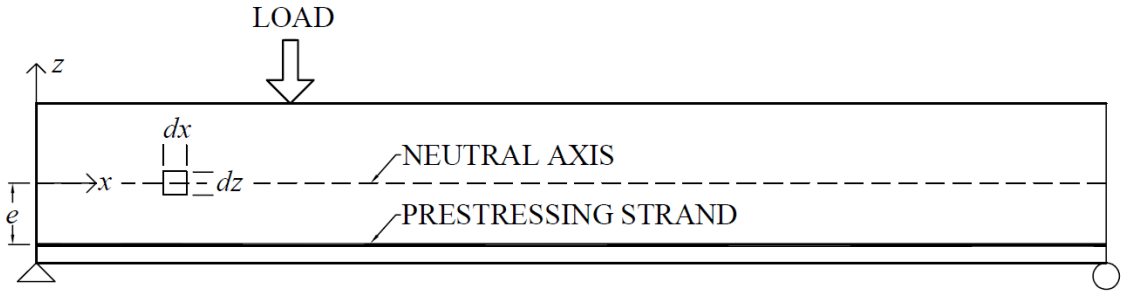

Figure E.1. Differential point located at the neutral axis of a member with a point load near the support

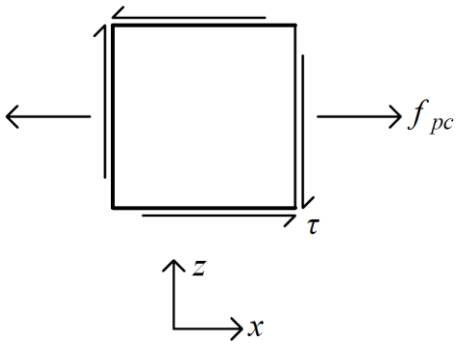

Figure E.2. Enlarged differential point with shear stress and axial stress along the x-axis

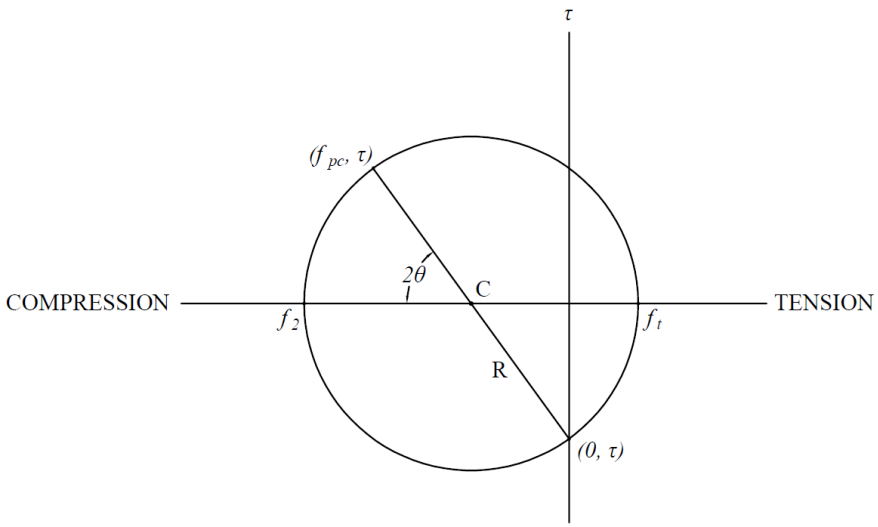

Figure E.3. Depiction of Mohr's circle for a differential point located along the neutral axis of a member under web-shear loading

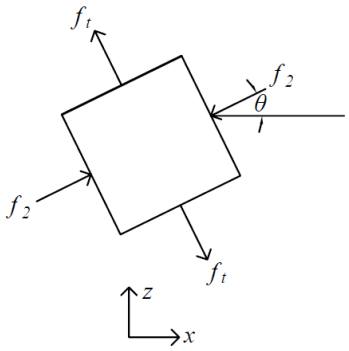

Figure E.4. Resultant principal stresses of a differential point rotated by θ located along the neutral axis of a member under web-shear loading

Appendix F: Actuator Operation

This appendix describes how the hydraulic system and actuator at the UMD structural laboratory were operated for the testing in this project. While this appendix provides a step-by-step guide for the actuator operation, proper comprehensive training should be obtained prior to operating the system. The following steps describe how to initiate the system, collect data, perform displacement-controlled loading, and shut down the system.

1. To start the system, press the power button on the auxiliary power pack and then press the power button on the computer, as shown in Figure F.1.
2. Once the computer has started, a password will be requested. The password is "hello."
3. Open the Shore Western startup application, as shown in Figure F.2.
4. Check the cooling unit housed outside of the lab and remove any snow blocking the cooling fans on top, as shown in Figure F.3.
5. The DEFAULT program of the Hydraulic Control panel will be shown upon startup of the software. Before the hydraulic system can be started, the emergency stop must be reset. First, press the "RESET" button in the program, as shown in Figure F.4. Next press the reset button on the emergency stop box. Notice the blue light surrounding the button switches from blue to blue and green, as shown in Figure F.5. Finally, clear the emergency stop warning at the top of the software window by pressing the yellow "E-STOP" button, as shown in Figure F.4. Once the hydraulic system is ready to be started, the window will look like Figure F.6.
6. Under the HPS CONTROL there are three settings: OFF, LOW, and HIGH. Select "LOW". Wait for two yellow lights to illuminate on the pump, as shown in Figure F.7. Following, select "HIGH" and wait for two green lights to illuminate on the pump, as shown in Figure F.8.
7. Next the actuator must be set to displacement control mode. Select "Portal Frame" under the panel drop down list. Select "Main Panel" under the program drop down list. These lists are identified in Figure F.9.

8. In the Portal Frame panel under the Main Panel program, the emergency stop indicator will be illuminated in yellow at the top of the window. Click the button to reset it. It will read “CLEAR” with green illumination.
9. Notice there are several buttons in the upper left corner of the window with a cross and quadrant highlighted in green. By selecting these buttons, a quadrant of the window will be made full screen. Use these buttons to enlarge the upper left quadrant titled “ACTUATOR 1.”
10. Select the DSP button, as shown in Figure F.10. Note, you will hear the actuator make a brief noise and the light next to the button will illuminate green.
11. Return to the Hydraulic Control panel and DEFULT program. Under HSM 1, select “LOW.” A message stating “AUTOBALANCE SUCCESSFUL” will appear three times, as shown in Figure F.11. Select “CONTINUE” each time. Following, select the “HIGH” button under HSM 1.
12. At this point, the actuator is ready for operation. Navigate to the Portal Frame panel, select the “Static Proof Test – McDermott” program, and enlarge the upper left quadrant.
13. As a safety precaution during test setup the actuator should be limited to a very small load. To do so, select the limits button on the right side of the window. A dialogue box will appear. Select the “LOAD CELL” from the list. On the right, enable the Soft Stop checkbox and enter a limit of +/- 2 kips, as shown in Figure F.12. Note, this limit will need to be reset to the appropriate limit prior to the initiation of testing.
14. Several settings must be checked and adjusted prior to loading. First, open the “Setup Test” button located near the top center of the window. Within the dialogue box that appears, the “Fracture Detection,” Auto Pause 1,” Auto Pause 2,” and “Secondary Endpoint Channel” options should not be enabled. Enable the “Fraction Detection” option, as shown in Figure F.13. Use the following settings under the Fraction Detection option:
    - Channel: LOAD CELL
    - Percent Drop: 90%

- Threshold: 110 kip

15. Select the “Setup Panel” button next to the “Setup Test” button. Ensure the appropriate channels are selected, as shown in Figure F.14. Use the following settings under the “Control Channel” options:
    - Command Channel: Actuator 1
    - Displacement Feedback Channel: LVDT
    - Load Feedback Channel: LOAD CELL
    - Select the “Displacement Control” radio button.
16. Select the “Setup Logger” button on the right. Set the desired destination directory. Enter a file name (make sure a new file name is entered prior to each test, otherwise previous testing will be overwritten). Use a Decimation Factor of 100 to record at 10 Hz. Select the proper channels desired to be recorded. Leave all other options as is, as shown in Figure F.15.
17. To ensure all external LVDTs are properly reading, navigate to the bottom right quadrant. A plot with several channels listed on the left will appear, as shown in Figure F.16. Ensure all the relevant external LVDT channels are selected. Select the “Start” button near the top of the window. Narrow the Y-axis range so the plots are more visible and unselect the “AUTO” checkbox. Change the number under the X-axis from 1000 to 200. Go to each external LVDT and move the stem inward. Look at the resulting plot and make sure that all LVDTs responded and moved downward. Also, make sure the order in which the LVDTs were excited matches the order of shown on the plot (this ensures the LVDTs were connected to the intended channels).
18. To provide useful data, the load cell and external LVDTs must be zeroed. On the left panel open SYSTEM →Portal Frame → Group 1, right click the LOAD CELL and select set tare. The TARE dialog box will appear. Select “Tare Current Value,” as shown in Figure F.17. Repeat this for all external LVDTs. Note, do not tare the LVDT housed within the actuator at this point (named “LVDT”).
19. Manually advance the actuator using the text box to the right of the slider bar. Use caution to not prematurely apply load to the specimen. Since the Load Cell was zeroed

in the last step, the Load Cell readout presented just above the slider bar should be about 0 kip. When the actuator crosshead approaches the surface of the specimen, very slowly advance the actuator by manually moving it 0.01 to 0.05 in. at a time. Continue moving actuator crosshead until 0.01 to 0.02 kips are applied to the specimen. Select the small "Tare" button on the far right. This will make the current position of the actuator cross head read 0.0 in., as shown in Figure F.18.

20. Set the Ramp Rate to 0.0008 in/s, or at the desired rate. Select the "Start DAS" and "Arm Logger" buttons of the right, as shown in Figure F.19.
21. Select the "Setup Limits" button on the right and enter the desired values for the Load Cell. Ensure no other limits are selected.
22. If video cameras are being used, begin recording.
23. Select the "Start Logger" button on the right. Note the "Logger On" light will illuminate green, as shown in Figure F.20.
24. Open the Windows File Explorer to the destination where the data is intended to be written. Ensure a new text file was generated when the logger initiated.
25. Select the "Run" button near the top left of the window to begin the test, as shown in Figure F.21. Loading will continue until stopped. To end loading, select "Soft Stop." During testing, the Ramp Rate may be adjusted by simply entering a new rate. To pause the test, select "Pause." To resume the test after pausing, reselect the "Pause" button.
26. When loading is complete, the actuator can be lifted by gradually entering actuator positions in the text box to the right of the slider. When the actuator load returns to about 0 kips, select the "Stop Logger" button. At this point, the test is complete, and the system may be left idle in this position.
27. To turn off the hydraulic system, navigate to the Hydraulic Control panel and DEFULT program. Ensure the actuator crosshead can either fully extend downwards with no obstructions or rest on a broken specimen. Note, the actuator cross head weighs about 0.8 kip. Alternatively, use straps to hold the actuator head in the fully retracted position. Select "OFF" under the HSM 1 buttons. Next, select "OFF" under the HPS CONTROL buttons.

28. When the Shore Western control software is closed a prompt will appear asking “Are You Sure You Want To Close MDOF CONTROL SYSTEM.” Select Yes.
29. Open the front panel of the computer and inset a flash drive. Copy the data collected from testing.
30. Shutdown the computer.
31. Once the computer has shutdown, the fans on will continue to run as well as anything else connected to the auxiliary power pack. Press and hold the power button on the auxiliary power pack until a beep is sounded to completely turn off the system.
32. Cover the electronics to protect from dust.

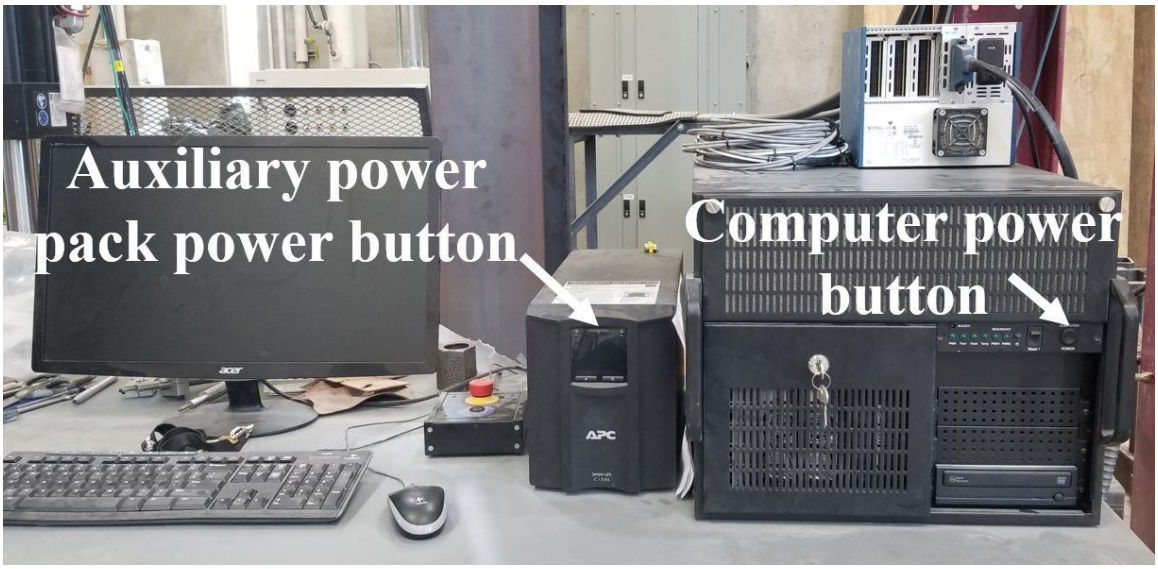

Figure F.1. Auxiliary power pack and computer power button locations

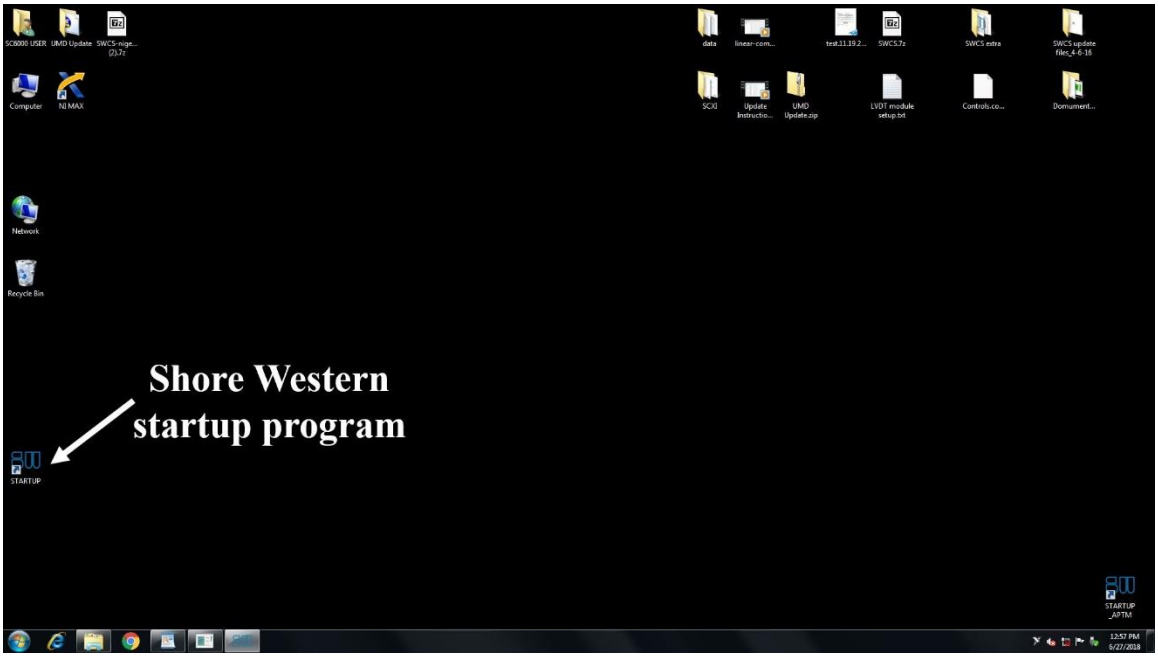

Figure F.2. Shore Western startup program icon

Figure F.3. Cooling unit housed outside of structural laboratory

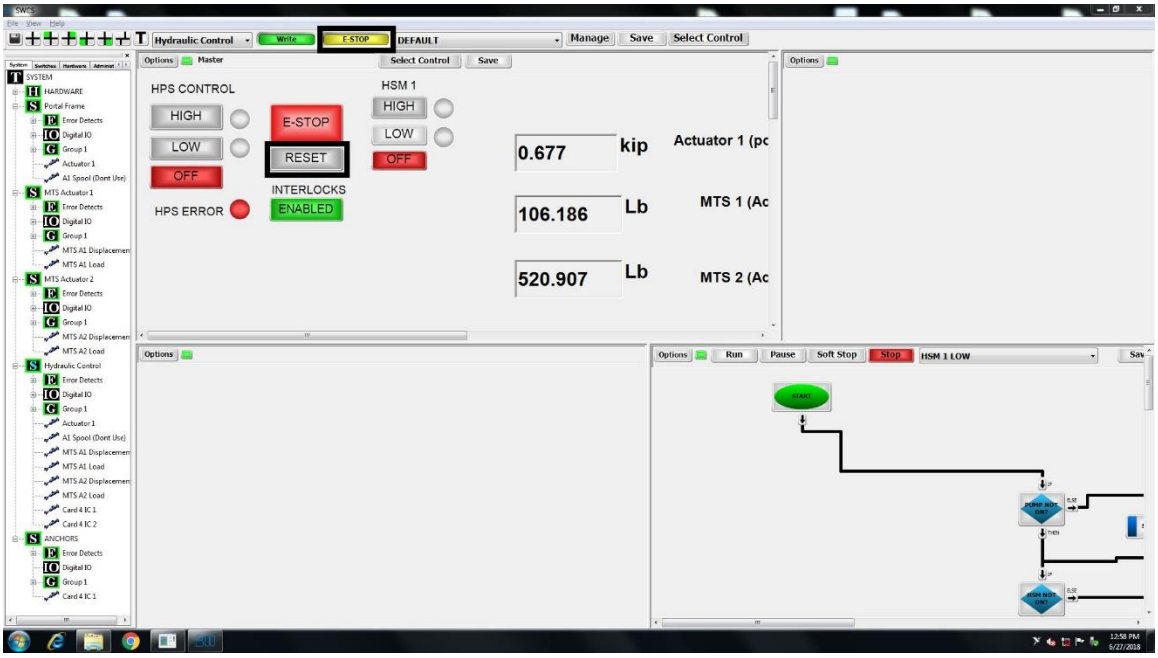

Figure F.4. “RESET” and “E-STOP” buttons in the software window

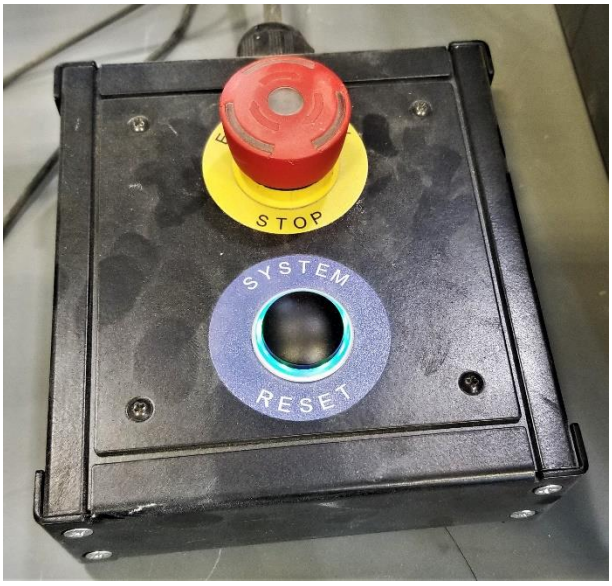

Figure F.5. Reset button illuminated with blue and green after being pushed

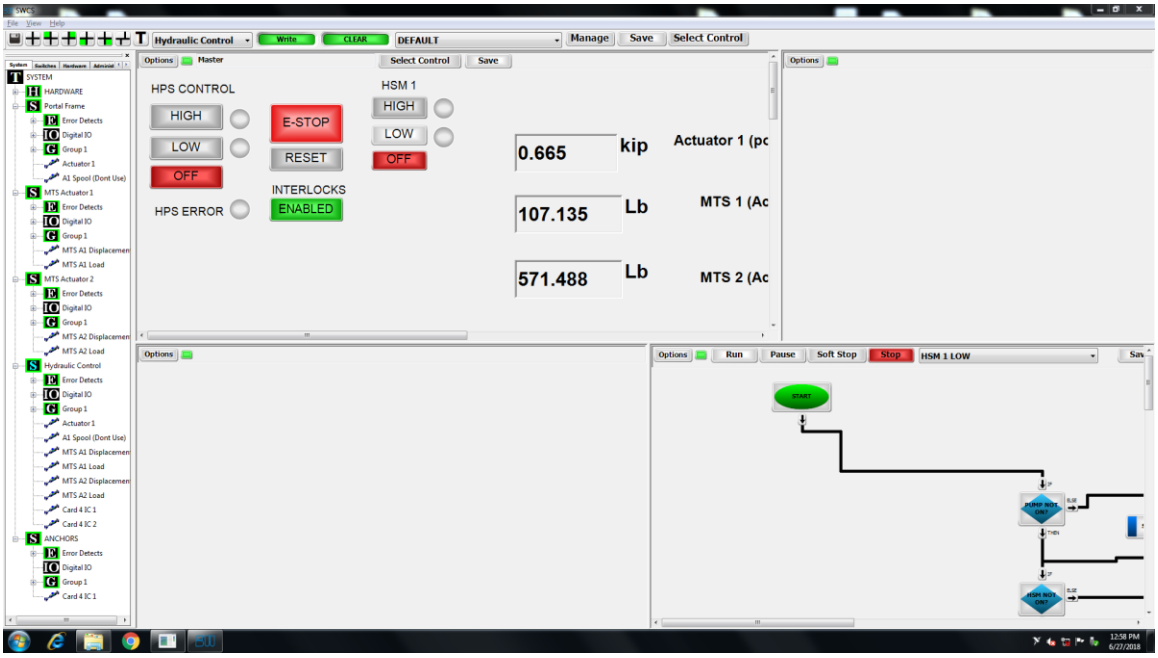

Figure F.6. Window status after system has been reset

Figure F.7. Two yellow pump lights illuminated on pump after HPS control has been set to “LOW”

Figure F.8. Two green pump lights illuminated on pump after HPS control has been set to “HIGH”

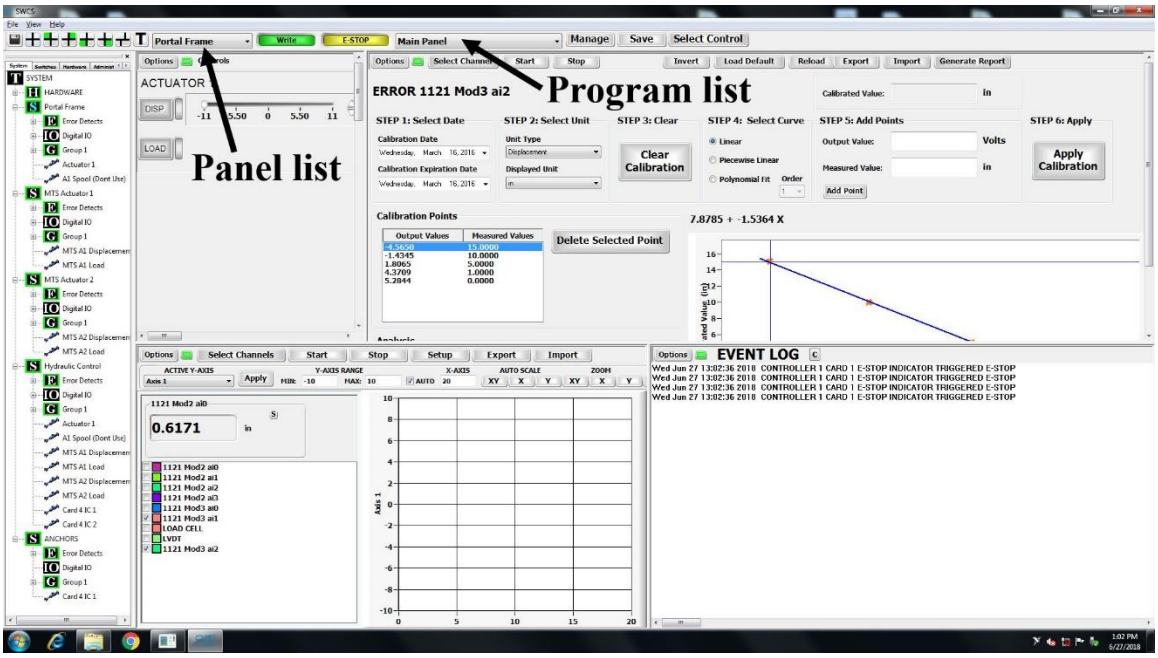

Figure F.9. Panel and program lists

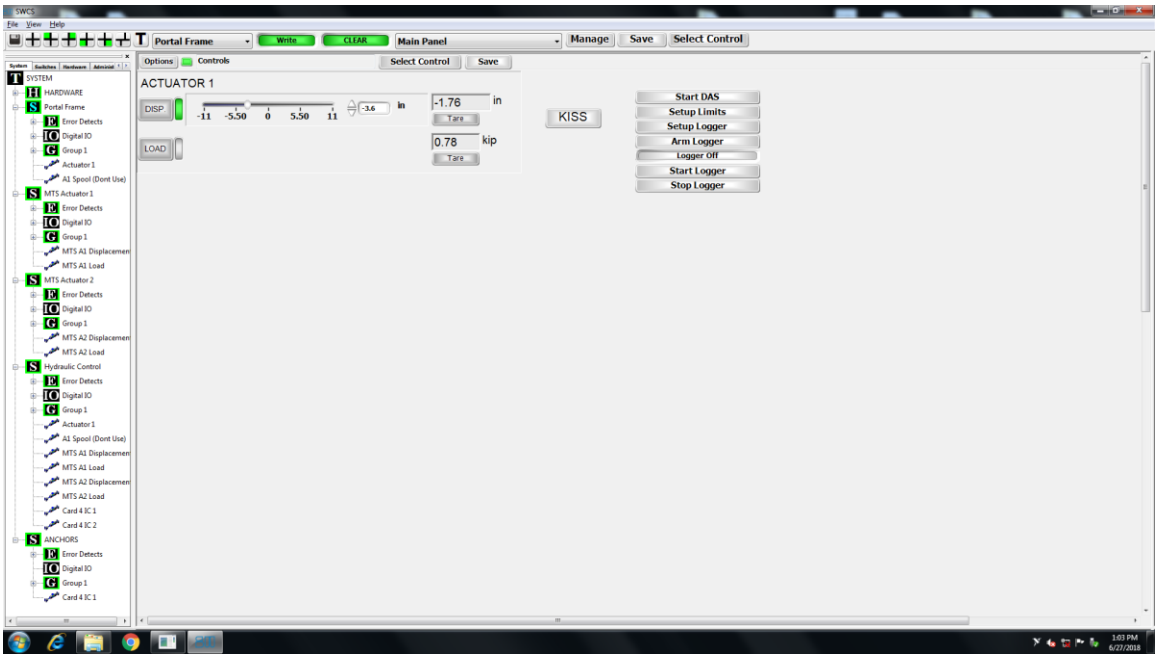

Figure F.10. Actuator 1 placed in displacement-controlled mode

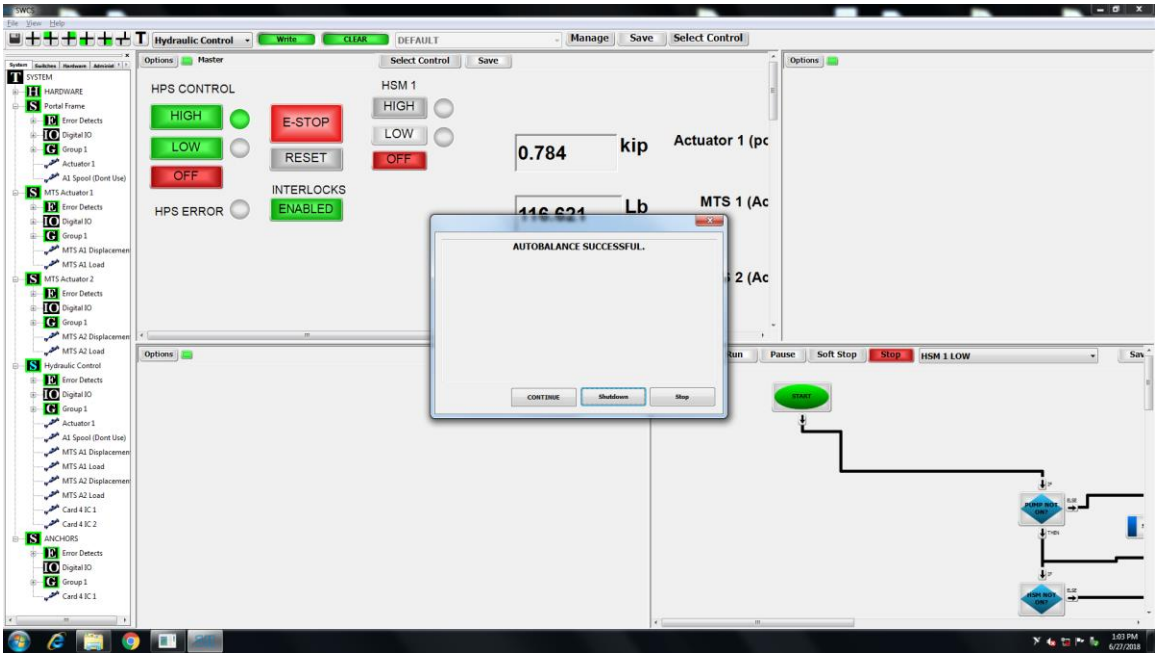

Figure F.11. Autobalance successful notification

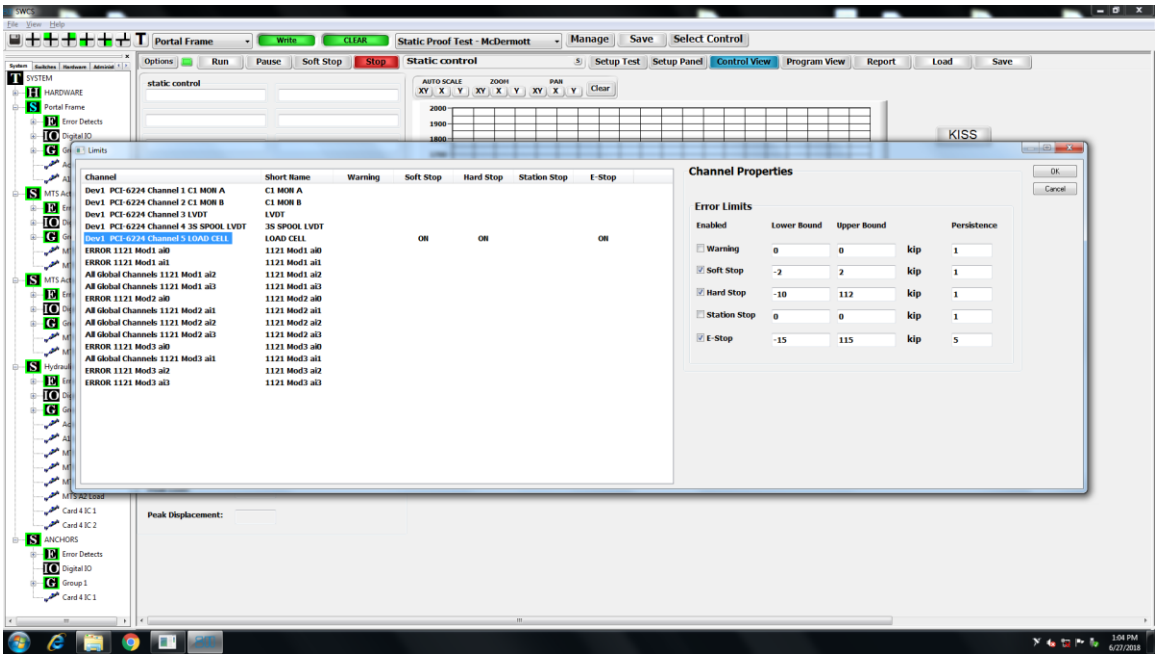

Figure F.12. Load cell limits decreased as a precaution during test setup

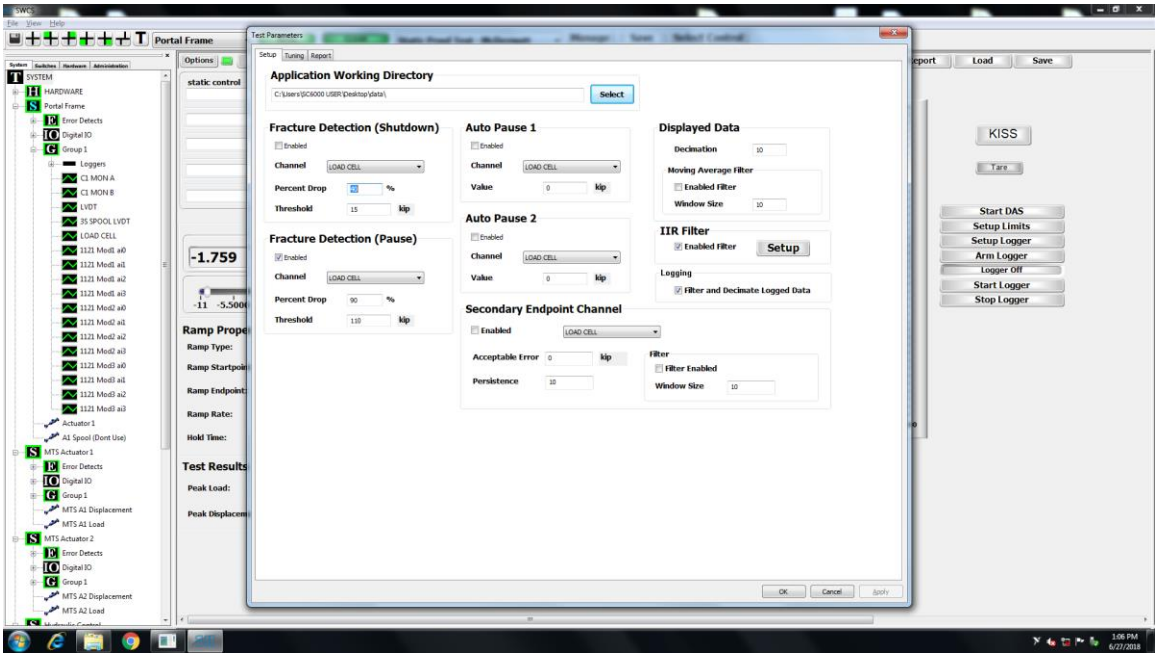

Figure F.13. Test parameters settings

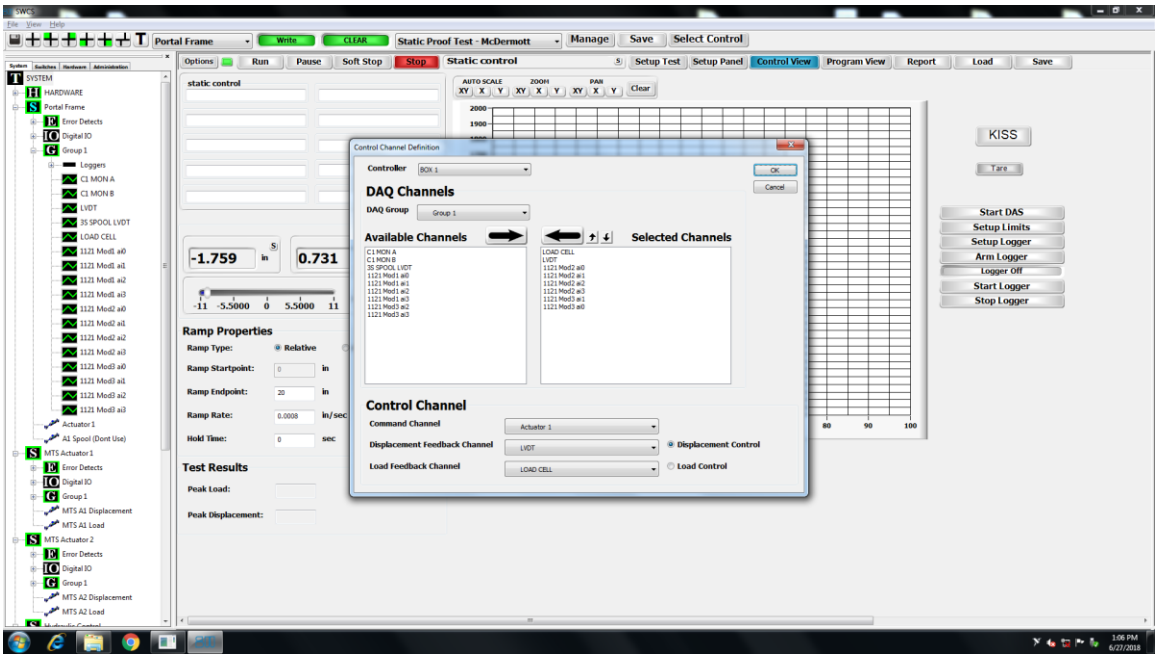

Figure F.14. Control channel settings

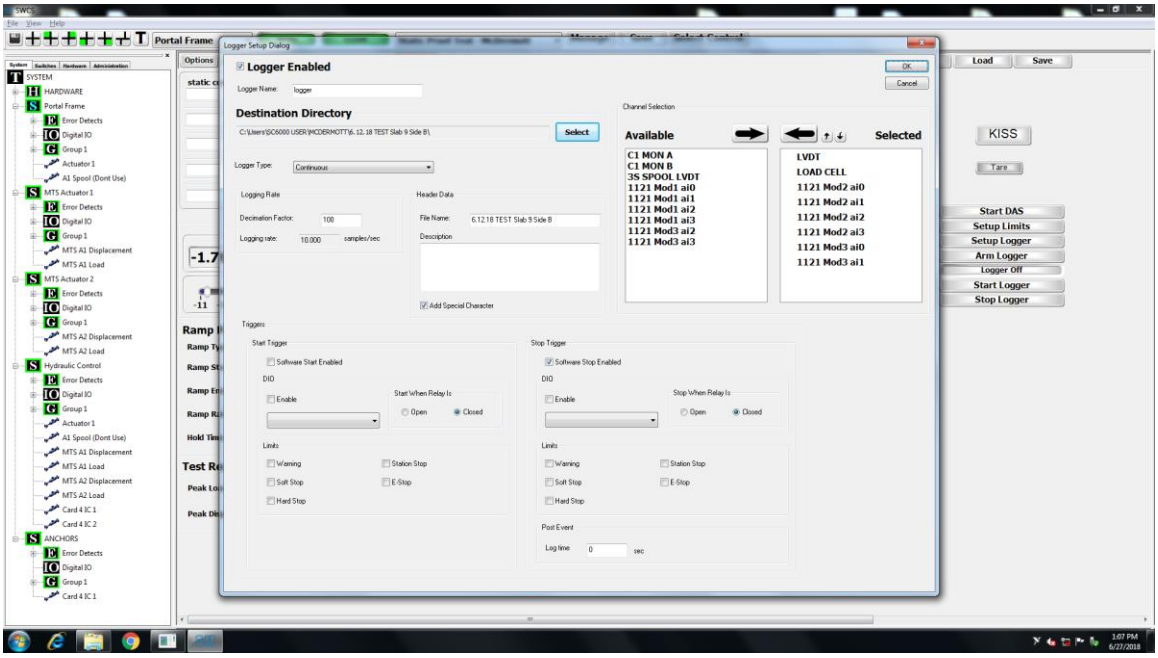

Figure F.15. Setup logger settings

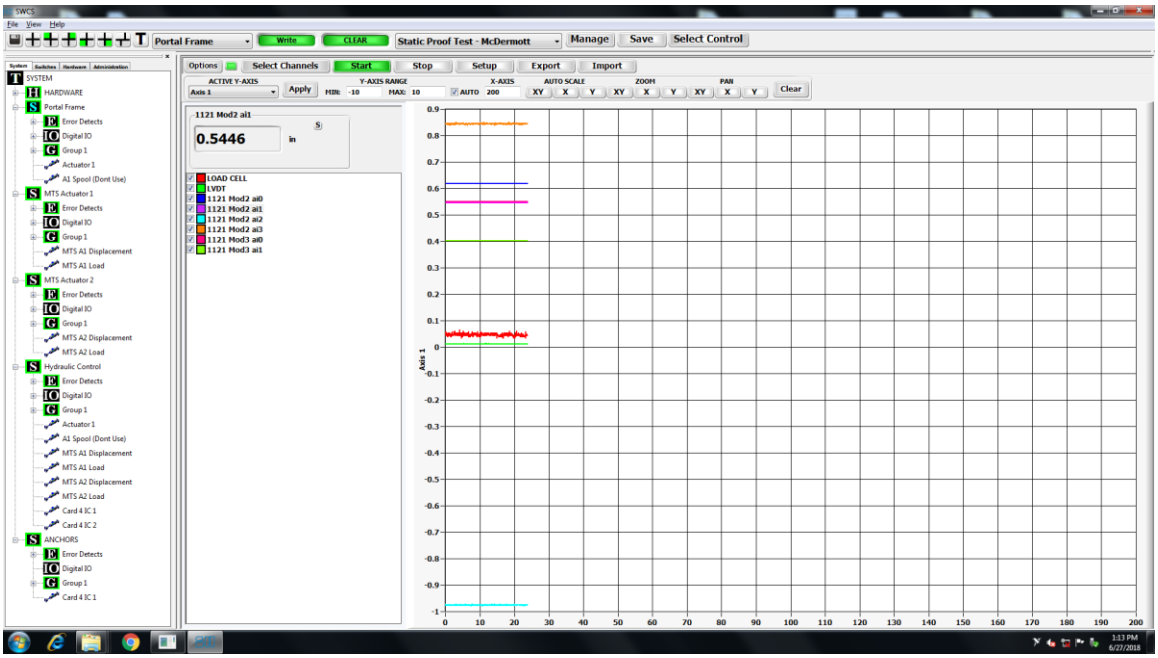

Figure F.16. Active display of instrumentation data

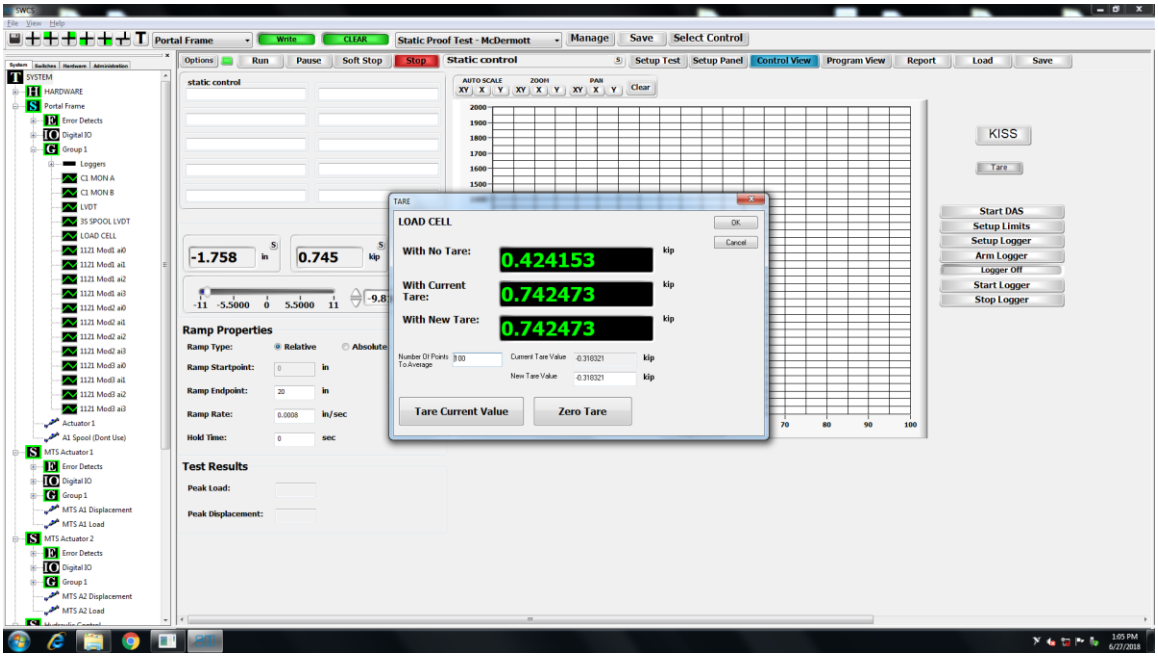

Figure F.17. Instrumentation tare dialogue box

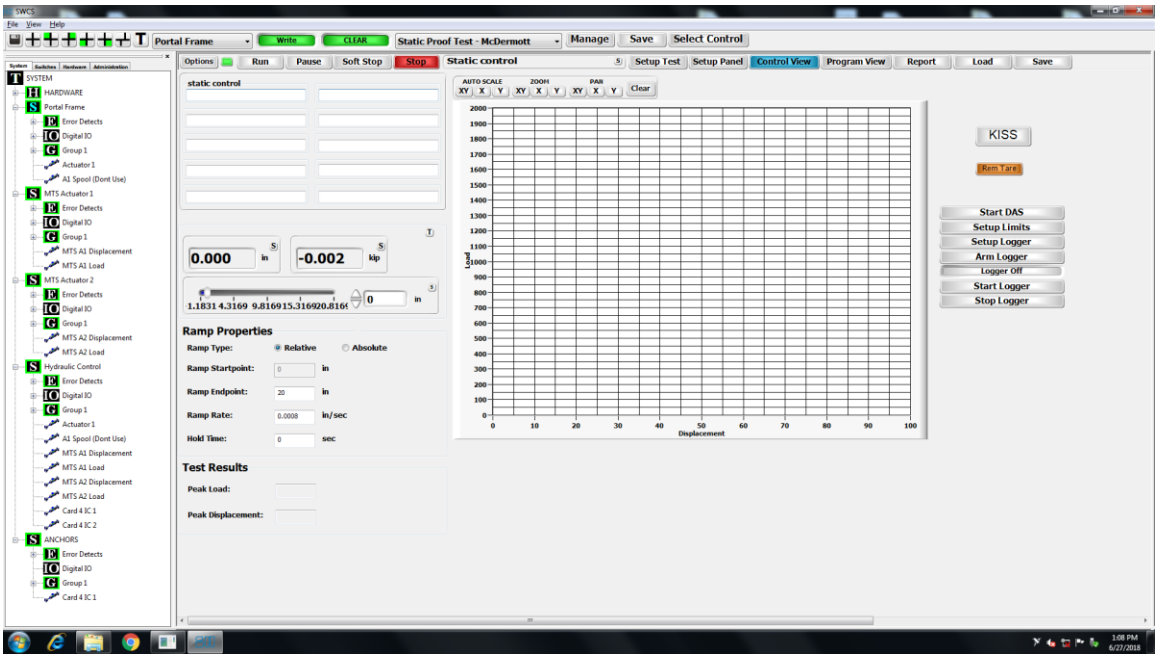

Figure F.18. Actuator cross head position tared

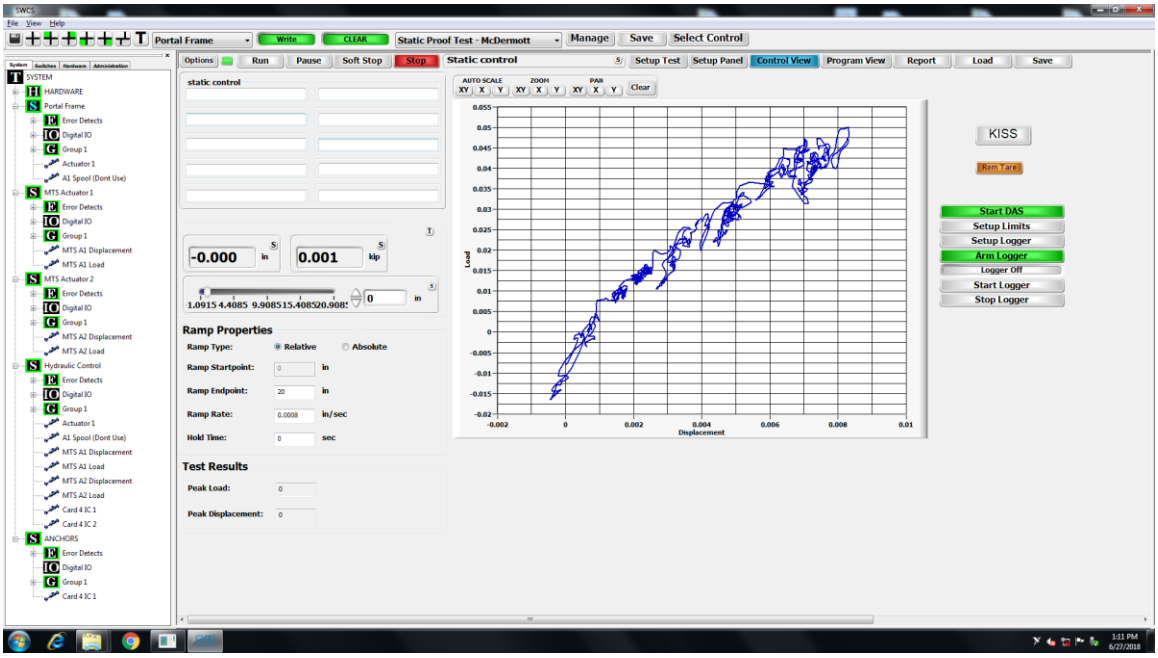

Figure F.19. “Start DAS” and “Arm Logger” buttons selected

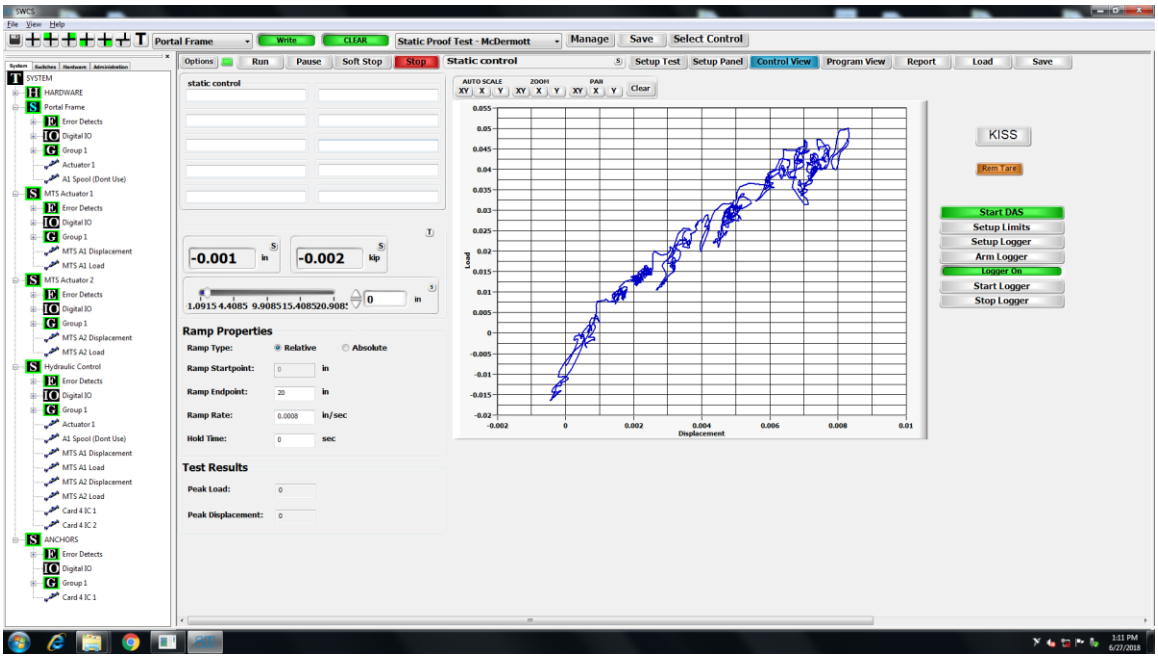

Figure F.20. Logger recording initiated

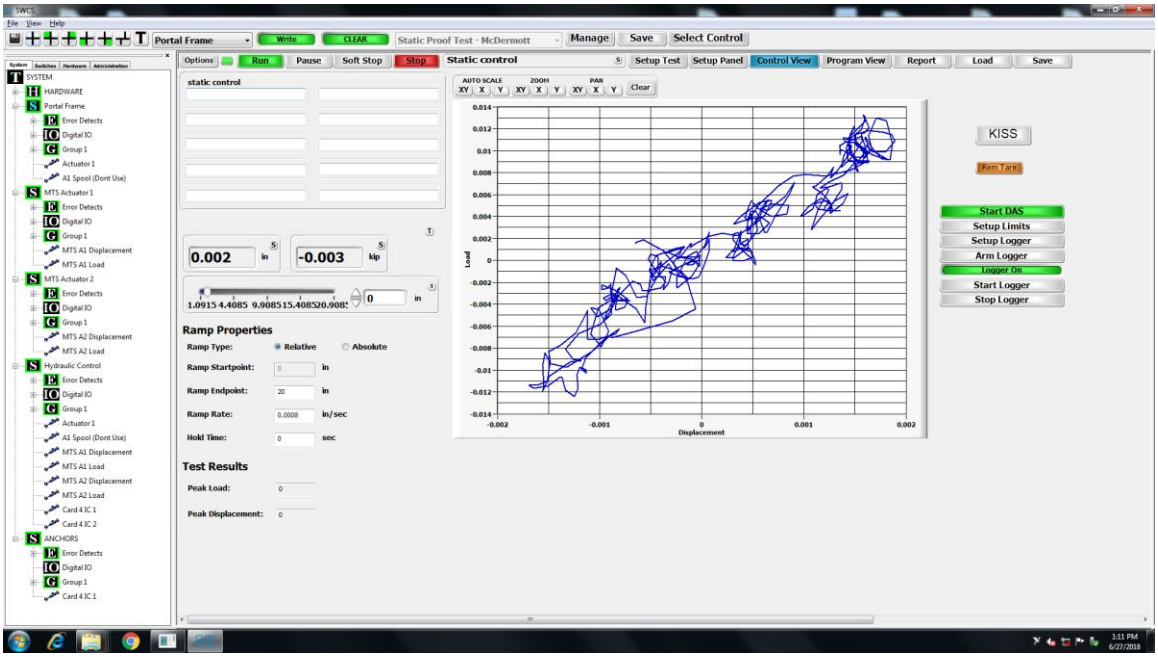

Figure F.21. Actuator loading commenced